PROCEEDINGS QTS'24

CONTENTS

Quantum Computing

Boris Arseniev Quantum Variational Least Squares Problem Solver 1

Danila Babukhin Echo-evolution data generation for quantum error mitigation via neural networks 3

Biriukov Yuri, Dyakonov Ivan, Svintsov Michail, Dryazgov Michail, Korneev Alexander, Straupe Stanislav, Kulik Sergei Boson sampling with optical feedback 5

Anton Vorobyev, Gleb Struchalin, Ivan Bobrov, Stanislav Straupe Image processing algorithms and automation detection of arrays of single neutral atoms 8

Ilya Gerasin, Nikita Zhadnov, Konstantin Kudeyarov, Ksenia Khabarova, Ilya Semerikov, Nikolay Kolachevskiy Design of Planar Pauli trap for quantum computing 11

Dmitry Guskov, Konstantin Antipin Performance of the QAOA algorithm in combinatorial problems in the presence of unital and non-unital noise 13

Semyon Zarutskiy, Aleksey Kadykov, Lianna Akopyan, Artur Matveev, Nikita Morozov, Kirill Lakhmanskiy Constructing Confocal Fabry-Perot cavity to stabilize multiple lasers for 40Ca+ optical qubit 16

Pavel Kamenskikh, Nikita Semenin, Ilia Zalivako, Ilia Semerikov, Nikolay Kolachevsky High-fidelity Light-Shift gate on the quadrupole transition in Yb ions 18

Andrei Kugut, Pavel Gladilovich, Grigory Mazhorin Quantum microwave link between fluxonium qubits 20

Arina Kuznetsova, Alena Kazmina, Ilya Simakov Demonstration of a parity–time symmetry breaking phase transition using superconducting qutrits 22

Alexey Moiseevskiy, Sofya Manko Simulation of quantum attack on S-AES with key leakage and reduced number of qubits 24

Varvara Mikhailova, Gleb Struchalin Compiler Development for Atomic Quantum Computing 25

Anastasiia S. Nikolaeva, Ilia V.Zalivako, Alexander S. Borisenko, Evgeniy O. Kiktenko, Ilya A. Semerikov, Nikolay N. Kolachevsky, Aleksey K. Fedorov Quantum algorithms with qubits packaged in trapped-ion qudits 27

Artem Rozanov, Boris Bantysh, Gleb Struchalin, Ivan Bobrov, Stanislav Straupe Randomized benchmarking of qubit arrays on a cold neutral atom quantum processor 29

Mikhail Sergeev, Gleb Fyodorov, Marina Bastrakova Quantum state preparation for qubit circuit using meta-heuristic and deep learning methods 31

Elizaveta Soboleva, Dmitriy Shcherbinin, Semyon Rudyi, Andrei Ivanov Optically controlled bistability of charged particles in surface ion traps 33

Elena Chernykh, Mikhail Saygin, Gleb Struchalin, Sergey Kulik, Stanislav Straupe Quantum optical neural networks with programmable Kerr nonlinearities 35

Alexander Chudakov Analysis of quantum computing resources in the implementation of basic quantum algorithms on qudit systems 37

Quantum Cryptography

Bugai Kirill, Zyzykin Artem, Bulavkin Daniil, Sushchev Ivan, Dvoretskiy Dmitriy Protection Method against Powerful Emission Attacks Based on Optical-Fiber Fuse Element 40

Daniil Bulavkin, Ivan Sushchev, Kirill Bugai, Anna Sidelnikova, Dmitriy Dvoretskiy Study on the dependence of the Backflash probability of single-photon detectors on the avalanche signal magnitude 43

Vakhrusheva V.M., Moiseeva E.A., Klimov A.N. Estimations of background noise and aperture losses for a free-space quantum key distribution 45

Mikhail Gellert, Boris Nasedkin, Vladimir Chistiakov, Vladimir Egorov Research of a time shift attack on a subcarrier wave quantum key distribution system 47

Yuliya Ivanova, Kirill Bugai, Artem Zyzykin, Daniil Bulavkin, Ivan Sushchev, Anna Sidelnikova, Dmitriy Dvoretskiy Method for evaluating the effectiveness of protection against combined beam splitting attack and laser damage attack on fiber-optical attenuators widely used in QKD systems 49

Dmitry Melkonian, Konstantin Kravstov, Sergei Kulik The effect of turbulent disturbances in atmospheric communication channels in entaglement-based QKD systems 52

Boris Nasedkin, Azat Ismagilov, Vladimir Chistiakov, Andrei Gaidash, Anton Tcypkin, Anton Kozubov, Vladimir Egorov Countermeasure to an attack with induced photorefraction in visible range on quantum key distribution systems 55

Daniil Reshetnikov, Andrey Sokolov, Evgenii Vashukevich, Victor Petrov, Tatiana Golubeva The Protocol of Quantum Key Distribution on Axially Symmetrical Polarization Beams in the Atmospheric Channel 57

Anna Sidelnikova, Daniil Bulavkin, Kirill Bugai, Ivan Sushchev, Artem Zyzykin, Dmitriy Dvoretskiy Investigation of spectral characteristics of the backflash from single-photon avalanche photodiode 59

Konstantin Stepanov, Alina Borisova Dead time duration influence of SPAD on quantum key distribution parameters 61

Ivan Sushchev, Daniil Bulavkin, Kirill Bugai, Anna Sidelnikova, Artem Zyzykin, Dmitriy Dvoretskiy Upper bounds for Trojan-horse attack key leakage in QKD systems 63

Vladislav Tretiakov, Andrey Klimov, Konstantin Kravtsov Phase-encoded quantum key distrivution system over multimode communication channels 65

Arkadiy Chernov, Aleksandr Khmelev, Vladimir Kurochkin Fast frequency recovery using qubits for practical satellite quantum communication 68

S.V. Alferov, M.V. Orlova, M.M. Shvygina1 Investigation of the effect of attenuator made by fusion splicing offset fiber ends on the excitation of cladding modes in a single-mode fiber. 70

Quantum Optics

E. N. Bashmakova, S. B. Korolev, T. Yu. Golubeva Generation of squeezed Fock states and their application to quantum error correction codes 72

Robert Grinshteil, Mikhail Saygin, Suren Fldzyan, Stanislav Straupe, Sergey Kulik The dynamics of spatial modes in curved multimode integral optical waveguides 74

A. Yu. Dmitriev, A.V. Vasenin, S.A. Gunina, T.R. Sabirov, A.A. Elistratov, S.V. Remizov, V.V. Pogosov and O.V. Astafiev Wave mixing of classical and non-classical signals on a single superconducting artificial atom 76

Ilenkov Roman Yaroslavovich, Prudnikov Oleg Nikolaevich, Taichenachev Alexey Vladimirovich, Yudin Valery Ivanovich Dynamics of laser cooling and trapping of alkali atoms in pure-optical two-frequency light trap 78

Peter Zacharenko, Dmitry Tsarev, Alexander Alodjants Random and superradiant lasers based on 2D materials with network structure 80

Danil Malyshev, Valentin Averchenko, Kirill Tikhonov Influence of dispersion on radiation of a synchronously pumped optical parametric oscillator (SPOPO) 85

Mansur Minnegaliev, Konstantin Gerasimov, Albert Khayrullin, Sergey Moiseev Narrow-band source of polarization-entangled photon pairs in the telecommunications wavelength range for quantum repeater 87

Pashin Dmitrii Sergeevich, Bastrakova Marina Valerievna The microwave transmission and the collective excitation of superconducting qubits coupled to a multilevel system 88

Dmitrii Potapov, Kirill Tikhonov Study of collective effects in spin-polarized atomic ensemble beyond mean-field theory approximation 90

Vladimir Chashchin, Olga Lyga, Evgeny Lipatov Magnetometry based on H3 color centers in diamond 92

Quantum Technology

Darya Bykova, Petr Skakunenko, Anton Afanasiev, Victor Balykin Microwave Spectroscopy of Cold Rb Atoms Localized Near an Atom Chip 94

Julia Zotova, Shtefan Sanduleanu, Gleb Fedorov, Rui Wang, Jaw-Shen Tsai, Oleg Astafiev Control and readout of a transmon using a compact superconducting resonator 96

Fedor Maksimov, Anastasia Goldt, Sergey Dozmorov, Yuriy Gladush, Albert Nasibulin, Alexander Chernov Optical properties of individual single-walled carbon nanotubes 98

Pavel Pikunov, Dmitry Pashin, Marina Bastrakova, Igor Soloviev, Nikolay Klenov Control of states of a two-terminal superconductor interferometer using Landau-Zinner transitions... 100

Rybin Dmitrii Andreevich, Pashin Dmitrii Sergeevich, Bastrakova Marina Valerevna, Shchegolev Andrei Evgenevich, Klenov Nikolai Viktorovich, Solovev Igor Igorevich Implementation of XOR logic in superconductor artificial neural network 102

Sergey Svyatodukh, Alexander Divochiy, Pavel Morozov, Vladislav Andreev, Gregory Goltsman Superconducting microstrip single-photon detectors with ultra high time resolution 104

Kseniia Urusova, Ilya Kondratyev, Artem Argenchiev, Sergey Kuzmin, Nikolay Skryabin, Ivan Dyakonov, Stanislav Straupe, Sergey Kulik Effective programming of a photonic processor with complex interferometric structure 107

Kirill Uyangulov, Gleb Struchalin, Stanislav Straupe Cold-atom array assembly with graph theory and combinatorial optimization 109

Emil Chiglintsev, Artem Abramov, Vasily Kravtsov, Alexander Chernov Development of Two-Dimensional Moire Structure Based Quantum Simulator: Optical Characterization 111

Chudakova Tatyana, Kazmina Alena, Mazhorin Grigory, Moskalenko Ilya Investigation of the decoherence channels of the fluxonium qubit 114

Andrei Chuchalin, Evgeniy Anikin, Kirill Lakhmanskiy MS gate infidelity due to high-order Lamb-Dicke terms 117

Nail' Shafeev, Akat'ev Dmitriy, Dinislam Turaykhanov, Alexey Kalachev Quantum hashing functions based on the orbital angular momentum of light 120

M.O. Yaushev, D. A. Mishin, D. O. Tregubov, D. I. Provorchenko, N. N. Kolachevsky, A. A. Golovizin A 2D MOT of Tm atoms as a compact source for continuous loading of a narrow-line 3D MOT 122

Miass, Russia February 25 – March 2, 2024
7th International School on Quantum Technologies

Quantum Variational Least Squares Problem Solver

Boris Arseniev[1*]

[1] *Skolkovo Institute of Science and Technology, Moscow, Russian Federation*
*E-mail: boris.arseniev@skoltech.ru

Abstract

The least squares method is a widely used technique in machine learning and other domains of science. It can be formulated as follows: Find $\mathbf{x}$ such that $\|\mathbf{b} + A\mathbf{x}\|$ is minimum, thus such $\mathbf{x}$ will be solution to $A\mathbf{x} = \mathbf{b}$, where $A \in \mathcal{R}^{N\times N}$ and $b, x \in \mathcal{R}^N$. In this research we present a way to implement this technique on a quantum computer. Additionally, we propose a similar implementation to solve systems of nonlinear equations using Newton's method.

Introduction

One of the most famous algorithms for achieving exponential speedup using a quantum computer is the HHL algorithm [1]. This algorithm provides a solution to a linear system; more precisely, the goal is to prepare a quantum state whose amplitudes are proportional to the desired solution. Thus, this algorithm cannot be used to efficiently obtain the solution itself, but only to obtain expected values for some observables.

The problem of solving a system of equations may be also approached by using variational algorithm [2, 3]. It is a quantum-classical hybrid approach where the evaluation of the cost function is delegated to a quantum computer, while the optimization of the variational parameters is performed using a conventional classical computer. In this case, difficulties might appear for finding the suitable cost function.

In this work we present a way for solving the least squares problem on a quantum computer. Additionally, we propose a similar implementation to solve systems of nonlinear equation using Newton's method. It is worth noting, that the solution to the system given by our quantum implementation is not encoded in the wave function, but in the variational parameters.

Quantum Variational Least Squares Problem Solver

Here, we present a variational quantum algorithm for solving the least squares problem, which for a system of N equations requires a total of $n = \lceil \log_2(N) \rceil + 1$ qubits. Consider a system of equations:

$$\begin{cases} f_1(\mathbf{x}) = 0 \\ \dots \\ f_N(\mathbf{x}) = 0 \end{cases}, \tag{1}$$

where $\mathbf{x} \in \mathcal{R}^N$ is vector of variables and $f_j(\mathbf{x})$ are nonlinear functions. We introduce the Hamiltonian

$$H(\mathbf{x}) = \begin{pmatrix} 0 & F^\dagger F \\ F^\dagger F & 0 \end{pmatrix}, \text{ where } F \equiv F(\mathbf{x}) = \begin{pmatrix} f_1(\mathbf{x}) & \dots & 0 \\ 0 & \ddots & 0 \\ 0 & \dots & f_N(\mathbf{x}) \end{pmatrix}. \tag{2}$$

Let's now consider the state $|\psi\rangle = e^{i\epsilon H(\mathbf{x})} |\phi_{init}\rangle$, where $|\phi_{init}\rangle = |0\rangle \otimes |+\rangle^{\otimes n} \equiv |0\rangle |+\rangle$. If we project $|\psi\rangle$ on state $|1\rangle |+\rangle$ and take a sufficiently small ϵ we get

$$\left| \langle 1| \langle +| e^{i\epsilon H(\mathbf{x})} |0\rangle |+\rangle \right| \approx \epsilon \left| \langle +| F^\dagger F |+\rangle \right| \sim \|\mathbf{f}(\mathbf{x})\|, \text{ with } \mathbf{f}(\mathbf{x}) = (f_1(\mathbf{x}), \dots, f_N(\mathbf{x}))^T. \tag{3}$$

We seek to variationaly minimize $\mathbf{x}^* = \arg\min_{\mathbf{x}} \left| \langle 1| \langle +| e^{i\epsilon H(\mathbf{x})} |0\rangle |+\rangle \right|$ since such $\mathbf{x}^*$ will be a solution to the system (1). If functions f_j are linear we can rewrite this system as $A\mathbf{x} = \mathbf{b}$ and then $\mathbf{x}^* = A^{-1}\mathbf{b}$.

Quantum Variational Newton Method

We can modify matrix $F(\mathbf{x})$ in (2) as follows:

$$F \equiv F(\mathbf{x}) = \begin{pmatrix} f_1(\mathbf{x}) & \dots & 0 \\ 0 & \ddots & 0 \\ 0 & \dots & f_N(\mathbf{x}) \end{pmatrix} + \begin{pmatrix} [J(\mathbf{x})\mathbf{y}]_1 & \dots & 0 \\ 0 & \ddots & 0 \\ 0 & \dots & [J(\mathbf{x})\mathbf{y}]_N \end{pmatrix}, \tag{4}$$

where we denote $[J(\mathbf{x})\mathbf{y}]_j$ as a j-th component of Jacobian matrix J for system (1) multiplied by some vector $\mathbf{y} \in \mathcal{R}^N$. Thus, minimization over $\mathbf{y}$ will end up with $\mathbf{y}^* \approx -J^{-1}(\mathbf{x})\mathbf{p}(\mathbf{x})$. The algorithm then consists on iteratively performing this minimization, followed by taking the variational parameters $\mathbf{y}_k^*$ and adding them together thus obtaining the solution via Newton method $\mathbf{x}_{k+1} = \mathbf{x}_k + \mathbf{y}_k^* \approx \mathbf{x}_k - J^{-1}(\mathbf{x}_k)\mathbf{p}(\mathbf{x}_k)$.

Results

We simulated and compared our variational quantum algorithms to their classical counterparts (meaning that the cost function $\|\mathbf{f}\|$ or $\|\mathbf{f} + J\mathbf{y}\|$ is implemented classically). We compared their performance on 100 randomly generated systems of quadratic polynomials of 4 equations, meaning we randomly generated coefficients for these equations. For both problems, performance turned out to be the same as in their classical counterparts. To the least squares problem we obtained $\|\mathbf{f}\| = 0.33 \pm 0.34$ for classical and $\|\mathbf{f}\| = 0.35 \pm 0.35$ for quantum. In the case of Newton's method the results are exactly the same for both classical and our quantum implementation. It is worth noting, that the solution to the system given by our quantum implementation is not encoded in the wave function, but in the variational parameters.

References

[1] *Harrow, Aram W., Avinatan Hassidim, and Seth Lloyd*, Quantum algorithm for linear systems of equations. Physical review letters 103.15 (2009): 150502.

[2] *Lubasch, Michael, et al*, Variational quantum algorithms for nonlinear problems. Physical Review A 101.1 (2020): 010301.

[3] *Cerezo, Marco, et al.*, Variational quantum algorithms. Nature Reviews Physics 3.9 (2021): 625-644.

Miass, Russia February 25 – March 2, 2024
7th International School on Quantum Technologies

Echo-evolution data generation for quantum error mitigation via neural networks

Danila Babukhin[1*]

[1] *Dukhov Research Institute of Automatics (VNIIA)*
*E-mail: dv.babukhin@gmail.com

Abstract

In this work we demonstrate a physics-motivated method to generate training data for quantum error mitigation via neural networks, which does not require classical simulation and target circuit simplification. In particular, we propose to use the echo evolution of a quantum system to collect noisy and noise-free data for training a neural network. Having a vector of observable values of the initial (noise-free) state and the resulting (noisy) state allows us to compose training data for a neural network. We demonstrate that a feed-forward fully connected neural network trained on echo-evolution-generated data can correct results of forward-in-time evolution.

Nowadays quantum computers are affected with different sources of noise (gate noise, decoherence and energy relaxation, crosstalk), which hinder advantage of these devices. Before quantum fault-tolerant computing (using error correction codes) becomes possible, quantum error mitigation - compensation of noise influence by classical postprocessing - will be the main method of obtaining meaningful results from quantum processors.

One of the prospective approaches to quantum error mitigation is using neural networks for data post-processing. We can train a neural network to compensate noise in the outcomes of quantum computing [1]. To train a neural network, we need to have both noise-affected and noise-free data of a target quantum computing problem. For small-size problems, we can use classical simulation to gather such data. Contrary, for quantum-advantage-size problems, we cannot afford classical simulation for generating training data.

In this work, we propose a method to generate training data without the use of classical simulation [2]. This method is applicable for any target quantum process (e.g., simulation of a many-body system evolution, or running a quantum algorithm), as this method only requires the ability to run the target unitary process. The method is called echo-evolution data generation, and the main idea is depicted in Fig. 1 for the case of simulation of quantum system dynamics. Consider we have a quantum system

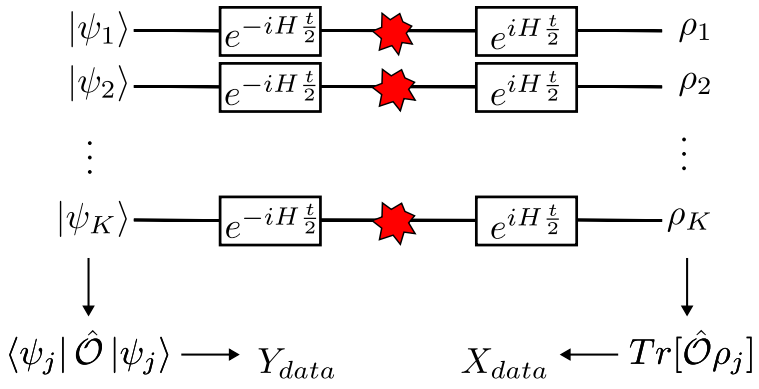

Figure 1: A schematic of echo-evolution data generation. Here the target quantum process is simulating dynamics of a quantum system with a hamiltonian H.

with a hamiltonian H, and we want to simulate its dynamics on a quantum processor. We can generate training data for a neural network, using echo dynamics - a kind of dynamics, when the system evolves forward and backward in time, and the final state of the system is the initial state. If we use a noisy

quantum processor for simulation, the final state will be different from the initial due to the influence of noise. Using the initial (noise-free) and the final (noisy) quantum states, we can gather noise-free and noisy data for training a neural network.

As a use-case for the proposed method, we simulate the dynamics of a spin system under the transverse field Ising hamiltonian

$$H = -h\sum_{i=1}^{N}\sigma_i^X - J\sum_{ij}^{N}\sigma_i^Z\sigma_j^Z. \tag{1}$$

Evolution of a quantum system then is applying an evolution operator - an exponent of the hamiltonian - to the initial state $|\psi(0)\rangle$:

$$|\psi(t)\rangle = e^{-iHt}\,|\psi(0)\rangle$$

The simulation of system dynamics on a quantum computer was implemented via Trotterization of the evolution operator - decomposition of a hamiltonian exponent into parts, which can be implemented with basis gates of a quantum processor:

$$e^{it(H_A+H_B)} \approx (e^{i\frac{t}{N}H_A}e^{i\frac{t}{N}H_B})^N$$

We demonstrate the echo-evolution data generation method via simulating an evolution of spins magnetization. We show, that a fully-connected neural network, trained on echo-generated data, can compensate noise influence in forward-in-time evolution of the spin system magnetization (see Fig.2).

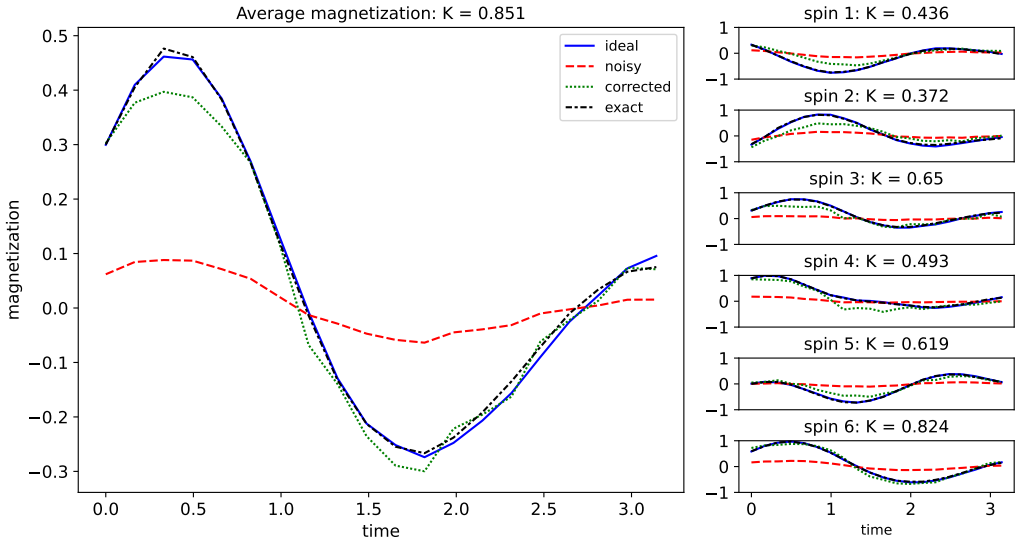

Figure 2: Dynamics of magnetization in a system of 6 spins without noise ("ideal"), with noise ("noisy"), after neural network postprocessing ("corrected"), and exact dynamics ("exact"). The K coefficient demonstrates cumulative difference between magnetization in all time points, for all 6 spins (left figure), and for single spins (right figures).

References

[1] *A.A. Zhukov, W.V. Pogosov*, Quantum error reduction with deep neural network applied at the post-processing stage. Quantum Inf Process 21, 93 (2022).

[2] *D.V. Babukhin*, Echo-evolution data generation for quantum error mitigation via neural networks, arXiv:2311.00487 [quant-ph]

Miass, Russia February 25 – March 2, 2024
7th International School on Quantum Technologies

Boson sampling with optical feedback

Yu. Biriukov[1*], I. Dyakonov[1], M. Svintsov[2],M. Dryazgov[2], A. Korneev[1,2], S. Straupe[1], S. Kulik[3,4]

[1] *Quantum technology centre, Lomonosov Moscow State University, Moscow, Russia*
[2] *National Research University Higher School of Economics, Moscow, Russia*
[3] *Lomonosov Moscow State University, Moscow, Russia*
[4] *Laboratory of quantum engineering of light, South Ural State University (SUSU), Russia, Chelyabinsk, 454080, Prospekt Lenina 76*
*E-mail: biriukov.ia18@physics.msu.ru

Abstract

We report a design, implementation and full characterisation of linear-optical interferometer with optical feedback. Several boson sampling experiments were conducted to get the information about simulation complexity of our device. The application of the device to the quantum simulation problems is also discussed.

Introduction

First of all, let us introduce the notion of "optical feedback". Imagine you have an ordinary linear-optical interferometer with transfer matrix U. Conventionally all output modes of the interferometer are followed by detection on optical radiation. We will call an "optical feedback" the case when some of the output modes are looped to the input modes through any optical path.
The motivation to use such interferometer comes from the fact that large-scale linear-optical interferometers are hard to align and fabricate. For example, if a 10-mode universal interferometer is required, it will contain about a hundred phase shifters [1], moreover, there is a so-called "crosstalk" between many of them: one phase shifter acts on neighboring ones and change the phase. From the experimenter's point of view, the task of calibrating such a circuit becomes very complicated. If we use temporal encoding of information, i.e. in addition to the interferometer modes themselves, using the time of arrival of the optical signal to the circuit input modes, it is possible to effectively increase the size of the interferometer without actually scaling it. Also using optical feedback will help to ensure connection between different timestamps in order to expand the class of transformations that can be performed. All of the mentioned above, in principle, allows us to study interferometers of arbitrarily large dimensions and go into an area that cannot be simulated on a classical computer[2].

1 Theoretical model

Let's move on to the theoretical description of the circuit with optical feedback. If we consider the time sweep of the interferometer (see Fig. 1), we can see that this scheme reduces to an interferometer of a larger dimension, whose transfer matrix depends on the transfer matrix of the base interferometer and on the way the input and output modes are connected.

Therefore, if we limit ourselves to a given number of iterations, for example, intentionally blocking feedback channels every N cycles, then the evolution of the state of photons in such a scheme is reduced to the usual problem of boson sampling in an interferometer with a given transfer matrix.
For example, if we have a multi-mode Fock state $|\vec{S}\rangle = |s_1 s_2 ... s_N\rangle$ (where s_i is the number of photons in i-th mode) in the input N modes of the interferometer with transfer matrix U then the probability to observe the state $|\vec{T}\rangle$ (which can be written as $|\vec{S}\rangle$) in the output modes is

$$P(\vec{T}|\vec{S}) = perm(U^{(S,T)}), \tag{1}$$

where $U^{(S,T)}$ is the matrix generated from U taking i-th column t_i times and j-th row s_j times, and $perm$ is a permanent of this matrix.

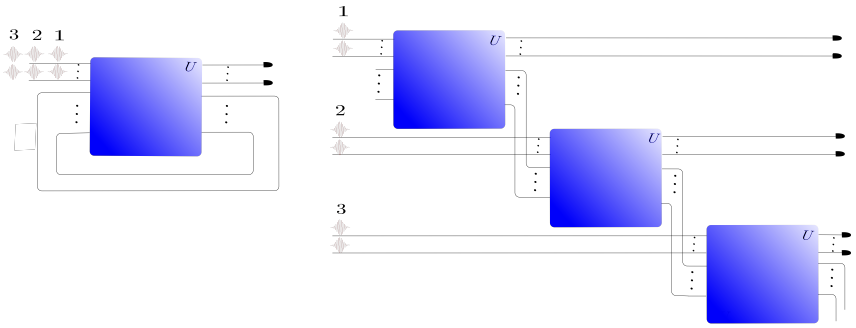

Figure 1: (On the left)The scheme of linear optical interferometer with optical feedback.(On the right) Time sweep of this interferometer.

It turns out that the computational complexity of calculation of a permanent grows exponentially with the matrix size, which makes the problem of calculating the whole output distribution and, as a consequence, getting samples out of it, classically intractable. That is why boson sampling problem is interesting: it is possible to show quantum supremacy just by counting photons in the output modes of a sufficiently large interferometer.

2 Experimental setup and results

On the Fig. 2 you can see a prototype of an experimental setup that includes a 12-mode interferometer with of of the output channels looped to the input. The optical feedback loop is a fiber delay with a

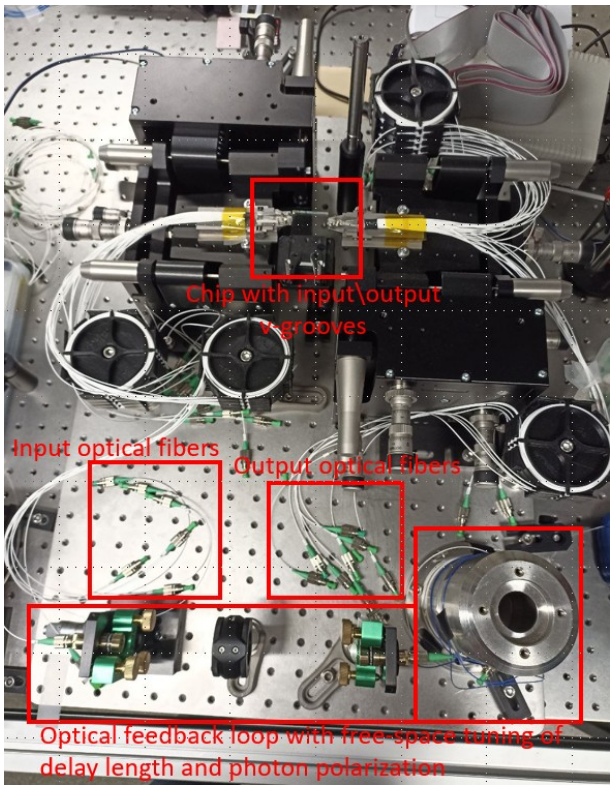

Figure 2: Experimental setup of the interferometer with one optical feedback loop.

free-space gap for fine-tuning of the delay length and adjusting the polarization of the radiation.
We conducted a boson sampling experiment with a single loop and 4 input photons and compared the

results of the experiment with simulation (see Fig. 2). Only 1- and 2-photon events are depicted. We achieved mean 90% fidelity between all multi-photon output distributions. The primary limitation is the accuracy of transfer matrix tomography procedure[3].

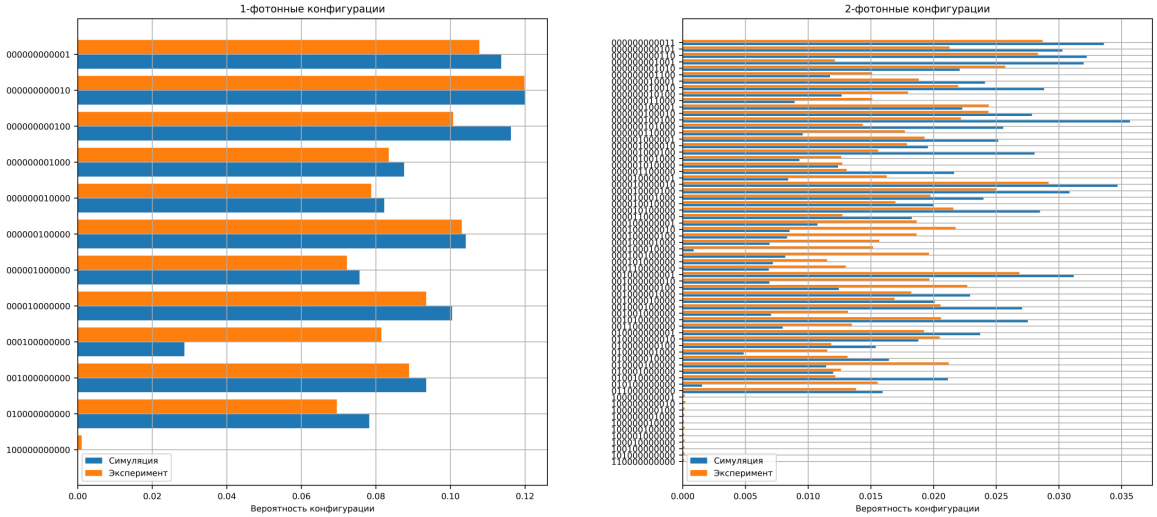

Figure 3: Boson sampling experimental and theoretical output configurations.

References

[1] *W.R. Clements, P.C. Humphreys, B.J. Metcalf, W.S. Kolthammer, and I.A. Walsmley.*, Optimal design for universal multiport interferometers. Optica, 3(12):1460–1465, 2016.

[2] *S. Aaronson, A. Arkhipov.*, The computational complexity of linear optics. Theory of Computing. 9: 143–252(2013).

[3] *R. Heilmann, M. Gräfe, S. Nolte and A. Szameit,* A novel integrated quantum circuit for high-order W-state generation and its highly precise characterization Sci. Bull. 60, 96–100 (2015).

Miass, Russia February 25 – March 2, 2024
7th International School on Quantum Technologies

Image processing algorithms and automation detection of arrays of single neutral atoms

Anton Vorobyev[1*], **Gleb Struchalin**[1], **Ivan Bobrov**[1], **Stanislav Straupe**[1,2]

[1] *MSU Quantum Technology Centre, M. V. Lomonosov Moscow State University, 119991 Moscow, Russia*
[2] *Russian Quantum Center, 121205 Moscow, Russia*
*E-mail: vorobev.ae20@physics.msu.ru

Abstract

We introduce an algorithm for determining scaling, rotation, and shift parameters of images in neutral-atom quantum computers. The algorithm includes noise suppression, Otsu binarization, contour search using Theo Pavlidis algorithm, and affine transformation via Coherent Point Drift (CPD) algorithm. CPD algorithm is enhanced for correspondence search between regular lattices and the entire process is implemented in C++ using Boost.GIL and Eigen libraries. The new algorithms are integrated into existing code to provide a faster and more accurate method for atom detection. Additionally, a method for refining atom recognition threshold is proposed.

For quantum simulators based on arrays of neutral atoms, a widely used method for measuring the state of a system is the detection of an optical fluorescence signal using highly sensitive cameras. As shown in [1], to study the interaction of many Rydberg atoms, it is necessary to increase the number of atomic traps. As the number of particles grows, there is a need for more accurate and faster methods for searching for atoms in images.

The purpose of this work is to develop an algorithm that will make it possible to determine the parameters of scaling, rotation and shift of the image relative to the reference position of the traps at the calibration stage in automatic mode.

In this work, optimal image processing algorithms were selected taking into account the specifics of the task and their implementation was carried out in the C++ programming language. A method for refining a custom threshold for atom recognition is also proposed.

Image processing

Image processing for our tasks consists of several stages.

1. Suppression and elimination of noise (for example, using morphological filters: dilation, erosion, closing and opening). All these methods are based on considering a certain neighborhood of the analyzed pixel.

2. Binarization — turning an image into two-color black and white. It can be reformulated into the problem of finding the optimal threshold value. Many well-known binarization algorithms require the use of a post-processing procedure (for example, the Bernsen method [2]) or have low performance (the Janowitz and Brookstein method [3]), which makes their use impractical within the framework of assigned task. The Otsu method [4] was chosen for implementation as the most effective in terms of global binarization quality and speed. This method is based on constructing an image histogram and selecting a threshold value that will ensure a minimum of inter-class variance in the resulting black and white pixels.

3. Search for contours — finding connected areas of a given color. Examples of algorithms are square tracing and Moore neighborhood tracing, as well as their more modern analogue — Theo Pavlidis algorithm [5], which was chosen for its ease of implementation and versatility.

4. Search for an affine transformation of image points (source set) to a given target set of points. In the simplest case, with a known bijection between two sets of points, the problem is reduced to a system of linear equations and can be solved analytically. However, in the problem we posed there is no information about the mutual correspondence of the points of the source and target sets, and the distortions introduced into the positions of the points during the measurement process (points missing in the regular lattice, etc.), further limit the methods for finding a solution. The Coherent Point Drift (CPD) algorithm [6] has been proposed as a way to deal with the above limitations. The authors use

a probabilistic approach for finding a solution. By moving points together, described by a mixture of Gaussians, using the EM (estimation-maximization) algorithm, it is possible to achieve maximum similarity between two sets of points. As a result, the values $\mathbf{R}, \mathbf{t}, s$ (rotation matrix, shift vector, and scaling coefficient, respectively) will be obtained, which will determine the desired affine transformation.

Atom detection

Atom detection begins with taking the sum of pixel intensities I_i^{Σ} for each square neighborhood of the target i-th point from the previous paragraph and assume that the atom is in the i-th trap if $I_i^{\Sigma} \geq I_i^{\mathrm{t}}$. However, this approach requires the user to manually adjust the threshold I_i^{t} of each trap individually, which has an extremely negative impact on scaling the experimental setup by the number of traps. So we turn to statistical methods to refine the value of I_i^{t} specified by the user.

The histogram of trap-pixels total intensity I_i^{Σ} usually has the form of three Gaussian peaks, which correspond to a filled trap, an empty trap and an intermediate case (for example, when an atom escaped from the trap during the camera exposure). Therefore, it is proposed to use a Gaussian Mixture Model (GMM) with three components to determine the parameters of each peak separately and then determine the value of the threshold intensity I_i^{t} from them. Subsequently, in order to reduce the number of image samples required for the correct operation of GMM, naive random initialization of GMM components was replaced by initialization using the MRIPEM algorithm [9]. This made it possible to improve the GMM performance, including the case of low samples number.

The algorithm for refining the value I_i^{t} is based on the idea of dividing GMM peaks into two groups: “dark” and “light”. The result of the algorithm is the threshold value I_i^{t} that minimizes the total error of the first and second types for such a binary criterion.

Results

The CPD algorithm was adjusted to the search for correspondence between regular lattices and the image processing was implemented in the C++ programming language using the Boost.GIL [7] and Eigen [8] libraries. New algorithms have been successfully integrated into the existing code base.

Figure 1 shows an example of processing stages of an atomic-array image using the implemented algorithms. The dilate filter causes the highlights to expand, which minimizes the chance of losing points later. After the Otsu method, a set of white areas of approximately the same shape and size without interference and noise is obtained — a good basis for subsequent processing. The contours search results in the center of mass and scale $(\delta x_i, \delta y_i)$ for the i-th contour. A square grid of 6×6 points with a period of $a = 10$ units was chosen as the target array for the CPD algorithm. The found parameters are: $\alpha \approx 0.69°$ — the camera rotation angle, $\mathbf{t} = \begin{pmatrix} 43.49 & 50.74 \end{pmatrix}^T$ — the shift vector, and $s = 0.82$ —the scaling factor.

Figure 2 shows a histogram of the trap total intensities. Three peaks are clearly visible, corresponding to different types of trap occupancy. There is also a noticeable improvement in the GMM fit result owing to the MRIPEM initialization algorithm.

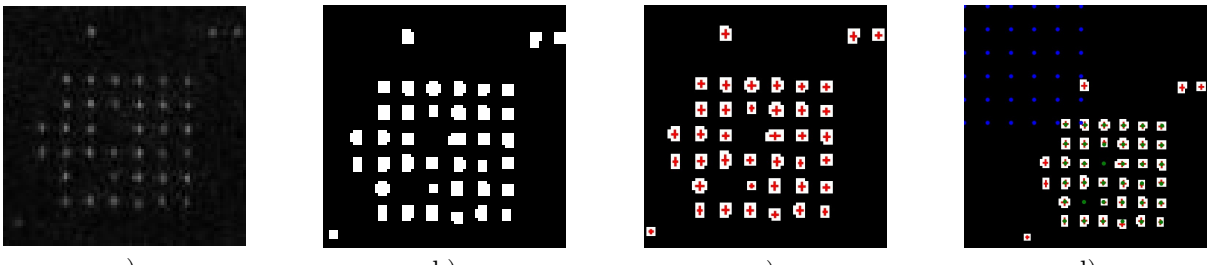

a) b) c) d)

Figure 1: The result of image processing stages: a) original photo, b) after applying the dilate and Otsu methods, c) after searching for contours using Theo Pavlidis method, d) the result of the CPD algorithm. Blue — target array of points, green — transformed array according to CPD data.

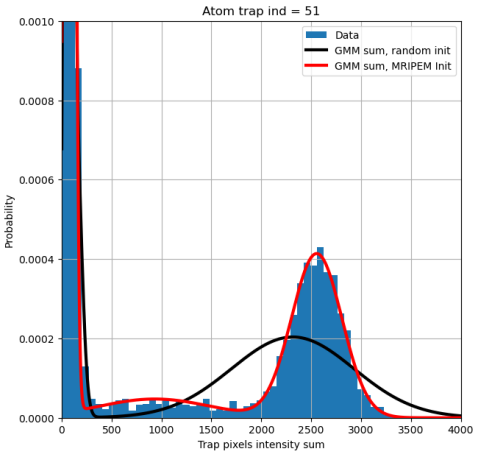

Figure 2: Comparison of GMM initialization algorithms. Black — random init, red — MRIPEM init.

Conclusion

The developed image processing methods allow one to further automate an experiment, which will speed up measurements and improve their quality. As a result of image preprocessing, both calibration parameters of the camera position and an array of points in the vicinity of which atoms are located can be obtained.

In the future, we plan to finish the work on refining the value of the atom-recognition threshold. Besides, improvement in atom detection may be achieved by taking into consideration the spatial distribution of pixel intensity in the atomic trap.

Acknowledgements

This work is supported by Rosatom in the framework of the Roadmap for Quantum computing (Contract No. 868-1.3-15/15-2021 dated October 5, 2021).

References

[1] *Labuhn, H.*, Rydberg excitation dynamics and correlations in arbitrary 2D arrays of single atoms. (2016), URL `https://api.semanticscholar.org/CorpusID:101982317`

[2] *Bernsen, J.*, Dynamic thresholding of grey-level images. *Eighth International Conference On Pattern Recognition. Proceedings.* pp. 1251-1255 (1986), URL `https://www.tib.eu/en/search/id/tema-archive:TEMAE87090699070`

[3] *Yanowitz, S. & Bruckstein, A.*, A new method for image segmentation. *Computer Vision, Graphics, And Image Processing.* **46**, 82-95 (1989), URL `https://doi.org/10.1016/S0734-189X(89)80017-9`

[4] *Otsu, N.*, A Threshold Selection Method from Gray-Level Histograms. *IEEE Transactions On Systems, Man, And Cybernetics.* **9**, 62-66 (1979,1)

[5] *Pavlidis, T.*, Contour Filling. *Algorithms For Graphics And Image Processing.* pp. 167-193 (1982), URL `https://doi.org/10.1007/978-3-642-93208-3_8`

[6] *Myronenko, A. & Song, X.*, Point Set Registration: Coherent Point Drift. *IEEE Transactions On Pattern Analysis And Machine Intelligence.* **32**, 2262-2275 (2010,12), URL `https://doi.org/10.1109/tpami.2010.46`

[7] Boost Generic Image Library, URL `https://www.boost.org/doc/libs/1_79_0/libs/gil/doc/html/index.html`

[8] *Guennebaud, G., Jacob, B. & Others*, Eigen v3 (2010), URL `http://eigen.tuxfamily.org`

[9] *You, J. & Li, Z. & Du, J.* A new iterative initialization of EM algorithm for Gaussian mixture models. *PLOS ONE.* **18**, 1-17 (2023,4), URL `https://doi.org/10.1371/journal.pone.0284114`

Design of Planar Pauli trap for quantum computing

Ilya Gerasin[1,2,3*], **Nikita Zhadnov**[1,2], **Konstantin Kudeyarov**[1,2], **Ksenia Khabarova**[1,2], **Ilya Semerikov**[1,2], **Nikolay Kolachevskiy**[1,2]

[1] *P.N. Lebedev Physical Institute, Russian Academy of Sciences, Moscow, Russia;*
[2] *Russian Quantum Centre, Moscow, Russia*
[3] *Moscow Institute of Physics and Technology, Dolgoprudny, Russia*
*E-mail: i.gerasin@rqc.ru

Abstract

In this paper, we consider surface-electrode ion trap for various applications in quantum computing. We optimize geometry of the electrodes with constant radio frequency voltage amplitude and stability parameter to achieve maximum potential depth. Also, we are trying to find dependency between geometrical parameters of the trap.

Using single cold ions as qubits today allows creating powerful quantum computers [1]. Besides, the larges quantum volume of 64 was achieved using ion quantum computer [2]. To carry out quantum gates, chains of ions are held in Pauli traps. In order to achieve scalability of quantum computers (increasing number of qubits while keeping connectivity) the QCCD architecture was proposed [3]. In such approach, the device is divided into zones with ion chains. In each zone manipulation such detection, loading, storing or quantum gates occur separately. This architecture is based on planar Pauli traps [4]. In such system, electrodes of the trap are located in one plane and the particle is located above this plane. Also, such traps allow simple optical access to the stored ion. Moreover, using of integrating photonics can help to minimize size of the whole system. Since the first planar trap, a lot of design was proposed [5]. However, such microchips demand high quality microfabrication process. Besides, these traps do not allow achieving high potential trap depth and contribute to heating rates of the particles. In this paper, we consider optimization of simple trap design, where rectangular RF and DC electrodes alternate (DC-RF-DC-RF-DC). This simple setup allows determining dependency between parameters that will be useful in more complicated setup.

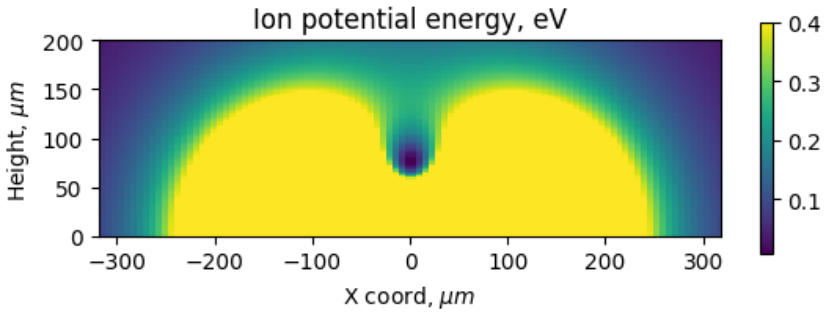

Figure 1: Typical picture of planar trap potential

The typical picture of the ion potential energy above the trap is presented in Fig. 1. The picture of potential is defined both by geometry, size of electrodes and by parameters of driving RF voltage (amplitude and frequency). Described above parameters set the height of the potential minima, stability parameter and trap depth. Varying the geometrical size of the electrodes allows to numerically optimize such parameters [6]. However, for experimental purposes, it is important to increase the height of the equilibrium to decrease heating rate and fix the stability parameter of the trap to maintain harmonic motion. In such way we fix height and stability parameter and find the maximal value of trap depth. Also, it is worth to keep in mind that amplitude of the driving voltage limited by RF breakdown on microfabricated chip. So we fix driving voltage amplitude too. Such approach allows designing planar trap appropriate for our experiments and find out dependencies between parameters.

References

[1] *J.S. Chen, E. Nielsen, M. Ebert, V. Inlek, K. Wright, V. Chaplin, A. Maksymov, E. Páez, A. Poudel, P. Maunz, J. Gamble*, Benchmarking a trapped-ion quantum computer with 29 algorithmic qubits. arXiv preprint arXiv:2308.05071 (2023).

[2] *J.M. Pino, J.M. Dreiling, C. Figgatt, J.P. Gaebler, S.A. Moses, M.S. Allman, C.H. Baldwin, M. Foss-Feig, D. Hayes, K. Mayer, C. Ryan-Anderson and B. Neyenhuis* . Demonstration of the trapped-ion quantum CCD computer architecture. Nature 592.7853 (2021): 209-213.

[3] *D.J. Wineland, C. Monroe, W.M. Itano, D. Leibfried, B.E. King, D.M. Meekhof.* Experimental issues in coherent quantum-state manipulation of trapped atomic ions. Journal of research of the National Institute of Standards and Technology 103.3 (1998): 259.

Wineland, David J., et al. "Coherent quantum state manipulation of trapped atomic ions." Advances in Quantum Chemistry. Vol. 30. Academic Press, 1998. 41-64.

[4] *S. Seidelin, J. Chiaverini, R. Reichle, J. J. Bollinger, D. Leibfried, J. Britton, J. H. Wesenberg, R. B. Blakestad, R. J. Epstein, D. B. Hume, W. M. Itano, J. D. Jost, C. Langer, R. Ozeri, N. Shiga, and D. J. Wineland*, Microfabricated surface-electrode ion trap for scalable quantum information processing. Physical review letters 96.25 (2006): 253003.

[5] *Z.D. Romaszko, S. Hong, M. Siegele, R.K. Puddy, F.R. Lebrun-Gallagher, S. Weidt and W. K. Hensinger* Engineering of microfabricated ion traps and integration of advanced on-chip features. Nature Reviews Physics 2.6 (2020): 285-299.

[6] *T. Abbasov, S. Zibrov, I. Sherstov.* Surface-electrode ion trap development. JETP Letters 118.3 (2023): 215-219.

Miass, Russia February 25 – March 2, 2024
7th International School on Quantum Technologies

Performance of the QAOA algorithm in combinatorial problems in the presence of unital and non-unital noise

Dmitry Guskov*, **Konstantin Antipin**

Skolkovo Institute of Science and Technology
*E-mail: dmitry.guskov@deepquantum.ai

Abstract

In this work, we investigate the influence of noise on the Quantum Approximate Optimization Algorithm (QAOA) concerning combinatorial optimization problems. Specifically, we focus on MAX 2-SAT instances, observing the emergence of barren plateaus and exploring the trainability of QAOA in the presence of noise. The study models various types of noise using both unital and non-unital quantum channels. Numerical analyses reveal that the optimal parameters of the noise-free solution remain largely unaffected by training with small amounts of introduced noise from both classes, while the algorithm can no longer achieve a solution. The cost function and fidelity concerning the noise-free solution are thoroughly examined, both numerically and theoretically.

1 Introduction

Contemporary approaches in quantum algorithms designed for noisy intermediate-scale quantum (NISQ) devices encompass variational quantum approaches, such as Quantum Approximate Optimization Algorithm (QAOA). These algorithms require an iterative optimization process to find a product state that minimizes the objective function of interest. Particularly, QAOA stands as a promising variational method for solving discrete combinatorial optimization problems on quantum hardware [1, 2, 3]. Leveraging parameterized quantum ansatz preparation alongside classical gradient descent optimization, QAOA has demonstrated efficacy for boolean k-SAT and maximum cut problems in noise-free conditions [4, 5, 6, 7]. Despite these achievements, the performance of the QAOA circuit encounters limitations partly due to phenomena known as barren plateaus, which concentrate gradients around zero, forcing optimization to a local minimum.

While the existence of noise imposes constraints on the capabilities of modern quantum devices [8], there is evidence suggesting that the inherent noise can be utilized to assist the optimization process in quantum computers[9]. Therefore understanding of the variational algorithms performance in the context of noisy circuits is interesting from both theoretical and practical sides.

Prior research on QAOA [10] focused on the maximum cut problem, focusing on the behavior of output state fidelity and the cost function. Notably, it was established that under conditions of relatively mild noise, the optimized parameters remain close to their noise-free values. This effect, optimal parameter resilience, was also observed in the context of variational quantum compiling [11].

However, it's important to note that not all variational algorithms exhibit such resilience to noise; some adjust their optimized parameters to mitigate its effects [12]. Specifically, for simulations involving random target states, where fidelity with respect to a random target state is maximized, two distinct cases were considered: noiseless training with noisy evaluation (*non-reoptimized* evaluation), and noisy training with noisy evaluation (*reoptimized* evaluation). The study demonstrated that in the presence of certain types of noise in the non-reoptimized case, the fidelity reaches a peak at a certain number of layers, after which it begins to decay. In contrast, in the reoptimized case, fidelity continues to grow monotonically with the number of layers.

Furthermore, investigations into the impact of noise on the cost landscape of parameterized quantum circuits [13, 14] have uncovered intriguing insights, such as the emergence of barren plateaus and distinctions between unital and non-unital noise channels. This research connects this transition to the controllability and complexity of QAOA circuits. We delve into the barren plateau regime for combinatorial optimization problems and investigate their noise resilience.

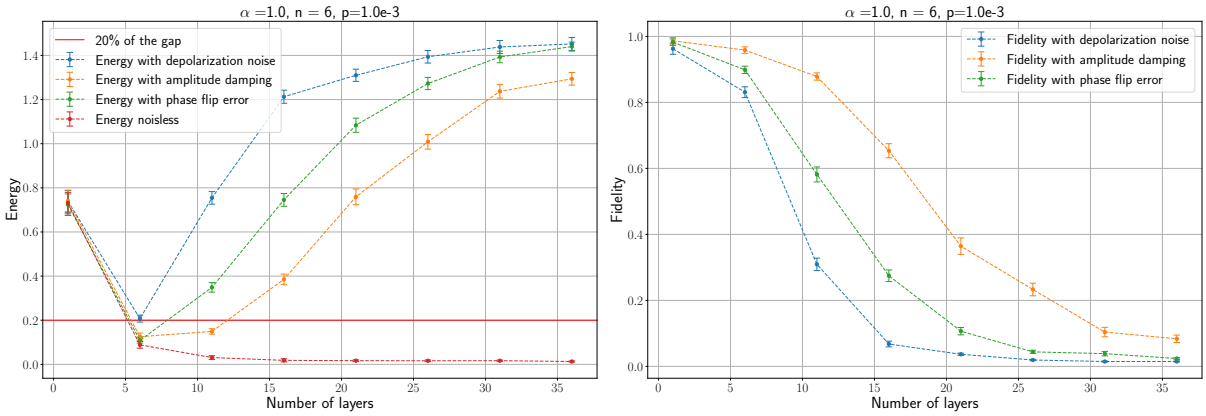

Figure 1: Entire caption for figure centered and below the illustration

In this study, our main goal is to assess the performance of QAOA in solving k-SAT problems in the presence of noise. Consequently, we study the optimization process with noise. Our observations indicate that with a small amount of noise, the solution energy exhibits a minimum for a relatively small circuit depth, as illustrated in Figure 1. The primary outcomes that we focus on include:

1. **Optimal parameter resilience** against commonly considered noise models.
2. The **exponential convergence** of the cost function towards specific values dependent on noise type for a high number of layers.
3. The **exponential decay** of fidelity to the noise-free solution concerning circuit depth.

References

[1] E. Farhi, J. Goldstone, and S. Gutmann. A quantum approximate optimization algorithm. arXiv:1411.4028, 2014.

[2] E. Farhi, J. Goldstone, and S. Gutmann. A quantum approximate optimization algorithm applied to a bounded occurrence constraint problem. arXiv:1412.6062, 2015.

[3] L. Zhou, S.-T. Wang, S. Choi, H. Pichler, and M. D. Lukin. *Phys. Rev. X*, 10:021067, 2020.

[4] S. Boulebnane and A. Montanaro. Solving boolean satisfiability problems with the quantum approximate optimization algorithm. arXiv:2208.06909, 2022.

[5] G. E. Crooks. Performance of the quantum approximate optimization algorithm on the maximum cut problem. arXiv:1811.08419, 2018.

[6] R. Herrman, L. Treffert, J. Ostrowski, P. C. Lotshaw, T. S. Humble, and G. Siopsis. *Quantum Information Processing*, 20:289, 2021.

[7] M.P. Harrigan, K.J. Sung, and M. Neeley et al. *Nat. Phys.*, 17:332, 2021.

[8] J. Preskill. *Quantum*, 2:79, 2018.

[9] Ernesto Campos, Daniil Rabinovich, Vishwanathan Akshay, and J Biamonte. Training saturation in layerwise quantum approximate optimization. *Physical Review A*, 104(3):L030401, 2021.

[10] C. Xue, Z.-Y. Chen, Y.-C. Wu, and G.-P. Guo. *Chinese Phys. Lett.*, 38:030302, 2021.

[11] K. Sharma, S. Khatri, M. Cerezo, and P. J. Coles. *New J. Phys.*, 22:043006, 2020.

[12] E. Fontana, N. Fitzpatrick, D. M. Ramo, R. Duncan, and I. Rungger. *Phys. Rev. A*, 104:022403, 2021.

[13] S. Wang, E. Fontana, M. Cerezo, K. Sharma, A. Sone, L. Cincio, and P. J. Coles. *Nat. Commun.*, 12:6961, 2021.

[14] E. Fontana, M. Cerezo, A. Arrasmith, I. Rungger, and P. J. Coles. *Quantum*, 6:804, 2022.

Constructing Confocal Fabry-Perot cavity to stabilize multiple lasers for 40Ca+ optical qubit

S. Zarutskiy[1,2*], **A.O. Kadykov**[1], **L. A. Akopyan**[1], **A. Matveev**[1], **N.V. Morozov**[1], **K. Lakhmanskiy**[1]

[1] *Russian Quantum Center, Moscow, Russia*
[2] *Faculty of Physics, Lomonosov Moscow State University, Department of Quantum Electronics, Moscow, Russia*
*E-mail: zarutskiysy@my.msu.ru

Abstract

We present the design and its characterization for the laser stabilization system for ion-based quantum computer. The design is based on the custom-constructed Fabry-Perot cavity locked to the stable Nd:YAG 532 nm laser. The target 866 nm laser used for $^{40}Ca^{+}$ cooling is then locked to the stabilized cavity.

The quantum computing field provides fundamentally new information processing approaches and opportunities for significant acceleration for certain problem solutions. A whole new type of hardware is required to achieve progress in this field. The platform based on trapped ions is one of the most promising for quantum computations. To perform quantum operations in such an architecture, lasers are used. Thus, the performance of quantum operations in the ion quantum computing platform largely relies on laser stability, implying frequency stabilization, power stabilization, and phase stabilization.

In this project we aim to build a device capable of the stabilizing the frequencies of multiple different lasers simultaneously. The laser frequency drifts can be eliminated by locking laser to an optical cavity [1]. To stabilize multiple lasers using a single cavity we select the confocal Fabry-Perot cavity geometry. It allows to separate spatially different laser beams as illustrated in Fig. 1.

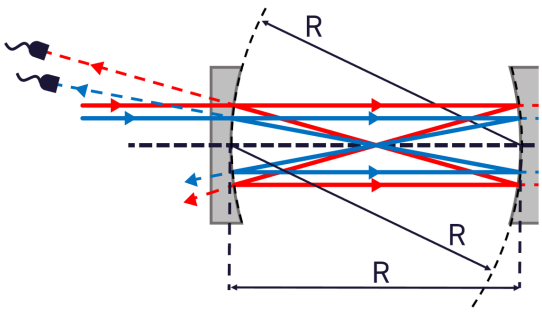

Figure 1: Laser beams with different aiming distances to the optical axis are spatially separated before and after leaving the cavity.

The custom-constructed Fabry-Perot cavity is built using a custom aluminum base. The moving mirror mount is attached to the piezoceramics glued to the base. Thus, the cavity length can be controlled by applying voltage to the piezoceramics. The cavity length is 15 cm, so the distance between two neighbouring cavity transmission lines is $\delta\nu = \frac{c}{4L} = 1$ GHz. For any laser wavelength for which the cavity mirrors have a high reflection coefficient, there is a cavity transmission line within the 0.5 GHz range that can be used to do locking between the cavity and the laser. Cavity finesse is order of magnitude $\sim 10^3$ for the 532 nm and 866 nm light.

First, the cavity was stabilized by locking it to a stable Nd:YAG 532 nm laser. Second, the non-stabilized diode 866 nm laser was locked to the stabilized cavity. To get the error signal and perform the locking, we apply the well-known Pound-Drever-Hall method [2, 3]. The locking was performed using PID controllers. That allowed us to reduce the frequency drift of the 866 nm laser from ≈ 100 MHz to ≈ 1 MHz scale, see Fig.2. 854 nm and 397 nm lasers are next in line.

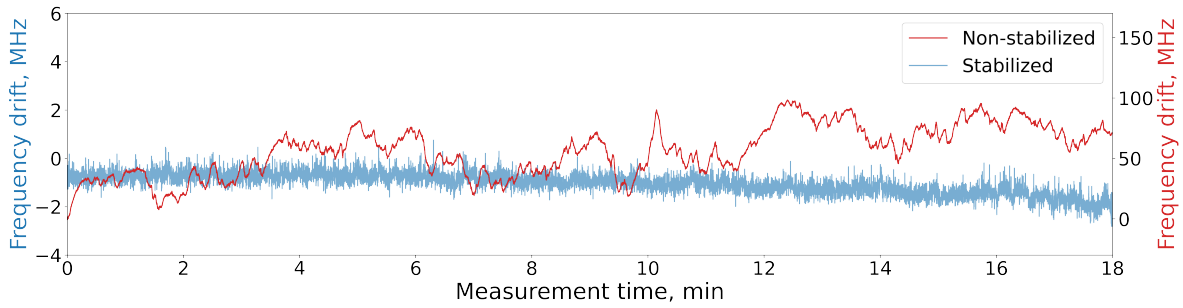

Figure 2: 866 nm laser frequency drift with and without stabilization.

The reporting author receives a scholarship from the Theoretical Physics and Mathematics Advancement Foundation "BASIS".

References

[1] *Riehle F.*, Frequency standards: basics and applications. John Wiley & Sons, (2006).

[2] *Nickerson M.*, A review of Pound-Drever-Hall laser frequency locking. JILA, University of Colorado and NIST (2019).

[3] *Black E.D.*, An introduction to Pound–Drever–Hall laser frequency stabilization. American journal of physics **69(1)**, 79-87 (2001).

Miass, Russia February 25 – March 2, 2024
7th International School on Quantum Technologies

High-fidelity Light-Shift gate on the quadrupole transition in Yb ions

Pavel Kamenskikh[1,2*], **Nikita Semenin**[1,2], **Ilia Zalivako**[1,2], **Ilia Semerikov**[1,2], **Nikolay Kolachevsky**[1,2]

[1] *Lebedev Physical Institute, Russian Academy of Sciences, Moscow, Russia*
[2] *Russian Quantum Center, Moscow, Russia*
*E-mail: kamenskikh.pa@phystech.edu

Abstract

The Light-Shift (LS) gate is a two-qubit gate commonly used to entangle ions. It is designed to be resistant to optical fluctuations in laser paths[1]. However, there are several factors that can reduce the fidelity of the LS gate, such as the excitation of side levels of a qubit and the Stark effect. In this study, we propose methods to reduce these errors. Through numerical simulations, we found that the error rate of this operation can be less than 10^{-4} with a gate time of 250 μs.

To achieve useful quantum algorithms on an ion-trapped quantum computer, high-fidelity two-qubit gates must be implemented. However, there are several imperfections that reduce gate fidelity. Firstly, non-resonant coupling causes the population of the excited states to become non-zero, resulting in a reduction in the qubit state population. Secondly, the Stark effect causes an energy shift in the levels, which leads to a change in the phase of electronic states. Thirdly, entanglement occurs through the motional modes of the ionic chain, which causes a decrease in fidelity due to the residual entanglement of the motional and electronic states of the ions.

In this work, a two-qubit operation is proposed to solve the above-mentioned problems. The proposed gate is similar to the operation implemented in [2], with the difference that a transition $\left|^2S_{1/2}.F=0\right\rangle \rightarrow \left|^2D_{3/2},F=2\right\rangle$ is involved, see Fig. 1a. This feature, combined with the original gate structure, eliminates the constant Stark level shift. However, this configuration leads to significant populations of excited states. To address this problem, the field is turned on and off adiabatically to smoothly change the external population from zero to a maximum value and back to zero. For instance, such a profile

$$E(t) \propto \sin^2(t/\delta t), \quad t < \delta t \tag{1}$$

is used for adiabatic switching.

The issues associated with non-ideal closure of phase trajectories and factors that influence the phase parameter of the gate can be resolved by dividing the gate into four parts, also called loops. Adiabatic switching is used after each part. After the 1$^{\text{st}}$ and 3$^{\text{rd}}$ loops, the phase of one of the lasers changes so that the force acting on the ions changes sign (see Fig. 1b). This ensures that the next loop closes the phase trajectory of the first two modes, whose frequencies are closest to the detuning $\mu = \omega_A - \omega_B$. Moreover, global single-qubit rotations are applied after 2$^{\text{nd}}$ and 4$^{\text{th}}$ loops. This sequence of operations implements the spin echo method (see Fig. 1c), which compensates for the phase error accumulated over the first two loops.

Numerical simulation was carried out using the QuTiP package [3] to implement all the above-mentioned methods for reducing the error of a two-qubit gate. The fidelity of the operation was defined as F:

$$F = \langle\psi_{\text{id}}|\rho|\psi_{\text{id}}\rangle\,, \tag{2}$$

where $|\psi_{\text{id}}\rangle$ - final ideal state after the LS-gate. It was revealed that an operation with an error of less than 10^{-4} could be implemented with a laser power of 0.32 mW and a gate time of 250 μs. Without these methods, errors are significant, see Fig. 2. Therefore, these methods enable the implementation of two-qubit gates that are robust to many errors.

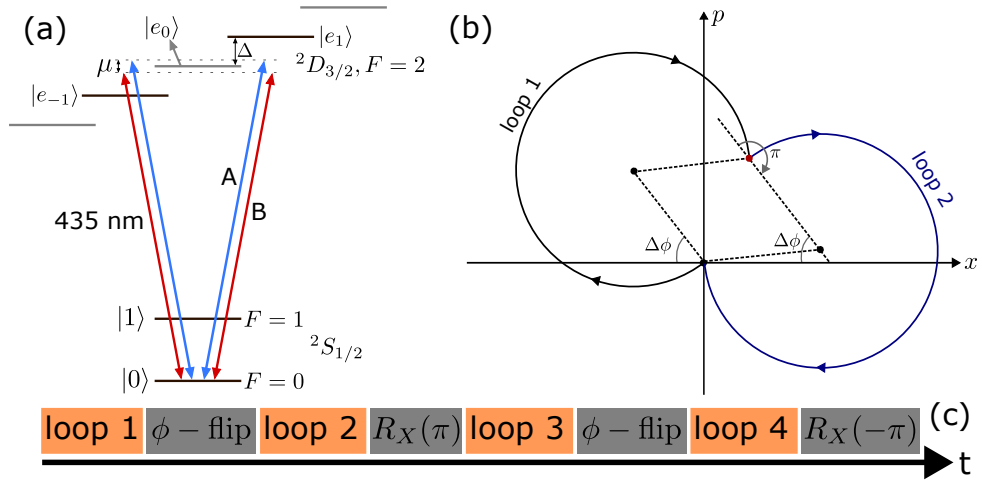

Figure 1: (a) Energy level scheme to implement LS gate. The polarisation and the direction of the lasers are chosen so that only $|e_{\pm 1}\rangle$ levels are driven. (b) Closure of the phase trajectory using the ϕ-flip method. (c) Gate sequence to realise the LS-gate.

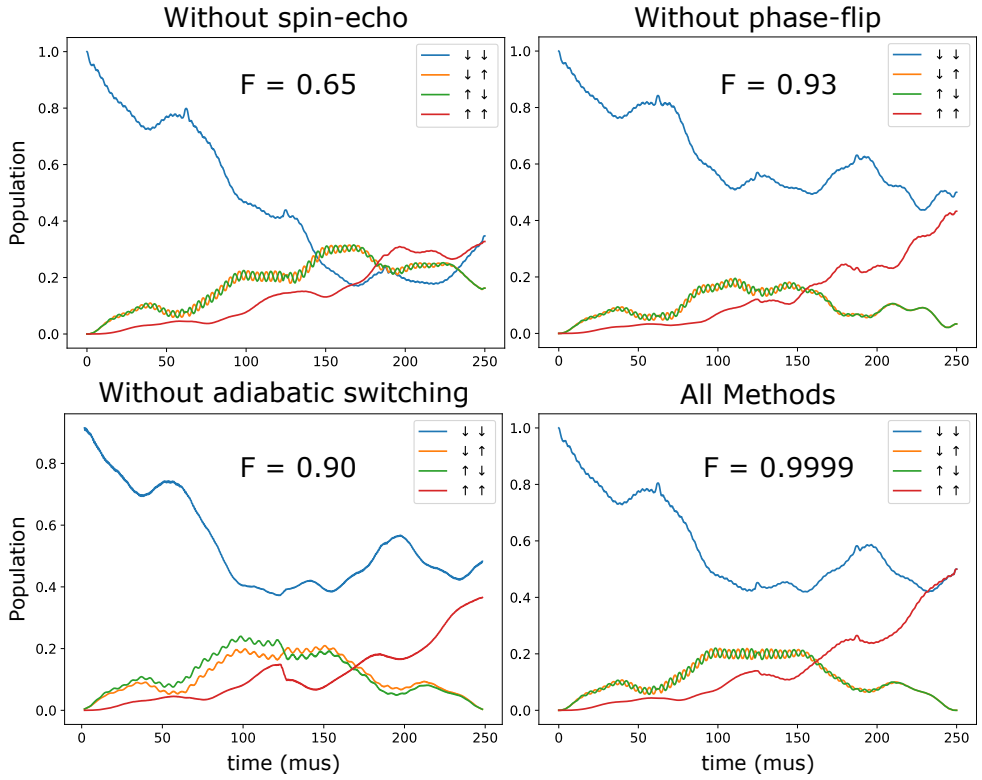

Figure 2: Time evolution of the population of qubit states for LS-Gate.

References

[1] *Roos, Christian F.*, Ion trap quantum gates with amplitude-modulated laser beams. New Journal of Physics 10.1: 013002 (2008).

[2] *Baldwin, C. H., Bjork, B. J., Foss-Feig, M., Gaebler, J. P., Hayes, D., Kokish, M. G., ... & Vittorini, G.*, High-fidelity light-shift gate for clock-state qubits. Physical Review A, 103(1), 012603, (2021).

[3] *Johansson, J. Robert, Paul D. Nation, and Franco Nori.*, "QuTiP: An open-source Python framework for the dynamics of open quantum systems." Computer Physics Communications 183.8: 1760-1772 (2012).

Quantum microwave link between fluxonium qubits

Andrei Kugut,[1,2,3*] **Pavel Gladilovich,**[3] **and Grigory Mazhorin**[1,2,3]

[1] *Moscow Institute of Physics and Technology, 141701 Dolgoprundiy, Russia*
[2] *Russian Quantum Center, Skolkovo, 143025 Moscow Region, Russia*
[3] *National University of Science and Technology "MISIS", 119049 Moscow, Russia*
*E-mail: kugut.aa@phystech.edu

Abstract

Scaling is a huge challenge towards building a high-performance quantum computer. One of the most promising ways for solving this issue is to utilize a distributed network of samples connected by a quantum link. Here we present a scheme consisting of two fluxonium qubits located on separated substrates coupled via a superconducting transmission line. The transfer of a quantum state is provided by a so-called "dark mode". We numerically investigate the system and optimize the sequence of controlled pulses required for implementing quantum state transition. The obtained fidelity of the quantum states transfer is over 99.3% under realistic coherence conditions, including qubit decoherence.

Distributed networks of superconducting devices wired by quantum channels is an effective path for scaling up a universal quantum processor. Nowadays, there are several scientific groups conducting pioneer research in this area [1, 2]. Inspired with the existed methods, we propose a new scheme for a quantum link, which provides the transfer of states between two distributed fluxonium qubits. We schematically represent the circuit in Figure 1. The key advantage of the scheme is the usage of the dark mode state [3].

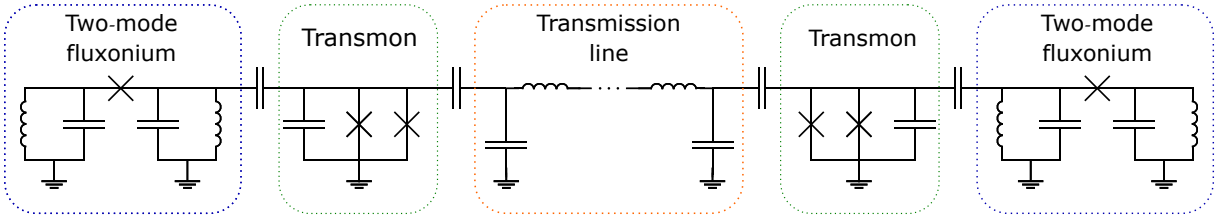

Figure 1: Quantum link schematic.

To create this state, we set up the transmission line and two transmons in resonance. Hybridized three part system Transmon-Line-Transmon includes eigenvector formed with the both transmons first exited states $|1\rangle_{\mathrm{T1}}$, $|1\rangle_{\mathrm{T2}}$ and the vacuum state of the transmission line $|0\rangle_{\mathrm{L}}$. This eigenvector corresponds to the dark mod. The dark mode structure provides resistance to transmission line decoherence sources, which makes this state preferable for our goals. To transfer quantum state from fluxonium-transmitter to fluxonium-receiver we initialise second one in the ground state and induce transmission sequence (Figure 2) with drive signals. One can see that we use dark mode in the role of the bridge between fluxonium qubits. We numerically modeled the induced system dynamic with lindblad equation:

$$\partial_t \rho = \frac{1}{i\hbar}\left[\hat{H} + \hat{V}(t),\, \rho\right] + \frac{1}{2\hbar}\sum_k \left(\left[\hat{L}_k, \rho\, \hat{L}_k^\dagger\right] + \left[\hat{L}_k\, \rho, \hat{L}_k^\dagger\right]\right) \tag{1}$$

which includes typical decoherence sources for the represented system.

The implementation of numerical optimisation of the drive signals afforded as to obtain a fifelity of the transfer protocol over 99.3%. The most difficult part of the protocol is transition $|2\rangle_1^{'} \rightarrow |2\rangle_2^{'}$, which optimal induced dynamic is illustrated in Figure 3.

References

[1] *Zhong Y., Chang H. S., Bienfait A., Dumur É., Chou M. H., Conner C. R., ... & Cleland A. N.* , Deterministic multi-qubit entanglement in a quantum network. Nature, 590(7847), 571-575 (2021).

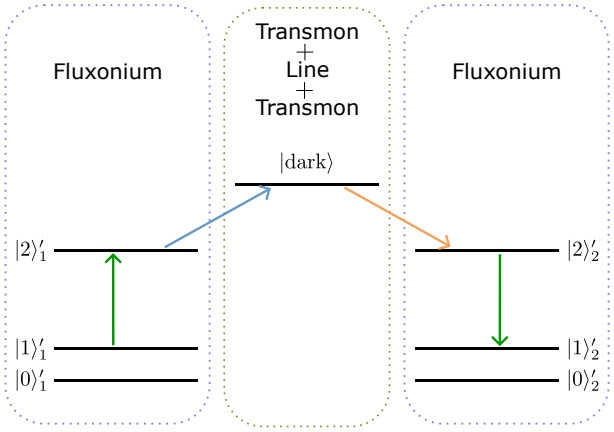

Figure 2: Scheme of the transition sequence

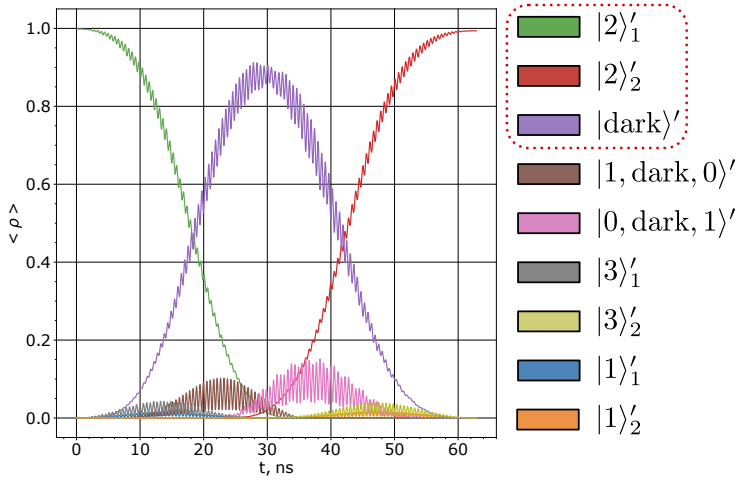

Figure 3: Dynamic of average populations induced by optimal external impulse for transition $|2\rangle'_1 \rightarrow |2\rangle'_2$

[2] *Magnard P., Storz S., Kurpiers P., Schär J., Marxer F., Lütolf J., ... & Wallraff A.*, Microwave quantum link between superconducting circuits housed in spatially separated cryogenic systems. Physical Review Letters, 125(26), 260502 (2020).

[3] *Wang Y. D., & Clerk A. A.*, Using dark modes for high-fidelity optomechanical quantum state transfer. New Journal of Physics, 14(10), 105010 (2012).

Demonstration of a parity–time symmetry breaking phase transition using superconducting qutrits

Arina Kuznetsova[1,2,3], Alena Kazmina[1,2,3], Ilya Simakov[1,2,3]

[1] *Russian Quantum Center, Skolkovo, Moscow 121205, Russia*
[2] *National University of Science and Technology MISIS, Moscow 119049, Russia*
[3] *Moscow Institute of Physics and Technology, Dolgoprudny 141700, Russia*

Abstract

Scalable quantum computers hold the promise to solve hard computational problems, such as prime factorization, combinatorial optimization, simulation of many-body physics, and quantum chemistry. While being key to understanding many real-world phenomena, simulation of non-conservative quantum dynamics presents a challenge for unitary quantum computation. In this work we focus on simulating non-unitary parity-time symmetric systems, which exhibit a distinctive symmetry-breaking phase transition as well as other unique features that have no counterpart in closed systems. We show that a qutrit, a three-level quantum system, is capable of realizing this non-equilibrium phase transition. Here, we introduce the technic for simultaneous three-states dispersive readout on superconducting qutrits and experimentally simulate the parity–time symmetry-breaking phase transition. Our results indicate the potential advantage of multi-level (qudit) processors in simulating physical effects, where additional accessible levels can play the role of a controlled environment.

Device description

The transmon-qubit[1] is one of the most widely used types of superconducting qubits. The simplest electrical circuit of a transmon consists of two main elements: a SQUID and a large shunt capacitance. Together they form a weakly amplified quantum oscillator. In this work we implement three-level quantum systems using transmons.

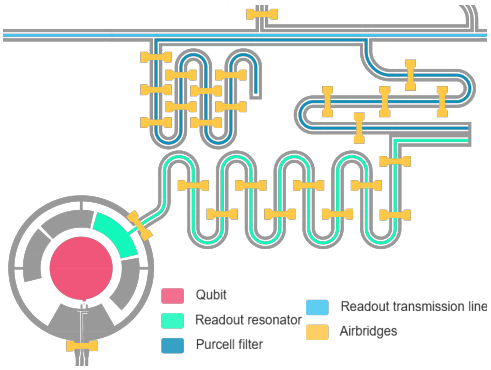

Figure 1: Transmon-qubit with it's individual readout resonator and parcell-filter coupled to readout transmission line

Qutrit readout

Dispersive readout technic is used to measure the state of a qutrit. Reflected signal from readout resonator is being processed with special marker functions, Finally, the state is plotted in the (I, Q) plane and logistic regression is used separate states. The readout confusion matrix shows probability of readout declaration error. The average value of diagonal elements represents the total readout fidelity of the experiment.

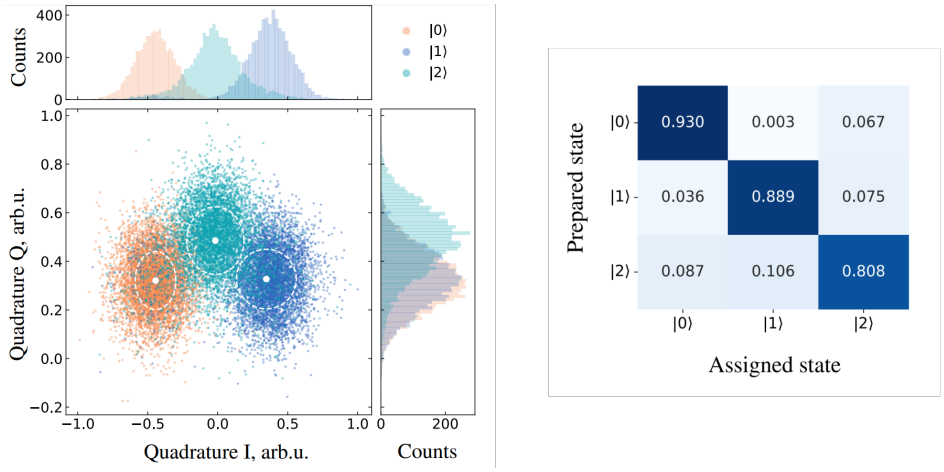

Figure 2: Left: The readout calibration trajectories of qutrit states are presented in the (I, Q) plane. Orange, blue, and aquamarine colored dots indicate measured Gaussian readout clouds corresponding to the $|0\rangle$, $|1\rangle$, and $|2\rangle$ states. The mean value and standard deviation of each cloud are denoted by white dots and dashed ellipses respectively. Right: The readout confusion matrix.

Observation of phase transition

The simplest parity time simetric system has two levels (qubit) and is its time evolution is generated by effective non-hermitian Hamiltonian ($\hbar = 1$).

$$H = \sigma_x + ir\sigma_z = \begin{pmatrix} ir & 1 \\ 1 & -ir \end{pmatrix} \tag{1}$$

The value $r = 1$ corresponds to the exceptional point.

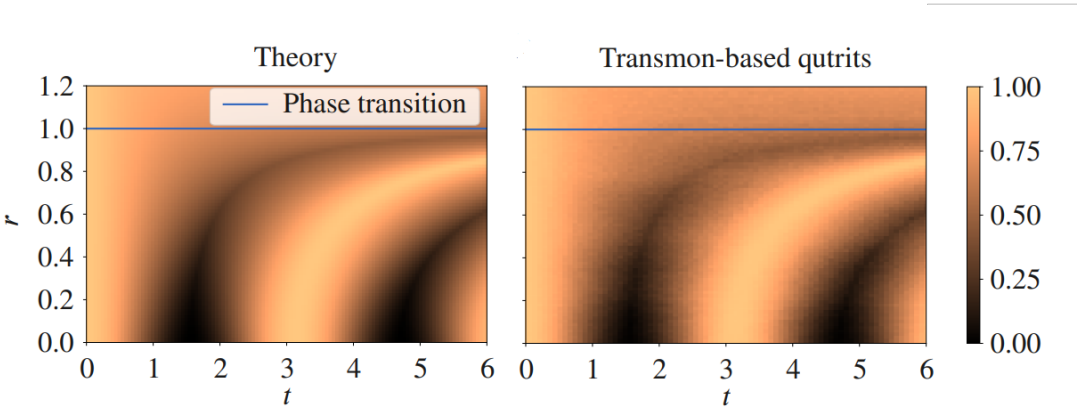

Figure 3: Dynamics ground state population for parity time symmetric two-level system (1) for a range of parameters $0 \leq r \leq 1.2$. $r = 1$ (blue line) is an exceptional point. Left: theory. Right: Experimental results obtained with the transmon-based qutrit. Each data point is an average of 8192 experimental samples.

References

[1] *Jens Koch, Terri M. Yu, Jay Gambetta et al.*, Charge-insensitive qubit design derived from the Cooper pair box. Physical Review A., **76**, 4 (2007).

Simulation of quantum attack on S-AES with key leakage and reduced number of qubits

Alexey Moiseevskiy[1,2], **Sofya Manko**[1*]

[1] *Infotecs Scientific Research and Advanced Developments Centre, Moscow, Russia*
[2] *MSU Quantum Technology Centre, Moscow, Russia*
*E-mail: Sofia.Manko@infotecs.ru

Abstract

This report presents the results of the simulation of Grover's attack with leak of key, which reduces the number of required qubits, on the Simplified-AES symmetric block encryption algorithm. Depending on the leak configuration, the attack requires 23–4n qubits with n consecutive leaked nibbles of the 16-bit key. Further research into this approach could enable the use of quantum computers for cryptanalysis in the near future.

It is known that using algorithms of Shor and Grover quantum computers can potentially be a threat to modern encryption algorithms. However, development in this direction is significantly hampered by the small size of the quantum register in modern quantum computers and the slow increase in the number of qubits for solving practically important problems, which significantly limits the size of the cipher key that can be attacked by a quantum computer.

Advanced Encryption Standard (AES) is one of the most widely used and important symmetric encryption algorithms today. But a full-fledged attack on AES requires hundreds of qubits and a circuit depth of thousands, which makes not only experimental research, but also computational simulation of this algorithm impossible [1]. However, it is more likely to be possible to carry out attacks on simpler encryption algorithms, such as Simplified-AES (S-AES) in near future. S-AES is a symmetric block cipher with a 16-bit key and two rounds of encryption. To attack such an algorithm, the required number of qubits and circuit depth are significantly lower.

Grover's quantum attack on S-AES can be implemented with just 32 qubits [2]. In the previously presented work [3], an original approach to constructing the oracle of Grover's algorithm was proposed. Now we present simulation of the attack on S-AES with significantly reduced requirements for the number of qubits, as well as the possibility of even greater resource savings in case of a partial key leak. Depending on the leak configuration, the proposed attack requires 23–4n qubits with n consecutive leaked nibbles of the 16-bit key.

References

[1] *Z. Huang, S. Sun*, Synthesizing Quantum Circuits of AES with Lower T-depth and Less Qubits. Advances in Cryptology – ASIACRYPT 2022, Lecture Notes in Computer Science, **13793** (2023).

[2] *K. B. Jang, G. J. Song, H. J. Kim and H. J. Seo*, Grover on Simplified AES. 2021 IEEE International Conference on Consumer Electronics-Asia (ICCE-Asia), pp. 1-4 (2021).

[3] *A. D. Moiseevskiy*, Partial key leak based qubit-optimized quantum Grover attack on Simplified-AES. 5-th International School on Quantum Technologies (2022).

Miass, Russia February 25 – March 2, 2024
7th International School on Quantum Technologies

Compiler Development for Atomic Quantum Computing

Varvara Mikhailova[1,2*], **Gleb Struchalin**[2]

[1] *Russian Quantum Center, 30 Bolshoy Boulevard, building 1, Moscow, 121205, Russia*
[2] *Quantum Technology Centre and Faculty of Physics, M. V. Lomonosov Moscow State University, 1 Leninskie Gory, Moscow, 119991, Russia*
*E-mail: varvara.mihailova@mail.ru

Abstract

We introduce a quantum compiler for neutral-atom quantum computers, written in C++ with ANTLR. The compiler validates OpenQASM 2.0 code and translates it into an internal binary format, which is a limited set of quantum instructions that are native to the atomic quantum computer. Also, we implemented a gate fusion optimization as a part of the compiler. The work is crucial for integrating quantum programs with hardware, addressing challenges in quantum algorithm execution.

Problem

The rapid advancement of quantum computing has led to the proliferation of quantum algorithms, prompting various companies and research groups to provide programming and execution capabilities. Programming quantum algorithms involves using languages like QUIL, QASM, Q#, Scaffold, and Silq, among others. Presently, OpenQASM [1] is a popular choice, mainly driven by IBM with its superconducting quantum processors. While the creation and optimization of quantum algorithms are independent to some extent of the hardware platform used (neutral atoms, ions, linear optics, superconductors), the execution of quantum programs requires consideration of hardware differences and low-level interfaces to the specific quantum processor. As members of the atomic-quantum-computer developers at MSU, we faced the challenge of integrating existing quantum programming languages with our hardware. This prompted the development of the compiler translating OpenQASM 2.0 code into instructions for our quantum computer, allowing us to couple existing quantum programming software with the hardware.

Compiler structure

Our quantum compiler is carefully designed software created to handle the intricacies of quantum programming on the atomic quantum computer. It has been developed using C++ and incorporates ANTLR4 [2] to benefit from the robust parsing capabilities and language recognition strengths that ANTLR4 provides.

After successful syntax validation, the compiler moves to the core of its functionality – binary code generation. It translates the validated OpenQASM 2.0 parse tree into an internal binary format, which is a limited set of quantum instructions that are native to our atomic quantum computer. This step is pivotal for the seamless execution of quantum programs on our specific hardware architecture. The current implementation covers a subset of OpenQASM 2.0, strategically excluding features like user-defined gates and multiple declarations of quantum registers `qreg`.

The distinctive aspect of the compilation process involves the transformation of quantum gates into three native gates – RX, RY, and CZ. Additionally, we have implemented a gate fusion optimization technique. This optimization streamlines quantum circuits by identifying and merging sequences of single-qubit gates, subsequently transforming them into at most three native rotations RX or RY.

The peculiar property of atomic quantum computers is the possibility for global single-qubit rotations, where all qubits in the register are rotated simultaneously. This operation has fidelity even higher than a single addressed rotation. The global rotations are implemented as compiler-intrinsic gates.

To distinctly separate classical and quantum computations, our compiler possesses the capability to precompute the results of mathematical expressions. This enables a clear delineation between the two domains, streamlining the compilation process and ensuring efficient execution on the quantum computer.

Future Developments

Looking ahead, we note that our development roadmap is ambitious. The planned switch to LLVM [3] for binary code generation promises improved performance and compatibility. Achieving full OpenQASM 2.0 language support and enabling OpenQASM 3.0 features are on the agenda, increasing the diversity of quantum programs. One of the anticipated features is the support of `defcal` blocks, where a gate-control sequence can be programmed in terms of laser pulses. Future versions of the compiler will introduce advanced optimizations, including qubit mapping and rerouting algorithms, essential for efficient circuit execution on atomic quantum computers.

Conclusion

The presented quantum compiler bridges the existing vast amount of applied software and execution on the real atomic quantum processor. It translates QASM code into the internal binary format suitable for execution. We tested our compiler in real-world tasks such as entangling-gate debugging, quantum tomography, and randomized benchmarking, where it performed as a reliable tool for experimentalists.

References

[1] *A. W. Cross, L. S. Bishop, J. A. Smolin, and J. M. Gambetta*, Open quantum assembly language. arXiv:1707.03429 (2017).

[2] *T. Parr*, The Definitive ANTLR 4 Reference. Pragmatic Bookshelf, (2013).

[3] *C. A. Lattner*, LLVM: An infrastructure for multi-stage optimization. Ph. D. Dissertation. Computer Science Dept., University of Illinois at Urbana-Champaign (2002).

Quantum algorithms with qubits packaged in trapped-ion qudits

Anastasiia S. Nikolaeva[1,2*], Ilia V.Zalivako[1,3], Alexander S. Borisenko[1,3], Evgeniy O. Kiktenko[1,2], Ilya A. Semerikov[1,3], Nikolay N. Kolachevsky[1,3], Aleksey K. Fedorov[1,2]

[1] *Russian Quantum Center, Skolkovo, Moscow 121205, Russia*
[2] *National University of Science and Technology "MISIS", Moscow 119049, Russia*
[3] *P.N. Lebedev Physical Institute of the Russian Academy of Sciences, Moscow 119991, Russia*
*E-mail: anastasiya.nikolayeva@phystech.edu

Abstract

In this work, we consider the problem of quantum algorithm implementation using trapped-ion-based qudits. We consider several realizations of universal set of qubit gates with qubits, which are packaged in qudit with dimensions $d = 3, \ldots, 8$. As a basic quantum operations, we use qudit versions of Pauli rotations and the Mølmer-Sørensen (MS) gate. We also investigate the issue of the reduction in the width and depth of the circuit for the implementation of multi-qubit quantum gates using qudits. We developed a multi-qubit gate decomposition that we test experimentally on an ytterbium-based ququart processor.

Most of the existing approaches to the development of quantum computing platforms involve the use of qubits, two-level quantum systems. At the same time, the physical systems usually have the ability to operate on a larger number of levels, i.e., they can be used as qudits [1]. Over the past few years, prototypes of qudit quantum processors based on ions in traps [2-4] have been developed. Therefore, the question of the efficient realization of qubit algorithms on them is crucial.

In a gate-based model of quantum computation, the circuit of a quantum algorithm consists of a set of quantum operations: single-qubit, two-qubit, and multi-qubit gates. It is known that an arbitrary qubit quantum circuit can be implemented with a set of single-qubit and two-qubit gates. Such a set of gates is called a universal set of gates. Thus, to implement an arbitrary qubit circuit with qudits, it is sufficient to implement single-qubit and two-qubit gates in qudits in a proper way, according to the embedding of qubit spaces in qudits. In our work [5], it is shown how a universal set of qubit gates, which contains a two-qubit entangling CZ gate and single-qubit Pauli rotations, can be efficiently implemented with a qudit version of native trapped-ion gates (MS gate and Pauli rotations), when the space of a qudit is used as a space of two ($d = 4$) or three qubits ($d = 8$). As an example of a quantum algorithm implementation with qudits, we consider Grover's algorithm realization with qutrits ($d = 3$) and ququarts ($d = 4$) (see Fig.1 and Table 1).

We also investigate the issue of the implementation of multi-qubit gates using qudits with trapped-ion-specific platform gates. Improvements were made to the circuit depth and length of the decompositions for qudit dimensions $d = 3, 5, 6, 7$. In the qubit scenario, $O(N^2)$ gates are necessary for decomposition without the need for extra auxiliary qubits. In our method, $O(N)$ gates are always sufficient. We demonstrate that as d increases, the constant before N and circuit decomposition depth decreases. Furthermore, unlike previously known decompositions, which are usually based on qudit CZ gate, these decompositions are initially expressed in terms of *qudit* version of Mølmer-Sørensen gate and Pauli rotations. Efficiency of the proposed decomposition technique is demonstrated *experimentally* on an ytterbium-based ququart processor.

Table 1: Number of entangling gates in Grover's algorithm realization with qubits, qutrits, and ququints. Realizations of Grover's circuits for the search through 2^2 and 2^3 elements are considered. In qubit-based realization decomposition with 6 two-qubit gates is used for C^2X gate and decomposition with 14 two-qubit gates is used for C^3Z gate.

Number of qubits	Num. of ent. gates with qubits	Qudit dimension	Num. of ent. gates with qudits
2	7	3	4
3	40	5	4

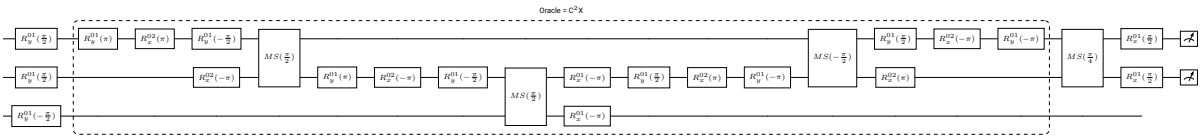

Figure 1: Grover's algorithm circuit for finding $\omega = 11$ on qubits embedded into qutrits with native qutrit trapped-ion qutrit gates .

The research is supported by RSF grant No. 19-71-10091.

References

[1] *E.O. Kiktenko, A.S. Nikolaeva, and A.K. Fedorov*, Realization of quantum algorithms with qudits. arXiv preprint arXiv:2311.12003. (2023).

[2] *M. A. Aksenov, I. V. Zalivako, I. A. Semerikov, et al.*, Realizing quantum gates with optically-addressable ^{171} Yb $^{+}$ ion qudits. arXiv preprint arXiv:2210.09121. (2022).

[3] *I.V. Zalivako, A.S. Borisenko, I.A. Semerikov, A. Korolkov, P.L. Sidorov, K. Galstyan, N.V. Semenin, V. Smirnov, M.A. Aksenov, A.K. Fedorov, K.Yu. Khabarova, and N.N. Kolachevsky*, Continuous dynamical decoupling of optical 171Yb+ qudits with radiofrequency fields, Frontiers in Quantum Science and Technology 2, 1228208 (2023); arXiv:2305.06071.

[4] *M. Ringbauer, M. Meth, L. Postler, et al.*, A universal qudit quantum processor with trapped ions. Nat. Phys. **18**, 1053–1057 (2022).

[5] *A.S. Nikolaeva, E.O. Kiktenko, and A.K. Fedorov*, Universal quantum computing with qubits embedded in trapped-ion qudits. arXiv preprint arXiv:2302.02966v2. (2023).

[6] *A.S. Nikolaeva, E.O. Kiktenko, and A.K. Fedorov*, Decomposing the generalized Toffoli gate with qutrits. Physical Review A **105**, 032621 (2022).

Randomized benchmarking of qubit arrays on a cold neutral atom quantum processor

Artem Rozanov[1*], **Boris Bantysh**[2,3], **Gleb Struchalin**[1], **Ivan Bobrov**[1], **Stanislav Straupe**[1,3]

[1] *Quantum Technology Centre and Faculty of Physics, M. V. Lomonosov Moscow State University, 1 Leninskie Gory, Moscow, 119991, Russia*
[2] *Valiev Institute of Physics and Technology, Russian Academy of Sciences, Moscow, 117218, Russia*
[3] *Russian Quantum Center, 30 Bolshoy Boulevard, building 1, Moscow, 121205, Russia*
*E-mail: rozanov.ad18@physics.msu.ru

Abstract

We present the benchmark results of the accuracy of one-qubit gate operations for a neutral-atom-quantum computer. The results are obtained with the protocol named direct randomized benchmarking. The protocol allows separate estimation of average gate fidelity and level of state preparation and measurement error by measuring outputs of random circuits with different depths. The results for one-qubit gates in 9- and 25-qubit arrays are demonstrated as well as the method for calibrating the pulses of one-qubit operations. The obtained fidelities vary from 99.92% to 99.97% depending on the qubit.

Cold neutral atoms in optical tweezers are a promising platform for quantum computing. Realizing fast and high-fidelity gates is of paramount importance for further development of this platform.

In our setup we use neutral atom qubits encoded in hyperfine states of ^{87}Rb: $|0\rangle = |5^2S_{1/2},\ F = 2,\ m_F = 0\rangle$ and $|1\rangle = |5^2S_{1/2},\ F = 1,\ m_F = 0\rangle$. For accuracy estimation, we benchmark single-qubit gates in arrays of ^{87}Rb atoms realized with radio-frequency (RF) field. For the calibration, we benchmark only one atom and then we estimate the accuracy for 9- and 25-qubit arrays globally impacted by RF-field.

To perform a rigorous assessment of single-qubit-gates quality we implemented a direct randomized benchmarking protocol (DRB) [1]. This protocol allows us to obtain an estimation of the average gate fidelity F_a of qubit operations using measurement results of randomly generated gate circuits of distinct depths. Moreover, an estimation of a state preparation and measurement error (SPAM) can be obtained from DRB curves. The basic idea of this protocol is the usage of randomly generated stabilizer states, i. e. the states obtained by applying the random Clifford-group gates to the $|0\rangle$ state. Then these states are used in the main circuit randomly formed from the generators of the Clifford group. The last layer of the circuit turns the obtained stabilizer state into either $|0\rangle$ or $|1\rangle$.

An example of the DRB curve is shown in Fig. 1(a). The data is fit by the expected dependence of success probability on the circuit depth [1]: $P = Ap^d + B$, where p is a parameter, related to the probability of the error absence, d is the circuit depth and A, B are coefficients related to SPAM. For the curves shown in Fig. 1(a) $F_a = 99.939 \pm 0.004\%$. Schemes corresponding to distinct expected outcomes demonstrate a clear shift of the P values, which is almost independent of d. This effect manifests asymmetric SPAM error in the atomic processor due to, e. g. atom losses.

The results for the 25-qubit array are shown in Fig. 1(b). DRB was applied for each atom and a value of mean gate fidelity was obtained. Fig. 1(b) shows mean infidelity $1 - F_a$ (for clarity) related to each atom in the lattice.

Before obtaining such fidelities we faced a problem with the calibration of one-qubit RF gates. RF signal has two parameters: a π-pulse time τ and relative phase φ. Due to the manual calibration of these parameters, a systematic error takes place. To eliminate this problem we simulated DRB circuits with different τ and φ values and then compared simulated results with experimental success probabilities. The obtained best-fit values served as the actual calibration for the RF signal.

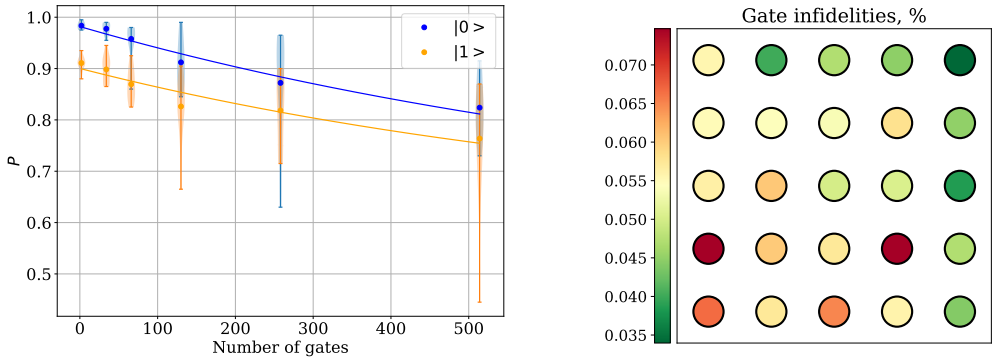

(a) (b)

Figure 1: (a) Experimental results of DRB. The success probability is depicted on the Y-axis. Solid curves are fits for the gate sequences ideally giving a $|0\rangle$ (blue) and a $|1\rangle$ output (orange). (b) Experimental results for a 25-qubit array obtained with DRB. Each circle is an atom in a 5×5 lattice. The color is related to the mean infidelity $1 - F_a$.

References

[1] *Polloreno, Anthony M., et al.* A theory of direct randomized benchmarking. arXiv preprint arXiv:2302.13853 (2023).

Quantum state preparation for qubit circuit using meta-heuristic and deep learning methods

Mikhail Sergeev[1*], **Gleb Fyodorov**[2], **Marina Bastrakova**[1,3]

[1] *Lobachevsky State University of Nizhny Novgorod, Nizhny Novgorod, Russia*
[2] *Moscow Institue of Physics and Technology, Moscow, Russia*
[3] *Russian Quantum Center, Moscow, Russia*
*E-mail: mas_135@mail.ru

Abstract

The possibility of preparing a quantum state in a register of interacting n-qubits using gradient-free optimizers such as random search and genetic algorihtm as well as one of the strongest deep reinforcement learning algorithms, AlphaZero, is demonstrated. Based on that approach, the possibility of quickly selecting optimal gate sequences consisting of one-, two-, and three-qubit operations to implement the required quantum state is shown.

Quantum state preparation is a key task in the vast majority of quantum algorithms. Algorithms such as linear system quantum computers [1], quantum Monte Carlo algorithm, quantum machine learning [2], and general variational quantum approaches [3] require fast and accurate encoding of classical data into quantum circuits. The state preparation routine is often considered the main bottleneck limiting the performance of quantum algorithms [4]. To prepare the overall quantum state of n-qubits, a circuit with $O(2^n)$ depth is required, since all 2^n internal parameters corresponding to amplitudes must be encoded using different gates [5]. These approaches do not solve the problem of exponential circuit growth with increasing number of encoding qubits and are impractical for large n. This work discusses a method for preparing quantum states on an n-qubit register using the AlphaZero deep learning algorithm [7] as well as meta-heuristic methods including random search and genetic algorithm[6]. The problem of preparing a quantum state from the point of view of reinforcement learning is a classical problem of interaction with the environment in the case of a discrete set of possible actions, which the chosen algorithms solve with high accuracy[7].

To prepare a quantum state on a register of interacting n-qubits $|\phi_{res}\rangle$, we use a variational quantum chain, represented as a set of unitary gate matrices $U(k)$ applied to the initial state $|\phi_i\rangle$. The task of preparing a certain state comes down to selecting the optimal sequence of gates. In this case, the final state was as close as possible to the required one, which is mathematically expressed in the operation accuracy criterion (fidelity):

$$F(\rho_1, \rho_2) = Tr[\sqrt{\sqrt{\rho_1}\rho_2\sqrt{\rho_1}}]^2 \quad (1)$$

where ρ_1, ρ_2 correlates to density matrices of input states.
To prepare the state, we sequentially use one-, two-, and three-qubit gates, which can be represented as possible actions for the AlphaZero algorithm. Using the standard procedure for encoding actions for this algorithm [8], we can obtain all possible combinations of quantum gates for a given chain. Gates with variable parameters, in particular, rotational (phase) gates, when used, are optimized using a modified Adam gradient descent algorithm [9]. As part of this task, the AlphaZero learning algorithm undergoes minor changes, in particular, the use of only one player (agent) instead of two in the original implementation of the algorithm. To compare genetic algorithm [6], random search algorithm and AlphaZero a series of experiments were performed, where each algorithm had to repeat the quantum state of a given randomly initialized circuit for 50 times per algorithm. The comparison results are shown in Fig.1.

The results of the work show the possibility of preparing a quantum state on a register of n-qubits using deep reinforcement learning algorithms. Using the abovementioned algorithms makes it possible to obtain the required sequence of quantum gates for preparing a given state, while demonstrating high accuracy in preparing a given state, expressed in the fidelity criterion, and also using the minimum optimal set of gate chains for quickly preparing the required state.

This work was supported by the Russian Science Foundation grant No. 22-72-10075.

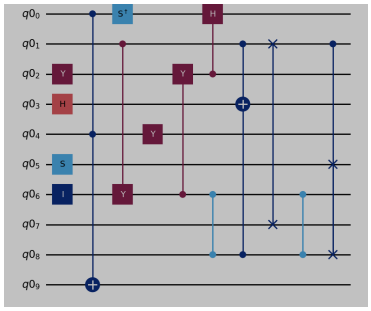

(a) Example target state 1.

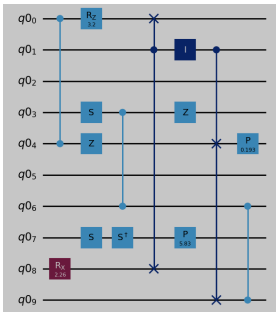

(b) Example target state 2.

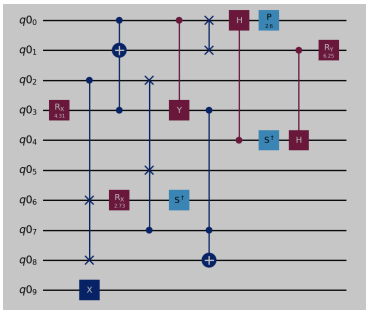

(c) Example target state 3.

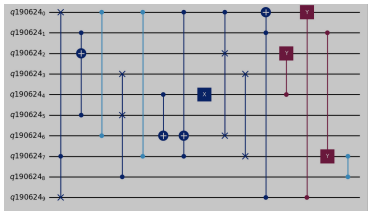

(d) Random search result for example state 1.

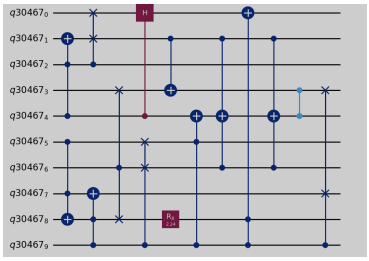

(e) Genetic algorithm result for example state 2.

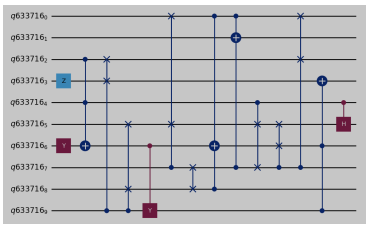

(f) AlphaZero result for example state 3.

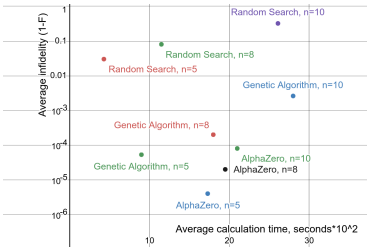

(g) Results comparison for all three algorithms.

Figure 1: (a-c): Example target gate sequences. (d-f): Prepared gate sequences for each of (a-c) sequences respectively with the same fidelity value of 0.99, using random search(d), genetic algorithm (e) and AlphaZero algorithm(f). (g): Comparison of average result measured in infidelity (1-F_{avg}) with the target state and computation time for different number (denoted n) of qubits for each algorithm. Results are averaged for 50 runs each, except for AlphaZero where we used only 10 runs.

References

[1] *M.R. Perelshtein, A.I. Pakhomchik, A.A Melnikov, A.A. Novikov, A. Glatz, G.S. Paraoanu, V.M. Vinokur and G.B. Lesovik*, Solving large-scale linear systems of equations by a quantum hybrid algorithm. Ann. Phys., Lpz. 534 2200082 (2022).

[2] *J. Biamonte , P. Wittek, N. Pancotti, P. Rebentrost, N. Wiebe and S. Lloyd*, Quantum machine learning. Nature 549 195–202 (2017).

[3] *M. Cerezo et al*, Variational quantum algorithms. Nat. Rev. Phys. 3 625–44 (2021).

[4] *M. Plesch and C. Brukner*, Quantum-state preparation with universal gate decompositions. Phys. Rev. A 83 032302 (2011).

[5] *K. Bharti et al*, Noisy intermediate-scale quantum algorithms. Rev. Mod. Phys. 94 015004 (2022).

[6] *P. Liashchynskyi and P. Liashchynskyi*, Grid Search, Random Search, Genetic Algorithm: A Big Comparison for NAS. arXiv:2108.11371 (2019).

[7] *D.Silver, T. Hubert, J. Schrittwieser et al*, Mastering Chess and Shogi by Self-Play with a General Reinforcement Learning Algorithm . arXiv:1712.01815 (2017).

[8] *T. McGrath, A. Kapishnikov et al*, Acquisition of Chess Knowledge in AlphaZero. arXiv:2111.09259 (2021).

[9] *D. Zou, Y. Cao, Y. Li, Q. Gu*, Understanding the Generalization of Adam in Learning Neural Networks with Proper Regularization. arXiv:2108.11371 (2021).

Optically controlled bistability of charged particles in surface ion traps

Elizaveta Soboleva*, **Dmitriy Shcherbinin**, **Semyon Rudyi**, **Andrei Ivanov**

IR&EC PhysNano, ITMO University, Saint-Petersburg, Russia
*E-mail: eliz.sobol239@gmail.com

Abstract

In the present work, we numerically simulate the dynamics of porous charged microparticles localized in surface radio-frequency trap under atmospheric conditions, taking into account laser irradiation. The dynamic system transition from bistability to states characterized by either one or three stable equilibrium points is revealed. The number of stable equilibrium points and their spatial position appear to depend on the magnitude of the particle gravity and optical pressure. The phase portraits of the particle trajectories are calculated for the each dynamic system state. The obtained results are generalized and discussed from a practical point of view.

Radiofrequency traps are a versatile tool for localizing, controlling, and investigating charged particles. Different trap configurations allow localizing particles with sizes from atomic ions to microparticles for applications in such fields as mass spectrometry [1], investigation of physical characteristics of micro- and nano-objects [2], and quantum computing [3]. It should be noted that radiofrequency traps can become a new promising element base for the realization of the Ising machine.

In order to realize calculations with the help of the algorithms used in the Ising machine, a controlled bifurcation in the system is necessary. At the same time, it is known that surface traps can be characterized by two stable equilibrium positions for charged microparticles [4]. In this work, we investigate the possibility of precisely adjusting the spatial position of the particle localization regions and switching between regimes characterized by one, two, and three stable equilibrium regions. In the present work, we propose a method for optical control of the bistability of the charged particle position in surface radiofrequency traps, where positions of localized particles are indicated blue and red dots (Fig. 1a). In this work the localization processes of porous single microparticles in a surface radiofrequency trap are numerically investigated. In the first part of the work numerical calculation is carried out for porous spherical CaCO3 particles with the size of 4 μm. The proposed surface trap geometry consists of 4 rectangular electrodes (Fig. 1b) and is a modification of the well-known 5-wire scheme [5]. Unlike the classical 5-wire scheme, the proposed geometry of electrodes provides stable controlled localization of charged particles along all degrees of freedom. The electrostatic interaction of the charged particle with the trap field, the particle gravity force (directed along the z-axis), viscous friction forces, and the optical pressure force from the exciting radiation side were taken into account in the modeling. For modeling it was assumed that the laser radiation is directed along the z-axis.

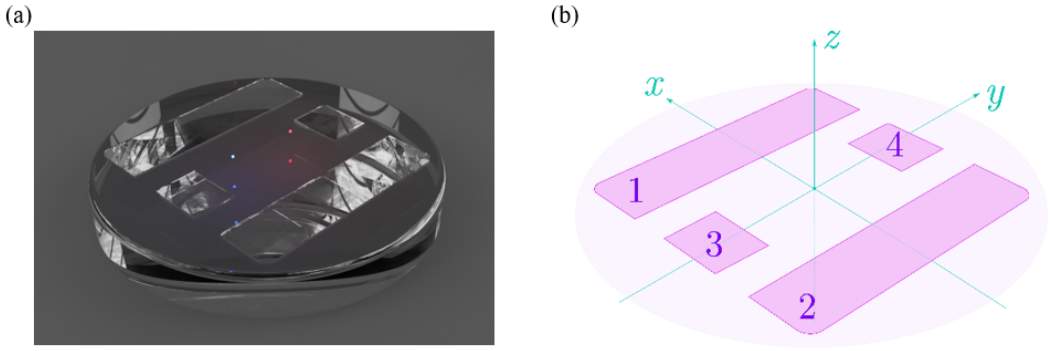

Figure 1: Surface ion trap model, (a) - 3D-model, (b) - circuit diagram of planar surface trap

Numerical modeling of the dynamics of charged microparticles of 2 μm size is carried out taking into account their interaction with the trap field, viscous friction and optical pressure force. Simulations are carried out for porous CaCO3 microspheres localized at atmospheric pressure in transparent ITO traps under the influence of laser radiation with a wave vector directed orthogonally to the trap surface. It is shown that the position of the particles depends on the direction and power density of the laser radiation acting on the particle localized in the surface radiofrequency trap (Fig. 2). Physical mechanisms of formation of several stable equilibrium positions are discussed.

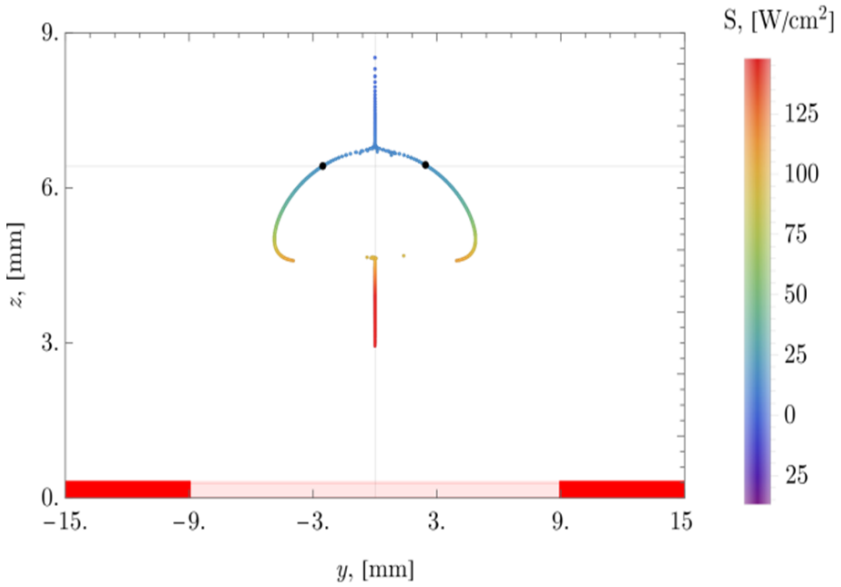

Figure 2: Dependence of the localized particle position on the laser radiation power density

References

[1] *D. Nolting, R. Malek, A. Makarov*, Ion traps in modern mass spectrometry. Mass spectrometry reviews. **38**, 2 (2019).

[2] *D.M. Bell, et al.*, Single CdSe/ZnS nanocrystals in an ion trap: charge and mass determination and photophysics evolution with changing mass, charge, and temperature. ACS nano. **8**, 3 (2014).

[3] *G.N. Nop, D. Paudyal, J.D. Smith*, Ytterbium ion trap quantum computing: The current state-of-the-art. AVS Quantum Science. **3**, 4 (2021).

[4] *D. Shcherbinin et. al.*, Charged Hybrid Microstructures in Transparent Thin-Film ITO Traps: Localization and Optical Control. Surfaces. **6**, 2 (2023).

[5] *M. House*, Analytic model for electrostatic fields in surface-electrode ion traps. Phys. Rev. **78**, 3 (2008).

Quantum optical neural networks with programmable Kerr nonlinearities

Elena Chernykh[1,2*], **Mikhail Saygin**[1,3], **Gleb Struchalin**[1], **Sergey Kulik**[1,3], **Stanislav Straupe**[1,2]

[1] *Quantum Technology Centre and Faculty of Physics, M.V. Lomonosov Moscow State University, 1 Leninskie Gory Street, Moscow, 119991, Russian Federation*
[2] *Russian Quantum Center, Bolshoy bul'var 30 building 1, Moscow, 121205, Russian Federation*
[3] *Laboratory of Quantum Engineering of Light, South Ural State University (SUSU), Russia, Chelyabinsk, 454080, Prospekt Lenina 76*
*E-mail: chernykh.ea18@physics.msu.ru

Abstract

Quantum optical neural networks (QONNs) potentially can solve different quantum computing problems. The key feature of QONNs is inclusion of nonlinear elements, which significantly expand the class of operations available to linear optics. To date QONNs have a structure similar to many classical neural networks, however these neural networks contain large number of the optimized parameters. In this work, we suggest original QONN architecture with variable nonlinearities. Our results indicate that our QONN is a promising architecture and a powerful tool for the different types of quantum computing problems.

To date the linear optical platform is one of the most promising for creating quantum computer. Information is encoded by photons propagating through multimode interferometers. However most of the operations performed by linear optics are non-deterministic. In addition, they require redundant physical resources, such as extra photons and optical elements, in addition to the ones that encode the quantum information [1]. This problem can be avoided by using nonlinear elements.

Nonlinear elements find an application in different fields and one of them is the physical implementation of quantum neural networks on a photonic platform. The principle of operation of quantum neural networks is similar to the idea for a classical neural network [2]. Namely, there is an alternation of linear layers with trainable parameters and nonlinear functions, also called activation functions. The Quantum optical neural network (QONN) implementation proposed to date operates according to the principle described above. Trainable linear layers are presented by multichannel linear optical interferometers separated by single nonlinear elements with fixed parameters in each mode. Quantum neural network training is performed by optimization methods on a classical computer, where the cost function C is defined as the fidelity function between the output state and the expected one from the training sample with size K and described by equation $C = \frac{1}{K}\sum_x^N \langle\psi_{ideal}|\rho_{out}|\psi_{ideal}\rangle$.

Thus, with an increase in the number of qubits, and with this the number of photons and modes encoding them, the space of optimized parameters becomes too complex. This causes problems for optimization algorithms. In this work, we propose an alternate approach. Linear elements are used as a fixed layer, while training is caused by optimizing the parameters of programmable nonlinear elements. Every nonlinear element has its own variable parameter χ and can be expressed as $\widehat{NS}(\chi) = \exp\left(i\hat{n}(\hat{n}-1)\frac{\chi}{2}\right)$.

We use dual-rail encoding to determine the qubit. It is a two-mode code where logical-zero state is represented by the photon in the first mode $|10\rangle$, while the logical-one state is represented by the photon in the second mode $|01\rangle$. It follows that so-called "non-qubit" states will arize as a result of photon propagation through the linear interferometer because its output corresponds to a system of N photons distributed among M modes. Therefore, linear elements with fixed parameters provide a "mixing" effect and redistribute photons between modes before passing through the programmable nonlinear layers, which change the phase only when there are two or more photons in the mode. QONNs based on static linear optics and nonlinear programmable elements possess a significant advantage, since the number of variable network parameters in each layer is linear in the number of modes. This makes the task less computationally difficult for various optimization algorithms.

Primitive example of such a neural network for a single qubit (two modes and one photon) is the nonlinear Mach–Zehnder interferometer (NMZI). The NMZI is a system of two beamsplitters and two programmable nonlinearities between them as it is shown in Fig. 1. Linear layers are represented by symmetrical beamsplitters here.

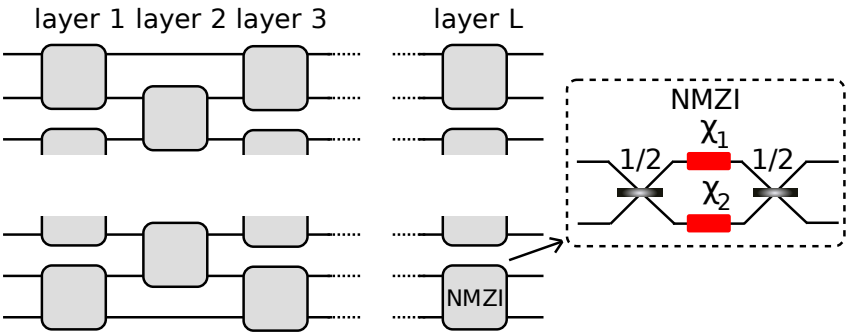

Figure 1: QONN architecture based on NMZI.

Scaling to a larger number of qubits can be performed in various ways. In our work, we suggest an original quantum optical neural network architecture consisting of NMZIs arranged in staggered formations (Fig. 1) and demonstrate architecture's capabilities in solving various quantum information problems such as preparing sophisticated quantum states and finding global minima of Hamiltonians by implementing a variational quantum algorithm. Our study suggests that the QONN with programmable nonlinearities can be less demanding than the traditional QONN and even advantageous for some specific tasks.

E.A. Chernykh is grateful to the Foundation for the Advancement of Theoretical Physics and Mathematics (BASIS) (Project No. 23-2-1-52-1).

References

[1] *E. Knill, R. Laflamme, and G.J. Milburn*, A scheme for efficient quantum computation with linear optics. Nature **409**, 46 (2001)

[2] *G. R. Steinbrecher, J. P. Olson, D. Englund, and J. Carolan*, Quantum optical neural networks. npj Quantum Inf. **5**, 60 (2019)

Analysis of quantum computing resources in the implementation of basic quantum algorithms on qudit systems

Chudakov Alexander[1*]

[1] *Quantum Technology Centre and Faculty of Physics, M.V. Lomonosov Moscow State University, 1 Leninskie Gory, Moscow, 119991, Russia*
*E-mail: RoskFaik@gmail.com

Abstract

The purpose of this work is to analyze quantum computing resources in the implementation of such basic algorithms as the quantum Fourier transform and Grover's algorithm on qudit systems. In the course of the work, a simulation of the QFT algorithm was implemented on qudit systems with dimension d from 2 to 8 to transform a vector with dimension 1024. A comparison of the number of one-qudit and two-qudit operations depending on the dimension of the qudit was also carried out and the corresponding graphs were obtained. A simulation of Grover's algorithm was implemented for qudits of dimension 2. An algorithm for large-dimensional qudits and further analysis is under development.

Consider the algorithm of the quantum Fourier transform in the case of qubits, that is, qudits of dimension 2. In this case, the action of the Fourier operator can be represented by the formula below

$$|j\rangle \xrightarrow{QFT} \frac{1}{\sqrt{N}} \sum_{k=0}^{N-1} e^{2\pi i jk/N} |k\rangle. \tag{1}$$

It is also important to mention that when implementing QFT, a controlling operation on qubits is used, where the gate R_k acts as this operation, the matrix of which has the following form

$$R_k \equiv \begin{bmatrix} 1 & 0 \\ 0 & e^{2\pi i/2^k} \end{bmatrix}. \tag{2}$$

So you can see the circuit of the QFT algorithm for the qubit system in Fig. 1.

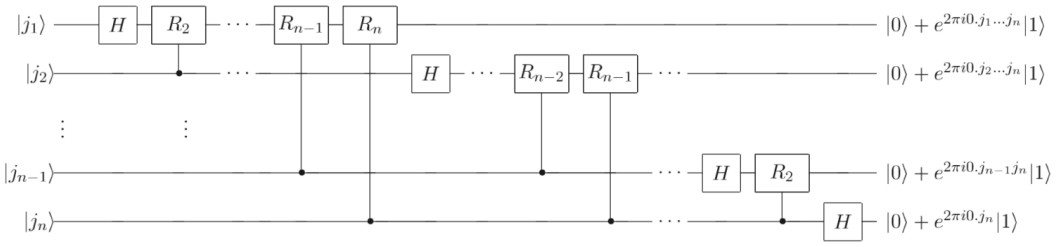

Figure 1: The circuit of the quantum Fourier transform algorithm in the case of a qubit system

Next, we consider the algorithm of the quantum Fourier transform in the case of qudits of dimension d [1, 2]. In this case, the action of the Fourier operator can be represented by the formula below

$$|j\rangle \xrightarrow{QFT} \frac{1}{d^{n/2}} \sum_{k=0}^{d^n-1} e^{2\pi i jk/d^n} |k\rangle. \tag{3}$$

It is also important to mention that when implementing QFT, a controlling operation on qudits is used, where the R_k^d gate [1] acts as this operation, which is a generalization of the R_k gate to the case of a qudit of dimension d. The matrix of this operator has the following form

$$R_k^d \equiv \begin{pmatrix} 1 & 0 & \cdots & 0 \\ 0 & e^{2\pi i/d^k} & \cdots & 0 \\ \vdots & \vdots & \ddots & \vdots \\ 0 & 0 & \cdots & e^{2\pi i(d-1)/d^k} \end{pmatrix}. \tag{4}$$

Thus, you can see the circuit of the QFT algorithm for the qudit system in Fig. 2.

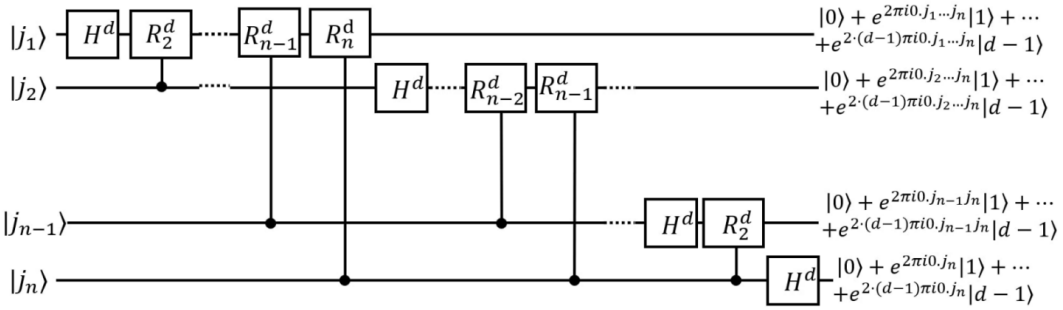

Figure 2: The circuit of the quantum Fourier transform algorithm in the case of a system of qudits of dimension d

Now let's consider a quantum search algorithm in an unstructured database, that is, Grover's algorithm in the case of qubits. One fundamentally important part of it is the oracle, which is a kind of black box that is able to recognize the solution of the problem. In the case when the phase of the ancilla has changed its sign, it means that a solution has been found. The action of the oracle can be represented as

$$|x\rangle \left(\frac{|0\rangle - |1\rangle}{\sqrt{2}} \right) \xrightarrow{o} (-1)^{f(x)} |x\rangle \left(\frac{|0\rangle - |1\rangle}{\sqrt{2}} \right). \tag{5}$$

Also, an equally important part is the Grover iteration, which includes a diffusion operator that rotates the state around the mean. Thus, you can see the circuit of the complete algorithm in Fig. 3.

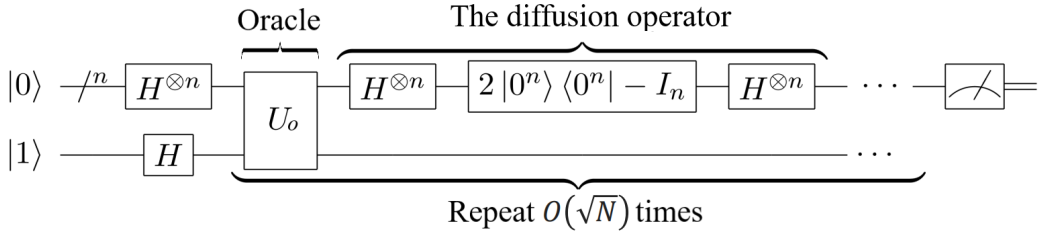

Figure 3: The circuit of the Grover algorithm in the case of a system of qubits

Next, let's return to the discussion of the QFT algorithm. As mentioned above, this algorithm was simulated on qudit systems with dimension d from 2 to 8 to transform the input state vector with dimension 1024. After that, a comparison of the number of one-qudit and two-qudit operations was carried out depending on the dimension of the qudit and the corresponding graphs were obtained, which are shown in Fig. 4.

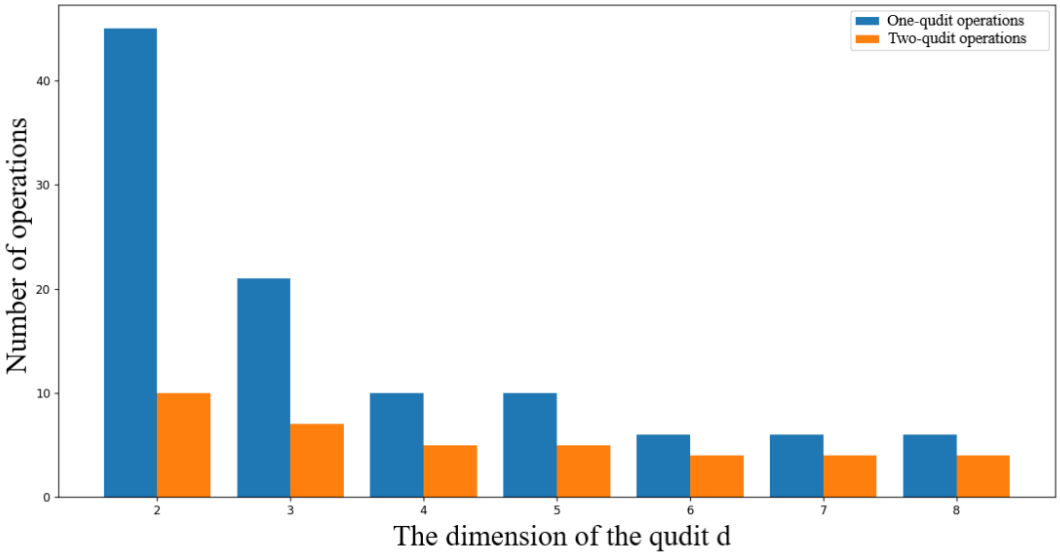

Figure 4: Graphs of the dependence of the number of one-qudit and two-qudit operations on the dimension of the qudit d when converting a state vector of dimension 1024

References

[1] *Yuchen Wang, Zixuan Hu, Barry C. Sanders, and Sabre Kais*, Qudits and high-dimensional quantum computing. Front. Phys. **8**, 479 (2020).

[2] *A.S. Nikolaeva, E.O. Kiktenko, and A.K. Fedorov*, Efficient realization of quantum algorithms with qudits. (2022).

Protection Method against Powerful Emission Attacks Based on Optical-Fiber Fuse Element

Bugai Kirill[1,2], **Zyzykin Artem**[1], **Bulavkin Daniil**[1], **Sushchev Ivan**[1,3], **Dvoretskiy Dmitriy**[1,2]

[1] *SFB Laboratory, Ltd, Moscow, 127273, Russia*
[2] *Bauman Moscow State Technical University, 2nd Baumanskaya str. 5-1, Moscow, Russia 107005*
[3] *Quantum Technology Centre and Faculty of Physics, M. V. Lomonosov Moscow State University, Moscow, 119991, Russia*
*E-mail: kirill.bugay@sfblaboratory.ru

Abstract

Unauthorized light injection has always been a critical threat to the practical security of quantum key distribution (QKD) systems. We have presented and implemented an optical fuse device based on the fiber fuse effect phenomenon, restricting the injection of eavesdropper's light. The proof-of-principle testing of the optical fuse was demonstrated. The methodology for testing and analysis presented here is applicable to other power-limiting components in QKD systems.

Introduction

The attacks on the transmitting unit (Alice), including laser-damage attacks [1, 2] and Trojan-horse attacks [3], compromise the security of quantum key distribution (QKD) implementation. One commonality of these attacks is that an adversary (Eve) injects unauthorized laser emission into the QKD transmitting apparatus to eavesdrop on secret key information.

Experimental setup and results

We developed an optical fuse device (DUT) designed to bolster the security of QKD transmitters. This destructible element enhances defense by leveraging the fiber fuse effect. We devised a testing scheme, which allows the passage of weak optical radiation inside the QKD system while ensuring destruction under laser radiation with the power of 200 mW. The experimental setup is shown in Fig. 1.

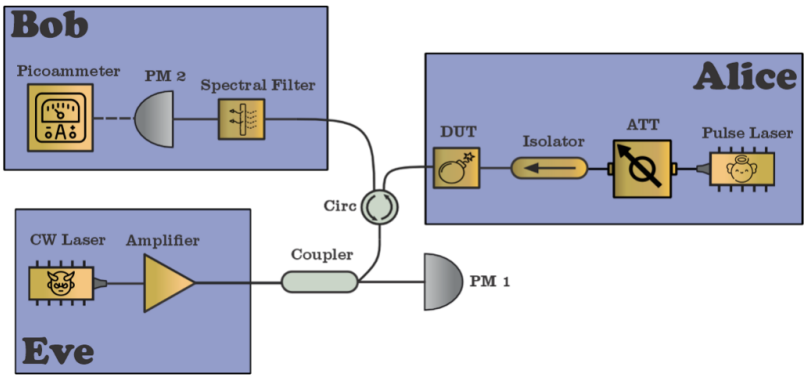

Figure 1: The scheme of studying the operability of the destructible element

The experimental setup comprises two main modules, each performing specific functions in imitation of the QKD system. The first module represents the QKD system's transmitter and includes the following components: the variable optical attenuator (ATT), the high-power fiber-optic isolator (Isolator) and the pulsed laser (Pulse Laser). It is worth noting that the composition of the elements in the transmitter module closely corresponds to the basic elements in a practical QKD system's transmitter.

We configured the pulsed laser to operate at the average power of 1.6 μW with a pulse frequency of 10 MHz. An important component in this module is the variable optical attenuator, which introduces attenuation at the level of 67 dB. As a result, the average power at the output of the attenuator was 0.0003 nW corresponding to weak coherent pulsed radiation, similar to the states implemented in QKD systems.

The mean photon number per pulse can be calculated using the following expression:

$$\mu = \frac{P\lambda}{2fch}. \tag{1}$$

We have achieved the following average photon number:

$$\mu = \frac{P\lambda}{2fch} = \frac{1550 \cdot 10^{-9} \cdot 0.0003 \cdot 10^{-9}}{2 \cdot 10 \cdot 10^{6} \cdot 3 \cdot 10^{8} \cdot 6.64 \cdot 10^{-34}} \approx 0.1. \tag{2}$$

The second module represents the receiver of the QKD system and includes the following components: the picoammeter (Picoammeter), the pin-diode (PM2) and the spectral filter (Spectral Filter). We performed the data registration using picoammeter method [4]. The module simulating the impact of a continuous laser with a power of 450 mW is also presented in the setup. This module consists of the continuous wave laser (CW Laser), the amplifier (Amplifier), the 50/50 beam splitter (Coupler) and the power meter (PM1). The 220 mW power was directed towards the destructible protective element by means of the beam splitter.

In the initial stage of the experiment, the pulsed laser source was activated. One minute later, the CW laser was activated, delivering optical power up to the level initiating the Fiber Fuse effect on the destructible protective element. At this stage, we observed the occurrence of the fiber fuse effect, manifesting as a phenomenon accompanied by bright luminescence and leading to the destruction of the specified protective element. The process of fiber fuse phenomenon is shown in Fig. 2.

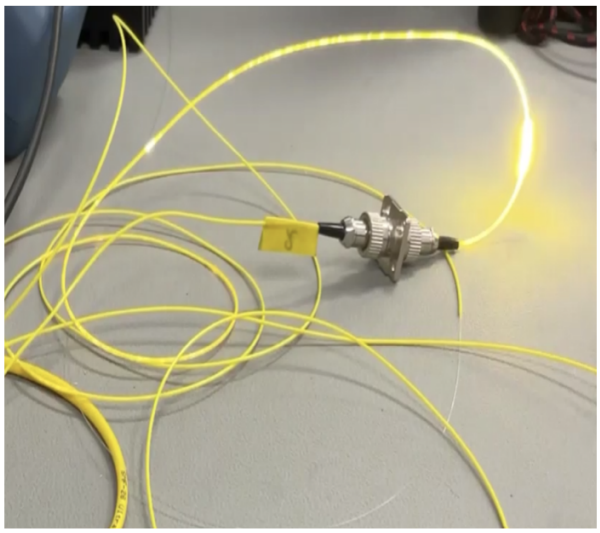

Figure 2: Photograph of the fiber fuse effect

The experiment results are depicted in the graphs shown in Fig. 3, 4.

The dependence of the laser radiation power on time, presented as the shape of the signal from the power meter PM1, is shown in Fig. 3.

The graph in Fig. 4 illustrates the dependence of the mean photon number on time. Due to experimental research, it can be concluded that, under the influence of a power equal to 212 mW, the optical fuse device caused a break in the fiber link. This occurred as the result of the DUT destruction, caused by an optical discharge during the phenomenon of the fiber fuse effect.

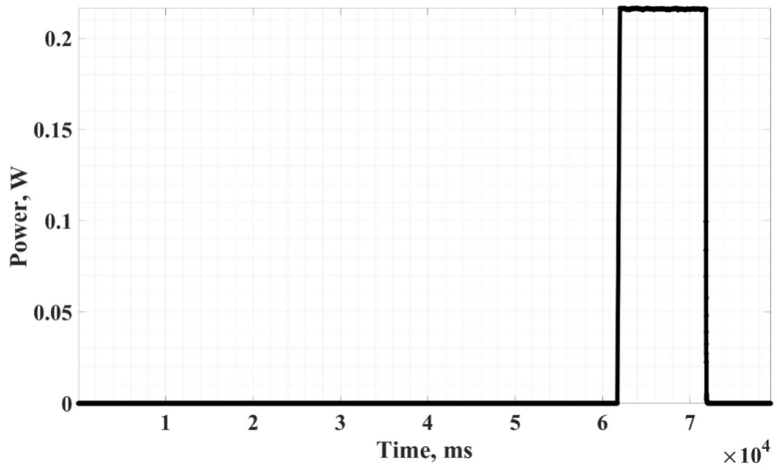

Figure 3: The dependence of laser radiation power on time as the shape of the signal from the first radiation receiver

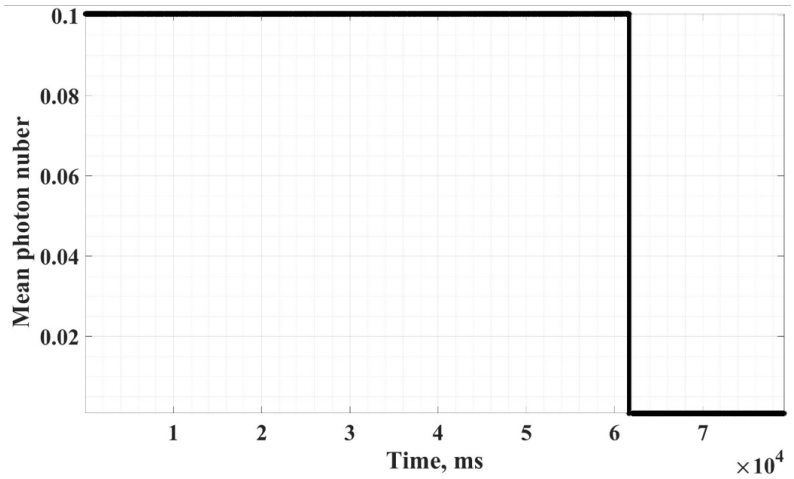

Figure 4: The dependence of the mean photon number on time, as the shape of the signal from the second radiation receiver

Thus, we offer a protection method based on the fiber fuse effect as a defense against the powerful laser emission attacks. We experimentally demonstrate that it is possible to protect a QKD system when high-power CW laser radiation reaches approximately 200 mW of optical power. We should note that, after the turning off the powerful continuous laser radiation and replacement of the damaged destructible element, the rest of QKD setup elements were not damaged. Accordingly, the proposed destructible element provides reliable protection against high-power radiation attacks.

References

[1] *Alferov, S.V., Bugai, K.E., Pargachev, I.A.* Study of the Vulnerability of Neutral Optical Filters Used in Quantum Key Distribution Systems against Laser Damage Attack. Jetp Lett. **116**, 123–127 (2022).

[2] *Anqi Huang, et.al.,* Phys. Rev. Applied **13**, 034017 (2020).

[3] *Boris Nasedkin, Fedor Kiselev, et.al.* Phys. Rev. Applied **20**, 014038 (2023).

[4] *Борисова А.В., Втюрина А.Г., et.al.* Методы измерения среднего числа фотонов в информационных импульсах систем квантового распределения ключей. Лазеры в науке, технике, медицине (2019).

Study on the dependence of the Backflash probability of single-photon detectors on the avalanche signal magnitude

Daniil Bulavkin[1*], **Ivan Sushchev**[1,2], **Kirill Bugai**[1,3], **Anna Sidelnikova**[1,2], **Dmitriy Dvoretskiy**[1,3]

[1] *SFB Laboratory, Ltd, Moscow, 127273, Russia*
[2] *Quantum Technology Centre and Faculty of Physics, M. V. Lomonosov Moscow State University, Moscow, 119991, Russia*
[3] *Bauman Moscow State Technical University, 2nd Baumanskaya str. 5-1, Moscow, Russia 107005*
*E-mail: Daniil.Bulavkin@sfblaboratory.ru

Abstract

Here we present the research on the dependence of the re-emission probability of InGaAs-based single-photon detectors on the magnitude of the avalanche signal caused by registration event. We exploited different mean photon number per pulse falling on the semiconductor structure of the detector.

Single-photon avalanche diodes (SPADs) based on InGaAs semiconductor structures have gained widespread application in quantum communication systems, particularly in quantum key distribution (QKD). However, these detectors have several drawbacks, which, to the developers' deep regret, can be exploited by an eavesdropper to compromise the transmitted secret key. One such shortcoming is the re-emission by the SPAD's semiconductor structure of photons (the backflash) during the events of signal registration or dark counts.

In study [1], it was demonstrated that the probability of re-emission does not depend on the mean photon number per optical pulse incident on the SPAD's semiconductor structure. However, the distribution of re-emission probability over different magnitudes of avalanche signals has not been previously investigated.

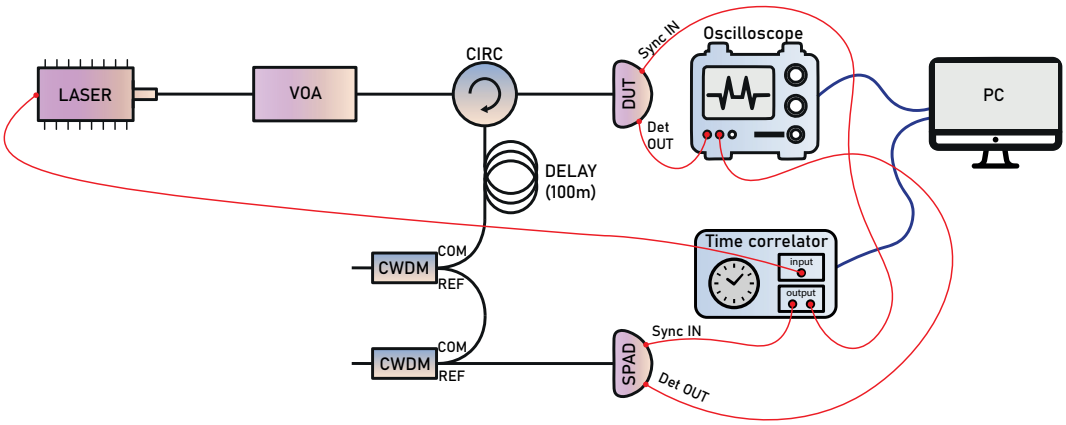

Figure 1: Experimental setup for investigation of the backflash probability depending on the avalanche signal magnitude during the SPAD count.

Based on the above, in this work, we attempted a more detailed investigation into the characteristics of re-emission. We conducted a study on the dependency of the backflash probability on the magnitude of the avalanche signal during a SPAD count. An experimental setup was developed for this experiment, as shown in Figure 1. The radiation source (LASER) is the pulsed laser operating at a wavelength of 1550 nm, which emits pulses to the single-photon detector under test (DUT) through the variable optical attenuator (VOA) and the circulator (CIRC). The second SPAD is used to detect the photons re-emitted by the DUT. Synchronization is achieved using a time correlator, which generates synchro-signals to the DUT and SPAD based on the electrical signal from the LASER. The registration of the avalanche signal during DUT re-emission is carried out using the oscilloscope, triggered by signals from the SPAD.

Consequently, we conducted studies on the dependence of re-emission probability on the avalanche signal magnitude during SPAD counts, which resulted in the statistics of backflash event distribution by avalanche signal magnitudes (Figure 2).

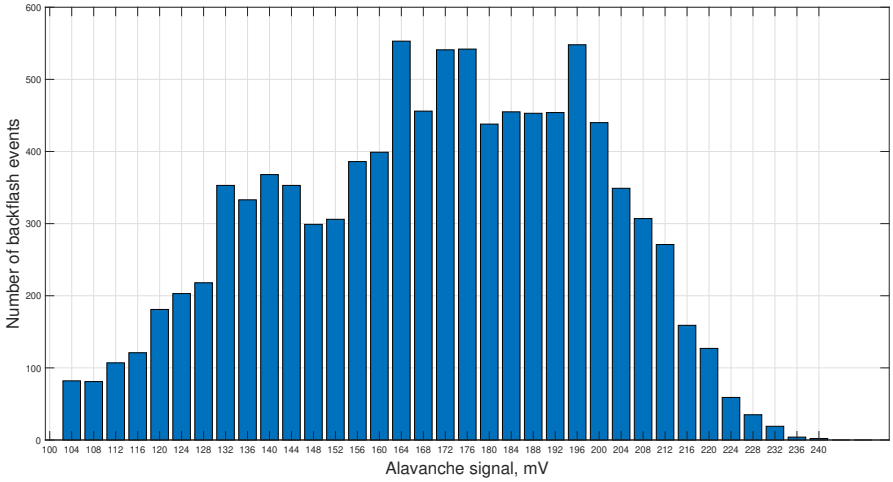

Figure 2: Backflash events distribution by avalanche signal magnitudes

Ultimately, this work presents the distributions of re-emission probabilities for optical signals over various mean photon numbers incident on the DUT. The findings of this research can be used for more detailed analysis of side-channel leakage in the future.

References

[1] *S. A. Bogdanov, I. S. Sushchev, A. N. Klimov, K. E. Bugai, D. S.Bulavkin, D. A. Dvoretsky*, Influence of QKD apparatus parameters on the backflash attack. In Quantum Technologies 2022 (Vol. 12133, pp. 90-95). SPIE (2022, May).

Estimations of background noise and aperture losses for a free-space quantum key distribution

Vakhrusheva V.M.[1,2*], **Moiseeva E.A.**[3], **Klimov A.N.**[4]

[1] *SFB Laboratory, Moscow, Russia*
[2] *JSC "InfoTeCS", Moscow, Russia*
[3] *Faculty of Physics, Moscow State University, Moscow, Russia*
[4] *MSU Quantum Technology Centre, Moscow, Russia*
*E-mail: vmvakhrusheva@gmail.com

Abstract

This work presents the results of theoretical estimates of background noise and aperture losses for daylight free-space quantum key distribution (QKD) systems operating on terrestrial horizontal paths.

Introduction

The operation of free-space quantum key distribution (QKD) systems in daytime conditions is significantly influenced by background illumination caused by solar radiation scattered by the atmosphere and reflected by various surfaces. The value of the quantum bit error rate (QBER), which directly depends on the signal-to-noise ratio (SNR) of a receiving device, is used to assess the quality of free-space QKD systems operation. To reliably distribute a secret key, the SNR must be at least 10. To reduce the influence of background noise spectral, temporal and spatial filtering is used. The last one is limiting of the receiver field of view and aperture. However, the latter also leads to a decrease in the value of the useful signal caused by an increase in aperture losses. Thus, when designing optical systems of daylight free-space QKD, their parameters must be selected to ensure the required SNR.

Results

We considered the case of the transmitter being located on a building against the background of a surface that can be considered as a Lambertian scatterer. The number of background photons in this case is given by

$$N_b = \frac{E_b \rho \pi \left(dNA\right)^2 \lambda \Delta\lambda \Delta t \eta \tau_a \tau_{oc}}{4hc}, \quad (1)$$

where E_b is the spectral irradiance of the Lambertian scatterer; ρ is the reflection coefficient (albedo) of the Lambertian scatterer; d and NA are the diameter and the numerical aperture of the receiving fiber; λ is the optical wavelength; $\Delta\lambda$ is the spectral filter bandpass; Δt and η are the temporal gate width and the quantum efficiency of a single photon detector (SPD); τ_a is the transmittance coefficient of the atmospheric path; τ_{oc} is the transmittance of the receiver optical system; hc are the Planck's constant and the speed of light.

The spectral irradiance of the Lambertian scatterer was determined using the SMARTS program (Simple Model of the Atmospheric Radiative Transfer of Sunshine) [1]. It calculates the spectral characteristics of solar radiation near the earth's surface in cloudless weather. The vertical surface illumination by direct solar radiation and radiation scattered by the atmosphere for a wavelength of 1550 nm depending on the time of day for different surface orientations relative to the direction to the north (azimuthal angle Az) is shown in Fig. 1a. The maximum spectral illumination for the summer period is 0.19 W/(m^{2}nm). To minimize background noise, it is proposed to isolate the Lambertian scatterer from direct solar radiation. Then the maximum spectral irradiance due to radiation scattered by the atmosphere is 0.025 W/(m^{2}nm). By blackening the scattering surface behind the transmitter, the reflection coefficient ρ=0.1 can be achieved. The calculation of the number of background photons was carried out for 2 km path length, 1550 nm wavelength and single-photon detectors with an input multimode fiber having a core diameter of 50 μm and a numerical aperture of 0.22. Then, assuming the transmittance coefficients of the

atmosphere and the receiving optical system are equal to 0.65 and 0.75, respectively, with the spectral filter bandpass of 1 nm, the temporal gate width of 1 ns and the SPD quantum efficiency of 10%, the number of background photons is $9 \cdot 10^{-5}$ photon per gate. It is two orders of magnitude higher than the dark count rate of the detector. Therefore, to decrease background noise, special efforts must be taken, in particular, reduction the gate and the spectral filter width.

In this work, we also calculated the value of aperture losses depending on the diameters of the transmitting and receiving optical systems apertures. The calculation was carried out taking into account the influence of atmospheric turbulence on the Gaussian beam propagating through a free-space path [2, 3]. Fig. 1b shows the dependence of the aperture losses taking into account turbulence on the diameters of the transmitting and receiving optical systems.

The dependence of the SNR on the transmitting and receiving optical systems diameters is shown in Fig. 1c. The SNR is given by

$$SNR = \frac{4hc * 10^{-l_A/10}}{E_b \rho \pi \left(dNA\right)^2 \lambda \Delta\lambda \Delta t}, \tag{2}$$

where μ is the mean photon number per pulse at the output of the transmitting system, equal to 0.1; l_A is the value of aperture losses, dB.

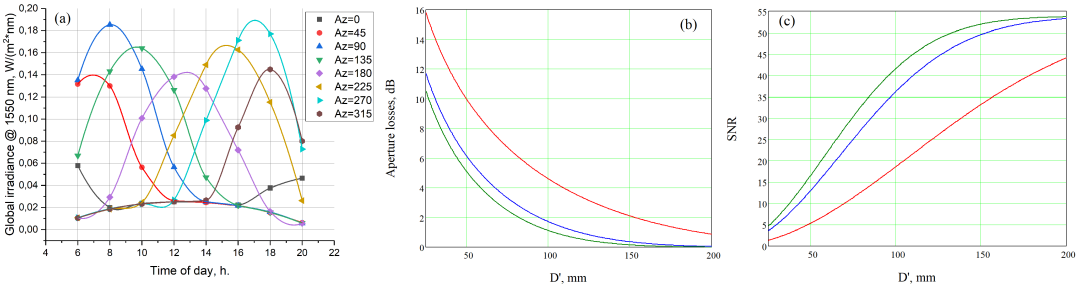

Figure 1: (a) The spectral irradiance of a vertical surface located in Moscow coordinates for June 21. (b) The aperture loss value for a path L = 2 km taking into account turbulence and (c) SNR depending on the diameter of the receiving system aperture with different diameters of the transmitting system aperture (50 mm – red, 100 mm – blue, 150 mm – green)

With aperture diameters of the transmitting and receiving systems equal to 100 mm, the aperture loss is 1.7 dB and the SNR is 36.

Thus, the free-space QKD system will be operational on 2 km terrestrial horizontal path on a bright sunny day with apertures of the transmitting and receiving systems of at least 70 mm, isolating of the scattering zone of the transmitter from direct solar radiation and blackening of the surface behind the transmitter.

References

[1] SMARTS https://www.nrel.gov/grid/solar-resource/smarts.html (2023).

[2] *J. Martos,L. Andrews, R. Phillips*, Analysis of beam wander effects for a horizontal-path propagating Gaussian-beam wave: focused beam case. Optical Engineering. **46** (2007).

[3] *V.E. Zuev*, Laser Beams in the Atmosphere, 215, (1988).

Miass, Russia February 25 – March 2, 2024
7th International School on Quantum Technologies

Research of a time shift attack on a subcarrier wave quantum key distribution system

Mikhail Gellert*, **Boris Nasedkin, Vladimir Chistiakov, Vladimir Egorov**

Laboratory of Quantum Communications, ITMO University, St. Petersburg, Russia
*E-mail: mihailgellert@yandex.ru

Abstract

The research investigates the loopholes of the subcarrier wave quantum key distribution system which are associated with the use of gating mode in single photon detectors. This paper illustrates the ability of an eavesdropper to control the data received by the receiver. The results can help in identifying similar attacks and developing a defense strategy for quantum key distribution systems.

Introduction

The most secure method of secret information transmission now is quantum key distribution (QKD) systems. In such systems security is guaranteed by the fundamental laws of quantum mechanics [1], rather than by the limited computing power of the eavesdropper. Although QKD protocols are theoretically secure [2, 3, 4], practical implementations of these systems may have loopholes that can be exploited by an eavesdropper to extract key information [5, 6]. One such loophole is the time window of operation of the single photon detector. Currently, many practical systems use optical fibers as quantum channels and operate at telecommunication wavelengths of 1550 or 1310 nm. Single photon detection in such systems is often accomplished using InGaAs avalanche photodiodes. To minimize dark counts, this type of detector typically operates in a gating mode. Therefore, by varying the timing of the pulse hitting the receiver detector, the information recorded by the receiver can be controlled. In this paper, we investigated the possibility of performing a time-shift attack on a subcarrier wave quantum key distribution system (SCW QKD). Commonly, SCW QKD systems have a Bragg grating in the optical circuitry that separates the subcarrier-waves from the center wave [7]. This fact allows the eavesdropper to perform additional manipulations of the radiation in order to trigger the detector on demand.

Results

To verify the realization of no triggering, the eavesdropper uses a tunable time delay line to shift the emissions relative to the triggering window of the single photon detector. The result is presented in Fig. 1. This paper investigates the operation of a SCW QKD system and an infiltrating intruder. The main aspect of this attack is the ability of the eavesdropper to influence the states measured by the receiver, therefore, to verify the feasibility of the time-shift attack, it is necessary to make sure that the eavesdropper can change the state "1" (single photon detector triggering) to state "0" (single photon detector no triggering) and reverse assertion. To test the realization of detector triggering, the eavesdropper must perform additional phase modulation of the radiation. With the help of phase modulators of the sender and the receiver will occur radiation at side frequencies, and phase shifts (Pa and Pb) are introduced into the modulating signals. single photon detector triggering occurs in the case of constructive interference (P_a - $P_b = 0$), no triggering in the case of destructive interference (P_a - $P_b = \pi$). Using a phase modulator, the eavesdropper modulates the sender's radiation with a phase shift P_e different from 0 and π. So the result of the subsequent modulation by the receiver, regardless of the selected modulation will lead to the result that completely side frequencies are not missing, thus it allows to provoke false triggering in the system. This fact is illustrated in Fig. 2.

This paper considers the simplest possible case and does not take into account important factors in realizing such an attack, such as quantum efficiency of the detector. However, the attack can also be modified and used in combination with other attacks.

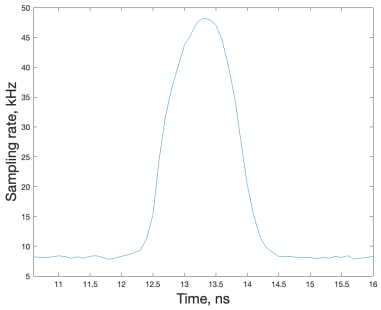

Figure 1: Experimental graph of sampling rate dependence on the time shift of the signal.

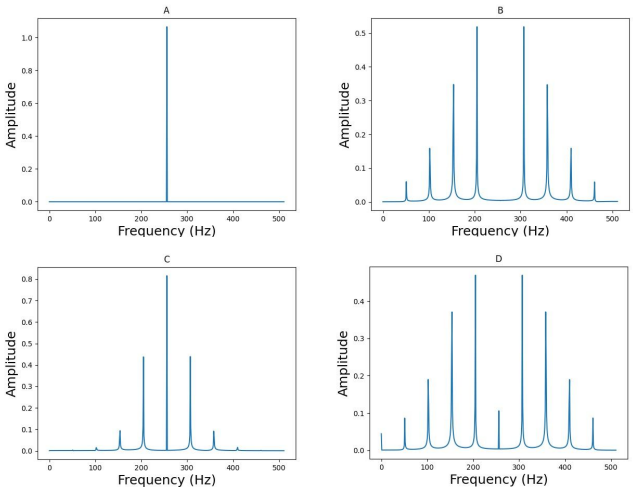

Figure 2: Spectrum of optical radiation after phase modulation obtained by modeling.(A,C) Modulation by sender and receiver. (B,D) Modulation by sender, receiver and eavesdropper. (A,B) Destructive interference case. (C,D) Constructive interference case.

Also in this paper it was shown that the time shift of the signal can be realized the absence of triggering the detector, and the use of phase modulator in turn allows you to increase the probability of triggering the detector.

References

[1] *Bennett C. H., Brassard G.*, Quantum cryptography: Public key distribution and coin tossing. Theoretical computer science. **560**, 7 (2014).

[2] *Lo H. K., Chau H. F.*, Unconditional security of quantum key distribution over arbitrarily long distances. Science.**283.5410**, 2050 (1999).

[3] *Shor P. W., Preskill J.* , Simple proof of security of the BB84 quantum key distribution protocol. Physical review letters.**85.2**, 441 (2000).

[4] *Gottesman D. et al.*, Security of quantum key distribution with imperfect devices.International Symposium onInformation Theory, 2004. ISIT 2004. 136 (2004).

[5] *Brassard G. et al.*, Limitations on practical quantum cryptography. Physical review letters.**85.6**, 1330 (2000).

[6] *Sun S., Huang A.* , A review of security evaluation of practical quantum key distribution system.Entropy. **24.2**, 260 (2022).

[7] *Sajeed S. et al.*, An approach for security evaluation and certification of a complete quantum communication system. Scientific Reports. **11.1**, 5110 (2021).

Method for evaluating the effectiveness of protection against combined beam splitter attack and laser damage attack on fiber-optical attenuators widely used in QKD systems

Ivanova Yuliya[2*], Bugai Kirill[1,2], Zyzykin Artem[1], Bulavkin Daniil[1], Sushchev Ivan[1,3], Sidelnikova Anna[1,3], Dvoretskiy Dmitriy[1,2]

[1] *SFB Laboratory, Ltd, Moscow, 127273, Russia*
[2] *Bauman Moscow State Technical University, 2nd Baumanskaya str. 5-1, Moscow, Russia 107005*
[3] *Quantum Technology Centre and Faculty of Physics, M. V. Lomonosov Moscow State University, Moscow, 119991, Russia*
*E-mail: yuliya@mpu.su

Abstract

We present a strategy combining the beam splitting attack and laser damage attack on quantum key distribution systems. We tested this strategy on the attenuators, which are widely used in fiber-based quantum key distribution systems. We simulated the deformation distributions in attenuators resulting from the propagation of powerful laser radiation.

Introduction

Quantum key distribution (QKD) System provides a secure exchange of information between legitimate users, guaranteed by the laws of quantum mechanics. However, if the eavesdropper (Eve) changes the absorption of the fiber optic attenuator widely used for single-photon state preparation, then the safety of such a system will be at great risk [1]. In Alice, a fiber optical attenuator is usually the last component that interacts with laser radiation before passing through the quantum channel. However, for eavesdroppers, the attenuator is the first component, which can be attacked by high-power laser radiation.

Experimental setup and results

We propose a novel attack strategy involving beam splitters for quantum key distribution (QKD) systems. Evaluating this strategy allows us to derive a criterion for the effectiveness of QKD system protection. The attack scheme is illustrated in Fig. 1.

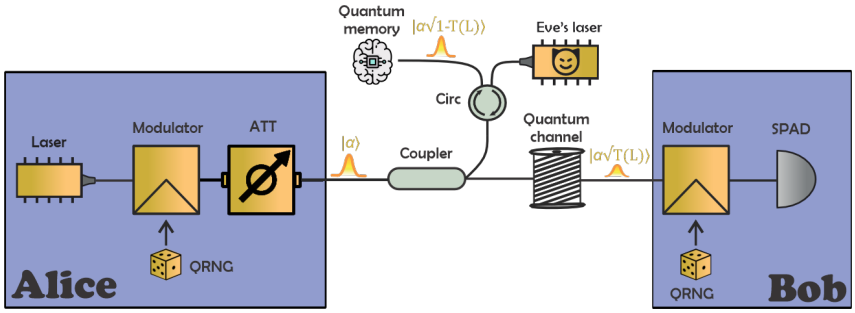

Figure 1: Schematic representation of the attack. SPAD — single photon avalanche diode, QRNG — quantum random number generator, ATT — Fiber-optic Attenuator

The proposed attack is based on a beam splitter attack, which is only feasible when a lossy channel is used [2]. In the initial stage of the attack, an eavesdropper infiltrates the quantum communication channel with a length of L. Alice sends the coherent pulses with mean photon number per pulse μ. During the attack, an eavesdropper uses a beam splitter with asymmetric transmission coefficients into the quantum communication channel. This action diverts a portion of the state $1-T(L)$ into Eve's quantum memory, while the remaining portion of the coherent state $T(L)$ is sent to Bob through a channel with lower or zero losses. Therefore, Bob receives undistorted states.

At the second stage of the proposed attack, an eavesdropper begins to change the absorption of the attenuator inside the Alice's setup by employing powerful laser radiation. Thus, the average photon number per pulse takes the form

$$\mu' = 10^{\frac{\Pi}{10}}\mu, \tag{1}$$

where Π is the magnitude of the attenuation coefficient variation.

We calculated the conditional von Neumann entropy to find an assessment of the protection efficiency against this attack. The von Neumann entropy serves as a measure of uncertainty and assesses the degree of key secrecy.

Considering the attack, the conditional von Neumann entropy

$$H(\rho_{XE}|\rho_E) = 1 - \overline{C}(\mu), \tag{2}$$

where the Holevo quantity equals:

$$\overline{C}(\mu) = e^{-\mu(1-T(L))10^{\frac{\Pi}{10}}} \Sigma_{n=1}^{\infty} \frac{\mu^n (1-T(L))^n (10^{\frac{\Pi}{10}})^n}{n!} = 1 - e^{-\mu(1-T(L))10^{\frac{\Pi}{10}}}. \tag{3}$$

It can be seen that the lack of Eve's information decreases with the rise of μ value. Hence, even the smallest drop of attenuation value compromises the QKD security.

To analyze protection against this "Photon Sabotage" attack, we designed an experimental setup with a powerful fiber laser acting as an eavesdropper. The test bench scheme is shown in Fig. 2. Continuous laser radiation with a power of up to 5.5 W at a wavelength of 1561 nm is directed towards the attenuator sample under test, thereby heating it, which can possibly result in alteration of the attenuator's absorption [3]. To monitor changes in the attenuation, another laser (LD2) at a wavelength of 1550.12 nm is installed in the scheme, acting as Alice. Two radiation detectors (PM1 and PM2) are used to measure Alice's radiation power before and after the attenuator under test (DUT). A spectral filter (SF) with a 2 nm bandwidth and the operating wavelength of 1550 nm is installed in the setup to suppress reflected radiation from the powerful laser LD1. Due to a powerful optical isolator (ISO), the intense continuous laser radiation from the eavesdropping laser LD1 cannot affect Alice's laser LD2 [4]. Since the samples under test may experience the Fiber Fuse Effect, a 100 m SMF-28 fiber spool (FS) was added as a protection against it.

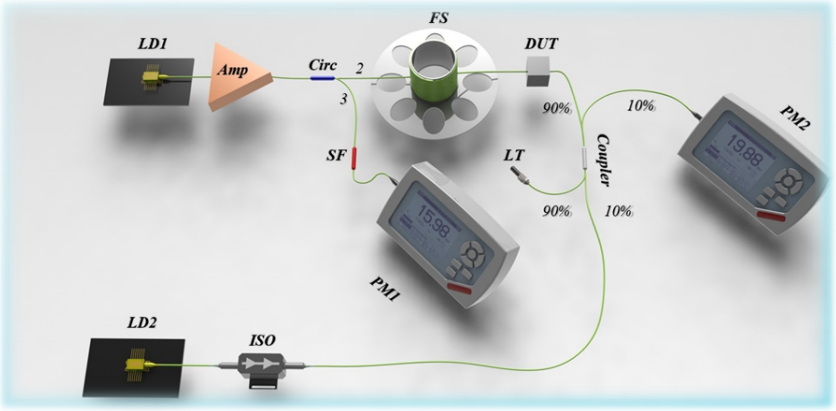

Figure 2: Experimental setup

Using this method, we studied the effect of LDA on 3 similar samples of widely used commercially available attenuators with 10 dB absorption, shown in Fig. 3b. Experimental data on the DUT attenuation variation under high-power CW radiation is shown in Fig. 3a. As seen from the graph, the investigated attenuators are not resistant to the Photon Sabotage attack.

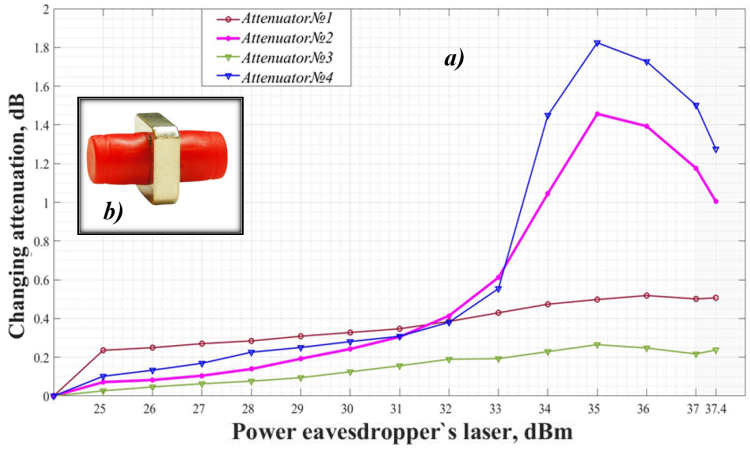

Figure 3: : (a) Attenuation deviation of DUT under high-power CW radiation, (b) Image of used 10-dB attenuator

We simulated the strain distribution depending on the power of laser radiation set at 5 W propagated through the DUT. The obtained results are presented in Fig. 4. The simulation was performed using COMSOL Multiphysics products.

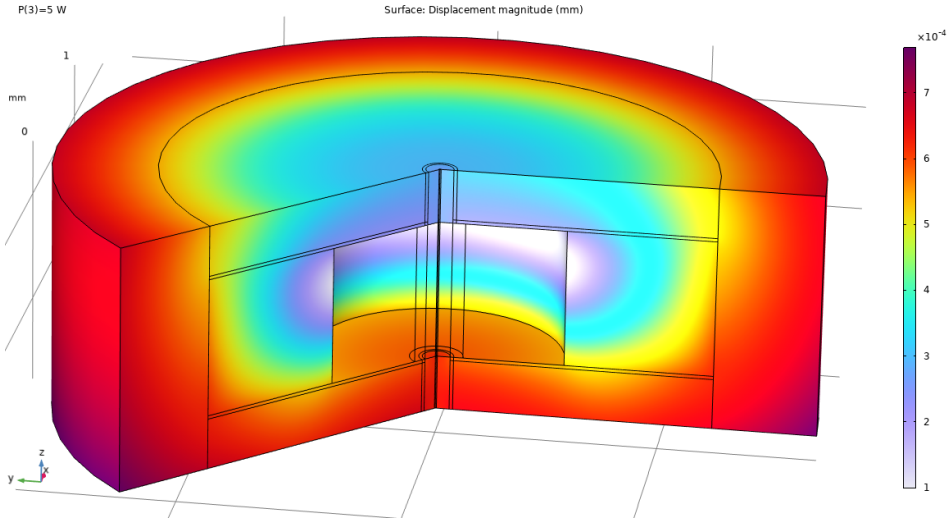

Figure 4: The results of modeling the strain distribution depending on the propagated power of laser radiation, set at 5 W

Through modeling, we achieved a more profound understanding of the laser damage attack processes. The proposed method for testing attenuators serves as a crucial tool for developers, enabling them to enhance the security of quantum key distribution systems.

References

[1] *Alferov, S.V., Bugai, K.E., Pargachev, I.A.* Study of the Vulnerability of Neutral Optical Filters Used in Quantum Key Distribution Systems against Laser Damage Attack. Jetp Lett. **116**, 123–127 (2022).

[2] *Bennett C.H., et al.,* J. Cryptology **5**, 3–28 (1992).

[3] *Anqi Huang, et.al.,* Phys. Rev. Applied **13**, 034017 (2020).

[4] *Huang, Alvaro Navarrete, et.al.,*, Phys. Rev. Applied **12**, 064043 (2019).

The effect of turbulent disturbances in atmospheric communication channels in entaglement-based QKD systems

Dmitry Melkonian[1,2,3*], **Konstantin Kravtsov**[1], **Sergey Kulik**[1]

[1] *MSU Quantum Technology Centre, 119991 Moscow, Russia*
[2] *SFB Laboratory, Ltd, Moscow, 127273, Russia*
[3] *Faculty of Physics, Moscow State University, Moscow, 119991, Russia*
*E-mail: dmitry.melkonian@gmail.com

Abstract

In this paper, the possible negative effects of the influence of turbulent disturbances in atmospheric communication channels for entanglement-based quantum key distribution systems have been considered. In order to decrease such influence an active tracking system has been developed and the results of its testing in a quantum key distribution system are demonstrated.

The main problem that communication participants face when transmitting quantum states through open space communication channels is the loss of photons due to interaction with the Earth's atmosphere and turbulent air flows. For example, in [1], the fraction of losses that occurred directly in the atmospheric data transmission channel due to optical path misalignment consists around 84% of all losses (-38dB). In this paper, we consider BBM92 quantum key distribution (QKD) protocol [2], which uses polarization-entangled photon states. A variation in the polarization of photons leads to errors in their detection, and, therefore, can lead to a violation of key generation along with photon losses during the passage of a turbulent medium. Thus, the problem of the possible effect of turbulence on photon polarization is also of particular interest. Theoretical studies and numerical experiments on this topic have been conducted before [3], [4]. However, in order to experimentally simulate a QKD system running BBM92 protocol, it is necessary, first of all, to experimentally verify the results of a numerical experiment demonstrating the absence of the effect of turbulent flows on the polarization angle in a real experiment. It can be achieved with a turbulent chamber, which allows modeling a turbulent atmospheric channel. Thus, an experimental verification of the polarization angle variation during the passage of an atmospheric channel is performed under real-world conditions. Then, a similar atmospheric channel is experimentally simulated and the efficiency of the developed tracking system designed for refraction losses compensation is evaluated.

Experiment

The experimental setup for determining the polarization angle variation when light passes through a turbulent medium is shown in Figure 1.

In this experiment, a collimated laser beam with a width D $\sim$ 1 cm at a wavelength $\lambda = 810$nm passes through the system (3-13). Using the system (3-5), by rotating the quarter-wave (4) and half-wave (5) plates, V-, H-, D-, A-, L- and R-polarized light is prepared. Passing through the turbulent chamber(6), it is exposed to turbulent air flows (7) (Fried's parameter for this turbulent medium equals r = 3mm, which allows us to assert that this medium is significantly inhomogeneous), and then measured using the system of the quarter-wave and half-wave plates (8) and (9), as well as the polarizer (10).Thus, it is possible to measure the power of the transmitted light and then to determine the Stokes parameters. By comparing the values of the Stokes parameters with the turbulent chamber turned on and off, it becomes possible to determine the difference in the polarization of light states during the passage of an atmospheric channel.

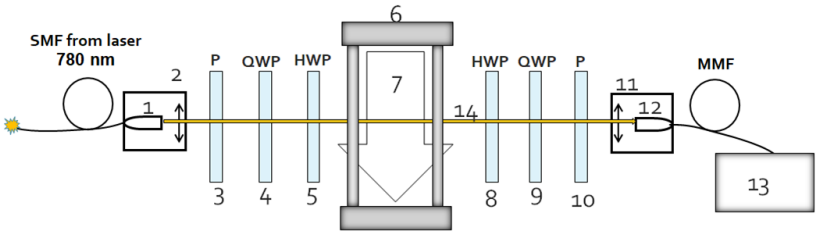

Figure 1: The scheme of the experimental setup for determining the effect of turbulent air flows on the polarization, where: 1 is the single–mode optical fiber connecting the 810 nm laser (14) and the input of the experimental setup, 2 and 11 are the collimators, 3 and 10 are the polarizers, 4 and 9 are the quarter-wave plates, 5 and 8 are the half–wave plates, 6- the turbulent chamber, 7 – turbulent air flows, 12 – the multimode optical fiber, through which light enters the input of the power meter 13.

The experimental setup for the QKD implementation with the system for experimental simulation of atmospheric turbulent channels using an active tracking system consists of two main parts: the source of entangled states (an untrusted center) with the detection and control electronics unit and the system for simulating an atmospheric channel with the active tracking system included. The active tracking system is designed to correct distortions of the beam propagation direction introduced by the atmospheric channel (Figure 2).

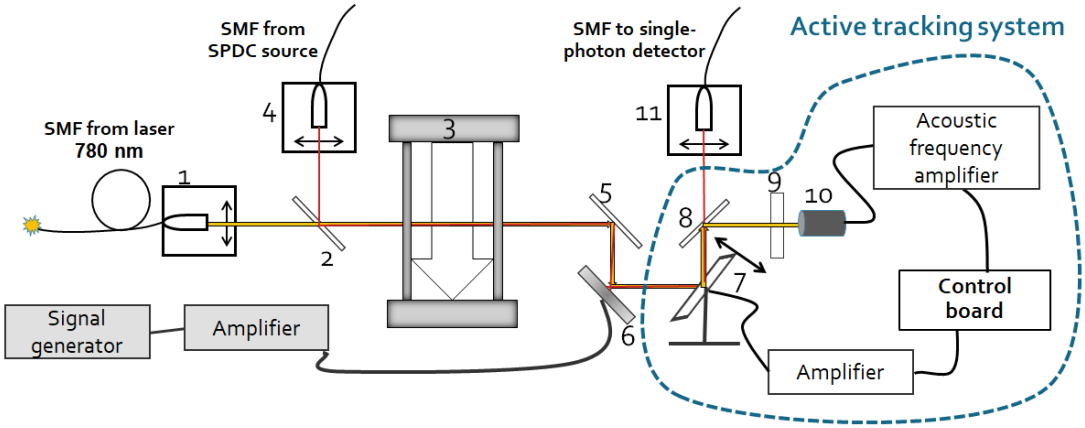

Figure 2: The setup for the active tracking system testing. 1) The lens system for a laser with λ = 780 nm 2) The beam splitter 3) The turbulent chamber 4) The output of the entangled photon source λ = 810 nm 5) The fixed mirror 6) The piezo mirror 7) The mechanical feedback system 8) The dichroic mirror 9) The light filter 10) The quadrant detector 11) The light filters and the single-mode fiber to the single-photon detector

In this experiment, polarization-entangled photons are directed to the single photon detectors. In this case, one photon is sent to the detector directly from the output of the source of entangled states, and the other additionally passes through the simulated atmospheric channel. The number of coincidences in the two channels is the measure for the quality of the active tracking system.

Thus, two signals are received at the input of the active tracking system from an untrusted center with a source of entangled photons: a signal at a wavelength of 810 nm, which represents polarization single-photon states and a tracking signal at a wavelength of 780 nm, designed to automatically adjust the receiver's system to maximize the number of registered photons at a wavelength of 810 nm.

Results

In this work, the absence of any significant influence excluding the refraction effect of atmospheric turbulence on polarization states during a QKD session has been experimentally demonstrated.

The developed active tracking system effectively compensates for the negative effects of photon refraction on turbulent inhomogeneities of the medium and mechanical fluctuations of the source of entangled photons. The application of the active tracking system increased the number of coincidences from ~ 1.5 % to 50-75 % (Table 1), depending on the conditions in the atmospheric communication channel.

Table 1: The number of registered photon coincidences observed by Alice and Bob under different conditions.

Experiment number	1	2	3	4	5	6	7	8
Active tracking system mode	off	off	on	off	on	on	on	on
Turbulent chambers ΔT, K	0	0	0	75	75	180	180	180
Piezo mirror signal	0	Sin(2πt)	Sin(2πt)	0	0	0	Sin(2πt)	Heavy-side
Coincidence frequency, Hz	3500 ± 41	47 ± 5	2246 ±37	48± 9	2613 ±60	2082±89	1821 ± 71	1692 ±115

Thus, this work demonstrates the possibility of efficient key distribution using polarization-entangled photons through the real atmospheric channel, due to the absence of changes in their state, as well as significant minimization of losses during the passage of a turbulent medium.

References

[1] *Nauerth S., Moll F., Rau1 M., Fuchs C., Horwath J, Frick S., Weinfurter H.*, Air-to-ground quantum communication. Nature Photonics, Letter, vol. 7, 382-386, 2013, doi 10.1038/nphoton.2013.46.

[2] *C.H. Bennett, G. Brassard, and N.D. Mermin*, Quantum cryptography without bell's theorem. Phys. Rev. Lett., 68:557, 1992.

[3] *Z. Tao, A. Abdukirim, C. Dai, P. Wu, H. Mei , Y. Ren, C Luo, R. Rao, H. Wei*, Atmospheric turbulence does not change the degree of polarization of vector beams. Journal of the Optical Society of America B, February 2023.

[4] *Q. Wang, S. Yu, Y. Zhou, L. Tan, J. Ma*, Influence of atmospheric turbulence on coherent source in a horizontal long-distance laser link. Optics and Laser Technology, Volume 122, February 2020, 105877.

Countermeasure to an attack with induced photorefraction in visible range on quantum key distribution systems

Boris Nasedkin[1,2*], **Azat Ismagilov**[1], **Vladimir Chistiakov**[2], **Andrei Gaidash**[1,3,4], **Anton Tcypkin**[1], **Anton Kozubov**[1,3,4], **Vladimir Egorov**[2,3]

[1] *Laboratory of Quantum Processes and Measurements, ITMO University, 199034, 3b Kadetskaya Line, Saint Petersburg, Russia*
[2] *Laboratory for Quantum Communications, ITMO University, 199034, 3b Kadetskaya Line, Saint Petersburg, Russia*
[3] *SMARTS-Quanttelecom LLC, Saint Petersburg, 199178, Russia*
[4] *Department of Mathematical Methods for Quantum Technologies, Steklov Mathematical Institute of Russian Academy of Sciences, 119991, 8 Gubkina St, Moscow, Russia*
*E-mail: banasedkin@itmo.ru

Abstract

In this work we studied transmission spectra of an isolator and a circulator in 400-800 nm range. We demonstrated that the circulator has a transmission window in the range of 400-506 nm, which can be used by an eavesdropper to implement an attack based on induced photorefraction. Moreover we propose to utilize the isolator as a potential countermeasure against the attack due to its spectral properties.

Introduction

The security of quantum key distribution (QKD) systems relies on the fundamental laws of physics. Nonetheless, imperfect devices in QKD systems introduce vulnerabilities that can be exploited by eavesdroppers during its attacks to extract additional information about the transmitted bits (often referred to as "quantum hacking"). The efficiency of certain attacks is contingent upon the spectral properties of the optical elements employed in the system.

In this context, a crucial methodology for identifying vulnerabilities involves spectral measurements of the components transmission within the considered system. Presently, various studies have explored spectral vulnerabilities within 600-2100 nm range for fiber-optic components of QKD systems [1, 2, 3, 4]. Moreover, it has been demonstrated that attacks utilizing even shorter wavelength radiation are conceivable. Among these attacks induced-photorefraction attack (IPA) [5, 6] is worthy of note, as its efficiency amplifies at lower wavelengths. The main aims of the attack are phase and amplitude modulators based on photo-refractive crystals, where alterations in refractive index or transmittance can occur under the influence of optical radiation.

We studied the transmission spectra of a dual-stage fiber-optic isolator and a circulator within the wavelength range of 400-800 nm in order to define if they can be used as countermeasures against IPA. The selection of these elements for investigation is motivated by their prevalent utilization as countermeasures against attacks occurring at different wavelength ranges.

Result

To measure the transmission spectra of the elements under study we assembled an experimental setup which consisted of a radiation source, three neutral filters, a system for introducing radiation into an optical fiber, and a spectrometer (USB-2000-FLG, Ocean Optics). In this work we used a laser pumped plasma broadband light source (XWS65, ISTEQ). As a result, we obtained transmission spectra presented in Figure1.

Measured transmittance of the isolator in the range up to 772 nm turned out to be less than the minimum power that can be measured in our setup (Fig.1a). This transmittance value in the considered range may be associated with strong absorption in the magneto-optical crystal used in the isolator, since an unpolarized broadband radiation source was used and it can potentially depend on the number of stages in an isolator. For 772-800 nm range the maximum transmission value was found to be -44.5 dB.

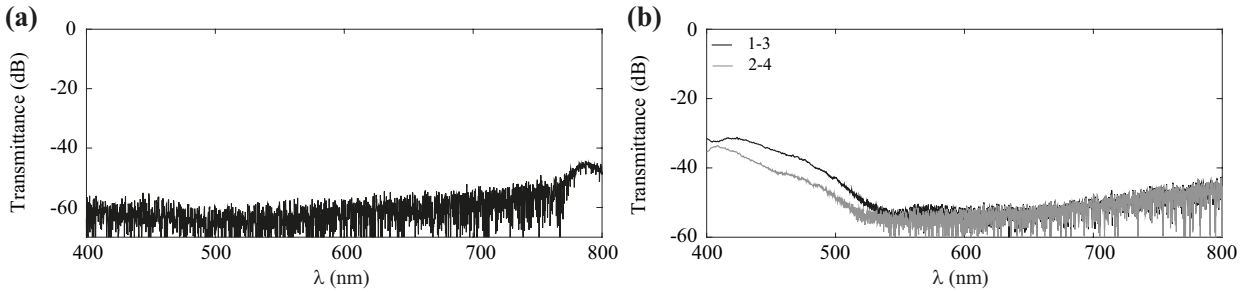

Figure 1: Measured transmittance for a) dual-stage isolator (reverse connection); b) circulator (black line is for transmittance from port 1 to port 3, grey line is for transmittance from port 2 to port 4)

Studying the circulator, we did not detect any signal when measuring transmission from port 1 to port 2 and vice versa. The measured transmittance of the circulator from port 1 to port 3 is presented in Figure 1b. It can be seen that the circulator transmits optical radiation in the range of 400-506 nm where transmittance is higher than for the standard QKD operational wavelength (1550 nm). Maximum transmittance was found to be -31.1 dB at 419 nm. Transmission in the reverse direction coincided with transmission in the direct connection.

Conclusion

We have demonstrated that the transmittance of the isolator over the considered wavelength range is less than -44.5 dB. Presumably, this level of transmission is due to the absorption of radiation by the magneto-optical crystal. The transmittance of the circulator varies from -30 to -45 dB for the 400-506 nm range. We assume that this may be due to reflections from the optical components used in the circulator.

The obtained results demonstrate that the investigated isolator can be used as a short-wave filter against IPA. The circulator could also be utilized in a similar way, but more complex circulator-based filtering systems require additional testing before installation into QKD systems.

The study is partially funded by the Ministry of Education and Science of the Russian Federation (Passport No. 2019-0903).

References

[1] *N. Jain, B. Stiller, I. Khan, V. Makarov, C. Marquardt and G. Leuchs*, Risk analysis of Trojan-horse attacks on practical quantum key distribution systems. IEEE J. Sel. Top. Quantum Electron. **21**, 3, 168–177 (2014).

[2] *B.A. Nasedkin, F.D. Kiselev, I.M. Filipov, D.A. Tolochko, A.O. Ismagilov, V.V. Chistiakov, A.A. Gaidash, A.N. Tcypkin, A.V. Kozubov and V.I. Egorov*, Loopholes in the 1500–2100-nm Range for Quantum-Key-Distribution Components: Prospects for Trojan-Horse Attacks. Phys. Rev. Appl. **20**, 1, 014038 (2023).

[3] *A.V. Borisova, B.D. Garmaev, I.B. Bobrov, S.S. Negodyaev, and I.V. Sinil'shchikov*, Risk analysis of countermeasures against the trojan-horse attacks on quantum key distribution systems in 1260–1650 nm spectral range. Opt. Spectrosc. **128**, 1892–1900 (2020).

[4] *I.S. Sushchev, D.M. Guzairova, A.N. Klimov, D.A. Dvoretskiy, S.A. Bogdanov, K.D. Bondar and A.P. Naumenko*, Practical security analysis against the Trojan-horse attacks on fiber-based phase-coding QKD system in the wide spectral range. Emerging Imaging and Sensing Technologies for Security and Defence VI **11868**, 57–63 (2021).

[5] *P. Ye, W. Chen, GW. Zhang, FY. Lu, FX. Wang, GZ. Huang, S. Wang, DY. He, ZQ. Yin, GC. Guo, and ZF. Han*, Induced-Photorefraction Attack against Quantum key Distribution. Phys. Rev. Appl. **19**, 5, 054052 (2023).

[6] *FY. Lu, P. Ye, ZH. Wang, S. Wang, ZQ. Yin, R. Wang, XJ. Huang, W. Chen, DY. He, GJ. Fan-Yuan, GC. Guo, and ZF. Han*, Hacking measurement-device-independent quantum key distribution. Optica **10**, 4, 520–527 (2023).

The Protocol of Quantum Key Distribution on Axially Symmetrical Polarization Beams in the Atmospheric Channel

Daniil Reshetnikov[1*], **Andrey Sokolov**[2], **Evgenii Vashukevich**[1], **Victor Petrov**[1], **Tatiana Golubeva**[1]

[1] *Saint Petersburg State University, 7/9, Universitetskaya nab., Saint Petersburg, 199034 Russia*
[2] *National Research University 'Moscow Power Engineering Institute', 14, Krasnokazarmennaya ul., Moscow, 111250 Russia*
*E-mail: d.d.reshetnikov@gmail.com

Abstract

The work proposes a protocol for quantum key distribution using axially symmetric polarization beams invariant to rotation of the radial coordinate in a plane normal to the beam propagation axis. It is shown that axial polarization symmetry makes such beams insensitive to rotations relative to the optical axis, which makes it possible to use them to transmit information in cryptographic protocols in space communication systems. The mechanism of mode formation using cube corner reflectors is shown in detail.

The development of quantum key distribution (QKD) systems is due to the increased requirements for the protection of information in communication networks [1]. The BB84 QKD protocol, which is basic for quantum cryptography, uses two bases of single-photon quantum states with linear polarization. With the use of advanced single-photon detectors and low-loss fiber lines, secret key distribution speeds of the order of 100 Mbit/s over distances of tens of kilometers have been achieved at the moment [2, 3].

It is important to note that the application of the BB84 protocol with linear polarized bases for the QKD tasks of low-orbit spacecraft is significantly difficult due to the need for fixation the position of the light polarization plane at each moment of time by both transmitting and receiving systems on Earth and in space. It was shown in [4] that in transmitting optical laser systems, the polarization state changes significantly for different points of the hemisphere. In the case of the polarization protocol, this means that the two bases rotated at 45° depend on the mutual orientation of the transmitting telescope and the spacecraft.

This problem can be eliminated if beams with an axially symmetric polarization structure are used [5]. It is proposed to use the polarization degree of freedom of such beams as an information carrier in QKD systems. Figure 1 shows the intensity profile of such beams, the arrow shows the direction of polarization at each point in transverse plane of beam.

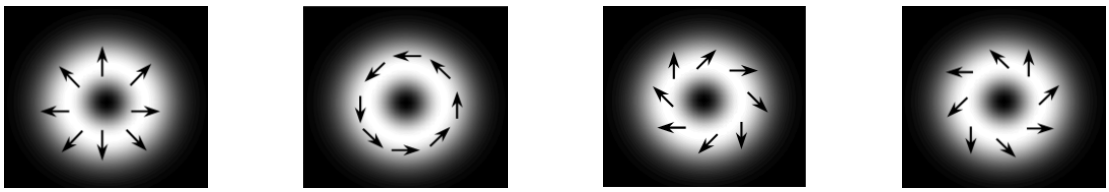

a) b) c) d)

Figure 1: Beams with axial symmetry intensity distribution: a) radial-polarized beam; b) axial-polarized beam; c) right-twisted polarized beam; d) left-twisted polarized beam

Obtaining beams with a given axial polarization structure and their detection are two individual tasks. The methods of their production can be divided into two main ones: the first is intracavity methods, when first–order modes are generated instead of the main laser mode [6], and non-resonant methods using diffraction optical elements [7].

It was shown in [8] that second-order beams are formed when a linearly polarized beam is reflected from a cube corner reflector (CCR), in particular, in the presence of a special interference coating of the faces, a second-order optical vortex is formed. The use of such optical elements allows quickly control the polarization of optical vector fields, which is a key point for their use in cryptographic systems. The

problem of beam detection in a classical cryptographic channel can be solved using a device acting as a radial polarizer [9].

However, for quantum channels, the use of absorbing elements — radial polarizers, is unacceptable. Based on this constraint, we consider the procedure for detecting polarization degrees of freedom in the configuration of the Mach-Zander interferometer, the elements of which are CCRs. In this work we propose a scheme for the rapid generation of beams with given axial polarisation structure, as well as the encoding and decoding of quantum information within the framework of the QKD protocol (Fig.2). Switching between the generation of different basis states is realized by changing the phase, which ensures faster operation of the generation scheme compared to schemes with spatial light modulators.

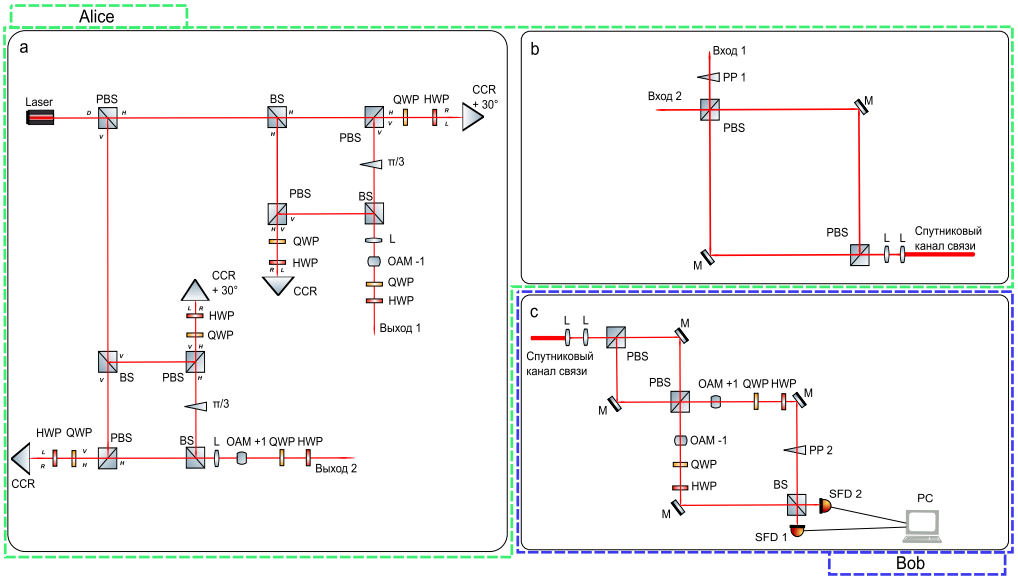

Figure 2: The optical scheme of Alice's transmitting device, consisting of a) a scheme for generating optical vortices using CCR, b) a Mach-Zander polarization interferometer and c) an optical scheme of Bob's receiving device. In the diagram: PBS, BS — polarization and regular beam splitters, HWP, QWP — half- and quarter-wave plates, PM – phase modulator, OAM ±1 — phase hologram changing the value of the topological charge of the beam, L — collecting lens, M — mirror, $\pi/3$ — phase plate, SFD — single-photons detector, PP — controlled phase plate.

References

[1] *C. Portmann, R. Renner*, Security in quantum cryptography. Rev. Mod. Phys. **94**, 025008 (2022)

[2] *F. Grünenfelder, A. Boaron, G.V. Resta, et al.*, Fast single-photon detectors and real-time key distillation enable high secret-key-rate quantum key distribution systems. Nat. Photon. **17**, 422-426 (2023)

[3] *A. Tanaka, M. Fujiwara, S. Woo Nam, et al.*, Ultra fast quantum key distribution over a 97 km installed telecom fiber with wavelength division multiplexing clock synchronization. Opt. Express. **16**, 11354-11360 (2008)

[4] *А. С. Акентьев, М. А. Садовников, А. Л. Соколов, Г. В. Симонов*, Поляризационный анализ системы наведения квантово-оптических систем. Оптика и спектроскопия. **122**, 6 (2017)

[5] *A. Tovar*, Production and propagation of cylindrically polarized Laguerr-Gaussian laser beams. J. Opt. Soc. Am. A. **15**, 2705 (1998).

[6] *R. Dorn, S. Quabis, G. Leuchs*, Generation of a radially polarized doughnut mode of high quality. Appl. Phys. B. **81**, 5 (2005).

[7] *А. В. Гаврилов и др*, Дифракционная нанофотоника. М.: Физматлит. (2011).

[8] *A. L. Sokolov*, Optical vortices with axisymmetric polarization structure. J. Opt. Soc. Am. A. **30**, 7 (2013).

[9] *Е. Ф. Ищенко, А. Л. Соколов*, Поляризационная оптика (учебное пособие, изд. 3). М.: Изд.–во. Физматлит. (2019)

Investigation of spectral characteristics of the backflash from single-photon avalanche photodiode

Anna Sidelnikova[1,2*], **Daniil Bulavkin**[2], **Kirill Bugai**[2,3], **Ivan Sushchev**[1,2], **Artem Zyzykin**[2], **Dmitriy Dvoretskiy**[2,3]

[1] *Quantum Technology Centre and Faculty of Physics, M. V. Lomonosov Moscow State University, Moscow, 119991, Russia*
[2] *SFB Laboratory, Ltd, Moscow, 127273, Russia*
[3] *Bauman Moscow State Technical University, Moscow, 105005, Russia*
*E-mail: lemurchik65@mail.ru

Abstract

The backflash attack is one of the various side channels attacks on quantum key distribution system (QKD). To test the sustainability to this attack for the QKD system, it is necessary to measure the maximum possible backflash probability from each detector inside the receiver setup. In this paper we report the result of research on backflash probabilities dependencies on the wavelength of stimulating laser.

Quantum key distribution (QKD) provides two legitimate users (Alice and Bob) with an absolute secure key. This level of security is ensured by the laws of quantum mechanics. The key remains secure as long as the implementation of the QKD system satisfy specific requirements. Any discrepancy in physical characteristics of the components can lead to the information leakage to an eavesdropper (Eve). A side channel of information leakage found in QKD systems is the backflash emission from InGaAs single-photon avalanche photodiodes (SPAD). That is so-called the backflash attack [1].

In recent decades, active studies of the properties of backflash emission have been carried out. The dependencies of the backflash intensity on the quantum efficiency of the SPAD, the temperature, the SPAD gate widths and the mean photon number per pulse of the stimulating emission were obtained previously [2, 3]. The backflash spectrum was also measured in [4]. In this paper, the dependency of the probability of the backflash on the stimulating laser's wavelength is investigated. A noticeable deviation of the backflash probability from the average value in a certain spectral range of the stimulating emission can either lead to a loophole in the QKD system for Eve or the opportunity to reduce information leakage through this side channel selecting the communication wavelength.

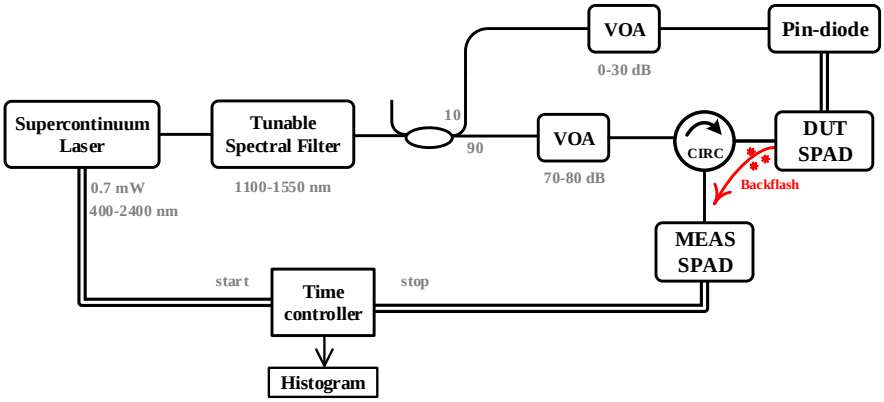

Figure 1: The scheme of backflash probability measurements dependencies on wavelength of stimulate laser by optical reflectometry.

A classical optical time-domain reflectometry (OTDR) scheme was used to measure the backflash probability [2]. The experimental setup is shown in Fig. 1. The pulsed supercontinuum laser operating in the range of 400-2400 nm was used as a source which stimulates detection events on the SPAD under test (DUT SPAD). The wavelength was selected by the tunable acousto-optic spectral filter operating

in the range of 1100-1550 nm. To minimize the reflection noise, the laser emission was attenuated to a weak coherent pulses level by the variable optical attenuator (VOA). All backflash photons from the DUT SPAD entered the measuring SPAD (MEAS SPAD) through the optical circulator. The laser and the SPADs operate at 10 MHz frequency. The generator of electrical synchro pulses is located in the laser. The MEAS DUT is synchronized with the laser by means of a time controller, while the DUT SPAD is synchronized with it via an optical channel using an additional pin-diode.

The histogram shows the backflash photons as a function of the time delay between the laser pulse and its detection by the MEAS DUT. Fig. 2 a) shows the combined backflash and reflected photons statistics, the separate statistics of reflected photons, and the difference between these statistics representing the separate backflash photons. The backflash probability is evaluated as [2]:

$$P_{BF} = \frac{N_{BF}}{N_P \eta_{meas} \eta_{ch}}, \tag{1}$$

where N_P - the number of the DUT SPAD counts, N_{BF} - the number of the backflash counts, η_{meas} - the detection efficiency of MEAS SPAD, η_{ch} - the optical channel transmission from the output of the DUT SPAD to the MEAS SPAD.

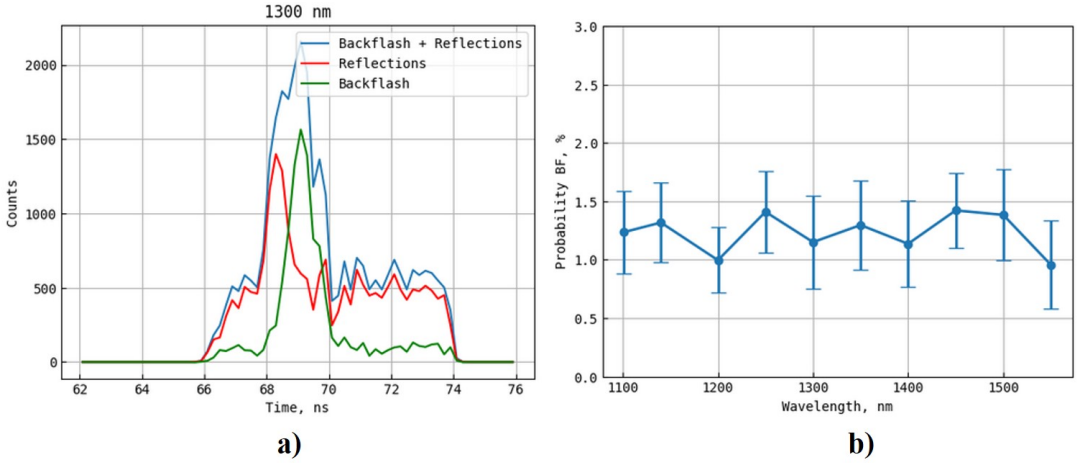

Figure 2: a) The histograms of backflash and reflected counts distribution for stimulating laser at 1300 nm; b) the relation of the backflash probability to the stimulating laser's wavelength.

As can be seen in Fig. 2 b), the backflash probability practically does not vary with the stimulating emission wavelength. The value is approximately 1.25 %. Therefore, it can be assumed that there will be no noticeable changes in information leakage through the side channel when the stimulating laser wavelength varies and the QKD system will be protected taking into account the system protection measures. However, considering a wider spectral range as well as minimizing the spectral step of the measurements, more accurate dependencies can be expected.

References

[1] *C. Kurtsiefer, P. Zarda, S. Mayer, and H. Weinfurter*, The breakdown flash of silicon avalanche photodiodes-back door for eavesdropper attacks? J. Mod. Opt. **48**, 2039–2047 (2001).

[2] *A. Meda, I. P. Degiovanni, A. Tosi, Z. Yuan, G. Brida, and M. Genovese*, Quantifying backflash radiation to prevent zero-error attacks in quantum key distribution. Light Sci. Appl. **6(6)**, e16261-e16261 (2017).

[3] *S. A. Bogdanov, I. S. Sushchev, A. N. Klimov, K. E. Bugai, D. S. Bulavkin, D. A. Dvoretsky*, Influence of QKD apparatus parameters on the backflash attack. Proc. of SPIE Vol **12133**, 90-95 (2022).

[4] *L. Marini, R. Camphausen, B. J. Eggleton, and S. Palomba*, Deterministic filtering of breakdown flashing at telecom wavelengths. Appl. Phys. Lett. **111(21)** (2017).

Miass, Russia February 25 – March 2, 2024
7th International School on Quantum Technologies

Dead time duration influence of SPAD on quantum key distribution parameters

Konstantin Stepanov*, **Alina Borisova**

JSC "InfoTeCS", Moscow, Russia
*E-mail: Konstantin.Stepanov@infotecs.ru

Abstract

The dead time duration influence of single photon avalanche diodes (SPAD) on the main parameters of a quantum key distribution (QKD) system is considered.

Introduction

In quantum key distribution systems, the signals responsible for transmitting encrypted data are transmitted over an open channel. In practice, these signals are pulsed radiation attenuated to a quasi-single-photon state. To registrate signals of such low power, SPADs are used, one of the parameters of which is the afterpulsing probability, that is, false SPAD's clicks after any previous clicks [1]. To reduce the afterpulsing probability, the SPAD is usually blocked for a specified time, called dead time [2]. The detector locking can be done in two ways: at the hardware level by reducing the voltage below the breakdown voltage of the SPAD or at the software level by skipping clicks.

We have conducted a study of the dead time influence of SPADs on the main parameters of the QKD system, such as the magnitude of quantum errors in the sifted key (QBER), the quantum key generation rate, the registration frequency of quantum states, etc. The study was carried out for two lines: 2 m and 50 km long. For each line, a procedure was carried out to obtain a sifted key for the following dead time values: 8, 400, 1000, 4000, 10000 ns.

Experimental results

The experiment was carried out on QKD system based on the phase-time coding [3]. The average results for 100 series of quantum key generation for each cases under consideration are shown in Fig. 1.

Based on the data obtained, the following conclusions can be drawn:

- For short lines, dead time has a more significant effect on the system parameters, especially on the registration efficiency of quantum states with one detector (Fig. 1a) and the length of the sifted key (Fig. 1e), up to complete generation failure.

  The reason for this is that losses on long lines lead to an overall decrease in the registering probability of arriving photons, thereby increasing the average time between clicks, which can be even longer than the set dead time.

- Reducing the number of received bits of the sifted key in a series can lead to the addition of missing bits from the next series. The consequence of this is an abrupt decrease in the secret quantum key generation rate (Fig. 1b) and, accordingly, the key generation time (Fig. 1d).

- It is worth noting that the magnitude of quantum errors in the sifted key (Fig. 1c) for the 2 m line reaches a minimum at a dead time of 8 ns ($QBER_{8ns}$=5.9%), and for other dead time values is ∼10% more ($QBER_{400-4000ns}$ = 6.6%). While for a 50 km line the minimum is achieved at dead time values of 400-1000 ns and is $QBER_{400-1000ns}$ = 6%, and in other cases also increased by about 10%.

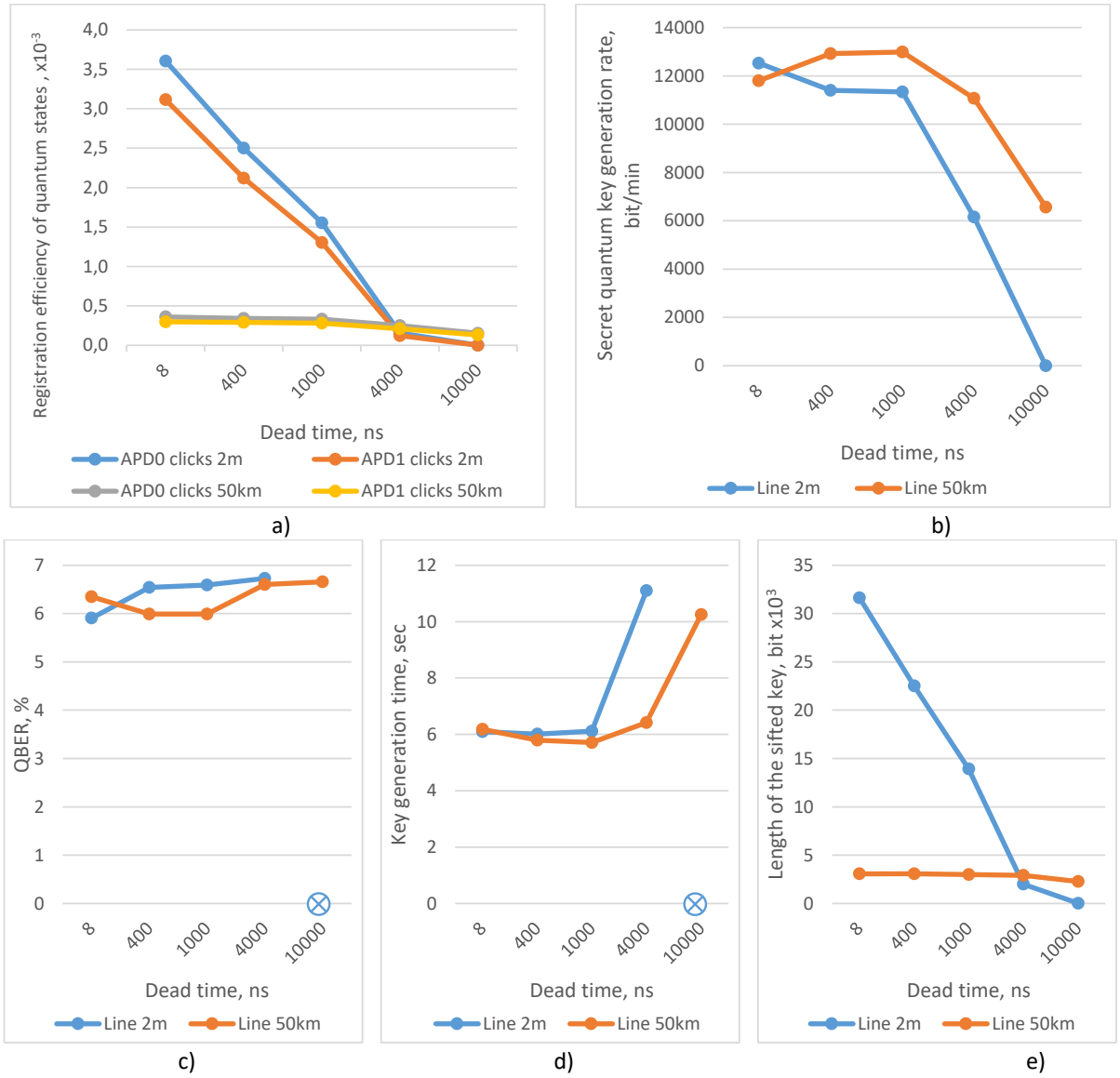

Figure 1: Averaged parameters during the quantum keys generation depending on different SPAD's dead time: (a) Registration efficiency of quantum states with one detector, clicks $x10^{-3}$; (b) Secret quantum key generation rate, bit/min; (c) Quantum error value in the sifted key (QBER), %; (d) Key generation time, sec; (e) Length of the sifted key, bit $x10^3$.

References

[1] *S.B. Bychkov, I.S. Korolev, S.V. Tikhomirov and A.V. Borisova*, Measurements of the quantum efficiency of single-photon photodetectors taking into account the probabilities of dark counting and afterpulsing for problems of metrological support of quantum cryptographic systems. Photon-Espress. **4**, 11 (2022).

[2] *A. V. Losev, V. V. Zavodilenko, A. A. Koziy, A. A. Filyaev, K. I. Khomyakova, Y. V. Kurochkin and A. A. Gorbatsevich*, Dead time duration and active reset influence on the afterpulse probability of InGaAs/InP single-photon avalanche diodes. IEEE J. Quantum Electron. **58.3**, 1 (2022).

[3] *S.N. Molotkov*, Cryptographic robustness of a quantum cryptography system using phase-time coding. JETP letters. **106**, 1 (2008).

Upper bounds for Trojan-horse attack key leakage in QKD systems

Ivan Sushchev[1,2*], **Daniil Bulavkin**[2], **Kirill Bugai**[2,3], **Anna Sidelnikova**[1,2], **Artem Zyzykin**[2], **Dmitriy Dvoretskiy**[2,3]

[1] *Quantum Technology Centre and Faculty of Physics, M. V. Lomonosov Moscow State University, Moscow, Russia*
[2] *SFB Laboratory, Ltd, Moscow, 127273, Russia*
[3] *Bauman Moscow State Technical University, 5 2nd Baumanskaya str., Moscow, 105005, Russia*
*E-mail: sushchev.is16@physics.msu.ru

Abstract

Quantum key distribution (QKD) systems are able to provide data transmission security guaranteed by the fundamental laws of physics. However, there are several attacks exploiting side-channels information leakage such as the Trojan-horse attack. The information leakage is determined by the Holevo bound of an eavesdropper's (Eve's) quantum system, which in turn depends on the fidelity between Eve's states. Here we present different upper bounds for the fidelity, considering BB84 polarization and phase-coding protocols.

Quantum key distribution (QKD) systems ensure data transmission security, underpinned by fundamental physical laws. Real-world implementations, however, exhibit technical imperfections, leading to inadvertent information leakage via side channels, such as the Trojan-horse attacks. Typically, QKD systems employ a phase modulator for state encoding or basis selection. The Trojan-horse attack aims to extract phase modulator information by injecting intense optical radiation into the sender's (Alice) or receiver's (Bob) setup and measuring the reflected signal. To mitigate such attacks, it is imperative to assess the level of reflected signal [1], as it determines the distinguishability of states correlating to different bits, thereby influencing attack success probability.

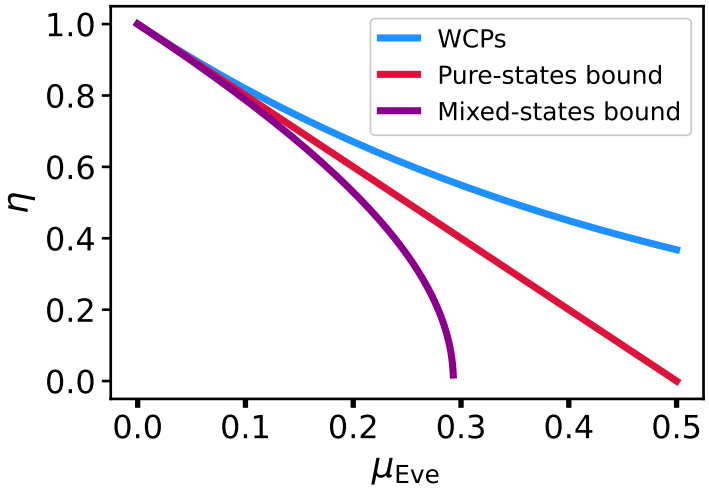

Figure 1: The pure-states (red) and mixed-states (purple) lower bounds and coherent states case (blue) for square root of fidelity between different bit phase-coded states.

The reflected signal level is quantified as the average photon number in pulses returning to Eve (μ_{Eve}). Previously, leakage information assessments were limited to coherent states or other model-based assumptions about Eve's radiation state [2]. This work establishes an upper limit for information accessible to Eve in Trojan-horse attacks on BB84 protocol-based QKD systems using polarization or phase coding. We derive an analytical expression for this limit, determined by the fidelity between Eve's various radiation states (generally mixed), which in turn is expressed through the vacuum component probability in her radiation. We demonstrate that this probability can be constrained using only (μ_{Eve}).

Additionally, we derive an explicit expression for the secret key length, utilizing the Holevo quantity. Surprisingly, the Holevo quantity for generalized attacks can be bounded by a function dependent only on the fidelity between different side channel states and Eve's auxiliary system states.

Fig. 1 illustrates the dependence of the square root of fidelity η between Eve's states on the average photon number in a pulse. The graph shows the derived bounds for pure states and the general case of mixed states. Notably, both bounds asymptotically align with the curve for coherent states as (μ_{Eve}) approaches zero, remaining consistently lower. This highlights that our derived bounds are more apt for security analysis.

Our approach can be extended to any side-channel information leakage in QKD systems and, combined with experimental data, can be employed for comprehensive security analysis of QKD systems. Furthermore, the approach is anticipated to be applicable to the Decoy-state method.

References

[1] *Sushchev, I. S., Guzairova, D. M., Klimov, A. N., Dvoretskiy, D. A., Bogdanov, S. A., Bondar, K. D., and Naumenko, A. P.*, Practical security analysis against the Trojan-horse attacks on fiber-based phase-coding QKD system in the wide spectral range. Emerging Imaging and Sensing Technologies for Security and Defence VI (Vol. 11868, pp. 57-63). SPIE (2021).

[2] *S. E. Vinay, P. Kok*, Extended analysis of the Trojan-horse attack in quantum key distribution. Phys. Rev. A, **97 4**, 042335 (2018).

Miass, Russia February 25 – March 2, 2024
7th International School on Quantum Technologies

Phase-encoded quantum key distrivution system over multimode communication channels

Vladislav Tretiakov[1*], Andrey Klimov[1], Konstantin Kravtsov[1]

[1] *MSU Quantum Technology Centre, 119991 Moscow, Russia*
*E-mail: tretiakov.vv18@physics.msu.ru

Abstract

Quantum key distribution (QKD) is a quantum communication protocol based on principles of quantum mechanics, information carriers in which are quantum objects such as photons. Implementations of QKD utilizing fiber communication lines are widespread. The phase encoding is commonly used in such lines. Meanwhile, in free-space channels, polarization-encoded protocols are usually used due to their relative implementation simplicity and robustness of polarization in free-space propagation. It would seem to be impractical to use a phase encoding across free-space channels due to distortions of temporal and spatial modes of photons during propagation through an atmospheric turbulence. Here, we investigate free-space different types of delay interferometers which perform passive optical correction of multi-mode signal. So far we have observed the interference visibility $\approx$ 97.3 % , which allows us to believe that practical QKD implementation with this interferometer is possible.

Introduction

Quantum key distribution (QKD) [1] is a method of sharing secret keys between two legitimate parties involved in the communication process. QKD over fiber communication channels has achieved great results and QKD experiments over 421 km fiber were demonstrated [2]. However, there is a fundamental limitation in increasing of communication distances over optical fiber due to its internal losses. Free-space QKD experiments are usually based on polarization-states protocols, since they are simple to implement and the polarization is almost not affected by the atmospheric turbulence.

Considering free-space quantum channels it is important to note that the implementation of polarization-state protocols implies quantum measurements to be conducted directly in the free-space channel, consequently the receiving telescope can not be separated from the measurement device by significant distances. However, sometimes it's convenient to collect signal after the receiving telescope into an optical fiber and transmit it to the place where it can be comfortably measured. Either single-mode or multi-mode optical fiber can be used for this purpose. In the first case, it's appeared to be impractical to collect into a single-mode fiber the signal which is distorted by atmospheric turbulence, because a large loss level occurs. In the second case we need to refuse from polarization-states protocols because information about the polarization is lost when signal enters a multi-mode fiber. A convenient alternative to them is a phase encoding [5]. However, commonly used delay interferometers don't allow to obtain required interference visibility with a multi-mode signal.

Here we investigate two types of multi-mode free-space delay interferometers for analyzing phase-encoded photons. Such interferometers can be used in implementation of QKD protocols based on phase encoding. Experiments on visibility measurements with such interferometers have been already conducted [3]. However, we are going to implement phase-encoded QKD system over multimode communication channels using a signal at the wavelength of 1550 nm, instead of 850 nm, which has been done in this work. Such a choice of the wavelength is caused by the requirement for the QKD system to operate sustainably during the daytime, which implies a presence of a background radiation. It leads do decrease of the secret key rate, which is undoubtedly undesirable. Also the important reason of using the specified wavelength is that the number of modes, propagating in a multi-mode fiber is inversly proportional to the square of the signal's wavelength, so at the input of a multi-mode interferometer there is much less modes in a laser beam, which leads to easier adjustment and maintaining of such an interferometer.

Experimental setup

The schematic setup for the visibility measurement experiment is depicted in the Fig. 1. We use a continuous wave laser at the wavelength of 1550 nm with an intensity modulator as a source of laser pulses, which propagate through a short (about 30 cm) free-space channel, enter a multi-mode fiber, and then the investigated interferometer. We register the output signal with a PIN diode and observe it as waveforms on the screen of an oscilloscope. As it was mentioned earlier, we investigate two types of multi-mode interferometers, the exact construction of which is depicted in the Fig 2, and also here you can see the signal at the output of these interferometers as well as visibility values corresponding to these signals.

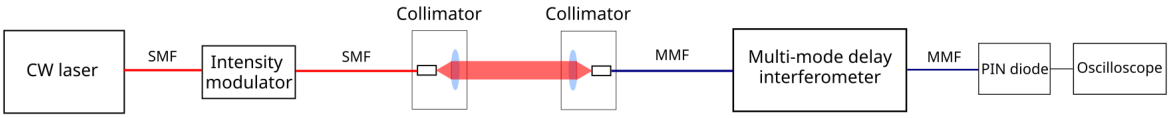

Figure 1: The schematic setup for the visibility measurements experiments.

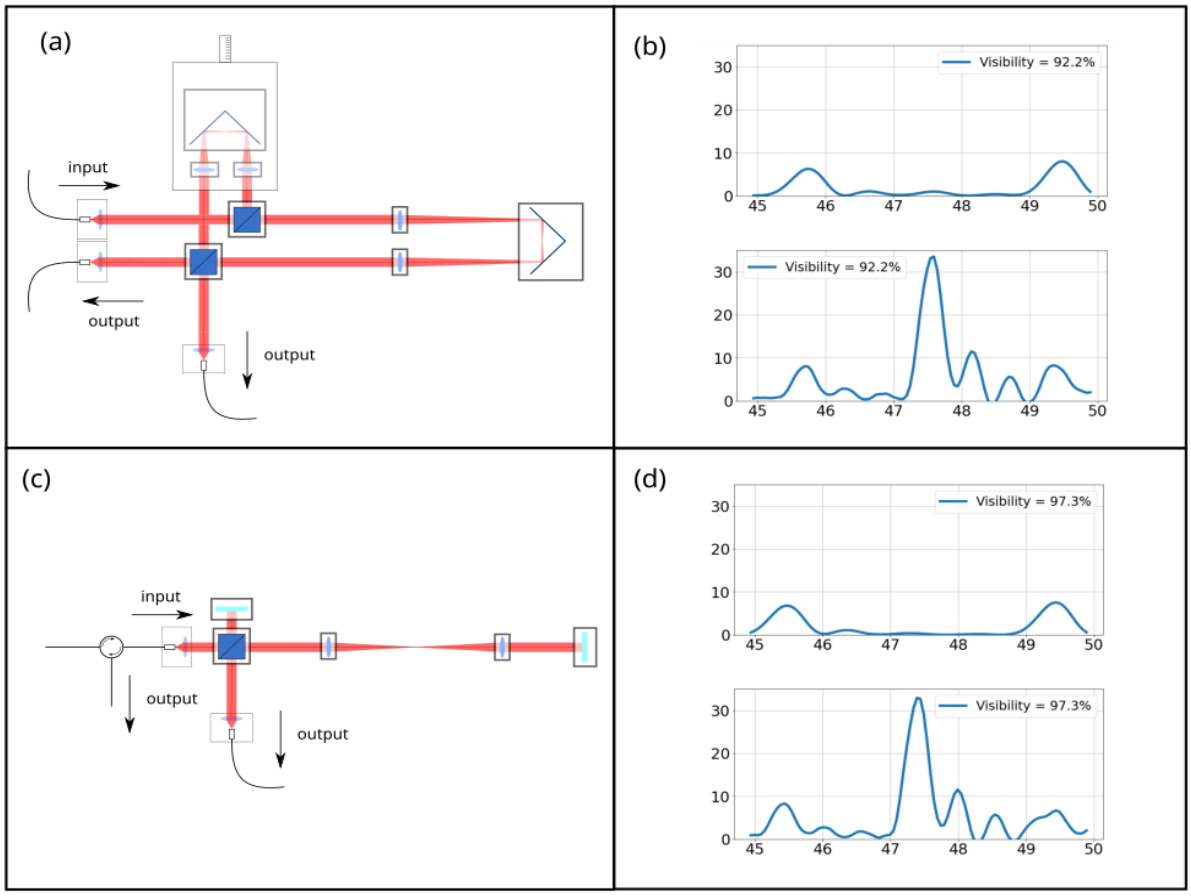

Figure 2: Multi-mode delay interferometers. (a) Interferometer scheme (type 1) proposed in article by J. Jin et al. [4]. (b) The signal at the output of type 1 interferometer (the dependence of a voltage (mV) on time(ns)). (c) Modified Michelson interferometer. (d) The signal at the output of modified Michelson interferometer.

During the following month we are aimed to conduct a complete QKD experiment at the base of the

existing commercial QKD system, produced by InfoTeCS company. The whole experimental setup for this experiment is depicted in the Fig. 3. Based on the obtained results we expect to achieve quantum bit error ratio (QBER) of 2% for Jin's interferometer and QBER of 5% for modified Michelson interferometer. It would be a great pleasure to present the results of our research on the 7th International School on Quantum Technologies.

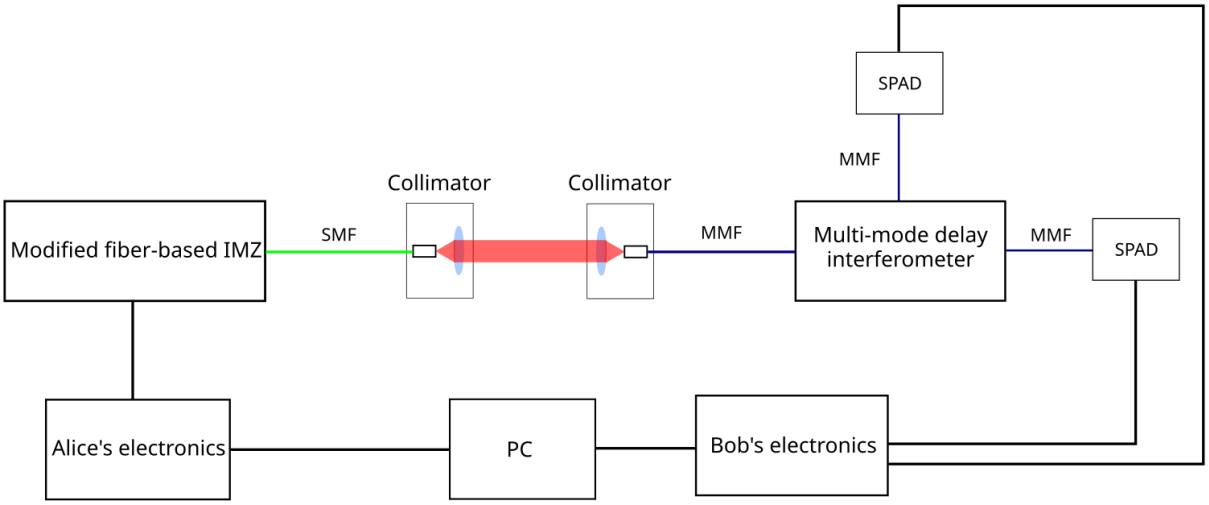

Figure 3: The schematic setup for the complete QKD experiment based on the commercial QKD system, produced by InfoTeCS company.

References

[1] C. H. Bennett and G. Brassard. Quantum cryptography: Public key distribution and coin tossing. In *Proceedings of IEEE International Conference on Computers, Systems, and Signal Processing*, page 175, India, 1984.

[2] Alberto Boaron, Gianluca Boso, Davide Rusca, Cédric Vulliez, Claire Autebert, Misael Caloz, Matthieu Perrenoud, Gaëtan Gras, Félix Bussières, Ming-Jun Li, Daniel Nolan, Anthony Martin, and Hugo Zbinden. Secure quantum key distribution over 421 km of optical fiber. *Phys. Rev. Lett.*, 121:190502, Nov 2018.

[3] Jeongwan Jin, Sascha Agne, Jean-Philippe Bourgoin, Yanbao Zhang, Norbert Lütkenhaus, and Thomas Jennewein. Demonstration of analyzers for multimode photonic time-bin qubits. *Phys. Rev. A*, 97:043847, Apr 2018.

[4] Jeongwan Jin, Jean-Philippe Bourgoin, Ramy Tannous, Sascha Agne, Christopher J. Pugh, Katanya B. Kuntz, Brendon L. Higgins, and Thomas Jennewein. Genuine time-bin-encoded quantum key distribution over a turbulent depolarizing free-space channel. *Optics Express*, 27(26):37214, dec 2019.

[5] Xiao-Tian Song, Dong Wang, Xiao-Ming Lu, Da-Jun Huang, Di Jiang, Li-Xian Li, Xi Fang, Yi-Bo Zhao, and Liang-Jiang Zhou. Phase-coding quantum-key-distribution system based on sagnac–mach-zehnder interferometers. *Phys. Rev. A*, 101:032319, Mar 2020.

Fast frequency recovery using qubits for practical satellite quantum communication

Arkadiy Chernov[1,2,3,4*], **Aleksandr Khmelev**[1,2,3] **and Vladimir Kurochkin**[1,3,4]

[1] *Moscow Institute of Physics and Technology, Dolgoprudny, Russia*
[2] *Russian Quantum Center, Moscow, Russia*
[3] *QSpace Technologies, Moscow, Russia*
[4] *NTI Center for Quantum Communications, NUST MISiS, Moscow, Russia*
*E-mail: chernov.an@phystech.edu

Abstract

The typical problem for satellite quantum key distribution (QKD) is the inability to accurately determine the background noise in the communication channel due to changes in the parameters over time, different weather conditions, and varied reflected light from the satellite. Here, we propose an original method for estimating the signal-to-noise ratio (SNR) that corresponds to a certain interval of a QKD session by using the fast qubit-based frequency recovery procedure. To validate our approach, we conducted an experiment that simulated a QKD session between the Micius satellite and the 600-mm aperture ground station, with extra random channel break.

Satellite-based quantum communication is a promising technology for the secure worldwide sharing of data [1, 2]. However, the restricted communication time and dynamic parameter changes limit the maximum secret key length. To acquire the maximum possible key length, the time frames with a permissible noise level during the QKD session must be determined. We suggest to estimate the SNR of each second of a communication session using time filtering based on frequency recovery approach.

Frequency recovery method

Frequency recovery is an important part of the time-synchronization procedure based on photon qubits. The method [3] consists of three steps: preliminary compensation of the Doppler effect, pulse-repetition frequency (PRF) scanning of the registered signals, compensation of the frequency drift.

Frequency drift compensation is performed in a manner that is independent of the phenomena causing this drift. According to our method, the time moments of registration are transformed as follows:

$$\Delta t_i = \int_{t_0}^{t_i} f(t) \left(\frac{1}{f_0} - \frac{1}{f(t)} \right) dt \tag{1}$$

where Δt_i is the time increment to the registration moment of the i-th pulse, $f(t)$ is the time dependence of the PRF of the signals that are registered on the ground station, $f = 10^8$ Hz is the target PRF, and t_i is the registration moment of the i-th pulse.

The proposed transformation utilizes the time-dependent function of PRF, which is calculated in the way as described in [4]. PRF scanning of the registered signals is carried out in a certain frequency range that corresponds to the maximum frequency shift around the initial frequency. Therefore, to reduce the scanning frequency range, we preliminarily use Doppler effect compensation.

Experimental setup and data

To verify the method, we simulate the satellite-to-ground QKD under cloudy conditions. We model the count rate with a source of signal state with attenuation at an arbitrary time, simulating floating clouds.

Weak coherent pulses with $\mu = 0.8$ photons per pulse and a pulse duration (FWHM) of 1.2 ns are used as information signals. The modulation depth of PRF (Δf) corresponds to the frequency drift that is caused by the Doppler effect. The calculated losses and influence of the Doppler effect correspond to the Micius satellite passage above the zenith of the Zvenigorod ground station, according to our satellite-to-ground QKD model [5]. The duration of the modeled session ($\Delta\tau$), ranges of changes of the elevation angle, the distance ($\Delta\theta, \Delta l$) and other simulated parameters are provided in Table 1.

Table 1: Key parameters of the model experiment.

f_0, MHz	Δf, kHz	FWHM, ns	$\Delta\theta$, degrees	Δl, km	$\Delta\tau$, sec
100	2.2	1.2	20 – 90	500 – 1186	285

The frequency recovery procedure is performed for each second of the acquired data, where we analyze the temporal distribution in the period of the signal and evaluate the mean noise for that second. The temporal distributions with high and low levels of signal are shown in Fig. 1. Here we propose that the signals are within the time frame with boundaries of ±1 ns from the peak of the histogram, and to estimate the level of noise, we average the signals at a considerable distance (±4 ns) from the distribution peak. Thus, the SNR is the ratio of the information signals to the mean noise for a given time interval.

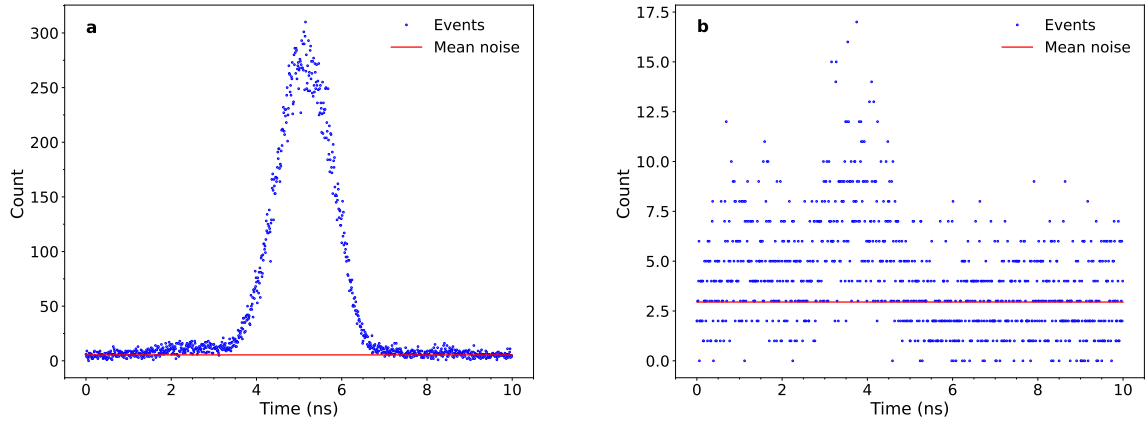

Figure 1: The temporal distribution of the registered photons for a second of the simulated QKD session. **a)** The typical temporal distribution for a second with the high SNR; **b)** The temporal distribution for a second that corresponds to the arbitrary attenuated part of the session.

We have presented a method that simplify the processing of the received quantum signal. This procedure based on frequency recovery procedure allows us to estimate the SNR for each time frame obtained during real satellite quantum communication session. As a result, only informative frames are selected from the entire communication session. Hence, we believe that our method will be effective for further satellite-based QKD experiments.

This work was supported by the Ministry of Education and Science of the Russian Federation in the framework of the Program of Strategic Academic Leadership “Priority 2030” (Strategic Project “Quantum Internet”).

References

[1] *C.-Y. Lu, Y. Cao, C.-Z. Peng , J.-W. Pan*, Micius quantum experiments in space Rev. Mod. Phys. **94**, 035001 (2022).

[2] *S.-K. Liao, W.-Q. Cai, W.-Y. Liu et al.*, Satellite-to-ground quantum key distribution Nature. **549**, 7670 (2017).

[3] *Chernov. A. N., Khmelev, A. V., and Kurochkin, V. L.*, Optimized frequency recovery of the satellite quantum signal, XIX International Conference on Luminescence and Laser Physics, 2023, pp. 216.

[4] *C. Wang, Y. Li, W. Cai, W. Liu, S. Liao, and C. Peng*, Synchronization using quantum photons for satellite-to-ground quantum key distribution. Opt. Express **29**, 29595-29603 (2021).

[5] *Khmelev, Aleksandr V., et al*, Semi-Empirical Satellite-to-Ground Quantum Key Distribution Model for Realistic Receivers. Entropy **25**, 4 (2023).

Investigation of the effect of attenuator made by fusion splicing offset fiber ends on the excitation of cladding modes in a single-mode fiber

S.V. Alferov[1], M.V. Orlova[1], M.M. Shvygina[1*]

[1] *JSC "InfoTeCS", Moscow, Russia*
*E-mail: Maria.Shvygina@infotecs.ru

Abstract

Effect of attenuator made by fusion splicing offset fiber ends on the excitation of cladding modes in a single-mode fiber was investigated. It was demonstrated that redistribution of light from the fiber core to the cladding caused by offset into attenuator can cause a vulnerability in QKD systems under certain conditions.

In theory, the security of quantum key distribution (QKD) systems is guaranteed by the fundamental laws of quantum mechanics [1]. Rigorous proof of protocol security suggests that quantum states are single-photon, but the use of single-photon sources is currently fraught with technical difficulties [2]. Most QKD systems utilize optical pulses attenuated to a quasi-single-photon level, however the mean photon number must not exceed a specified value. Various types of attenuators exist, including: bulkhead attenuators of the "female-female" with a fixed set of attenuation values, attenuators based on a collapsing mirror [3], cascade attenuators [4], attenuators based on the offset of the fiber cores during fusion [5, 6, 7]. The latter type allows to create an attenuation of any value depending on the offset of the cores of two fibers relative to each other. The design of the attenuator is such that upon offset and subsequent fusion, the core of one fiber is fused to part of the cladding of another fiber, as shown in Fig.1, which can stimulate the excitation of cladding modes and create vulnerability of QKD systems under certain conditions. For example, if an eavesdropper finds a way to obtain information about the transmitted states as a result of excitation of cladding modes, or can change the preset attenuator value and increase the mean photon number in order to subsequently perform a photon number splitting attack (PNS attack).

The aim of this work is to study the effect of fused fiber optic attenuators on the excitation of cladding modes in a single-mode fiber and the conditions under which vulnerability of QKD systems containing these attenuators may arise.

Fig.1a schematically shows the ends of the fibers brought together in the optical fusion splicer, as well as images of the fused site with different lateral offsets. For the study, standard single-mode fibers with a core diameter of 9 μm, cladding diameter of 125 μm, and acrylic buffer of 250 μm were used.

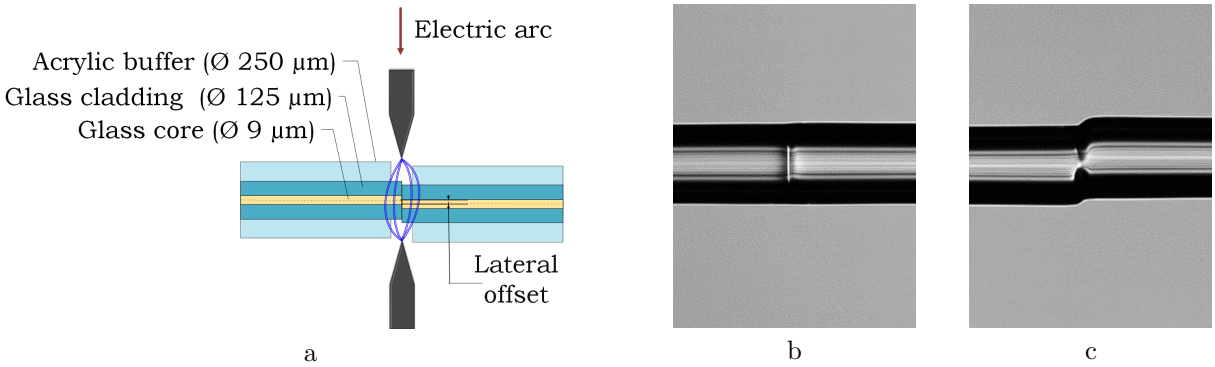

Figure 1: Realization of the attenuator. a – scheme of the attenuator, b – image of fused site without offset, c – image of fused site with lateral offset

Initially, an attenuator with a nominal value of 24 dB was produced by fusion of two pieces of fiber (pigtail) (Fig.2a). Acrylic buffer stripping (removing) stages are shown in Fig.2(b, c, d). At each stripping stage, the mean power was measured by a power meter. A laser with a pulse repetition rate of 10 MHz, a pulse width of 0.5 ns, and a wavelength of 1550 nm was used in the experiments.

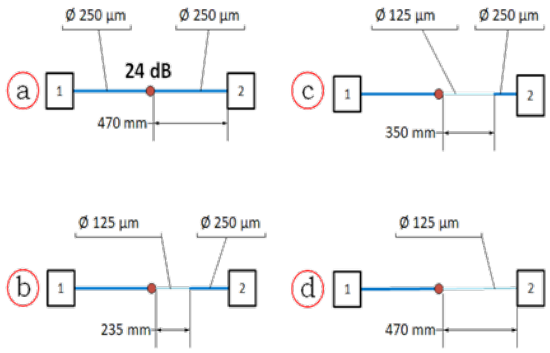

Figure 2: Experiment scheme. 1 – laser, 2 – power meter, red dot is fused site; a – fiber completely in the acrylic buffer (initial attenuation), b – 235 *mm* of the acrylic buffer removed, c – 350 *mm* of the acrylic buffer removed, d – fiber completely without acrylic buffer

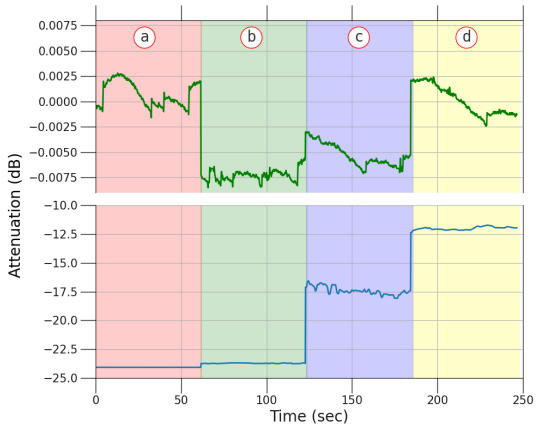

Figure 3: Change in attenuation as the acrylic buffer is removed: a, b, c, d – the stages of the acrylic buffer removal are similar to Fig. 2. Upper graph – attenuator without offset, lower graph – attenuatior with offset, initial attenuation 24 *dB*

It is evident that the attenuation decreases, (Fig.3) as the area of the fiber with the removed acrylic buffer increases, i.e. an increase in the power of transmitted radiation is observed. This occurs due to the improvement of conditions for the propagation of radiation in the glass cladding due to the removal of the acrylic buffer, which has a higher refractive index than the glass cladding. Moreover, if the fiber fused site was made without offset, the power does not increase as the acrylic buffer is removed. In this case fluctuations in the laser power ($Mean = 4.337\ \mu W$, $STD = 4\ nW$) are observed.

It can be concluded that the use of mentioned attenuator leads to the excitation of cladding modes , which increases the transmitted radiation power when the acrylic buffer is removed near the attenuator. However, the acrylic buffer also functions as a cladding mode filter, so in the presence of such coating, the modes in the cladding quickly decay. In actual conditions, access to QKD equipment is restricted, therefore eavesdropper does not have the physical ability to remove any amount of the acrylic buffer near the attenuator. Acrylic buffer removal in a quantum channel is an ineffective strategy for an eavesdropper, since the acrylic buffer inside the equipment absorbs and dissipates the cladding modes. We assume that an attack with powerful radiation from the quantum channel aimed to remove the acrylic buffer fail due to the damage of the optical components. Further work will be aimed at studying other types of attenuators.

References

[1] *I.M. Arbekov*, Elementary quantum cryptography for cryptographers unfamiliar with quantum mechanics. URSS, (2022).

[2] *S. Castelletto*, Silicon carbide single-photon sources: challenges and prospects. Mater. Quantum. Technol. No. 1023001 (2021)

[3] *S.V. Alferov, K.E. Bugai, I.A. Pargachev*, Device for protecting optical systems from powerful laser radiation. Utility model. Utility model. No. 2022123786 (2022).

[4] *V.G. Krishtop*, Stepped optical attenuator. Invention No. 2022105109 (2022).

[5] *S.G.Elizarov, M.M. Lenin, D.A. Ivanov, M.Ya. Yakovlev*, Fused multimode attenuators for harsh operating conditions. Foton-express **6**, 174 (2022).

[6] *O.V. Ivanov, S.A. Nikitov*, Cladding modes of fiber light guides and long-period fiber gratings. FIZMATLIT, 17 (2012).

[7] *W. Zheng, O. Hulten*, Optical fiber attenuator made by fusion splicing offset fiber ends with extended heating after fusing, Invention, No. US5897803A, (1995).

Generation of squeezed Fock states and their application to quantum error correction codes

E. N. Bashmakova[1*], **S. B. Korolev**[1,2], **T. Yu. Golubeva**[1]

[1] *St.Petersburg State University, Universitetskaya nab. 7/9, St.Petersburg, 199034, Russia*
[2] *Laboratory of Quantum Engineering of Light, South Ural State University, pr. Lenina 76, Chelyabinsk, 454080, Russia*
*E-mail: bashmakova.elizaveta@mail.ru

Abstract

In this work we propose a protocol of the generation of squeezed Fock states by the one or more photon subtraction from a two-mode entangled Gaussian state. We have demonstrated the construction an error correction code for quantum calculations based on squeezed Fock states. It is shown that the first squeezed Fock state corrects both photon loss and dephasing errors better than higher-order states.

Non-Gaussian states and non-Gaussian operations are vital elements of the modern quantum computation and quantum information in continuous-variable. First of all, the interest to non-Gaussian states and non-Gaussian operations is motivated by the potential use of such states in quantum error correction (QEC) protocols. Today error correction protocols have been proposed for various quantum non-Gaussian states [1, 2].

Squeezed Schrodinger cat (SSC) states [3] are the one of the example of quantum states applied for QEC codes. Based on them, the QEC has recently been developed [4]. It is capable of correcting two types of errors simultaneously: phase errors and photon loss errors. In contrast to QEC protocols on ordinary Schrodinger cat states [3], the protocol on SSC operates with states with small amplitude. However, the question of efficient generation of these quantum states with high fidelity and probability remains open. It is important to note that in all QEC protocols [1, 2], the non-Gaussian states proposed as the logic basis states cannot be exactly generated in conventional evolution processes. In view of this issue, of special interest would be a non-Gaussian state which, one side, is efficient in an QEC protocol, and which, on the other side, can be obtained as the result of a conventional evolution process.

As a good candidate for the aforementioned state one can consider the squeezed Fock (SF) states [5]. With resects to their performance in QEC protocols, the SF states are quite competitive with the Schrodinger cat states [3] and the SSC states [3], which were recently proposed for such protocols [1, 2]. As for a possibility to generate a SF state in a conventional evolution process, it was shown [5] that it is possible by the subtraction of a photon form the state resulted from the interference of the vacuum and squeezed vacuum at a beam splitter.

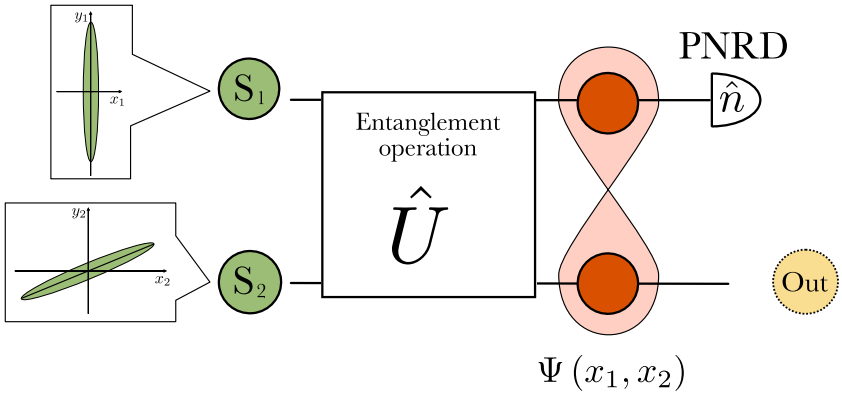

Figure 1: Scheme for generating squeezed Fock states. In the figure: S_1, S_2 are two quantum oscillators in squeezed states, $\Psi(x_1, x_2)$ is entangled state of two input oscillators, PNRD is photon number resolving detector, Out is output state.

In our work, we will consider the scheme for generating SF states in a general form (see Fig. 1), taking into account the procedure for measuring photons in one of the modes of a two-mode entangled Gaussian state [6]. We will show how to choose a resource Gaussian state to obtain an exact (with fidelity equal to 1) SF state in the given configuration. The peculiarity of our work is that the relations we find are valid for the generation of any SF state: with any squeezing degree and any number. We also address the probability of generation of a SF state under the condition of its fixed degree of squeezing.

We have studied in detail the problem of QEC in a quantum channel with particle loss and dephasing errors are present [7]. We have shown that SF states can be used to encode information in such a channel. These states have a certain parity and a structure in the phase space. That is why we considered them as the main resource for QEC. It is important to note that these states used for encoding can be accurately generated experimentally [6].

To compare different quantum codes with each other, we exploit the KL cost function [4]. Using this function, one can give a quantitative measure for evaluating different code words. Applying this measure, we have shown that the first SF state is the best for information protection in a channel with both particle loss and dephasing errors. In this case, the squeezing degree should be large enough. In this work, we have found that for a squeezing parameter $r > 1.7$, the code based on the first SF state performs better than the code based on SF states with any other number.

We compared code words based on the first SF state with code words based on the SSC states. We have shown that the code based on the first SF state is better suited for information protection in a channel where both particle loss and dephasing errors are present. We demonstrated that for the same squeezing degree of the two states, the KL cost function of the SF state is smaller for a channel with two types of errors. In other words, the first SF states better protect the information in a channel where both particle loss and dephasing errors are present.

This work was financially supported by the Russian Science Foundation (Grant No. 24-22-00004 and Grant No. 24-22-00318) and the Theoretical Physics and Mathematics Advancement Foundation "BASIS" (Grants No. 21-1-4-39-1). SBK acknowledges support by the Ministry of Science and Higher Education of the Russian Federation on the basis of the FSAEIHE SUSU (NRU) (Agreement No. 075-15-2022-1116).

References

[1] *T. C. Ralph, A. Gilchrist, G. J. Milburn, W. J. Munro, and S. Glancy*, Quantum computation with optical coherent states. Phys. Rev. A. **68**, 042319 (2003).

[2] *J. Hastrup and U. L. Andersen*, All-optical cat-code quantum error correction. Phys. Rev. Res. **4**, 043065 (2022).

[3] *A. L. Grimsmo, J. Combes, and B. Q. Baragiola*, Quantum Computing with Rotation-Symmetric Bosonic Codes. Rev. X. **10**, 011058 (2020).

[4] *D. S. Schlegel, F. Minganti, and V. Savona*, Quantum error correction using squeezed Schrödinger cat states. Phys. Rev. A. **106**, 022431 (2022).

[5] *S. Olivares and M. G. A. Paris*, Squeezed Fock state by inconclusive photon subtraction. J. Opt. B: Quantum Semiclassical Opt. **7**, S616-S621 (2005).

[6] *S. B. Korolev, E. N. Bashmakova, A. K. Tagantsev and T. Y. Golubeva*, Generation of squeezed Fock states by measurement. arXiv. 2312.14643v2 (2023).

[7] *S. B. Korolev, E. N. Bashmakova, and T. Y. Golubeva*, Error Correction Using Squeezed Fock States. arXiv. 2312.16000 (2023).

Динамика пространственных мод в изогнутых многомодовых интегрально-оптических волноводах

Роберт Гринштейн[1*], **Михаил Сайгин**[1,2], **Сурен Флджян**[1,3], **Станислав Страупе**[1,3], **Сергей Кулик**[1,2]

[1] *Центр Квантовых Технологий МГУ им. М.В. Ломоносова, г. Москва, Россия*
[2] *Лаборатория "Квантовая инженерия света", ЮУрГУ, г. Челябинск, Россия*
[3] *Российский Квантовый Центр, г. Москва, Россия*
*E-mail: alejudorob@yandex.ru

Аннотация

Интегральная фотоника широко применяется в квантовых технологиях. Традиционные квантовые интегрально-оптические схемы, как правило, основаны на одномодовых волноводах. Однако информацию в интегральных оптических устройствах можно кодировать в пространственные моды многомодовых волноводов, что может обладать преимуществом. Анализ собственных мод является затруднительной задачей для изогнутых волноводов по причине сложной динамики собственных мод, которые подвержены смешению, что приводит к использованию затратных по времени вычисления численных методов. В данной работе предложен более эффективный способ расчета их динамики.

Использование линейно-оптических схем является одним из ведущих подходов квантовых вычислений [1]. Однако, использование одномодовых оптических волноводов сопровождается увеличением масштабов линейно-оптической схемы. Выходом из этой ситуации может служить использование многомодовых волноводов. Сложность их расчета заключается в остутствии аналитического решения для некоторых типов, которые используются в интегрально-оптических схемах, например для прямоугольных волноводов, окруженных средой с иным показателем преломления.

Объектом исследования данной работы является произвольный изогнутый многомодовый волновод с прямоугольным поперечным сечением. Сердцевина волновода задается функцией кривизны $\kappa(s)$.

Для нахождения собственных мод и их постоянных распространения для многомодового волновода необходимо решить уравнение Гельмгольца для напряженности электрического поля. Было получено уравнение на собственные моды с учетом криволинейных координат ξ, η, s для участков волновода с постоянной кривизной

$$\Delta_{\eta\xi}^{(\kappa)}\mathbf{U}_m(\boldsymbol{\rho},\kappa) + \left[k_0^2 n^2(\boldsymbol{\rho}) - \frac{\beta_m^2(\kappa)}{(1+\kappa\xi)^2}\right]\mathbf{U}_m(\boldsymbol{\rho},\kappa) = 0 \tag{1}$$

где $\mathbf{U}_m(\boldsymbol{\rho},\kappa)$ – пространственный профиль моды с индексом m, $\beta_m(\kappa)$ – постоянная распространения пространственной моды с индексом m, $n(\boldsymbol{\rho})$ – поперечное распределение показателя преломления около сердцевины, дифференциальный оператор $\Delta_{\eta\xi}^{(\kappa)} = \dfrac{\partial^2}{\partial\eta^2} + \dfrac{\kappa}{1+\kappa\xi}\dfrac{\partial}{\partial\xi} + \dfrac{\partial^2}{\partial\xi^2}$, $k_0 = 2\pi/\lambda$ – волновое число для данной длины волны λ при распространении в вакууме.

Метод расчета динамики собственных мод опирается на уравнение (1) и не требует использования вычислительно затратной разностной численной 3D схемы, обычно использующейся при расчетах интегрально-оптических элементов и поэтому может быть использован при проектировании оптических элементов на основе многомодовых волноводов. Он может ускорять дизайн таких элементов. Для иллюстрации работы предложенного метода исследуется структура с сердцевиной из кремния и окружающей средой из оксида кремния (Рисунок 1).

Изгибы в многомодовом волноводе делают возможным смешение собственных мод. Смешение собственных мод позволяет задавать значимые преобразования между входным и выходным сигналом, которые определяются следующим уравнением

$$\mathbf{C}^{(out)} = T(\{p\},\kappa(s))\mathbf{C}^{(in)} \tag{2}$$

где $\mathbf{C}^{(out)}$ и $\mathbf{C}^{(in)}$– векторы амплитуд входных и выходных сигналов, T – матрица преобразования (смешения) мод, которая зависит от набора параметров $\{p\}$, задающих геометрию и оптические

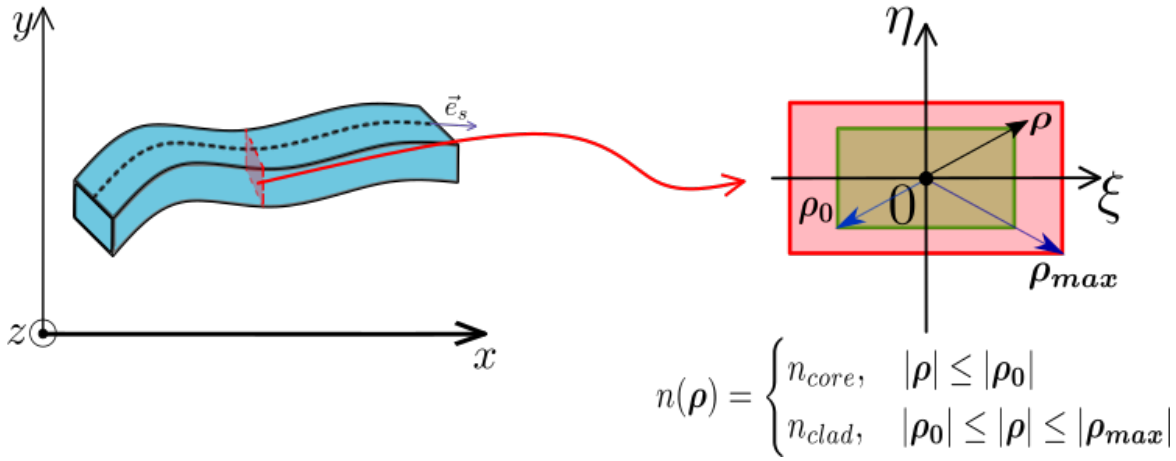

Рис. 1: Рисунок исследуемого многомодового волновода с заданными новыми криволинейными координатами ξ, s, η и плоскостью сечения, в которой обозначены области с различными показателями преломления: n_{core} - показатель преломления сердцевины, n_{clad} - показатель преломления окружающей среды.

свойства в поперечной плоскости, и кривизны $\kappa(s)$, которая зависит от продольной координаты s $(0 \le s \le L)$, где L – длина волновода. Зависимость матрицы T от параметров исследуемой структуры приводит к необходимости рассчитывать смешение мод в волноводах с произвольной ведущей функцией.

Анализ смешения мод в основном производится методом FDTD, который является затратным с точки зрения времени вычислений. В настоящей работе решается дифференциальное уравнение на амплитуды собственных мод с учетом их смешения, благодаря которому можно произвести оценку динамики пространственных мод многомодового изогнутого волновода менее затратным способом.

Список литературы

[1] *Jeremy L. O'Brien.* "Optical Quantum Computing". B: Science 318.5856 (2007)

Wave Mixing of Classical and Non-Classical Signals on a Single Superconducting Artificial Atom

Aleksei Dmitriev[1*], **Andrei Vasenin**[1,3], **Sergei Gunin**[1,3], **Timur Sabirov**[1], **Andrei Elistratov**[2], **Sergei Remizov**[2], **Walter Pogosov**[2] **and Oleg Astafiev**[1,3]

[1] *Laboratory of Artificial Quantum Systems, Moscow Inst. of Physics and Technology, Dolgoprudny, Russia*
[2] *Dukhov Research Institute of Automatics (VNIIA), 127055 Moscow, Russia*
[3] *Skolkovo Institute of Science and Technology, Nobel St. 3, 143026 Moscow, Russia*
*E-mail: aleksei.j.dmitriev@phystech.edu

Abstract

A cascade of two superconducting artificial atoms — a source and a probe atom — strongly coupled to semi-infinite waveguide is a promising tool for the observation of non-trivial phenomena in quantum nonlinear optics. In particular, the probe atom may act as a scatterer for antibunched output from the source, which lead to specific properties of the field generated by the probe atom. We experimentally demonstrate the wave mixing between nonclassical light from the coherently cw-pumped source atom and another coherent wave acting directly on the probe atom. We observe the specific features of wave mixing stationary spectrum and show that they could not be reproduced by any combination of two classical waves mixed on the probe atom. These features are perfectly described by the theory [1] for a strongly coupled cascaded system of two atoms. We further use theory to calculate the entanglement of atoms in stationary state, make predictions about the non-classical spectra of mixing for various ratios of atom's radiative constants. We illustrate the connection between expected correlation function of the source field and wave mixing side peaks corresponding to a certain number of scattered photons.

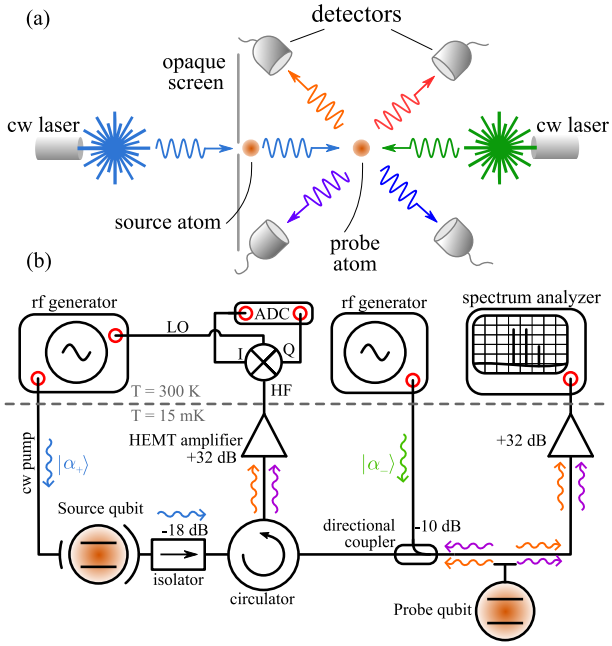

Figure 1: (a) The optical concept of the experiment. The probe atom scatters two coherent fields: the non-classical one cominng from the source excited through small aperture in opaque screen, and the classical wave comes from external rf generator. In turn, the field from the probe is carefully detected and analyzed. (b) The simplified sketch of waveguide-QED microwave setup for the same type of experiment with two superconducting transmon qubits in the dilution refrigerator.

Superconducting electrical circuits in quantum regime could be treated as single artificial atoms with arbitrarily engineered and controllable energies and transition rates. We place a single two-level superconducting atom into the coplanar waveguide, and a strong coupling between the circuit and electromagnetic

modes of the continumm is easily achieved [2]. We study nonlinear mode mixing (intermodulation) on the single atom [3, 4], and find specific features of nonlinear spectra, which could be attributed to the quantum nature of the scatterer. Particularly, we construct and study the cascaded quantum system of two artificial atoms, and observe non-classical features of nonlinear intermodulation within the system.

The observed effects may be useful in future applications of nonlinear optics and photonics. The cascade quantum system consists of two artificial atoms, ans the radiation of the source atom is directed to a probe atom connected to the same waveguide through a cryogenic circulator. When both atoms are in resonance and irradiated with nearly resonant microwaves, it is possible to measure the wave mixing spectrum and show that it has non-classical features due to nonlinear intermodulation in the atom-probe system. The observed behavior is well explained by the theory developed by Gardiner and others [1] for cascade atomic systems, in which unidirectional coupling is accounted for by a Lindblad term:

$$\mathcal{L}_{\text{int}}\hat{\rho} = \alpha\sqrt{\gamma\Gamma}\Big([\hat{\sigma}_1^-\hat{\rho}, \hat{\sigma}_2^-] + [\hat{\sigma}_2^-, \hat{\rho}\hat{\sigma}_1^-]\Big) \tag{1}$$

As a result of experiments, we record the spectrum of coherent emission of the probe. The spectrum reveals the suppression of nonlinear processes where more than one photon from the source is involved, and the domination of processes where only one photon from source is taken.

This work is carried out within the framework of the Roadmap for the development of high-tech direction “Quantum Computing” for 2020-2024. All samples are made on the equipment of the MIPT Center for Collective Usage.

References

[1] *Gardiner, C. W., Parkins, A. S.* Driving atoms with light of arbitrary statistics. Physical Review A, **50(2)**, 1792 (1994).

[2] *Astafiev O. et al.* Resonance fluorescence of a single artificial atom. *Science*, **327**, 840-843 (2010)

[3] *Dmitriev A., Shaikhaidarov R.S., Hônigl-Decrinis, T., Antonov, V.N., Astafiev, O.V.* Probing photon statistics of coherent states by continuous wave mixing on a two-level system. *Physical Review A*, **100(1)**, 013808 (2019)

[4] *Dmitriev, A., Shaikhaidarov R.S., Hônigl-Decrinis, T., Antonov, V.N., Astafiev, O.V.* Quantum wave mixing and visualisation of coherent and superposed photonic states in a waveguide. *Nature Communications* **8**, 1352 (2017).

Dynamics of laser cooling and trapping of alkali atoms in pure-optical two-frequency light trap

Roman Ilenkov[1,2], **Oleg Prudnikov** [1,2], **Alexey Taichenachev** [1,2], **Valery Yudin** [1,2]

[1] *Institute of Laser Physics SB RAS, Novosibirsk, Russia*
[2] *Novosibirsk State University, Novosibirsk, Russia*
*E-mail: ilenkov.roman@gmail.com

Abstract

The laser cooling and trapping of alkali metal atoms in pure-optical two frequency trap is studied in details. The atoms with initially high velocity can be cooled and trapped by bichromatic laser field that opens up possibility to realize principally new type of optical trap.

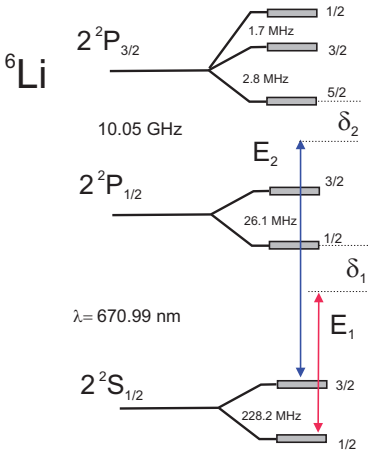

Figure 1: Level structure of ^{6}Li atom.

Laser cooling of atoms is used for a wide range of scientific research: quantum sensors; to studding Bose condensates and Fermi gases; to create optical frequency standards [1, 2]. For solve these problems, the development of efficient methods for deep laser cooling of atoms are required. We consider two-frequency light field configuration where both fields have a dissipative effect on atoms, which make possible to achieve fast and efficient laser cooling and trapping of alckali atoms [3].

The cooling of lithium atoms was considered as an example, but the method can be applied to other atoms, for example the rubidium atom. The complexity of the implementation of laser cooling of ^{6}Li Fig. 1 lies in fact that the width of hyperfine splitting of energy sublevels is comparable to γ - the natural linewidth that results to pumping both hyperfine sublevels of the ground state.

The results represent achieved kinetic energy of cooled atoms for various light field configurations are represented on the Fig. 2. $S_i = |\Omega_i|^2/(4\delta_i^2 + \gamma^2)$, where Ω_i - Rabi frequncy of standing wave, δ_i - detaining between light and resonant transition, and γ - spontaneous relaxation. The possibility of cooling atoms below the Doppler limit in fields double $lin \perp lin$ configuration has been demonstrated.

In addition, a study was carried out of the dynamics of the capture of atoms into a macroscopic superlattice formed by a two-frequency field Fig. 3. The possibility of capturing atoms with a speed of about 60 m/s has been demonstrated, which corresponds to the speed of capturing atoms in a magneto-optical trap.

The study was supported by a grant from the Russian Science Foundation №23-12-00182, https://rscf.ru/project/23-12-00182/.

References

[1] *D. Ludlow, M. M. Boyd, J. Ye, E. Peik, P. O. Schmidt*, Optical atomic clocks. Rev. Mod. Phys. **87**, 637 (2015).

[2] *A. V. Taichenachev, V. I. Yudin, S. N. Bagaev*, Ultraprecise optical frequency standards based on ultracold atoms: state of the art and prospects. Phys. Usp. **59**, 184 (2016).

[3] *O. N. Prudnikov, R. Ya. Ilenkov, A. V. Taichenachev, V. I. Yudin, and S. N. Bagaev*, Deep macroscopic pure-optical potential for laser cooling and trapping of neutral atoms. Phys. Rev. A **108**, 043107 (2023).

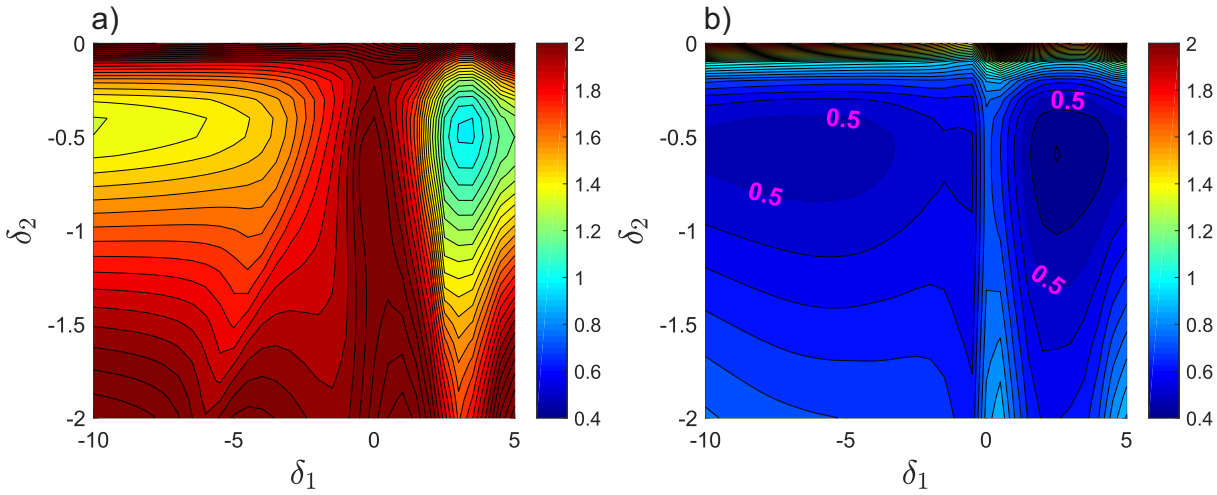

Figure 2: $k_B T_{eff} =< p^2/M >$ value in $\hbar\gamma$ units for different polarisation configuration configuration of bichromatic field (parameters $S_2 = 0.1, S_1 = 0.1$): a) double $\sigma^+ - \sigma^-$; b) double $lin \perp lin$

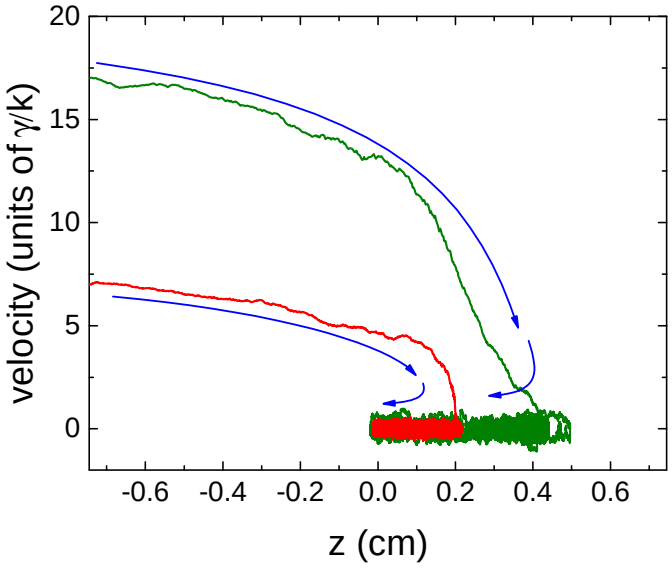

Figure 3: The phase-space trajectory of an atom entering to the macroscopic trap formed by double $lin \perp lin$ configuration of bichromatic field. The red (lower) line corresponds to atom trajectory in the trap with parameters ($\delta_2 = -1.5\gamma$, $\delta_1 = -\gamma$, $S_2 = 0.1$, $S_1 = 0.3$). The initial velocity of atoms on the trap boundary $v = 7\,\gamma/k \simeq 25$ m/s. The green (upper) line corresponds to the atom's trajectory in the trap with $\delta_2 = -10\gamma$, $\delta_1 = -2.5\gamma$, $S_2 = 0.05$, $S_1 = 0.5$. The initial velocity of atoms on the trap boundary $v = 17\,\gamma/k \simeq 60$ m/s. The blue arrows define the direction of the trajectory evolution.

Random and superradiant lasers based on 2D materials with network structure

Peter Zacharenko[1*], Dmitry Tsarev[1], Alexander Alodjants[1]

[1] *Institute of Advansed Data Transfer Systems, ITMO University, 197101 St. Petersburg, Russia*
*E-mail: p.zaxarencko2015@yandex.ru

Abstract

In this work, we offer new quantum sources of light based on 2D network materials that obey the power law degree distribution. These sources are the random (A-class) laser and the superradiant (D-class) one. We introduce a novel network-enforced cooperativity parameter and justify it for the interaction of quantum two-level systems placed in network nodes with laser irradiation. We show that in such media the collective effects may be strongly enhanced in the quantum domain.

Introduction

Random lasers can be called one of the most interesting manifestations of the formation of macroscopic coherence as a result of random scattering of light in a disordered, optically active medium cf. [1]. Since such lasers do not require external resonators, their properties are determined by the amount of radiation scattered in the medium. On the other hand, superradiant sources of light may be considered in the cavity-free (or bad cavity) limit. In [2] it is shown that at the steady-state vanishing number of photonis is enough to establish a macroscopic polarization of the media that causes the quantum field release and leads to superradiant lasing phenomenon. To achieve superradiance in practice a number of conditions is required to fulfill. To describe them we introduce the cooperativity parameter

$$\mathcal{C}_0 \equiv \frac{g^2}{\kappa\gamma_D}, \tag{1}$$

which usually characterizes the interaction of a single two-level system with a quantized field within various problems of quantum optics. In (1), g is the single-photon Rabi frequency; κ, $\gamma_D \simeq 1/\tau_s$ are the cavity decay and spontaneous emission rates, respectively. τ_s is the spontaneous emission time in vacuum. Collective effects occur with rate $\gamma_c \simeq \mathcal{C}_0\gamma_D$. Thus, the superradiant state needs γ_P much larger than γ_D and depolarization rate Γ. More generally, we require $N\gamma_c \gg \gamma_D$ or

$$\mathcal{C}_N = N\mathcal{C}_0 = \frac{g_N^2}{\kappa\gamma_D} \gg 1, \tag{2}$$

where $g_N \equiv g\sqrt{N}$ is the collective Rabi splitting parameter. Thus for superradiance establishment, the large value of the cooperativity parameter is crucial.

In this paper, we show that 2D material with a network structure provide unique opportunity to enhance the cooperativity in the media, e.g. [3]. The network properties are vital in this case, determining both the lasing threshold and the transition between random and supperradiant lasing regimes. We focus here on the specific class of the networks, described by power-law degree distribution (PLDD), cf. [4] (number of nodes $N \gg 1$)

$$p(k) = \frac{(\eta-1)k_{min}^{\eta-1}}{k^{\eta}}, \tag{3}$$

where η is a degree exponent; k is the node degree; k_{min} is the smallest degree, for which Eq. (3) holds; $p(k)$ obey normalization condition $\int\limits_{k_{min}}^{+\infty} p(k)dk = 1$.

Laser models based on 2D network structured materials

Now consider a laser designed in a 2D material with a network structure. In this case, assume that in each node of this network, a two-level system (TLS) is placed, which can be in a ground ($|g\rangle_i$) or excited ($|e\rangle_i$) state. These TLSs interact with quantized e.m. field via the set of waveguides representing edges of the material network graph; this e.m. field we describe by annihilation (creation) $\hat{a}_j(\hat{a_j}^\dagger)$ operators. Another field in this system, R, is a classical weak injection (control) field. Thus, we represent the Hamiltonian of the system in the form

$$\hat{H} = \frac{1}{2}\sum_{i=1}^{N}\omega_{0,i}\hat{\sigma}_i^z + \sum_{i=1}^{M}\omega_{ph}\hat{a_i}^\dagger\hat{a_i} + g\sum_{i=1}^{N}\sum_{j=1}^{\langle k\rangle}(\hat{a_j}^\dagger\hat{\sigma}_i^- + \hat{a_j}\hat{\sigma}_i^+) + \sum_{i=1}^{N} iR(\hat{a_i}^\dagger - \hat{a_i}), \tag{4}$$

where $\hat{\sigma}_i^z = |e\rangle_{ii}\langle e| - |g\rangle_{ii}\langle g|$ is the operator of population inversion for the i-th TLS ($i = 1, ..., N$); $\hat{\sigma}_i^- = |g\rangle_{ii}\langle e|$, $\hat{\sigma}_i^+ = (\hat{\sigma}_i^-)^\dagger$ are the ladder operators; $\omega_{0,i}$ is the resonant frequency of the i-th TLS transition from the ground, $|g\rangle_i$, state to the exited, $|e\rangle_i$, one; g represents the strength of a single TLS interaction with the photonic mode of frequency ω_{ph}. The number of modes is $M = N\langle k\rangle$, where $\langle k\rangle$ is the average node degree of the network structure. Thereafter we use units when Planck constant $\hbar = 1$ for simplicity of notation.

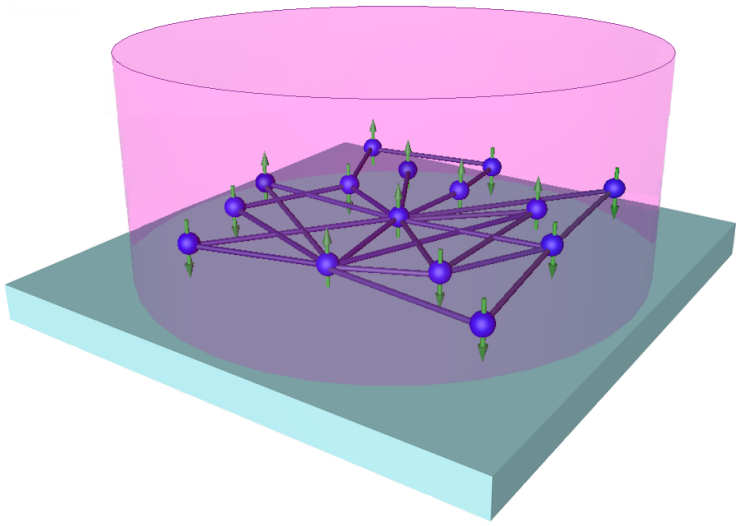

Figure 1: Sketch of the laser, which represents an ensemble of two-level (spin) systems located within complex network nodes. The network edges may represent projections of photon-guiding channels on a plane. The pink cylinder represents a classical pump field.

Current quantum technologies provide a variety of facilities for the realization of 2D materials with network interface plotted in Fig. 1. For example, we can exploit two-level atoms trapped at the surface of a 2D structure by Casimir–Polder effect leading to the attractive van der Waals forces, cf. [5]. Thus, we can vary broadly the material parameters of TLS networks depending on particular realization.

For the model described by Hamiltonian (4) the cooperativity parameter may be introduced as (c.f. (1))

$$C_0 \equiv \frac{g^2}{\kappa\Gamma}. \tag{5}$$

In the framework of the rotating wave approximation we also introduce collective mean-field variables as

$$E = \langle\hat{E}\rangle; \qquad J_- = \frac{1}{N}\sum_{i=1}^{N}\langle\hat{\sigma}_i^\pm\rangle; \qquad D = \frac{1}{N}\sum_{i=1}^{N}\langle\hat{\sigma}_i^z\rangle, \tag{6}$$

where E, J_-, and D are the average photon field, TLS polarization, and population inversion in the network, respectively. Taking into account the Gorini– Kossakowski–Sudarshan–Lindblad approach from (4),

we get mean-field equations (cf.[6]):

$$\dot{E} = -\big(i\Delta_i + \frac{\kappa}{2}\big)E - ig_K N J_- + \sqrt{\langle k\rangle}R, \tag{7a}$$

$$\dot{J}_- = -\frac{\Gamma}{2}J_- + ig_K D E, \tag{7b}$$

$$\dot{D} = (\gamma_P - \gamma_D) - (\gamma_P + \gamma_D)D + 2ig_K(E^* J_- - E J_+), \tag{7c}$$

where dots denote derivatives with respect to time; $g_K = g\sqrt{\langle k\rangle}$ is the modified Rabi frequency; $\Delta_i = \omega_{ph} - \omega_{0,i}$ is the detuning; $\Gamma \equiv \gamma_P + \gamma_D + 2\Gamma_2$ is the total depolarization rate; γ_P is the TLS incoherent pumping rate; Γ_2 is the dephasing rate inherent to inhomogeneous spectrum broadening. Eqs. (7) are the subject of our analysis in this work.

A-class laser

Eqs. (7) may be considered in the framework of various classes of lasers. These classes are relevant to the ratio between key parameters of the system which are κ, Γ, γ_D, and Δ_i. For A-class lasers we suppose that solution of (7) obeys condition $\Gamma \gg \kappa, g, \gamma_D, \gamma_P, |\Delta_i|$. In this case, polarization and population imbalance may be eliminated. For the normalized photon field $\Psi = E/\sqrt{N}$ we obtain

$$\dot{\Psi} = \Big(\frac{2\big(g\sqrt{\langle k\rangle}\big)^2 N D_0}{\Gamma} - \frac{\kappa}{2}\Big)\Psi - \frac{16\big(g\sqrt{\langle k\rangle}\big)^4 N^2 D_0}{\Gamma^2(\gamma_P + \gamma_D)}\Psi^3 + r, \tag{8}$$

where $r = \sqrt{\langle k\rangle}R/\sqrt{N}$. Eq. (8) represents a mean-field equation characterizing the photon field evolution in the A-class (random) laser. Noteworthy, all network peculiarities are encoded in average node degree $\langle k\rangle$. The nonlinear term proportional to Ψ^3 plays an important role in the non-equilibrium phase transition occurring in the random laser. For the steady-state solution of (8), $\dot{\Psi} = 0$, we obtain

$$0 = A\Psi - B\Psi^3 + r, \tag{9}$$

where

$$A = \frac{\kappa}{2}\left(C_\Gamma D_0 - 1\right), \qquad B = \frac{C_\Gamma^2 \kappa^2}{(\gamma_P + \gamma_D)}D_0, \tag{10}$$

where we have introduced cooperativity parameter

$$C_\Gamma = \frac{4g_K^2 N}{\Gamma\kappa} = \frac{4g^2\langle k\rangle N}{\Gamma\kappa}, \tag{11}$$

which may be recognized as a total network-enforced cooperativity (NEC) parameter that includes depolarization/dephasing rate. In (10) $D_0 = (\gamma_P - \gamma_D)/(\gamma_P + \gamma_D)$ is steady-state population imbalance. Equations (9), (10) define the second order phase transition to lasing for real order parameter Ψ, when $r \simeq 0$ and

$$C_\Gamma D_0 \geq 1, \tag{12}$$

where the condition (12) is fulfilled and lasing occurs, $\Psi = \sqrt{A/B}$.

In Fig. 2(a), we plot time-dependent normalized field amplitude $|\Psi|$, collective polarization of TLS $|J_-|$, and their population imbalance D as a solution of (8) ($r' = r/\kappa$). As seen, the steady state tends to establish some non-zero photonic field, which clearly corresponds to the lasing regime.

D-class superradiant laser

Now let us examine superradiant state formation for the 2D system. Although such a state is relevant to quantum features of TLSs (dipoles) polarization, some vital properties may be elucidated in the framework of (7). For superradiance, we require the bad cavity limit that corresponds to fulfillment of inequalities $\kappa \gg \Gamma, g, \gamma_D, |\Delta_i|$. In this case, photon field E may be eliminated together with population imbalance, while for the polarization variable we obtain (see [6])

$$\dot{J}_- = \frac{\gamma_D}{2}\big(\mathcal{C}_\gamma - \gamma\big)J_- - \frac{\gamma_D \mathcal{C}_\gamma^2}{\gamma}J_-^3. \tag{13}$$

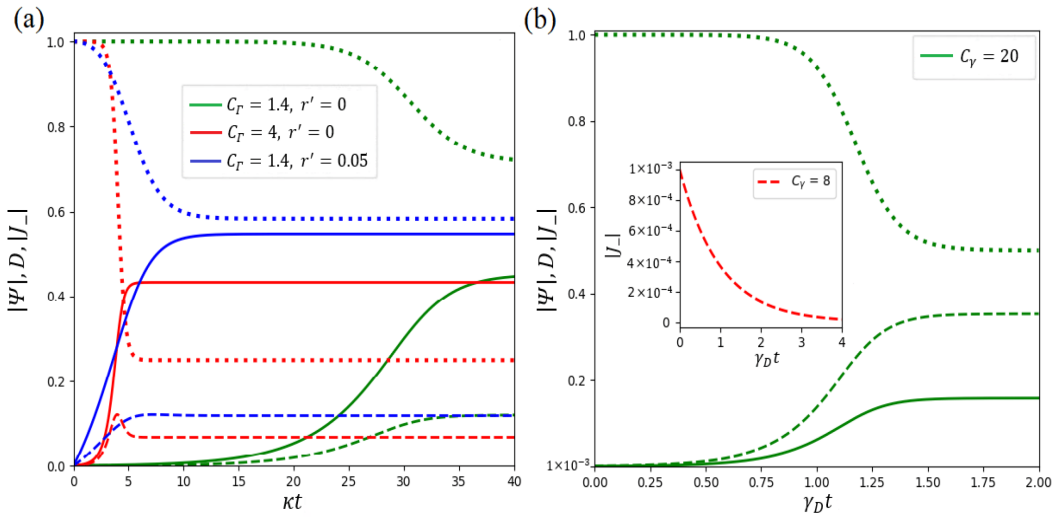

Figure 2: Mean-field dependence of normalized field amplitude $|\Psi|$ (the solid lines), TLS polarization $|J_-|$ (the dashed lines), and population imbalance D (the dotted lines) on dimensionless time t for (a) A-class and (b) D-class (superradiant) lasers, respectively. The control field is normalized as $r' \equiv r/\kappa$, $\Delta_i = 0$, $D_0 = 1$. The other parameters are $\kappa/(\gamma_P + \gamma_D) = 0.5$; $\kappa/\Gamma = 0.1$ for (a) and $\gamma = 10$; $\gamma_D/\kappa = 0.01$; $r' = 0$ for (b). Dependence of $|J_-|$ vs. $\gamma_D t$ below the threshold is shown in the insert to (b).

From Eqs.(13), it is clear that for the superradiant laser, it is more suitable to consider macroscopic polarization J_- as the order parameter instead of the field Ψ. Then consider the steady-state $\dot{J}_- = \dot{D} = 0$. E is complex now, while J_- is real, and we obtain $D = 1/C_\Gamma$. Then the normalized is field amplitude may be obtained as

$$|\Psi| = \sqrt{\frac{\gamma_D}{2\kappa}}\sqrt{\gamma - 1 - (\gamma + 1)(\gamma + 1 + \mathcal{G})\frac{1}{\mathcal{C}_\gamma}}, \tag{14}$$

where we introduce dimensionless pumping ($\gamma \equiv \gamma_P/\gamma_D$) and dephasing ($\mathcal{G} \equiv 2\Gamma_2/\gamma_D$) rates. In (14), we define another NEC parameter

$$\mathcal{C}_\gamma \equiv \frac{4g_K^2 N}{\kappa\gamma_D}, \tag{15}$$

which characterizes cooperative effects for superradiance in a complex network structure.

Similar to the A-class laser, the curves for $|\Psi|$, $|J_-|$, and D are ploted in Fig. 2(b). One possible to find the superradiant lasing effect that implies non-zero $|\Psi|$ and $|J_-|$.

Conclusion

To summarize, in this work we have proposed the laser model based on 2D network structured material and analyzed it in two limiting cases. The first limit corresponds to the A-class (random) laser, and the second limit - to the D-class (superradiant) laser. We have revealed the nonequlibrium phase transitions to lasing in both cases. We have shown that in such media the cooperativity parameter, which provides the random and superradiant lasing effects takes a form of network-enforced cooperativity strongly dependent on the network properties. Thus, the collective effects may be strongly enhanced in network-structured media, which opens new perspectives in random and superradiant laser implementations.

Funding

This work was funded by the Russian Science Foundation, project number 23-22-00058.

References

[1] *D. Wiersma, and S. Diederik*, The physics and applications of random lasers. Nature Phys. **4**, 359-367 (2008).

[2] *D. Meiser, and P. Meystre*, Superstrong coupling regime of cavity quantum electrodynamics. Phys. Rev. A. **74**, 065801 (2006).

[3] *A. Y. Bazhenov, M. M. Nikitina, D. V. Tsarev, and A. P. Alodjants*, Random Laser Based on Materials in the Form of Complex Network Structures. JETP Letters. **117**, 814-820 (2023).

[4] *B. Zhou, X. Meng, and H. E. Stanley*, Power-law distribution of degree–degree distance: A better representation of the scale-free property of complex networks. Proceedings of the national academy of sciences. **117**, 14812 (2020).

[5] *S. P. Yu, J. A. Muniz, C. L. Hung, and H. J. Kimble*, Two-dimensional photonic crystals for engineering atom-light interactions. Proceedings of the National Academy of Sciences. **116**, 12743-12751 (2019).

[6] *A. Alodjants, P. Zacharenko, D. Tsarev, A. Avdyushina, M. Nikitina, A. Khrennikov, and A. Boukhanovsky*, Random Lasers as Social Processes Simulators. Entropy. **25**, 1601 (2023).

Miass, Russia February 25 – March 2, 2024
7th International School on Quantum Technologies

Influence of dispersion on radiation of a synchronously pumped optical parametric oscillator (SPOPO)

Danil Malyshev[1*], **Valentin Averchenko**[1], **Kirill Tikhonov**[1]

[1] *Saint-Petersburg State University, St. Petersburg, Russia*
*E-mail: malyshev.wrk@yandex.ru

Abstract

In this work, the generation of quantum light in the synchroniously pumped optical parametric oscillator (SPOPO) taking into account the influence of dispersion in a nonlinear crystal is investigated. For this purpose, a theoretical model based on a system of coupled quantum harmonic oscillators was cosidered. We estimated the degree of squeezing of the received light in balanced homodyne detection and suggested a way how it can be optimised depending on the strength of dispersion.

Quadrature-squeezed states of light play a huge role in the study of many fundamental and applied questions of quantum optics and information theory. For example, squeezed light can be used to encode information in a quantum communication system with a high degree of its security [1, 2] or to increase the sensitivity of gravitational wave detectors [3].

A common way to obtain quadrature-squeezed light is to use a synchroniously pumped optical parametric oscillator (SPOPO) represented in the Fig. 1. In SPOPO, due to the nonlinear process of paramatric down-conversion, a high-energy pump photon with frequency ω_p splits into two photons of the signal and idler modes with frequencies ω_s and ω_i, respectively. With a specific choice of cavity parameters and dielectric susceptibility of the nonlinear crystall, photons of signal and idler modes would be absolutely indistinguishable, resulting in the generation of a squeezed (or entangled) state of light.

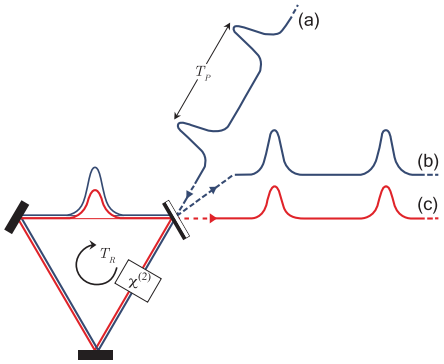

Figure 1: Scheme of the SPOPO consisting of a ring cavity with a nonlinear $\chi^{(2)}$-crystal inside. The pumping is depicted by a blue line (a, b), output light – by a red line (c). The traversal time T_R of cavity is equal to the repetition rate of pump pulses, i.e. $T_R = T_P$.

In this work, we analyzed the quantum properties of SPOPO light using its representation as a set of superemodes [4]. The supermodes are temporal modes obtained from the linearization of the Hamiltonian describing the parametric down-conversion process inside the SPOPO. We demonstrated that the presence of dispersion leads to the coupling of the supermodes, i.e. the time evolution of such a system is governed by the set of differential equation for coupled quantum harmonic oscillators.

The influence of mode coupling in the presence of dispersion is shown in Fig. 2. Here for simplicity the spectral density of a photocurrent are plotted in the case of equal amplification of an every supermode with/and without dispersion. The upper panels correspond to the local oscillator (LO) phase $\varphi = 0$ and the stretched quadrature of light. In contrast, the lower panels correspond the the LO phase $\varphi = \pi$ and the squeezed quadrature of light.

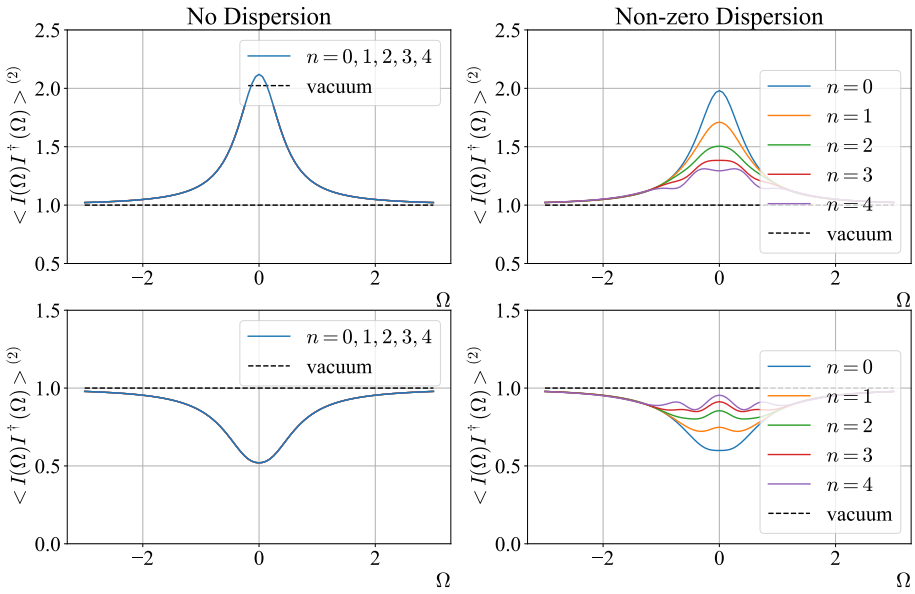

Figure 2: Photocurrent spectral density for the two different local oscillators homodyne phases: $\varphi = 0$ (the upper panel), $\varphi = \pi$ (the lower panel).

Acknowledgements

This study was carried out under financial support of the Russian Science Foundation (grant № 24-22-00318).

References

[1] *Furrer, F. et al.*, Continuous Variable Quantum Key Distribution: Finite-Key Analysis of Composable Security against Coherent Attacks // Phys. Rev. Lett. 2012. Vol. 109, № 10. P. 100502.

[2] *Gehring T. et al.*, Implementation of continuous-variable quantum key distribution with composable and one-sided-device-independent security against coherent attacks // Nat Commun. 2015. Vol. 6, № 1. P. 8795.

[3] *J. Aasi et al.*, Enhanced sensitivity of the LIGO gravitational wave detector by using squeezed states of light // Nature Photon. 2013. Vol. 7, № 8. P. 613–619.

[4] *G. J. De Valcárcel, G. Patera, N. Treps, C. Fabre.*, Multimode squeezing of frequency combs // Phys. Rev. A. 2006. Vol. 74, № 6. P. 061801.

Narrow-band source of polarization-entangled photon pairs in the telecommunications wavelength range for quantum repeater

Mansur Minnegaliev[1*], Konstantin Gerasimov[1], Albert Khayrullin[1], Sergey Moiseev[1]

[1] *Kazan quantum center, KNRTU-KAI, Kazan, Russia*
*E-mail: minnegaliev.mansur@yandex.ru

Abstract

A bright source of polarization-entangled photon pairs with a wavelength of ~ 1.5 μm and a spectral width of ≤ 5 MHz has been developed. The source operates on the basis of spontaneous parametric down conversion in a PPKTP crystal placed in a high-Q optical cavity. The wavelength and spectral width of entangled photon pairs are adapted to be stored in an optical quantum memory based on an atomic frequency comb protocol in a $^{167}Er^{3+}$:Y_2SiO_5 crystal.

Entangled photon pair sources are a fundamental component of various quantum information science applications, including optical quantum computing, quantum repeaters, quantum teleportation, and quantum communications [1, 2]. One of the main methods for generating entangled photon pairs is spontaneous parametric down conversion (SPDC) in nonlinear crystals [3, 4]. Two-photon states generated by SPDC in a free-space typically have a spectral width from 100 GHz to THz [5], which is several orders of magnitude greater than the line-width of typical optical transitions in rare-earth doped crystals used in optical quantum memory (≤ 1 GHz) [6]. However, it has been demonstrated that SPDC sources in a cavity can generate bright, narrow-band biphotons, which allows them to be used to store photonic qubits in quantum memories and quantum repeaters [7]. In this work we present the implementation of a narrow-band source of polarization entangled photon pairs using a type - II SPDC crystal placed in a hiqh-Q optical cavity. The generated states are adapted for storage in optical quantum memory based on the atomic frequency comb protocol in the $^{167}Er^{3+}$:Y_2SiO_5 crystal, which was also experimentally implemented in this work.

References

[1] *D. Bouwmeester, A. Ekert, A. Zeilinger.*, The Physics of Quantum Information. Heidelberg: Springer Berlin, 2000. — 315 p

[2] *Wei S. et.al.*, Towards Real-World Quantum Networks: A Review. Laser Photon. Rev. **16**, 2100219 (2022)

[3] *C. Hong, Z. Ou and L. Mandel* , Measurement of subpicosecond time intervals between two photons by interference. Phys. Rev. Lett. **59**, 18, 2044 (1987).

[4] *A. Anwar, C. Perumangatt, F. Steinlechner, T. Jennewein, and A. Ling*, Entangled photon-pair sources based on three-wave mixing in bulk crystals. Rev. Sci. Instrum. **92**, 1 (2021).

[5] *A. Migdall, S. V. Polyakov, J. Fan, J. C. Bienfang*, Single-Photon Generation and Detection: Physics and Applications. Experimental Methods in the Physical Sciences.Academic Press, 2013. — 616 p.

[6] *C. Simon, M. Afzelius, J. Appel et al.*, Quantum memories.Eur. Phys. J. D 58, 1–22 (2010).

[7] *O. Slattery, L. Ma, K. Zong, and X. Tang*,Background and Review of Cavity-Enhanced Spontaneous Parametric Down-Conversion. J. Res. Natl. Inst. Stand. Technol. **124**, 124019 (2019)..

The microwave transmission and the collective excitation of superconducting qubits coupled to a multilevel system

Dmitrii Pashin[1*], **Marina Bastrakova**[1,2],

[1] *Lobachevsky State University of Nizhni Novgorod, Nizhny Novgorod, Russia*
[2] *Russian Quantum Center, Moscow, Russia*
*E-mail: pashindmi@gmail.com

Abstract

The work studies microwave transmission through a one-dimensional waveguide with an array of qubits coupled to a multilevel system. Examples of such systems include various Josephson amplifiers and couplers. Dependences were obtained for transmission and reflection coefficients, and a probability amplitude of a qubits excitation. For the case when the qubit is connected to a Josephson bifurcation amplifier, it is shown that the shift of the effective frequency of the qubit increases with the number of quanta of the measuring amplifier, and the resonance curves have a non-trivial form. The effects of collective excitations of the qubits array are discussed.

At present, experiments on nondemolition measurement of arrays of non-interacting qubits placed in a one-dimensional open waveguide [1] have been implemented, as well as metamaterials have been created that allow controlling the band gap of such a waveguide by tuning the qubits frequencies [2]. Often in experiments, qubits interact not only with the waveguide line, but also with other multilevel systems, which inevitably leads to complex nonlinear effects. To describe and predict such effects, it is important to be able to quantitatively calculate the influence of the state of multilevel systems on experimentally measurable characteristics. As a model, we consider a one-dimensional waveguide containing an array of qubits that interacts with Josephson bifurcation amplifiers.

To describe and study microwave transport processes, we find it convenient to use the projection operator formalism and the method of the effective non-Hermitian Hamiltonian. In the one-photon approximation there is the probability of photon absorption by a qubit in addition to the probabilities of transmission and reflection. Note that one of the first applications of this method for investigating microwave transmission through a one-dimensional qubit chain was presented in the paper [3].

When the measuring amplifier is in the ground state it introduces a minimal perturbation into the behavior of the photon. Fig.1a-c shows that the effect on microwave transmission increases with an increase in the average occupation number of the measuring oscillator initial state. Such a non-trivial change in the resonance curves is due to the the Fock basis is not eigen for the measuring amplifier.

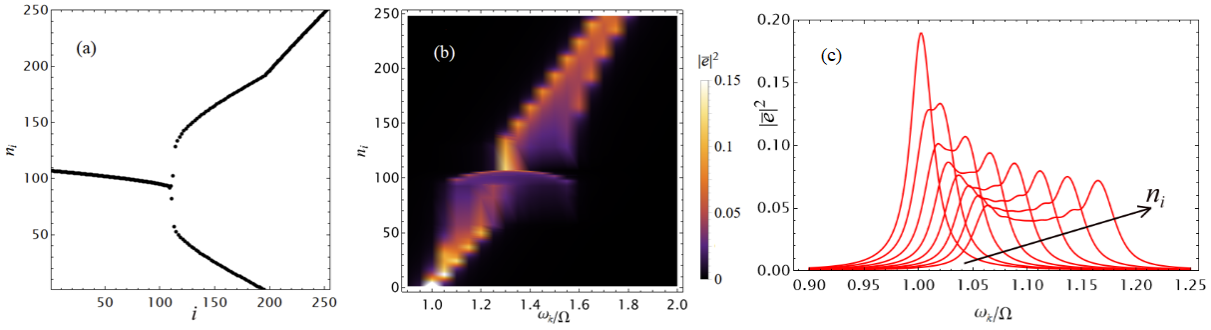

Figure 1: (a) Dependence of the average occupation number on the measuring amplifier level number. The separation of the spectrum into two branchs occurs near the separatrix energy [4]. (b) Dependence of the qubit excitation probability on the average occupation number of the measuring amplifier initial state and the incident photon frequency. (c) The cross-sections of the Fig.1b for different levels of the measuring amplifier.

When calculating an array of qubits coupled to multilevel systems, the non-Hermitian Hamiltonian method quickly increases in complexity. We propose to use a generalized method to solve the scattering

problem, taking into account the interference of the incident and reflected photons when propagating from one qubit to another. As a result of numerical modeling, for an array of qubits, the dependences of the probability amplitude of excitation of an individual qubit were found. Fig.2 shows the calculation results for the reflection coefficient for two qubits for various system parameters.

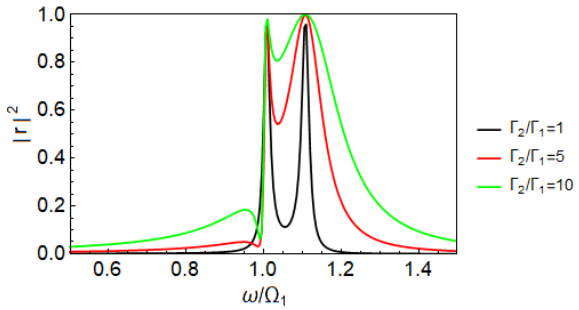

Figure 2: The reflection coefficient of a single-photon field with a frequency ω from two qubits with a frequency $\Omega_2 = 1.1\Omega_1$. The results are presented for different spontaneous emission rates Γ_2/Γ_1, with $\Gamma_1 = 0.01\Omega_1$.

The results obtained can be useful for effectively shifting the frequency of two-level systems, as well as selective qubits excitation with close frequencies. In addition, the demonstrated method allows us to calculate the microwave transmission in arrays of qubits placed in a waveguide line and numerically study the effects of collective excitations.

The work was supported by the Ministry of Science and Higher Education of the Russian Federation (State Assignment FSWR-2023-0035).

References

[1] *V. Schmitt, X. Zhou, K. Juliusson, B. Royer, A. Blais, P. Bertet, D. Vion, and D. Esteve*, Multiplexed readout of transmon qubits with Josephson bifurcation amplifiers. Phys. Rev. A **90**, 062333 (2014).

[2] *J.D. Brehm, A.N. Poddubny, A. Stehli, T. Wolz, H. Rotzinger, and A.V. Ustinov*, Waveguide bandgap engineering with an array of superconducting qubits. npj Quantum Mater. **6**, 10 (2021).

[3] *Ya.S. Greenberg, and A.A. Shtygashev*, Non-Hermitian Hamiltonian approach to the microwave transmission through a one-dimensional qubit chain. Phys. Rev. A **92**, 063835 (2015).

[4] *D.S. Pashin, M.V. Bastrakova, A.M. Satanin, N.V. Klenov,* Bifurcation Oscillator as an Advanced Sensor for Quantum State Control. Sensors **22**, 6580 (2022).

Study of collective effects in spin-polarized atomic ensemble beyond mean-field theory approximation

Dmitrii Potapov[1,2*], **Kirill Tikhonov**[2]

[1] *ITMO University, Saint-Petersburg, Russia*
[2] *Saint-Petersburg State University, Saint-Petersburg, Russia*
*E-mail: 13dmitry.pot@gmail.com

Abstract

We considered a time evolution of a spin-polarized atomic ensemble continuously optically pumped and probed by the external light fields. Due to the collective scattering of photons at large optical depth, the quantum state of atoms does not correspond to an uncorrelated tensor-product state, as is usually assumed. Instead of this, one can find the ensemble in the multipartite entangled states. Here we employed the Dicke model and cumulant analysis to study the dynamics of such states beyond mean-field theory approximation. We obtained a time hierarchy of high-order cumulants, representing pure multipartite correlations between atoms of the ensemble.

The Dicke model is a fundamental model of quantum optics, which describes the interaction between light and matter. It was inspired by the pioneering work of R. H. Dicke on the superradiant emission of light in free space [1] and named after him. According to the Dicke model, the dense arrangement of atoms continuously pumped by the external light fields leads to the creation of a radiating collective dipole moment, resulting in the generation of superradiation pulses. In this case, the cooperative transitions can be conveniently described with states which are symmetric with respect to particle permutations. These states are related to each other by the action of collective raising and lowering ladder operators and form the so-called many-body "Dicke ladder". However, the study of real atomic systems implies that one should account not only collective effects, but individual processes as well, e.g. the spontaneous decay of atoms. These incoherent processes give rise to additional ladders (subladders) of subradiant states. The entire set of states, including superradiant and all subradiant ones, is known as the Dicke basis.

The Dicke basis is a natural choice for description of collective effects in light-matter quantum systems. In this work we examined a superradiant laser operating in an extreme bad cavity regime [2]. The model represents an ensemble of N two-level atoms continuously pumped and probed by the external light fields. The evolution of the system is governed by various collective and individual atomic processes. Since it is extremely challenging to obtain a precise numerical solution of a master equation for such a system in case of a large atomic ensemble [3, 4], we considered a small amount of atoms. Our goal was to seek for general tendencies and laws of distribution of atomic populations between the Dicke basis states at various initial conditions (see Fig. 1(a)) and predict how it changes with increasing number of atoms N. Moreover, we performed a cumulant analysis to study the dynamics of pure correlations between atoms of the ensemble and obtain the optimal conditions for maximum value of atom-atom correlations (see Fig. 1(b)).

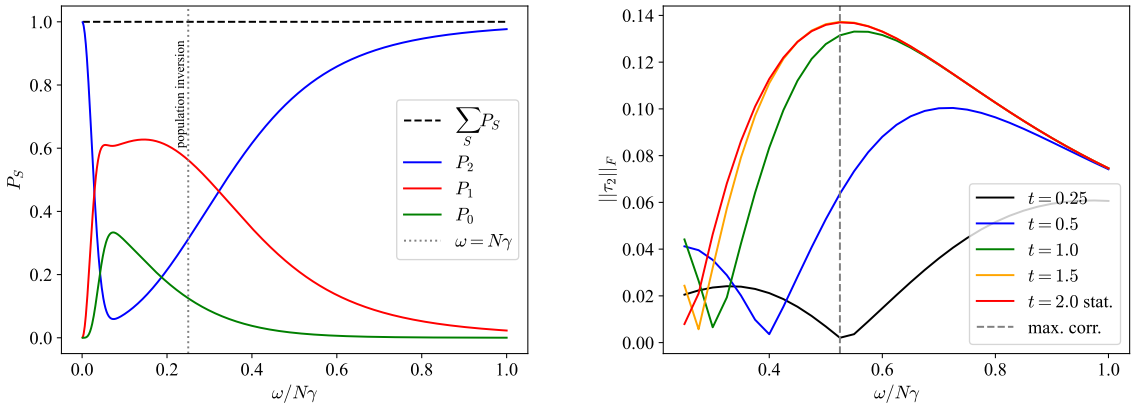

Figure 1: (a) Sum of populations for different Dicke subladders with moment $S = 2$ (blue), $S = 1$ (red), $S = 0$ (green) and number of atoms $N = 4$. (b) The time evolution of atom-atom correlations versus dimensionless single-atom pump rate.

Acknowledgements : This study was carried out under financial support of the Russian Science Foundation (grant № 21-72-00049).

References

[1] *R.H. Dicke*, Coherence in Spontaneous Radiation Processes. Phys. Rev. **93**(1), 99–110 (1954).

[2] *A. Roth, K. Hammerer, and K.S. Tikhonov*, Light–matter quantum interface with continuous pump and probe. J. Phys. B: At. Mol. Opt. Phys. **56**(5), 055502 (2023).

[3] *N. Shammah, S. Ahmed, N. Lambert, S. De Liberato, and F. Nori*, Open quantum systems with local and collective incoherent processes: Efficient numerical simulations using permutational invariance. Phys. Rev. A **98**(6), 063815 (2018).

[4] *G. Ferioli, A. Glicenstein, F. Robicheaux, R.T. Sutherland, A. Browaeys, and I. Ferrier-Barbut*, Laser-Driven Superradiant Ensembles of Two-Level Atoms near Dicke Regime. Phys. Rev. Lett. **127**(24), 243602 (2021).

Miass, Russia February 25 – March 2, 2024
7th International School on Quantum Technologies

Magnetometry based on H3 color centers in diamond

Vladimir Chashchin[1,2*], **Lyga Olga**[1], **Evgeny Lipatov**[1,2]

[1] *Tomsk State University, 634050, Tomsk, Russia*
[2] *Institute of High Current Electronics SB RAS, 634055, Tomsk, Russia*
*E-mail: lloodia@yandex.ru

Abstract

The results of the dependence of the photoluminescence intensity of the color centers in diamond under the influence of an external magnetic field are presented, photoluminescence spectra for different temperatures are presented. The dependences of the change in photoluminescence intensity on temperature and the presence of an external magnetic field for two color centers (NV^- and N_2V^0) for samples with different concentrations of the studied centers have been established.

Currently, there is an active development of quantum technologies, including the development of new types of sensors, detectors, etc. A promising material for these devices is a diamond containing various color centers in it. The color centers in diamond are nitrogen atoms embedded in the lattice, associated with vacancies present in the lattice.

For example, a well-studied NV^- center in a diamond is one substitutive nitrogen atom embedded in the lattice during sample synthesis or as a result of ion implantation, associated with one vacancy resulting from radiation treatment of a diamond sample (Fig. 1). Laser generation in diamond was previously obtained on the basis of the NV^- center [1, 2]. In addition to the described color center, other color centers are present in such diamond samples, for example, the N_2V^0 center (also known in the literature as the H3 center).

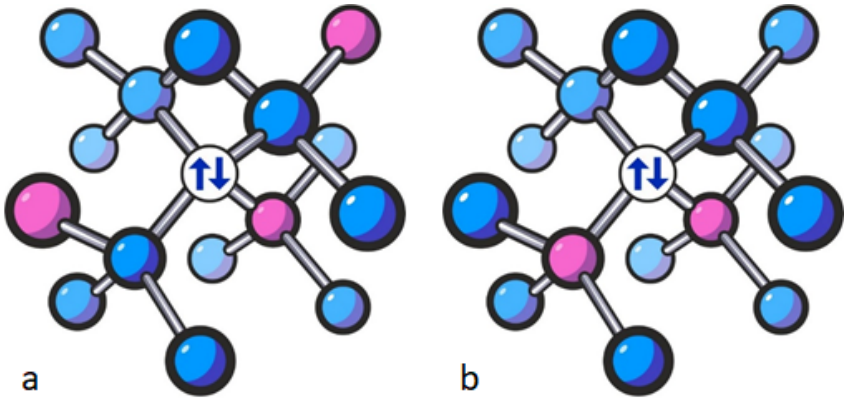

Figure 1: Structures of a) NV^- and b) N_2V^0 centers.
Carbon atoms are indicated in blue, nitrogen atoms in the replacement position are indicated in red, two arrows in a white circle indicate two electrons localized in the vacancy

Based on the luminescence of the color centers, it is possible to create various detectors and sensors, including a magnetometer. The basic principle of operation of a diamond quantum magnetometer is the use of the Zeeman effect. Thus, the intensity of photoluminescence of the color centers decreases when exposed to an external magnetic field. However, during the experiment, an effect not previously described in the literature was discovered: when exposed to an external magnetic field on samples containing both NV^- and N_2V^0 centers, the photoluminescence intensity of the first center (NV^-) decreased due to triplet-singlet transitions, but at the same time, the photoluminescence intensity of the second center (N_2V^0) increased [3, 4] (Fig. 2).

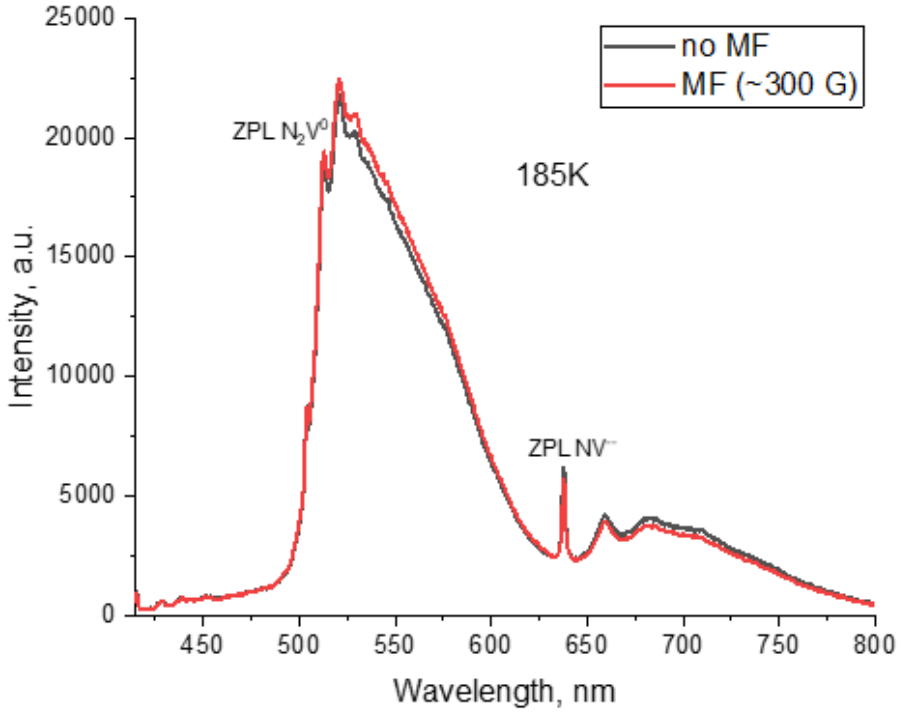

Figure 2: The photoluminescence spectrum of a sample with NV^- and N_2V^0 centers under the influence of an external magnetic field (300 G)

Acknowledgement

The research was carried out with the support of the Tomsk State University Development Program (Priority 2030), project No. 2.4.4.23 of the IG "N_2V^0 diamond coloring centers for quantum magnetometry".

References

[1] *Lipatov, E.I., Genin, D.E., Shulepov, M.A., Tel'minov, E.N., Savvin, A.D., Eliseev, A.P., Vins, V.G.*, Superluminescence in the phonon wing of the photoluminescence spectrum of NV centres in diamond optically pumped at $\lambda = 532$ nm. Quantum Electronics. **52(5)**, 465 (2022).

[2] *Lipatov, E.I., Genin, D.E., Shulepov, M.A., Tel'minov, E.N., Burachenko, A.G., Ripenko, V.S., Vins, V.G.*, Superluminescence at Nitrogen-Vacancy Centers in the Synthetic Diamond Pumped by Laser Radiation in the Range of 532-575 nm. Russian Physics Journal **65(11)**, 1881-1885 (2023).

[3] *Zayavka na patent na izobretenie* № 2023136053 Rossijskaya Federaciya, MPK G01V 3/14, G01R 33/02. Kvantovyj magnitometr na osnove N_2V^0 centrov v almaze: № 2023136053 : zayavl. 29.12.2023 / Burachenko A.G., Vins V.G., Genin D.E., Eliseev A.P., Lipatov E.I., Lyga O.I., Ripenko V.S., Chashchin V.V., Shulepov M.A

[4] *Lyga, O.I., Shulepov M.A.*, Opredelenie temperaturnyh zavisimostej spektrov fotolyuminescencii NV-centrov almazov pod dejstviem prilozhennogo magnitnogo polya. Materialy XIX Mezhdunarodnoj molodezhnoj konferencii po lyuminescencii i lazernoj fizike, Irkutsk 131 (2023).

Microwave Spectroscopy of Cold Rb Atoms Localized Near an Atom Chip

Darya Bykova[1,2*], **Petr Skakunenko**[1], **Anton Afanasiev**[1], **Victor Balykin**[1]

[1] *Institute of Spectroscopy, Russian Academy of Sciences, Troitsk, Moscow, Russia*
[2] *National Research University Higher School of Economics, Moscow, Russia*
*E-mail: dvbykova@edu.hse.ru

Abstract

Atom chip is a universal platform for quantum sensors. The use of localized atoms near the surface of an atom chip makes it possible to create compact systems that can be used on board of portable platforms. A new version of the atom chip with an additional wide U-shaped microwire allows to trap 3.5 times more cold Rb-87 atoms in a magneto-optical trap. On the way to realizing an atomic clock on an atom chip, the Rabi spectrum and Ramsey spectrum of freely falling cold Rb-87 atoms were obtained. A microwave spectrum of Rb-87 atoms localized in a magnetic trap near the atomic chip represents spectral line with a width of 9.6 MHz limited by the temperature of the atomic ensemble.

Atom chip technology allows neutral atoms to be effectively cooled by trapping them in a magneto-optical trap (MOT) and then in a magnetic trap near the surface of the chip. In this case, the magnetic fields of the traps are created by the flow of current through the microwires of the atomic chip in the presence of an external uniform magnetic field. The advantages of using such a device over using a classical MOT are 1) achieving a large magnetic field gradient when a relatively small current flows through microwires, 2) relatively easy and fast cooling of an atomic ensemble down to a Bose-Einstein condensate (BEC), 3) energy efficiency and compactness [1].

These advantages make atom chip technology attractive in the field of quantum sensing [2] (for the construction of gravimeters [3], accelerometers, gyroscopes), creating compact frequency standards [4] and BEC research in microgravity conditions [5].

This paper is dedicated to the development and use of atom chip technology at the Institute of Spectroscopy of the Russian Academy of Sciences (ISAN), where the first atom chip in Russia was created [6]. The goal of the research is to implement a compact atomic clock and then a gravimeter on an atom chip. Atomic clocks on an atom chip can be, on the one hand, more compact than atomic fountains, and, on the other hand, more accurate than miniature atomic clocks using thermal ensembles of atoms [7]. Thus, atomic clocks on an atom chip can occupy an intermediate niche of mobile and precise frequency standards.

A new version of the atom chip, developed at ISAN, makes it possible to trap more rubidium-87 atoms in the MOT by optimizing the magnetic field distribution near the chip surface. The main feature of the new version of the atom chip is an additional wide U-shaped microwire, the central part of which measures 2.9 mm x 6.2 mm. The flow of current through a wide wire makes it possible to create a magnetic field closer to quadrupole [8] than when using thin wires. This led to an increase in the effective volume of the MOT on the chip and, consequently, in the number of trapped atoms. Using the new version of the atom chip, it was possible to obtain a gain in the number of localized atoms by 3.5 times. A special feature of our approach is the production of an atom chip using single-layer technology, which allows us to maintain the relative compactness of the device and the consumption of small electrical currents.

On the way to realizing an atomic clock on an atom chip, we are using various microwave spectroscopy approaches. Thus, the Rabi oscillations of the clock transition, the Rabi spectrum (linewidth 5 kHz, see Fig. 1) and the Ramsey spectrum (linewidth 1 kHz, see Fig. 2) were obtained by interaction of freely falling rubidium-87 atoms with microwave radiation at a frequency of 6.8 GHz.

A microwave spectrum of rubidium-87 atoms localized in a magnetic trap near the atomic chip was also obtained (see Fig. 3). To obtain this spectrum, atoms localized in a magnetic trap were irradiated with microwave radiation, and when the radiation frequency coincided with the resonance frequency, the number of atoms in the magnetic trap decreased due to the transition of atoms to a magnetic sublevel that was not localized in the trap. Thus, the spectrum represents a dip in the dependence of the number of localized atoms on the frequency of the microwave field. The resulting spectral line width was 9.6 MHz and was determined by the temperature of localized atoms. Further cooling of the ensemble of atoms will lead to a narrower resonance line.

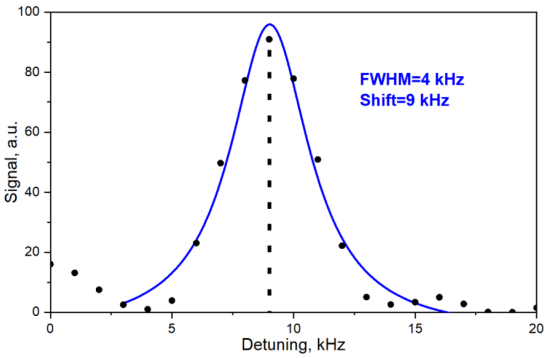

Figure 1: The number of atoms in the excited state depending on the detuning of microwave radiation upon interaction with the π-pulse.

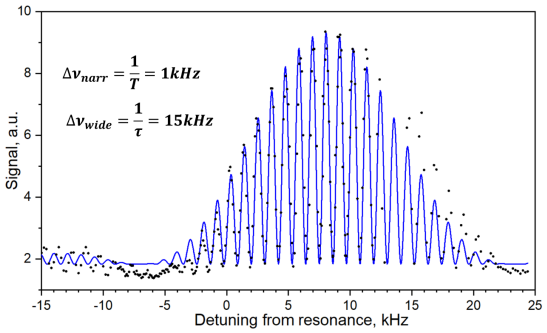

Figure 2: The number of atoms at the excited state depending on the detuning of microwave radiation during interaction with two $\pi/2$-pulses.

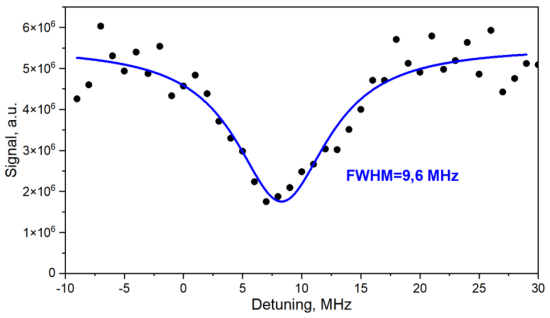

Figure 3: Number of atoms in a magnetic trap after interaction with a microwave field.

This study was supported by a grant of Russian Science Foundation No. 23-22-00255.

References

[1] *J. Reichel and V. Vuletic (Eds.)*, Atom chips. John Wiley & Sons, (2011).

[2] *M. Keil, O. Amit, S. Zhou, D. Groswasser, Y. Japha, and R. Folman*, Fifteen years of cold matter on the atom chip: promise, realizations, and prospects. J. Mod. Opt. **63**, 1840 (2016).

[3] *D. Li, W. He, S. Shi, B. Wu, Y. Xiao, Q. Lin, and L. Li*, Review of Atom Chips for Absolute Gravity Sensors. Sensors. **23**, 5089 (2023).

[4] *R. Szmuk, V. Dugrain, W. Maineult, J. Reichel, and P. Rosenbusch*, Stability of a trapped-atom clock on a chip. Phys. Rev. A. **92**, 12106 (2015).

[5] *D. Becker, M. D. Lachmann, S. T. Seidel, et al.*, Space-borne Bose–Einstein condensation for precision interferometry. Nature. **562**, 391 (2018).

[6] *A. E. Afanasiev, A. S. Kalmykov, R. V Kirtaev et al.*, Single-layer atom chip for continuous operation: Design, fabrication and performance. Opt. Laser Technol. **148**, 107698 (2022).

[7] *F. Reinhard*, Design and construction of an atomic clock on an atom chip. Diss. Université Pierre et Marie Curie-Paris VI, (2009).

[8] *S. Wildermuth, P. Krüger, C. Becker et al.*, Optimized magneto-optical trap for experiments with ultracold atoms near surfaces. Phys. Rev. A. **69**, 30901 (2004).

Control and readout of a transmon using a compact superconducting resonator

Julia Zotova[1,2,3,4*], **Shtefan Sanduleanu**[2,4,5], **Gleb Fedorov**[2,4,5], **Rui Wang**[6,7], **Jaw-Shen Tsai**[6,7] **and Oleg Astafiev**[1,2]

[1] *Skolkovo Institute of Science and Technology, 121205 Moscow, Russia*
[2] *Moscow Institute of Physics and Technology, Institutskiy Pereulok 9, Dolgoprudny 141701, Russia*
[3] *RIKEN Center for Emergent Matter Science (CEMS), 2–1 Hirosawa, Wako, Saitama 351–0198, Japan*
[4] *National University of Science and Technology 'MISIS', 119049, Russia*
[5] *Russian Quantum Center, 121205 Skolkovo, Moscow, Russia*
[6] *Research Institute for Science and Technology, Tokyo University of Science, 1-3 Kagurazaka, Shinjuku-ku, Tokyo 162-8601, Japan*
[7] *RIKEN Center for Quantum Computing (RQC), Wako, Saitama 351-0198, Japan*
*E-mail: yuliya.zotova@phystech.edu

Abstract

We demonstrate control and readout of a superconducting artificial atom based on a transmon qubit using a compact lumped-element resonator. The resonator consists of a parallel-plate capacitor (PPC) with a wire geometric inductor. The footprint of the resonators is about 200 μm by 200 μm, which is similar to the standard transmon size and one or two orders of magnitude more compact in the occupied area comparing to coplanar waveguide resonators. We observe coherent Rabi oscillations and obtain time-domain properties of the transmon. The work opens a door to miniaturize essential components of superconducting circuits and to further scaling up quantum systems with superconducting transmons.

In this work, we experimentally develop cQED systems with compact resonators and demonstrate coherent qubit control and dispersive readout. One of the approaches to realize compact resonators with similar to qubit sizes is based on a planar lumped-element design [1]. Such parallel-plate capacitor (PPC) resonators, differently from coplanar ones, do not have higher frequency modes and are based on the standard oxidation process. In this work, we experimentally develop cQED systems with such resonators and demonstrate coherent qubit control and dispersive readout. It consists of a common feedline (shown in orange in Fig. 1(c)) for 20 units of compact resonators (shown in green in Fig. 1(c)) and flux-tunable (via a superconducting interference device, SQUID) transmon qubit (shown in blue in Fig. 1(c)) connected by a coupling capacitor (shown in red in Fig. 1(c)). The chip with the structure is shown in Fig. 1(a,b).

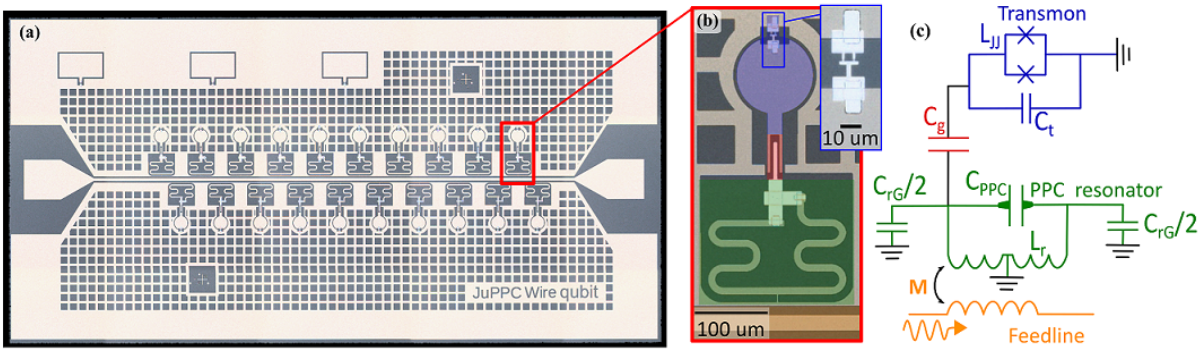

Figure 1: Investigated system and their chip. (a) The chip image. (b): The resonator-transmon system. (c): An equivalent electric scheme of the circuit in (b).

Then, we record transmission spectra of the resonators as a function of the external magnetic field. As discussed above, the magnetic flux through a SQUID loop tunes the transmon frequency by modulating E_J. A conventional indication of a resonator-transmon coupling is the periodic appearance of the avoided

crossing, see Fig. 2(a, left), which marks the strong coupling regime. For better understanding of the system energy structure vs. external magnetic field, we perform cross-Kerr two-tone spectroscopy where the first tone is set to the resonator frequency $f_r = \omega_r/(2\pi)$, and the second tone (whose frequency is on the y-axis) is aimed to excite the transitions between the eigenstates, see Fig. 2(b-d, left). To identify the obtained transitions, we fit the two-tone spectra by numerically solving the Hamiltonian of the resonator-qubit system. The transitions we found are labeled in Fig. 2(b-d, left). Then, we obtain coherent Rabi

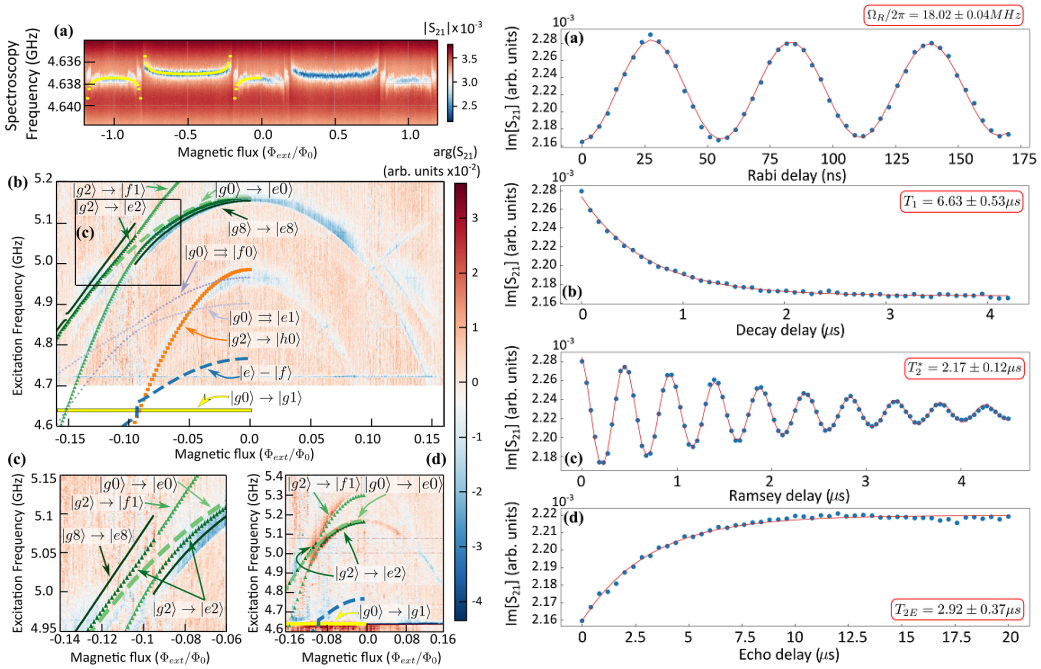

Figure 2: Left: Experimental spectra of (a) the readout resonator of the transmon 1 A (b)-(d) transmon transitions as a function of the normalized magnetic field for the first resonator-transmon pair. (c) Enlarged part of the (b), (d) qubit spectra with higher excitation power. Fit indicates different transitions, marked with different styles and colors. Right: Experimental results of the readout of the transmon states for the first qubit. **(a)** Rabi oscillations. **(b)** The energy relaxation curve. **(c)** The Ramsey dephasing measurements. **(d)** The Hahn-Echo dephasing measurements.

oscillations to demonstrate the quantum state control, see Fig. 2(a, right). The conventional pump-probe technique is used to read out the transmons. We obtain the population of the first excited state of a transmon as a function of the excitation pulse length. We extract the length of the π-pulse for the transmon excitation to the first exited state. Then we measure the relaxation time $T_1 = 6.63 \pm 0.53$ μs (Fig. 2(b, right)) by varying the delay between the π-pulse and the readout pulse. Ramsey dephasing time $T_{2R}^* = 2.17 \pm 0.12$ μs (Fig. 2(c, right)) are obtained by varying the delay between two $\pi/2$-pulses with following readout. The Hahn-Echo dephasing time $T_{2E} = 2.92 \pm 0.37$ μs (Fig. 2(d, right)) was obtained by varying the delay between π-pulse and two $\pi/2$-pulses with subsequent readout.

References

[1] *Julia Zotova, Rui Wang, Alexander Semenov, Yu Zhou, Ivan Khrapach, Akiyoshi Tomonaga, Oleg Astafiev and Jaw-Shen Tsai*, Compact Superconducting Microwave Resonators Based on Al-AlO x-Al Capacitors. Physical Review Applied 19, no. 4 (2023): 044067.

The manuscript of this work can be found on the arXiv platform: https://arxiv.org/abs/2312.15753

Optical properties of individual single-walled carbon nanotubes

Fedor Maksimov[1,2*], Anastasia Goldt[3], Sergey Dozmorov[3], Yuriy Gladush[3], Albert Nasibulin[3], Alexander Chernov[1,2]

[1] *Russian Quantum Center, 30, Bolshoy Bulvar, Building 1, Skolkovo Innovative Center, Moscow, Russian Federation*
[2] *Center for Photonics and 2D Materials, Moscow Institute of Physics and Technology (MIPT), Dolgoprudny, Russian Federation*
[3] *Skolkovo Institute of Science and Technology, Bolshoy Boulevard 30, bd. 1, Moscow, 121205, Russian Federation*
*E-mail: maksimov.fm@phystech.edu

Abstract

We perform the Raman and photoluminescence spectroscopy on individual and small bundles of deposited single-walled carbon nanotubes, that further can be used for future applications in quantum technologies as single-photon source.

Introduction

Single-walled carbon nanotubes (SWCNTs) are promising low-dimensional material with many applications in quantum technologies. One of the applications that stems from the optical properties of SWCNTs [1], [2] is using them as a basis for a single photon source. The main advantages of such emitters are the possibility of obtaining single photons at room temperature, as well as the possibility of choosing the wavelength of emission in the near infrared range by selecting the chirality of the nanotube, which allows, for example, to tune the emitters to the wavelength of telecommunication networks 1550 nm [3]. Such sources are necessary for quantum computing on photons and also for quantum communication.

Here we investigate low-concentration nanotubes deposited on sapphire substrates using resonant Raman spectroscopy and detect the photoluminescence response in the near-IR range.

Results

In this work, we investigate single-walled carbon nanotubes created by aerosol method [4] that were deposited on sapphire substrate. The concentration of nanotubes was verified by AFM and is close to the condition of single nanotubes. Sapphire was chosen as a substrate due to low background signal in the near infrared region, which is important for the subsequent photoluminescence study. The absorption spectrum was measured for the synthesized SWCNTs, that allowed to estimate the requirements for the resonant excitation. The measurements were performed with a tunable CW laser at a wavelength of 488 nm with a Mitutoyo x100 NIR objective and a spot size of about 1 μm. The MadCityLabs Nano T-225 nanostage was used for mapping and the signal was collected with a Horiba spectrometer. As a result, a map of G-band Raman peak signal of a sample that contained several nanotubes with a length of about 2-3 μm was obtained 1. Further the photoluminescence mapping of functionalized nanotubes was performed. Functionalization of SWCNTs with aryl groups allows the creation of localized sp^3 defects on the surface of the nanotube and increases the quantum efficiency of the photoluminescence, which is necessary for the subsequent creation of a single-photon source [5]. Mapping of a single functionalized nanotube allows to determine the position of the defect and finally to integrate them into resonant nanostructures that provide further increase of the photoluminescence efficiency.

Conclusion

In this work we have performed the mapping of a low-concentration nanotube sample using Raman spectroscopy. Further we perform the photoluminescence mapping of low-concentration functionalized nanotubes. Unambiguous detection, characterization and further measurement of optical properties allow to reveal the possibility of implementation of individual SWCNTs as a single-photon source.

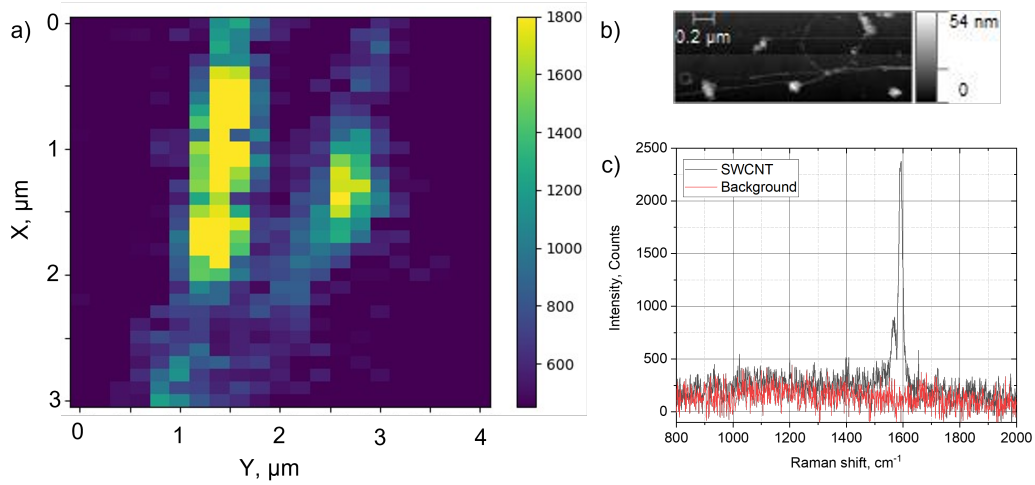

Figure 1: Raman signal map of low-concentrated SWCNTs (a), AFM image of SWCNT on sapphire (b), Raman signal of SWCNT and background (c).

References

[1] *Eremina, Valentina A., et al.*, Separation and optical identification of semiconducting and metallic single-walled carbon nanotubes. Physica status solidi (b) 254.5 2017

[2] *Chernov, Alexander I., and Elena D. Obraztsova*, Metallic single-wall carbon nanotubes separated by density gradient ultracentrifugation. Physica status solidi (b) 246.11-12 2009

[3] *He, Xiaowei, et al.*, Tunable room-temperature single-photon emission at telecom wavelengths from sp 3 defects in carbon nanotubes. Nature Photonics 11.9 2017

[4] *Ilatovskii, Daniil A., et al.* Photophoretic deposition and separation of aerosol-synthesized single-walled carbon nanotubes. Carbon 2023

[5] *Zaumseil, Jana.* Luminescent Defects in Single-Walled Carbon Nanotubes for Applications. Advanced Optical Materials 10.2 2022

Control of states of a two-terminal superconductor interferometer using Landau-Zinner transitions

Pavel Pikunov[1*], **Dmitry Pashin**[1], **Marina Bastrakova**[1,2], **Igor Soloviev**[3,4], **Nikolay Klenov**[4,5]

[1] *Lobachevsky State University of Nizhny Novgorod, Nizhny Novgorod, Russia*
[2] *Russian Quantum Centre, Moscow, Russia*
[3] *D. V. Skobeltsyn Institute of Nuclear Physics, Lomonosov Moscow State University, Moscow, Russia*
[4] *MISIS University of Science and Technology, Moscow, Russia*
[5] *Faculty of Physics, Lomonosov Moscow State University, Moscow, Russia*
*E-mail: pavel.pikunov@internet.ru

Abstract

The possibility of controlling the states of a two-terminal superconducting interferometer using Landau-Zener transitions has been studied. The possibility of implementing high-precision quantum operations in such a system when controlling single flux quantum pulses is demonstrated. The optimal range of inductive parameters of the system and the input signal is found.

Superconducting artificial quantum systems are currently widely used to create prototypes of quantum processors [1] and hybrid quantum-classical neuromorphic systems [2]. In this paper we propose to use a two-terminal superconductor interferometer (see the scheme on fig. 1.)as an auxiliary qubit whose states are controlled by Landau-Zinner transitions by the single flux quantum (SFQ) pulses. It should be noted that this element can also operate in both classical and quantum neuromorphic modes [3].

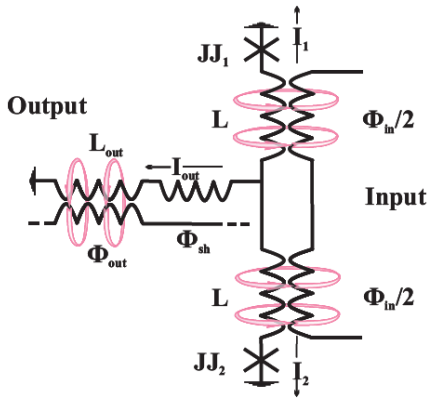

Figure 1: Fig.1 Scheme of a two-terminal superconductor interferometer.

The Hamiltonian of a system is given by the expression:

$$H = \frac{E_C}{\hbar^2}\left(p_\Theta^2 + p_\Psi^2\right) + E_J\left(\frac{(\Theta-\phi_{sh})^2}{2(2l_{out}+l)} + \frac{(\Psi-\phi_{in})^2}{2l}\right) + E_J(1-\cos\Psi\cos\Theta), \quad (1)$$

where E_C and E_J are the charge and Josephson energies, respectively; Ψ, Θ are half-sum and half-difference of phase difference on the Josephson contacts. The coefficients l and l_{out} are dimensionless inductances determined experimentally and ϕ_{sh} is a external shifting flux (see more details in [3]). Dynamic control of the system states is carried out by SFQ pulses:

$$\phi_{in}(t) = A\left(\frac{1}{1+e^{-2D(t-t_1)}} + \frac{1}{1+e^{2D(t-t_2)}}\right), \quad (2)$$

where the parameters A and D tune the level and the rise/fall rate of the input magnetic flux respectively.

By changing the parameters of the system and the parameters of the incoming flux, we have found the configuration of the system that involves the anti-crossing of the ground and first excited levels (fig. 2c).

During the time of action of the external flux the transition of the system from the ground state to the excited state (NOT operation) is possible (fig. 2a-b). Fidelity of the operation shown in fig. 2a-b is 99.99%. At the same time, the system parameters are chosen so that the leakage to the overlying levels is minimal. It is significant that an estimated duration of the NOT operation is 20-60 ns.

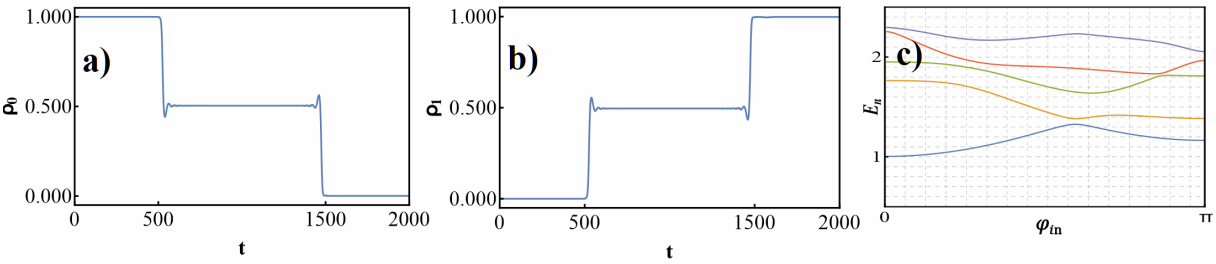

Figure 2: Population of the ground and first excited levels (a,b) under the influence of an external magnetic field; (c) the spectrum of the system as a function ϕ_{in}. Parameter of the system are: $A = \pi$, $l_{out} = 5$, $l = 2.65$, $E_j/2E_C = 1$, $D = 0.008$, $t_1 = 500$, $t_2 = 1500$, $\phi_{sh} = \pi/10$.

The optimal region of parameters l and D was found to achieve the maximum first excited level population fig. 3. It is significant that the exact selection of inductance in the system (which is difficult to change in real systems) is not required - it is possible to achieve high accuracy by tuning the external flux.

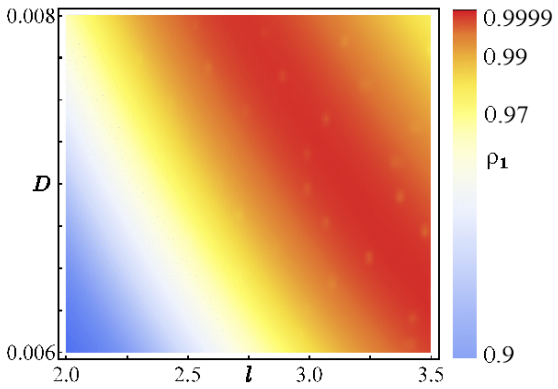

Figure 3: Population parameter map of the first excited level after passing the input flux (2). Parameter of the system are: $A = \pi$, $l_{out} = 5$, $E_j/2E_C = 1$, $\phi_{sh} = \pi/10$.

Thus, the paper demonstrates the possibility of implementing quantum operations in a superconducting interferometer based on SFQ control by implementing Landau-Ziner transitions.

This work was financially supported by the Russian Science Foundation 22-72-10075.

References

[1] *P. Krantz, M. Kjaergaard, F. Yan, T. P. Orlando, S. Gustavsson, and W. D. Oliver*, A quantum engineer's guide to superconducting qubits. Applied Physics Reviews **6**, 021318 (2019).

[2] *I. Soloviev, A. Schegolev, N. Klenov, S. Bakurskiy, M. Kupriyanov, M. Tereshonok, A. Shadrin, V. Stolyarov, A. Golubov*, Journal of Applied Physics **124**, 152113 (2018).

[3] *Schegolev, A. E.; Klenov, N. V.; Bakurskiy, S. V.; Soloviev, I. I.; Kupriyanov, M. Y.; Tereshonok, M. V.; Sidorenko A. S.*, Tunable superconducting neurons for networks based on radial basis functions. Beilstein Arch. **16**, 202216 (2022).

Implementation of XOR logic in superconductor artificial neural network

Dmitriy A. Rybin[1*], Dmitrii S. Pashin[1], Marina V. Bastrakova[1,2], Andrei E. Shchegolev[3], Nikolai V. Klenov[4], Igor I. Solovev[3,4]

[1] *Lobachevsky State University of Nizhni Novgorod, Nizhny Novgorod, Russia*
[2] *Russian Quantum Center, Moscow, Russia*
[3] *Skobeltsyn Institute of Nuclear Physics, Lomonosov Moscow State University, Moscow, Russia*
[4] *National University of Science and Technology MISIS, Moscow, Russia*
*E-mail: rybin@asgap.ru

Abstract

The paper studies the functioning of the simplest artificial neural network (ANN) based on superconducting adiabatic neurons. Analytical expressions for the scheme with two input neurons and one output neuron are obtained. Based on the connection of three neurons, an ANN functioning in accordance with XOR logic is designed.

Currently, the basic elements of neural networks (both the simplest perceptron and radial basis function networks, RBF networks) have been proposed, investigated and designed based on the concepts of the most energy-efficient adiabatic superconducting logic. We have demonstrated a superconductor neuron with a sigmoidal output function capable of operating in classical and quantum modes [1, 2]. In the current work, we consider the coupling of three neurons representing the simplest ANN.

The original connection scheme of the three neurons is shown in Figure 1(b). As an input signal,

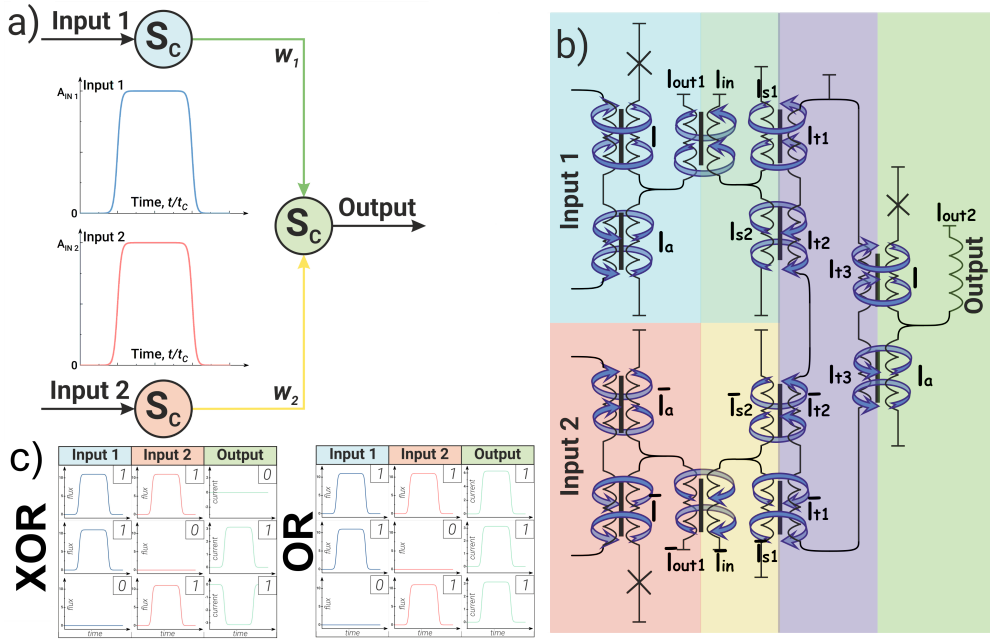

Figure 1: a) Schematic representation of the 3-neuron XOR network and b) its superconducting realisation (different colors corresponds to the different parts of the scheme). In the a) figure part typical inputs (smoothed trapezoids) with magnitudes A_{in1} and A_{in2} are demonstrated. c)The table for XOR and OR operations.

each neuron of the input layer is fed with a magnetic flux, the shape of which was set as a smoothed trapezoid:

$$\varphi_{in}(t) = A_{in} \cdot \left\{ \frac{1}{1+\exp(-2D(t-t_1))} + \frac{1}{1+\exp(2D(t-t_2))} \right\} - A_{in}. \quad (1)$$

The parameters A_{in} and D tune the level and the rise/fall rate of the input magnetic flux respectively. In the following, all magnetic fluxes are normalised by the magnetic flux quantum: e.g. $\varphi_{in} = 2\pi\Phi/\Phi_0$, $\Phi_0 = h/(2e)$. Writing down Kirchhoff's equations and relations for magnetic fluxes in the corresponding circuits, we can describe the system in Fig. 1(b) by the following system of equations:

$$\begin{cases} i_1 + i_{a1} + i_{out} = 0, \\ \bar{i}_1 + \bar{i}_{a1} + \bar{i}_{out} = 0, \\ \varphi_1 - \frac{\varphi_{in}}{2} + i_1 l = i_{out1} l_{out1} - m_1 i_{in}, \\ \bar{\varphi}_1 - \frac{\bar{\varphi}_{in}}{2} + \bar{i}_1 \bar{l} = \bar{i}_{out1} \bar{l}_{out1} - \bar{m}_1 \bar{i}_{in}, \\ \varphi_1 - \frac{\varphi_{in}}{2} + i_1 l = i_{a1} l_a + \frac{\varphi_{in}}{2}, \\ \bar{\varphi}_1 - \frac{\bar{\varphi}_{in}}{2} + \bar{i}_1 \bar{l} = \bar{i}_{a1} \bar{l}_a + \frac{\bar{\varphi}_{in}}{2}, \\ i_{in} - i_{s1} - i_{s2} = 0, \\ \bar{i}_{in} - \bar{i}_{s1} - \bar{i}_{s2} = 0, \\ i_{s1}(l_{s1} + l_p) + m_2 i_{cr} = i_{s2}(l_{s2} + l_p) - m_2^* i_{cr}, \\ \bar{i}_{s1}(\bar{l}_{s1} + l_p) + \bar{m}_2 i_{cr} = \bar{i}_{s2}(\bar{l}_{s2} + l_p) - \bar{m}_2^* i_{cr}, \\ i_{s1}(l_{s1} + l_p) + m_2 i_{cr} = -i_{in}(l_{in} + lp) + m_1 i_{out1}, \\ \bar{i}_{s1}(\bar{l}_{s1} + l_p) + \bar{m}_2 i_{cr} = -\bar{i}_{in}(\bar{l}_{in} + lp) + \bar{m}_1 \bar{i}_{out1}, \\ (l_{t1} + l_{t2} + \bar{l}_{t1} + \bar{l}_{t2} + l_{t3} + l_{t4}) i_{cr} = (-i_{s1} m_2 - \bar{i}_{s1} \bar{m}_2 + i_2 m_3 + m_2^* i_{s2} + \bar{m}_2^* \bar{i}_{s2} - m_3^* i_{a2}), \\ i_2 + i_{a2} + i_{out2} = 0, \\ \varphi_2 - m_3 i_{cr} + i_2 l = i_{out2} l_{out2}, \\ \varphi_2 - m_3 i_{cr} + i_2 l = i_{a2} l_a + m_3^* i_{cr}. \end{cases} \tag{2}$$

where $\varphi_{1,2}, \bar{\varphi}_1$ is the phase difference at the Josephson contacts of the neurons, $m_j, \bar{m}_j$ and $m_j^*, \bar{m}_j^*$ are the mutual induction coefficients of the corresponding transformers ($j = 1..3$). All currents in (2) are normalized to the critical current of the output neuron I_{C_2}.

The solution of the optimisation problem for this system of equations allows to configure the neural network to operate both as an XOR logic element and as an OR logic (see Figure 1(c)) element, which is quite expectable. An obvious choice for such a neural network configuration will be the choice of weight coefficient values: for XOR they should be antisymmetric, and for OR – on the contrary, symmetric. In case of deviation from this principle, the output of the network produces a result that does not coincide with the truth table for the given elements. By tuning the coupling parameters of the three neurons, we managed to achieve full functioning of the circuit according to XOR logic in the classical regime. The input of each neuron receives signals of different levels in the form of smoothed trapezoids corresponding to logical 0 and 1 (see Figure 1(a)). The case when there is no signal at the input of both input neurons is not demonstrated – in case of absence of signals on both inputs of the circuit there is no signal on the output as well ("0" + "0" = "0"). One point concerning the OR logic element is worth mentioning. The point is that in the case of a classical OR gate, if two "1" are applied to the input, the output will also generate a "1" with the same signal level as the input (peculiarities of digital circuits). In our case it is not true: when two "1" are applied to the input, the output generates a signal whose level exceeds the same for the cases ("1"+ "0" or "0"+ "1") by two times.

In previous works we have performed numerical analysis and showed that adiabatic neurons can operate also in the quantum mode [2]. In the next step we will numerically analyze the XOR scheme in the case of quantum mode.

References

[1] *M.V. Bastrakova, A.A. Gorchavkina, A.E. Schegolev, N.V. Klenov, I.I. Soloviev, A.M. Satanin, and M.V. Tereshonok*, Dynamic Processes in a Superconducting Adiabatic Neuron with Non-Shunted Josephson Contacts. Symmetry **13(9)**, 1735 (2021).

[2] *M.V. Bastrakova, D.S. Pashin, D.A. Rybin, A.E. Schegolev, N.V. Klenov, I.I. Soloviev, A.A. Gorchavkina, and A.M. Satanin*, A superconducting adiabatic neuron in a quantum regime. Beilstein J. Nanotechnol. **13**, 653 (2022).

Superconducting microstrip single-photon detectors with ultra high time resolution

Sergey Svyatodukh[1,2,3*], **Alexander Divochiy**[3], **Pavel Morozov**[2,3], **Vladislav Andreev**[1,2,3], **Gregory Goltsman**[1,2,3,4]

[1] *National Research University Higher School of Economics, 34 Tallinskaya St., Moscow, Russia*
[2] *Physics Department, Moscow State Pedagogical University, 1/1 Malaya Pirogovskaya St., Moscow, Russia*
[3] *LLC Scontel, Derbenevskaya Naberezhnaya, 11kA, 102-A, Moscow, Russia*
[4] *Russian Quantum Center, Skolkovo, Bolshoy Bulvar, 30, bld. 1, Moscow, Russia*
*E-mail: sergey.svetodux@gmail.com

Abstract

In this work we demonstrated superconducting microstrip single photon detector (SMSPD) with the width of active area of 1, 3 and 5 um, that have saturating internal quantum efficiency up to 1700 nm and have system timing jitter as low as 14 ps at 0.8 K. Obtained results will find usage in single photon lidars, high-speed quantum communication, and lifetime measurement of single-photon sources.

Superconducting nanowire single photon detectors developed in 2001 [1], now demonstrates outstanding performance in different fields including lidars, quantum communications, quantum computing and others [2, 3, 4]. Main reasons for this are high system quantum efficiencies, low system jitter values and high count rate of SNSPD [5]. Despite all the advantages of SNSPD, it has one main drawback – when increasing the detector area, it is not possible to maintain high timing resolution of the detector due to sufficiently large values of the kinetic inductance of the detector. One of the possible solutions to this problem is the fabrication of superconducting single-photon detectors from micrometer-scale strips - superconducting microstripe single photon detectors (SMSPD). However, unfortunately, these detectors show low time resolution, due to the high values of the internal jitter of the detector, far from saturation of the internal quantum efficiency of the detector [6]. Our recently demonstrated work have shown SMSPD, with 100% internal quantum efficiency in the infrared wavelength range [7]. In this work, thin films of niobium nitride (NbN) obtained in previous work were used to develop SMSPD with ultrahigh time resolution. We fabricated superconducting bridges with widths of 1, 3, 5 μm. Scanning electron microscope images of fabricated superconducting microstipe bridges, with width of 1 um, shown on Fig. 1 **Left**, Fig. 1 **Right**, shows devices layout with every layer of the structure. Setup for jitter and internal detection efficiency measurement shown of Fig. 2, it consists of SMSPD integrated in sorption cooler, with base temperature $2.2K$ or $0.8K$, depending on cryogenic key position, femtosecond laser and TCSPC module, used as correlator. Internal detection measurements results shown on Fig. 3 **Left** where a), b) and c) are 1, 3 and 5 μm, respectively. Jitter measurments results are shown of Fig. 3 **Right** where a), b) and c) are 1, 3 and 5 μm, respectively.

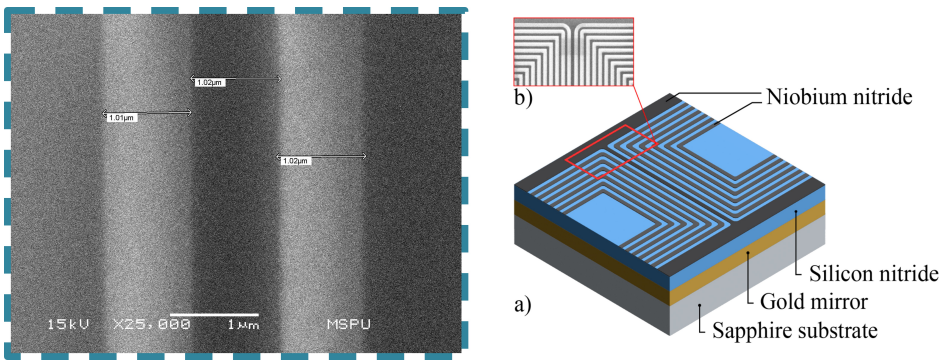

Figure 1: **Left** Scanning electron microscope of fabricated SMSPD bridge, with width of 1 um, **Right** Device layers layout of fabricated SMSPD bridges.

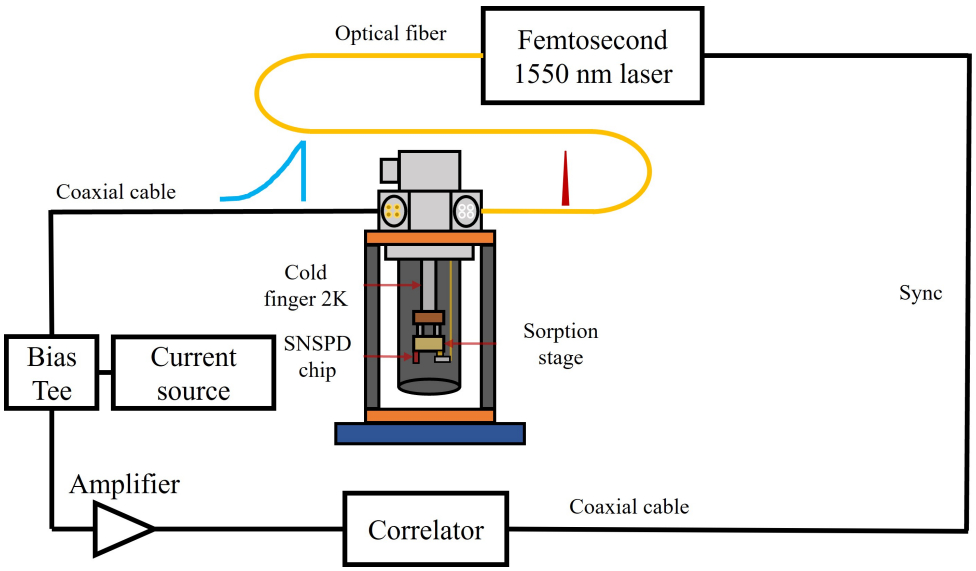

Figure 2: Schematic representation of experimental setup used for jitter and internal quantum efficiency measurement.

Acknowledgement
The study was supported by a grant from the Russian Science Foundation (№ 23-65-10005)

References

[1] *Gol'Tsman, G. N., Okunev, O., Chulkova, G., Lipatov, A., Semenov, A., Smirnov, K., Sobolewski, R.*, Picosecond superconducting single-photon optical detector. Applied physics letters **79(6)**, 705-707 (2001).

[2] *Todaro, S. L., Verma, V. B., McCormick, K. C., Allcock, D. T. C., Mirin, R. P., Wineland, D. J., Slichter, D. H.*, State readout of a trapped ion qubit using a trap-integrated superconducting photon detector. Physical review letters, **126(1)**, 010501 (2021).

[3] *Wang, S., Yin, Z. Q., He, D. Y., Chen, W., Wang, R. Q., Ye, P., Han, Z. F.*, Twin-field quantum key distribution over 830-km fibre. Nature photonics, **16(2)**, 154-161 (2022).

[4] *Taylor, G. G., Morozov, D., Gemmell, N. R., Erotokritou, K., Miki, S., Terai, H., Hadfield, R. H.*, Photon counting LIDAR at 2.3 µm wavelength with superconducting nanowires. Optics express, **27(26)**, 38147-38158 (2019).

[5] *Holzman, I., Ivry, Y.*, Superconducting nanowires for single-photon detection: progress, challenges, and opportunities. Advanced Quantum Technologies, **2(3-4)**, 1800058 (2019).

[6] *Vodolazov, D. Y., Manova, N. N., Korneeva, Y. P., Korneev, A. A.*, Timing jitter in NbN superconducting microstrip single-photon detector. Physical Review Applied, **14(4)**, 044041 (2020).

[7] *Zolotov, P., Svyatodukh, S., Divochiy, A., Seleznev, V., Goltsman, G.*, High-resistivity niobium nitride films for saturated-efficiency SMSPDs at telecom wavelengths and beyond. Applied Physics Letters, **122(15)** (2023).

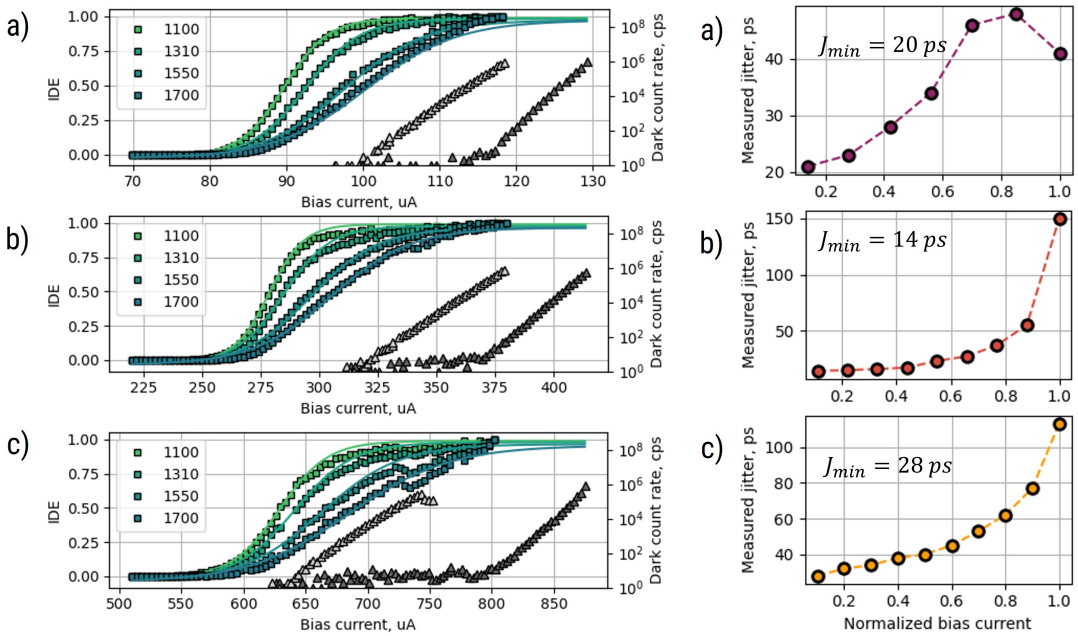

Figure 3: **Left** Internal detection efficiency measurements results **Right** System jitter measurements results, inserted values J_{min}, shows minimal obtained jitter. a), b) and c) represents 1, 3 and 5 μm superconducting bridges, respectively.

Effective programming of a photonic processor with complex interferometric structure

Kseniia Urusova[1*], Ilya Kondratyev[1], Artem Argenchiev[1], Sergey Kuzmin[1], Nikolay Skryabin[1], Ivan Dyakonov[1,2], Stanislav Straupe[1,2] and Sergey Kulik[1,3] ,

[1] *Quantum Technology Centre and Faculty of Physics, M.V. Lomonosov Moscow State University, 1 Leninskie Gory Street, Moscow 119991, Russian Federation*
[2] *Russian Quantum Center, Russia, Moscow, 121205, Bol'shoy bul'var 30 building 1*
[3] *Laboratory of quantum engineering of light, South Ural State University (SUSU), Russia, Chelyabinsk, 454080, Prospekt Lenina 76*
*E-mail: urusova.kn21@physics.msu.ru

Abstract

In this work we have successfully programmed a 4×4 reconfigurable photonic processor, consisting of two 4×4 directional couplers and a three tunable phase shifters. The programming procedure was performed by utilizing global approximation of the chips' calibration data. To verify the quality of programming of our optical processor we measured 100 unitary transformations on chip and compared them with prediction by the obtained from programming interferometer model - the average fidelity between unitary matrices was 98.5 %. We have also demonstrated optical port-to-port switching on our processor in a broadband wavelength region from 915 to 975 nm with no optimization on chip. This research opens up possibilities for further efficient programming of photonic processors.

Programmable integrated optical circuits believed to be a promising platform for scalable quantum computation in future [1]. One of the technologies for manufacturing such integrated optical circuits is femtosecond laser writing of waveguiding structures in optically transparent samples, which is a simple, fast and not expensive technology for prototyping low and medium scale integrated photonic devices, which can be usefully exploited [2].

In this work we have fabricated reconfigurable 4×4 integrated optical chip in fused silica glass by femtosecond laser writing. The structure of our photonic processor is demonstrated in Fig 1a and consisted of two 4×4 directional couplers and three tunable phase shifters. Thermo-optical phase-shifters were used for the reconfiguration of the processor.

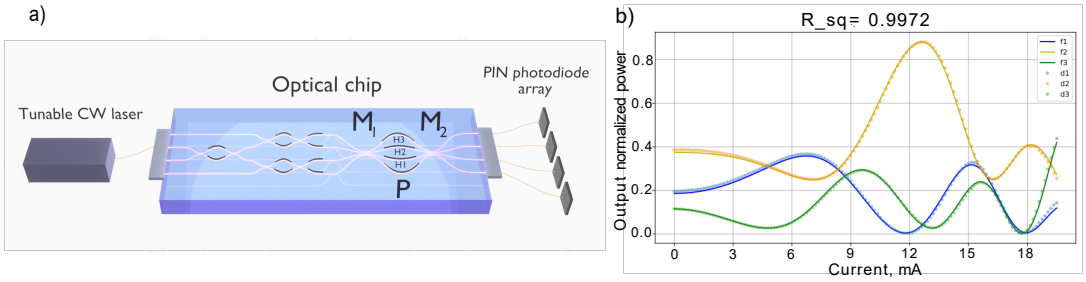

Figure 1: (A) Schematic image of the experimental setup, which is consisted of tunable CW laser, programmable multiport interferometer and 4 photodetectors. (B) An example of the measured calibration data from all four output ports for the fourth input port, the third heater was calibrated.

Under programming of the reconfigurable optical chip we mean the total construction of its' digital model, which can be used for prediction of the chips' unitary transformation with given phase shifts set on the phase layer of the chip. The programming procedure was performed by utilizing global approximation of the chips' calibration data, example of which is shown in Fig. 1b.

For testing the obtained chip model, a 100 sets of random currents were applied to chips' heaters, producing 100 different optical chips' transformations, which can be either predicted by the model and directly measured on chip. The measured unitary matrices were compared with ones predicted by the model, yielding the average fidelity of 98.5 % (see Fig. 2a).

As another test of the quality of our programming of the chip, a port-to-port optical switching on the chip for different wavelengths was demonstrated. Necessary phase shifts were obtained by running an optimization procedure on a standard PC. Obtained phase shifts were then applied on the chips' heaters and output power distribution was registered. An example of experimentally measured and predicted switches is shown in Fig. 2b. It can also be seen from the Fig. 2c that the average switching fidelities for the experiment and prediction are in good agreement.

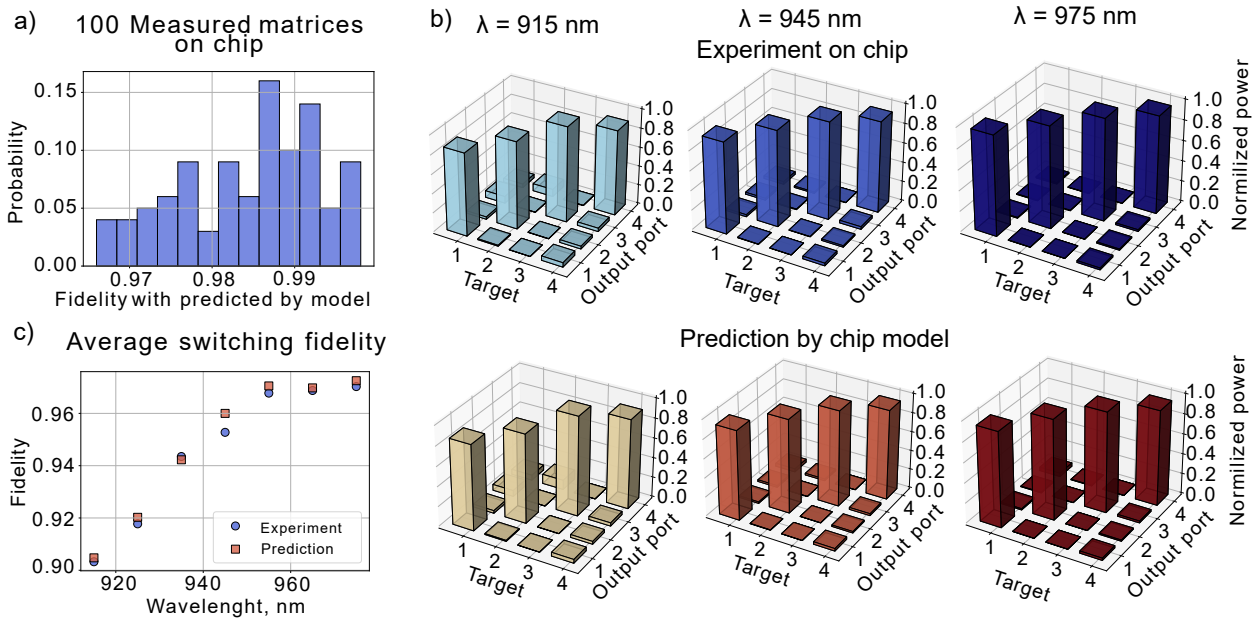

Figure 2: (A) Fidelity distribution between 100 unitaries directly measured on chip and predicted by the chips' model. The average fidelity value is 98.5 %. (B) An example of port-to-port optical switching from third input port of the chip for three wavelength. (C) The dependence of the average fidelity on the wavelength for the output power distributions predicted by the model and experimentally obtained. The average fidelity for each input channel is higher 90 %.

Both demonstrated results confirm the validity of the model and demonstrate the successful programming of the optical chip with complex interferometric structure. In future we plan to show on our chip the implementation of the Haar random unitaries, and the potential applicability for an information processing task solving.

Acknowledgements

This work was supported by Rosatom in the framework of the Roadmap for Quantum computing (Contract No. 868-1.3-15/15-2021 dated October 5 and Contract No. P2154 dated November 14, 2021)

References

[1] *Ilya V. Kondratyev, Veronika V. Ivanova, Sergey A. Zhuravitskii, et al.*, Large-scale error-tolerant programmable interferometer fabricated by femtosecond laser writing, arXiv preprint arXiv:2308.13452, **4**(1), (2023).

[2] *C.Cai and J.Wang*, Femtosecond laser-fabricated photonic chips for optical communications: A review, Micromachines, 10.3390/mi13040630, **4**(2), (2022).

Cold-atom array assembly with graph theory and combinatorial optimization algorithms

K.A. Uyangulov*, **G.I. Struchalin, S.S. Straupe**

Quantum technology centre, Faculty of Physics M.V. Lomonosov Moscow State University, Moscow, Russia
*E-mail: uiangulov.ka20@physics.msu.ru

Abstract

We present an algorithm that finds optimal and collision-free pathways for relocating atoms with an optical tweezer from initial sites to user-defined destination traps. We also demonstrate high probabilities of loading target traps experimentally.

Arrays of atoms are a useful resource for quantum information. However, deterministic loading of trap arrays is practically difficult; only randomly loaded arrays with filling fraction of 50% are attainable. We select a subset of traps to be utilized for further quantum computation, and we fill them with atoms by transporting those from other traps. Since the lifetime of atoms and the tweezer speed are both finite, a crucial optimization problem arises: atom transfer must be accomplished in the shortest time possible. Furthermore, in order to avoid atom collisions and interference between optical trap fields, the tweezer is not permitted to trespass the vicinity of stationary atoms.

We developed an algorithm to solve the above problem. It contains two phases and is based on graph theory and combinatorial optimization techniques. The algorithm begins by using the Hungarian method [1] to assign available atoms to empty traps in the desired region. At this stage modified Euclidean metric is used to avoid trespassing paths, which are optimal in terms of distance. The following phase finds a collision-free ordering of the previously computed list of movements. This is achieved by organizing movements into a dependency graph and applying topological sorting algorithm [2, 3]. If the latter is impossible, partial reassignment of source and target sites is performed.

Our experimental cycle begins with a CCD camera shot to determine trap occupancy, followed by a pushout removal of atoms from all the target traps. We then compute a routing plan, and use an optical tweezer to transport atoms to target traps. After that, another CCD image is taken, and the next attempt to accomplish atom array assembly is made. The number of filled traps is evaluated after each experimental cycle. The data obtained after repeating this cycle 5000 times is shown in Figure 1. The target region is located exactly in the center of the trap array shown in this picture. Traps in this location have a greater than 80% chance of getting filled when applying the above procedure.

References

[1] *Woojun Lee, Hyosub Kim, and Jaewook Ahn*, Defect-free atomic array formation using Hungarian matching algorithm. Phys. Rev. A **95**, 053424 (2017).

[2] *A. B. Kahn*, Topological sorting of large networks. Commun. ACM, **5**, 11 (1962).

[3] *Remy El Sabeh, Jessica Bohm, Zhiqian Ding, Stephanie Maaz, Naomi Nishimura, Izzat El Hajj, Amer Mouawad, and Alexandre Cooper*, Efficient algorithms to solve atom reconfiguration problems. II. Assignment-rerouting-ordering algorithm. Phys. Rev. A **108**, 023108 (2023).

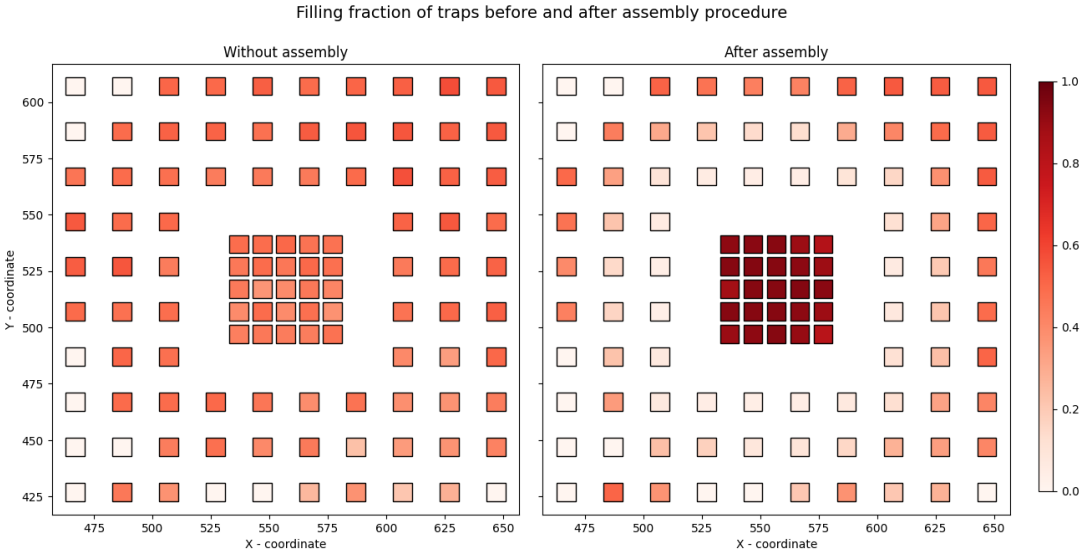

Figure 1: Filling probability of each trap without assembly (left) and after several attempts of assembly (right). Squares represent traps. The darker the color of a related square, the greater the likelihood of a trap to be filled.

Miass, Russia February 25 – March 2, 2024
7th International School on Quantum Technologies

Development of Two-Dimensional Moire Structure Based Quantum Simulator: Optical Characterization

Emil Chiglintsev[1,2,*], **Artem Abramov**[1,3], **Vasily Kravtsov**[1,3], **Alexander Chernov**[1,2]

[1] *Russian Quantum Center, Skolkovo, Moscow, Russia*
[2] *Moscow Institute of Physics and Technology (National Research University), Dolgoprudny, Russia*
[3] *School of Physics and Engineering, ITMO University, Saint Petersburg, Russia*
*E-mail: chiglintsev.eo@phystech.edu

Abstract

The work is devoted to development, assembly and optical study of two-dimensional twisted Moire structure made of tungsten diselenide homobilayers for quantum simulation of strong correlated states of matter.

Introduction

Twisted van der Waals heterostructures are of great interest because of their many remarkable properties and potential for creating new states of matter in the laboratory. These systems can serve as an efficient platform for quantum simulations in strongly correlated physics and topology in quantum materials. These materials have several properties that make them versatile tools. First, their properties can be tuned using available external parameters such as gating, strain, carrier density, and twist angle. Second, they allow the realization and control of many fundamental multiparticle quantum models from the field of condensed state physics. Third, experimental reading protocols are available that display their complex phase diagrams under both equilibrium and non-equilibrium conditions. These heterostructures allow the creation and functionalization of new forms of matter, broaden the scope for the study of physics, and open up prospects for future applications in technology. Together with that, they might be applied to the commercial purposes in pharmacological and optimization tasks.

Our general work is devoted to the realization of several phases of matter on a two-dimensional twisted structure. Here we investigated photoluminiscence response of the created structure. We used two rotated TMDC monolayers to create a Moire potential [1], while the choice of such a material was due to a prominent optical response [2].

Results

In this work we assembled Moire structure device with top and bottom electric voltage gates for independent variation both carriers filling factor and electric field penetrating twisted structure using dry transfer and tear-and-stack techniques. This structure configuration allowed us to study exciton behaviour in different displacement fields and carrier filing factors. The twisted structure was made of two tungsten diselenide monolayers rotated by two degrees relative to each other. The gold contacts are created on graphite that each acts as gate and contacted to the twisted structure using lithography. The area lateral size for optical interrogation is around 7 $\mu m \times 5$ μm as marked on Fig. 1.

Photoluminescence measurements were carried out at temparature (8 K) using HeNe laser source with wavelenghth 633 nm. Experimental observation revealed peculiar exciton behaviour with changing electrical gates voltages. Below 1.6 eV we observed interlayer exciton splitting and linear Stark shift due to electrical field in bilayer as in the previous work [3] Fig. 2. The slope of the curve allows to calculate the distance between a hole and an electron in an interlayer exciton. It is about 35 nm that is smaller than interlayer separation (60 nm). Probably these observations are related to superposition interaction of interlayer excitons: exchange attraction and dipole repulsion due to layer degeneracy of homobilayer structure [4]. We also detected the drastic jump in interlayer exciton PL with increasing filling factor from zero to one carrier at one Moire lattice site. We speculate that it might be due interlayer excitons strong dipole interaction. This problem requires detailed theoretical and experimental study.

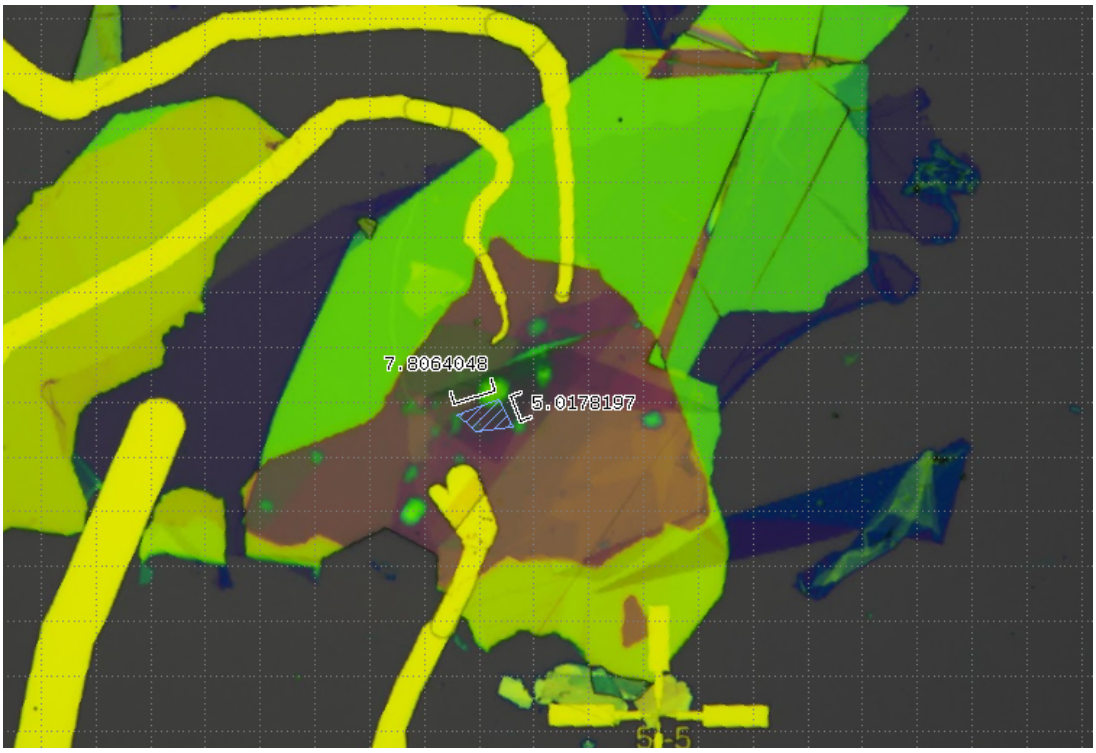

Figure 1: Completed device for exciton behaviour studying.

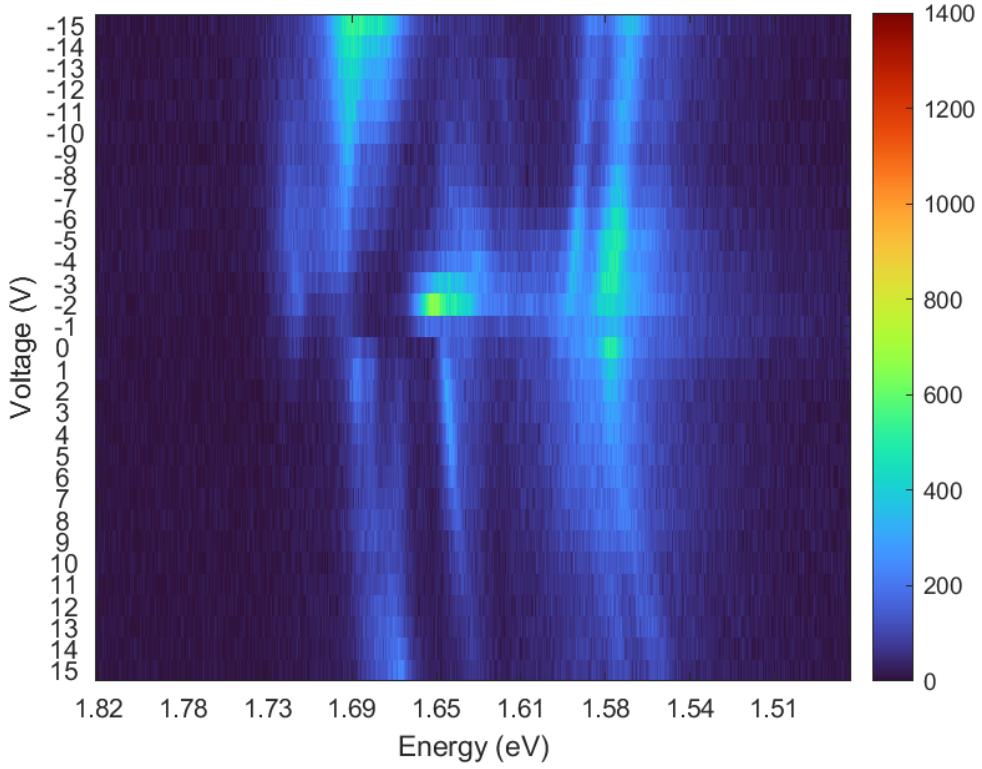

Figure 2: The photoluminescence (PL) map of the sample. The PL response depending on the applied voltage at the top gate at a constant voltage of 0.5 V at the bottom gate. The step of voltage is 1 V.

Above 1.6 eV we detected intralayer excitons whose behavior depend on carriers concentration, but not on electrical displacement field. These excitons are concentrated in one layer and do not experience an electrical field gradient. Variation of concentration brings to the creation of charged excitons, dark excitons, biexcitons and etc. [5].

Conclusion

In this work, we revealed and characterized intralayer and interlayer excitons of a twisted structure. The former are caused by the Moire potential. We have observed the hybrid physics of the interactions of interlayer excitons. Our next step is to study the dipole interaction of interlayer excitons depending on the degree of polarization of carriers in different layers, which might allow to access Bose-Hubbard physics. We are also planning simultaneous to optical transport measurements in order to register an increase in peak resistivity at a filling factor of one carrier per Moire lattice site [6], that will result in Mott insulator transition in Hubbard physics.

References

[1] *Fengcheng Wu, Timothy Lovorn, Emanuel Tutuc, and A.H. MacDonald*, Hubbard Model Physics in Transition Metal Dichalcogenide Moiré Bands. Phys. Rev. Lett. **121** (2018).

[2] *Vasily Kravtsov, Tatiana Ivanova, Artem N Abramov, Polina V Shilina, Pavel O Kapralov, Dmitry N Krizhanovskii, Vladimir N Berzhansky, Vladimir I Belotelov, Ivan A Shelykh, Alexander I Chernov, Ivan V Iorsh*, Valley polarization of trions in monolayer MoSe2 interfaced with bismuth iron garnet. 2D Materials (2021).

[3] *Giovanni Scuri, Trond I. Andersen, You Zhou, Dominik S. Wild, Jiho Sung, Ryan J. Gelly, Damien Bérubé, Hoseok Heo, Linbo Shao, Andrew Y. Joe, Andrés M. Mier Valdivia, Takashi Taniguchi, Kenji Watanabe, Marko Lončar, Philip Kim, Mikhail D. Lukin, and Hongkun Park*, Electrically Tunable Valley Dynamics in Twisted WSe_2/WSe_2 Bilayers. Phys. Rev. Lett. **124** (2020).

[4] *Tagarelli, F., Lopriore, E., Erkensten, D. et al.*, Electrical control of hybrid exciton transport in a van der Waals heterostructure. Nat. Photon. **17** (2023).

[5] *Zhipeng Li Zhipeng Li Department of Chemical and Biological Engineering, Rensselaer Polytechnic Institute, Troy, New York 12180, United StatesMore by Zhipeng Li, Tianmeng Wang, Zhengguang Lu, Mandeep Khatoniar, Zhen Lian, Yuze Meng, Mark Blei, Takashi Taniguchi, Kenji Watanabe, Stephen A. McGill, Sefaattin Tongay, Vinod M. Menon, Dmitry Smirnov, and Su-Fei Shi*, Direct Observation of Gate-Tunable Dark Trions in Monolayer WSe_2. Nano Lett. (2019).

[6] *Wang, L., Shih, EM., Ghiotto, A. et al.*, Correlated electronic phases in twisted bilayer transition metal dichalcogenides. Nat. Mater. **19** (2020).

Investigation of the decoherence channels of the fluxonium qubit

Chudakova Tatyana[1*,2,3], **Kazmina Alyona**[1,2,3],
Majorin Grigory[1,2,3], **Moskalenko Ilya**[2]

[1] *Russian Quantum Center*
[2] *University of Science and Technology MISIS*
[3] *Moscow Institute of Physics and Technology MIPT*
*E-mail: sidelnikova.ta@phystech.edu

Abstract

A promising alternative to the popular transmon qubit for implementing a scalable quantum processor is the fluxonium qubit. However, the presence of a control line limits the lifetime of the qubit due to the connection with the external environment, which can be expressed as a set of oscillators associated with the qubit at the transition frequency. A study of the relaxation of a qubit into a magnetic flux control line, depending on its geometry, has been carried out. The topology of the circuit was selected, in which the relaxation times of the qubit, limited by the stream line, were on the order of 1 millisecond. The influence of the distribution of the electromagnetic field for a given geometry was also studied and the dielectric losses at the interfaces were estimated, on the basis of which the design was changed and compared with the losses on the previous sample. Based on the work done, the qubit-fluxonium circuit was optimized, which showed lifetimes of over 200 microseconds during the experiment

Fluxonium

Superconducting fluxonium qubits is a Josephson contact shunted by a large inductance, such that the inductive energy is $E_L \ll E_J$ and is described by the following Hamiltonian [1] Equation (1):

$$\begin{aligned} H_{\text{Fluxonium}} &= 4E_C N^2 + E_J\left(1-\cos\left(\phi-\frac{\Phi_x}{\Phi_0}\right)\right)+\frac{E_L}{2}\phi^2 \\ E_L &= \frac{{\Phi_0}^2}{(2\pi)^2 L}, \quad E_C=\frac{e^2}{2C}, \quad E_J=\frac{I\Phi_0}{2\pi} \end{aligned} \tag{1}$$

where $\phi-$ is the phase, N-is the operator of the number of electron pairs, $\Phi_{ex}--$ external magnetic flux through the loop, E_L- is the inductive energy, E_c- is the charging energy, E_J- is the Josephson energy.

The fluxonium qubit adjusts in frequency by changing the external magnetic flux in the circuit, and in the depth the magnetic flux quantum has a double-well potential with a tunnel connection between the wells, which leads to splitting of the levels. The transition energy between lower levels is determined by the probability of tunneling between two potential wells. Distinctive characteristics of fluxonium are low transition frequency in half a magnetic flux quantum, high coherence times and large anharmonicity. The equivalent electrical circuit of a fluxonium qubit is shown in the Figure (1).

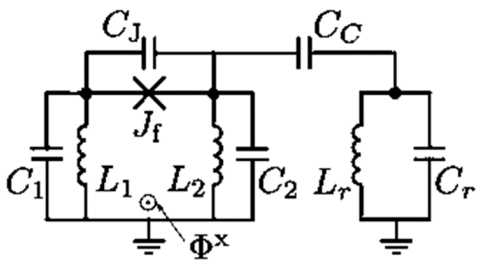

Figure 1: Electrical circuit of a fluxonium qubit.

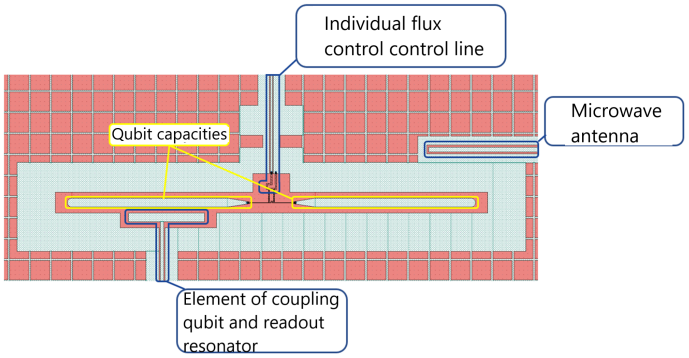

Figure 2: Fluxonium qubit topology.

Dielectric loss

One of the main loss channels of a superconducting qubit is dielectric losses, which refers to the relaxation of the qubit due to the transfer of energy to defects in the material. Electromagnetic energy distributed throughout the chip interacts with defects on the surface of the dielectric material. These defects are usually described as two-level systems (TLS) [2]. TLS can be low-energy (fluctuators) and high-energy, that is, comparable to the transition energy of a qubit. Low-frequency TLS can interact with high-frequency ones associated with the qubit, and as a result cause fluctuations in the frequency of the qubit, that is, cause its dephasing. High-frequency TLS, due to tunneling between its own low levels, leads to relaxation of the qubit, that is, to energy losses. The mechanism of dielectric losses consists in the interaction of the dipole moment of the TLS with electric fields on the surface of the dielectric, and the frequency of the qubit directly determines the relaxation constant. Since the thickness of the dielectric layer is small, the total loss coefficient in the dielectric can be described by Equation (2) .

$$\gamma = \omega\varepsilon \left(\int \frac{E^2}{2} dS_1 + \int \frac{E^2}{2} dS_2 + \int \frac{E^2}{2} dS_3 \right) \tag{2}$$

where S_1, S_2, S_3 is interface areas.

We consider only three types of surfaces:interface between aluminum on the substrate and between aluminum and air (direct deposition, optical lithography); interface between aluminum and silicon Josephson junction and between this aluminum and air (shadow deposition, electron lithography); interface between air and substrate (Figure 3 (b).

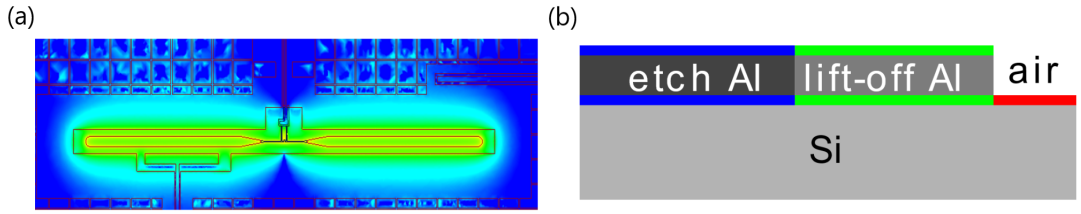

Figure 3: Calculation of dielectric losses. (a)Distribution of the electrostatic field across the chip. (b) Schematic representation of the interfaces.

The contribution of various surfaces to the distribution of electric fields was calculated using the Ansys Maxwell program (Figure 3 (a)). The integrals of the electric field energy over the lower surfaces of the regions were calculated, as well as the total energy of the electric field corresponding to a given voltage, after which the ratio of the surface integral to the total electric field energy was calculated. The resulting ratio has the dimension of the inverse length. In order to obtain the calculated loss value, these participation shares should be multiplied by the effective thickness of the interfaces and the tangents of the dielectric loss angles in them.

Control magnetic flux line

An individual magnetic flux bias line makes it possible to control the frequency of each qubit, which is necessary for system scalability. However, due to the connection with the environment, the line is a source of loss and causes the qubit to relax. The control line is inductively connected to the qubit. The lifetime of qubits due to losses in the flux control line can be estimated according to Fermi's golden rule, in which losses are caused by flux noise due to the mutual inductance of the qubit and the flux line [3] Equation (3):

$$\Gamma = \vartheta_{0-1} \frac{\pi R_Q}{Z_0} \frac{M^2}{L^2} |\langle 0 | \hat{\varphi}_q | 1 \rangle|^2 \tag{3}$$

where $\hat{\varphi}_q$-is the matrix element of fluxonium mode, and $M = \mathrm{L_{DC}}$

For the parameters of the fluxonium qubit, characteristic times are on the order of 1 ms. Another way to think about these losses is to use a model in which the qubit is connected via a flux line to a 50 ohm resistor (the characteristic impedance of electronic devices). In this case, the flow line will be a thermal reservoir characterized by an infinite set of modes. The most important modes are the modes at the qubit frequencies, since it is with them that the resonant interaction occurs.

Using the universal finite element analysis software Ansys HFSS in the eigenmode analysis mode, a study was carried out of the relaxation of a qubit into a flow control line depending on its geometry, namely the length and width of the region near the connection of the flow line with the qubit. The double-well potential was set using the negative inductance of the element (this is how the issue with the nonlinear inductance of the Josephson junction was resolved). The quality factors of the mode with frequent transition of the qubit were obtained depending on changes in parameters of length and width of the region. The optimal geometry with mode lifetimes exceeding 1 ms was selected Equation (4) .

$$\mathrm{T_1} = \frac{Q}{2\pi\vartheta_{0-1}} \tag{4}$$

where Q is the quality factor.

Figure (4) shows a comparison of experimental data on qubit relaxation for the new optimized (a) and old topologies (b).

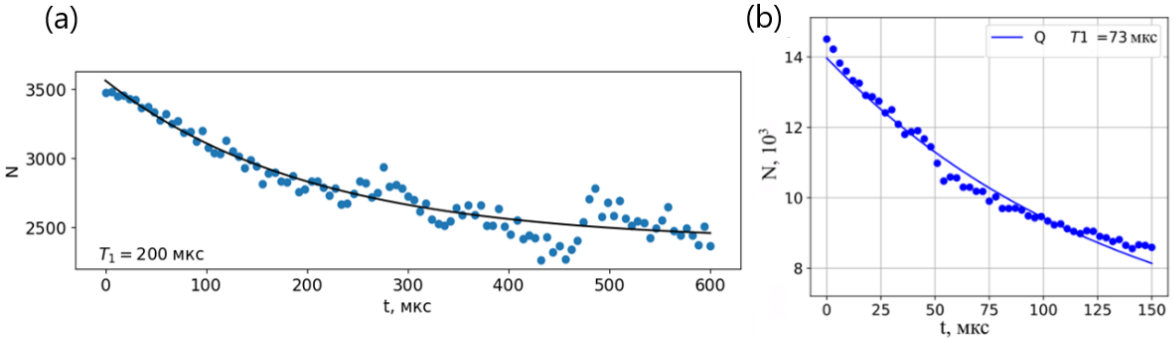

Figure 4: Relaxation time of the new topology (a) and the old topology (b).

References

[1] *Ilya N. Moskalenko, Ilya A. Simakov, Nikolay N. Abramov, Alexander A. Grigorev, Dmitry O. Moskalev, Anastasiya A. Pishchimova, Nikita S. Smirnov, Evgeniy V. Zikiy, Ilya A. Rodionov and Ilya S. Besedin*, High fidelity two-qubit gates on fluxoniums using a tunable coupler Appl. Phys. Lett., 119 (19): 194001 (2021).

[2] *C. Müller, J.H. Cole and J. Lisenfeld*, Towards understanding two-level systems in amorphous solids – insights from quantum devices. Rep. Prog. Phys. 82, 124501 (2019).

[3] *Helin Zhang, Srivatsan Chakram, Tanay Roy, Nathan Earnest, Yao Lu, Ziwen Huang, D.K. Weiss, Jens Koch, and David I. Schuster*, Universal Fast-Flux Control of a Coherent, Low-Frequency Qubit. Phys. Rev. X, Vol. 11, January 2021. P. 011010.

Miass, Russia February 25 – March 2, 2024
7th International School on Quantum Technologies

MS gate infidelity due to high-order Lamb-Dicke terms

Andrei Chuchalin[1*], **Evgeniy Anikin**[1], **Kirill Lakhmanskiy**[1]

[1] *Russian Quantum Center, Moscow, Russia*
*E-mail: a.chuchalin@rqc.ru

Abstract

Molmer-Sorensen gate is used to entangle ions in Paul's trap. To realize the MS-gate, high-order Lamb-Dicke terms are neglected in the Hamiltonian. However, the error occurs due to this assumption. In order to estimate it we at first considered the simplest model involving two ions and one oscillation mode and then expanded the approach to the general case of N ions and 2N modes. The perturbation theory (Dyson series) was applied and the second order corrections have been calculated and compared with the numerical simulation.

Quantum computing is a rapidly advancing field that has the potential to revolutionize the way of information processing and provides the ability to solve problems that are currently intractable for classical computers. Ion chains are a good candidate for quantum computing due to their long coherence times, high entangling gate fidelities, and all-to-all qubit connectivity. The ions are trapped and manipulated using electromagnetic fields, allowing to control their internal states and perform entangling gates. One of the proposed schemes which decouples internal states of ions from motional ones is the MS gate. It is realized by radiating the bichromatic laser field with frequencies $\omega \pm \mu$ on two ions, where $\hbar\omega$ is the energy splitting of the qubit states. We consider the case of counter-propagating beams. The resulting Hamiltonian in the interaction picture becomes[1]:

$$\hat{H} = -\sum_i \Omega_i(t) \sin(\mu t + \psi_i + k_{ia}\hat{r}_\alpha)\sigma_{\theta_i} \tag{1}$$

$$k_{i\alpha}\hat{r}_\alpha = -\sum_m \eta_{im}\left(\hat{a}_m e^{-i\omega_m t} + \hat{a}_m^\dagger e^{i\omega_m t}\right) \tag{2}$$

where $\hat{a}_m$ ($\hat{a}_m^\dagger$) annihilation (creation) operators of m-th motional mode, ω_m is its frequency and $\sigma_{\theta_i} = \sigma_x cos(\theta_i) + \sigma_y sin(\theta_i)$. Hence, the Hamiltonian becomes:

$$\hat{H} = -\sum_{i,m} \Omega_i(t) \sin\left(\mu t + \psi_i - \eta_{im}\left(\hat{a}_m e^{-i\omega_m t} + \hat{a}_m^\dagger e^{i\omega_m t}\right)\right)\sigma_{\theta_i} \tag{3}$$

By considering the Lamb-Dicke regime: $\eta_{im} \ll 1$ one can expand the sine function to obtain:

$$\hat{H} = -\sum_{i,m} \Omega_i(t)(\sin\left(\mu t + \psi_i\right) - \eta_{im}\left(\hat{a}_m e^{-i\omega_m t} + \hat{a}_m^\dagger e^{i\omega_m t}\right) cos(\mu t\ + \psi_i))\,\sigma_{\theta_i} \tag{4}$$

Therefore, the evolution operator:

$$\hat{U} = e^{-i\sum_{i<j}\chi_{ij}\sigma^i_{\theta_i}\sigma^j_{\theta_j}} \prod_m D\left(\sum_i \sigma^i_{\theta_i}\alpha_{im}\right) \tag{5}$$

$$\alpha_{im}(t) = -i\int_{t_0}^{t} \eta_{im}\Omega_i(t')\, cos(\mu t' + \psi_i)\, e^{-i\omega_m t'} dt' \tag{6}$$

$$\chi_{ij}(t) = -2Im\int_{t_0}^{t}\int_{t_0}^{t'} \alpha^*_{im}(t')\,\alpha_{jm}(t'')\, dt'' dt' \tag{7}$$

However, the error occurs due to this expansion. At first, we considered the simplest model involving two ions and one motional mode. We computed the second order perturbation theory and compared it with the numerical simulation, see Fig. 1. Next, we considered the general model involving N ions and

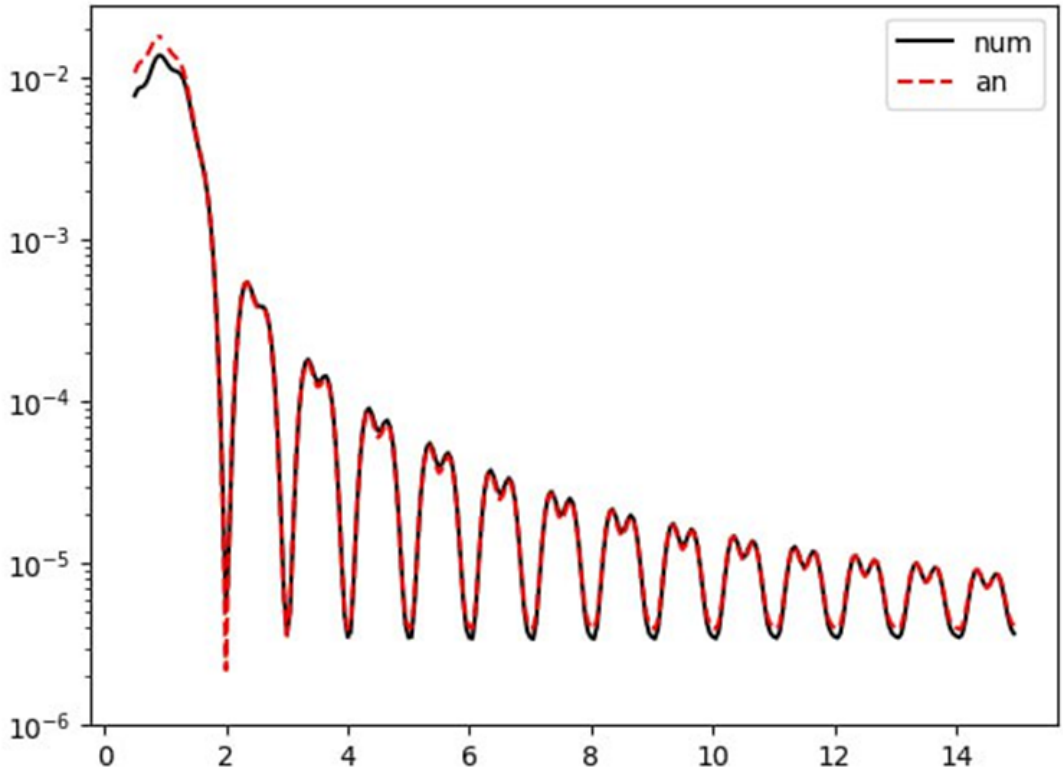

Figure 1: Simplest model

$2N$ motional modes. We computed the infidelity by using the perturbation theory:

$$1-F = \frac{1}{N(N-1)2^{N+1}} \sum_{smm_1} |\sum_i (-1)^{s_i} f_{imm_1}|^2 + \frac{1}{N2^{N+1}} \sum_{sm} |\sum_i (-1)^{s_i} f_{imm}|^2 + \frac{1}{N2^N} \sum_{sm} |\sum_{im_1jk} (-1)^{s_i+s_j} h_{imm_1jk}|^2 \tag{8}$$

$$f_{imm_1} = \int_{t_0}^{t} \eta_{im}\eta_{im_1}\Omega_i(t) sin(\mu t + \psi_i) e^{i(\omega_m+\omega_{m_1})t} dt \sigma^i_{\theta_i} \tag{9}$$

$$h_{imm_1jk} = \int_{t_0}^{t} \Omega_i(t)\eta_{im}\eta_{im_1} sin(\mu t + \psi_i) e^{i\omega_m t}(\alpha_{jk} e^{-i\omega_{m_1} t} + \alpha^*_{jk} e^{i\omega_{m_1} t}) dt \sigma^i_{\theta_i} \sigma^j_{\theta_j} \tag{10}$$

We plotted the resulting infidelity, see Fig. 2.

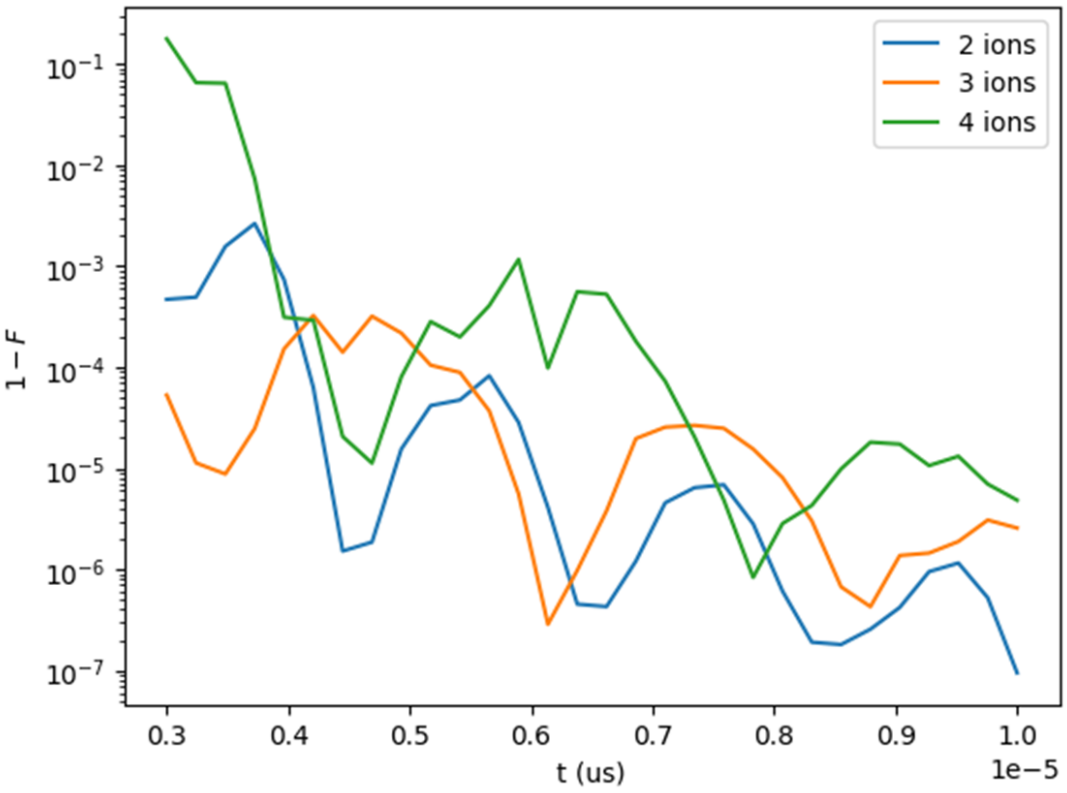

Figure 2: General model

References

[1] *A. Sørensen and K. Mølmer*, Entanglement and quantum computation with ions in thermal motion. Phys. Rev. A **62**, 022311 (2000).

Quantum hashing functions based on the orbital angular momentum of light

Nail' Shafeev[1,2*], Akat'ev Dmitriy[2], Dinislam Turaykhanov[2], Alexey Kalachev[1,2]

[1] *Institute of Physics, Kazan Federal University, Kazan, Russia*
[2] *Zavoisky Physical-Technical Institute, FRC Kazan Scientific Center, Russian Academy of Sciences, Kazan, Russia*
*E-mail: leovaldez242@gmail.com

Abstract

In the present work we investigate the properties of single-photon wave packets with orbital angular momentum generated in the process of spontaneous parametric down-conversion, consider the implementation of a quantum tomography protocol and implement a quantum hashing protocol based on multidimensional single-photon states of light.

Introduction

Encoding of information based on multidimensional single-photon states (qubits) has a greater information capacity, which increases the transmission range or increases the speed of distribution of the secret key by a number of times proportional to the dimension of the qubit [1], [2], [3]. The generation of high-dimensional quantum states is one of the important tasks in quantum optics. One of the most promising ways to solve it is to use the spatial degrees of freedom of the photon, for example, the orbital angular momentum of light. Under conditions of spontaneous parametric down-conversion, it is convenient to obtain multidimensional spatial single-photon states of light [4]. Thanks to this, we can apply spatial modes to transmit information over long distances through free space where it is impossible to implement fiber-optic communication, namely, for long-range quantum communication and communication with a satellite [5].

Quantum hashing functions

To be used, cryptographic hashing functions must have two main properties: unidirectionality and collision resistance. We have to fulfill the following conditions:

$$P_{\text{extraction}} = \frac{d^s}{2^n} \ll 1, \tag{1}$$

where n is the size of the hashed classical message in a 2-dimensional Hilbert space built on the states of s qudits, d is the dimension of the qudit state space, otherwise we will not be able to extract the full amount of information from the received message. As for the condition of resistance to collisions, we cannot formulate it in the same way as for classical states, because we can reliably distinguish only orthogonal states. Therefore, it has been proposed that the measure of collision resistance is the degree of orthogonality of two quantum hashes (quantum states obtained as a result of hashing):

$$P_{\text{collision}} = \max_{x_1,x_2,x_1\neq x_2} |\langle \Psi(x_1) \mid \Psi(x_2)\rangle|^2 = \max_{x_1,x_2,x_1\neq x_2} \frac{1}{d^{2m}} \tag{2}$$

$$\prod_{j=1}^{m} \left| 1 + e^{\frac{2\pi s_{j,2}(x_1-x_2)}{q}} + \cdots + e^{\frac{2\pi s_{j,2}(x_1-x_2)}{q}} \right|^2,$$

To do this, we took the worst case for two pairs of input messages x_1 and x_2: consider the simple case when $x_1 = 0$, x_2 is the maximum scalar product of two quantum states (hash sums). This procedure was performed for cubes and cutrites, depending on the number of quantum information carriers used in the hashing process (Table 1)

Table 1: The values of x_1 for the worst case, calculated for different dimensions d and a different number of quantum states m, used in the procedure of quantum hashing of 8 bits of classical information.

m	$d = 2$	$d = 3$
1	1	97
2	9	69
3	24	93
4	114	95
5	97	123
6	76	–
7	69	–

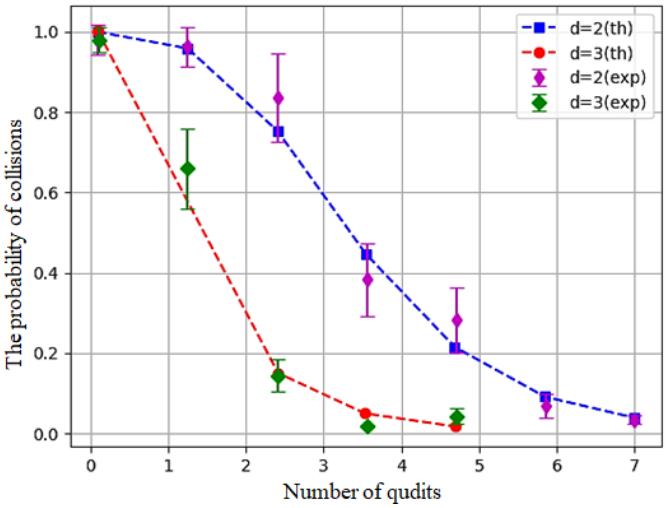

Figure 1: The probability of observing a collision as a function of the number of qudits for different dimensions of the quantum state of qudits

Conclusion

The obtained results demonstrate that the use of high-dimensional states makes it possible to speed up the operation of the quantum hashing protocol by reducing the number of quantum information carriers necessary to achieve optimal hashing parameters.

References

[1] *N.K. Langford, R.B. Dalton, M.D. Harvey, J.L. O'Brien, G.J. Pryde, A. Gilchrist, S.D. Bartlett, A.G. White*, Measuring entangled qutrits and their use for quantum bit commitment. Physical review letters. **93**, 053601 (2004).

[2] *P. Sharapova, A.M. Pérez, O.V. Tikhonova, M.V. Chekhova*, Schmidt modes in the angular spectrum of bright squeezed vacuum. Physical Review A. **91**, 043816 (2015).

[3] *D.N. Klyshko, A. N. Penin, B. F. Polkovnikov*, Parametric luminescence and light scattering by polaritons. Soviet Journal of Experimental and Theoretical Physics Letters **11**, 5 (1970).

[4] *M.N. O'Sullivan-Hale, I.A. Khan, R.W. Boyd, J.C. Howell*, Pixel Entanglement: Experimental Realization of Optically Entangled $d = 3$ and $d = 6$ Qudits. Physical review letters. **94**, 220501 (2005).

[5] *D.A. Turaykhanov, D.O. Akat'ev, A.V. Vasiliev, F.M. Ablayev, and A.A. Kalachev*, Quantum hashing via single-photon states with orbital angular momentum. Physical Review A. **104**, 052606 (2021).

[6] *D.O. Akat'ev, A.V. Vasiliev, N.M. Shafeev, F.M. Ablayev, A.A. Kalachev*, Multiqudit quantum hashing and its implementation based on orbital angular momentum encoding. Laser Physics Letters. **19**, 125205 (2022).

Miass, Russia February 25 – March 2, 2024
7th International School on Quantum Technologies

A 2D MOT of Tm atoms as a compact source for continuous loading of a narrow-line 3D MOT

M. Yaushev[1,2*], **D. Mishin** [1,2], **D. Tregubov** [1,2], **D. Provorchenko** [1,2], **N. Kolachevsky** [1,2], **and A. Golovizin** [1,2]

[1] *P. N. Lebedev Physical Institute of the Russian Academy of Sciences*
[2] *Russian Quantum Center*
*E-mail: iaushev.mo@phystech.edu

Abstract

We present a novel setup for cooling thulium atoms based on a two-dimensional magnito-optical trap. This setup is expected to be capable of producing atomic fluxes of more than 10^8 atoms per second at relatively low oven temperatures around 800 K. Such a source can be used not only as a convenient and more efficient replacement for current setups based on Zeeman slower, but will also make it possible to proceed to fundamentally new experiments where a continuous flux of cold atoms is required.

Ensembles of neutral atoms are widely used for experiments in quantum computing [1], quantum simulations [2] and quantum sensing [3]. Laser cooling is the first step in these experiments. There is a lot of effort being put into developing new laser cooling schemes. One promising direction is the application of a two-dimensional magneto-optical trap (2D MOT) for creating a continuous flux of cold atoms. The advantages of this source include:

1. Compactness in comparison with the classical Zeeman slower. This is essential for transportable systems (e.g., optical clocks)

2. Absence of hot atoms flow from the atomic oven into the main ("science") vacuum chamber, which allows to reach ultrahigh vacuum, which is necessary for experiments with degenerate quantum gases, as well as for quantum computing.

3. The possibility of operation of secondary MOT with deep laser cooling in continuous mode, which is necessary for realization of optical clocks with continuous interrogation of the clock transition [4, 5] and experiments with continuous BEC [6]

Earlier we have demonstrated the advantages of thulium atoms for creating a transportable frequency standard [7], namely: low sensitivity to black-body radiation [8], convenient magic wavelength for optical lattice formation [9], and the synthetic frequency technique allowing to eliminate the Zeeman effect of the second order [10]. Thulium is also a promising platform for quantum simulators [11].

Here we discuss the design of a source of cold thulium atoms based on a two-dimensional magneto-optical trap on a broad transition at a wavelength 410 nm alongside numerical simulation results of its performance [12]. Similarly to three-dimensional case, we use three pairs of counter-propagating laser beams. The only difference is the hole in the mirror along one axis through which atoms are accelerated to the next vacuum chamber. In this chamber the remaining stages of the experiment can be carried out, vacuum level will not be degraded by the abundance of hot atoms, and the continuous resonant emission of the two-dimensional trap can be spatially separated from the spectroscopic region.

The simulation showed that, in the optimal configuration, with a total radiation power of 50 mW and an atomic oven temperature of 800 K, the source can provide a flux of $4 \cdot 10^8$ cold atoms per second, and when the temperature of the oven is increased, it can reach values of the order of 10^{11} atoms per second. The cold atomic beam has narrow longitudinal velocity distribution with center at $v = 8$ m/s and FWHM of 1 m/s. The angular spread of the atomic beam is less than $\phi = 50$ mrad. Such beam characteristics should allow direct capturing of almost all atoms in the MOT on the narrow transition at 530 nm.

References

[1] M. Saffman, "Quantum computing with atomic qubits and rydberg interactions: progress and challenges," *Journal of Physics B: Atomic, Molecular and Optical Physics*, vol. 49, p. 202001, oct 2016.

[2] I. M. Georgescu, S. Ashhab, and F. Nori, "Quantum simulation," *Rev. Mod. Phys.*, vol. 86, pp. 153–185, Mar 2014.

[3] K. Bongs, M. Holynski, J. Vovrosh, P. Bouyer, G. Condon, E. Rasel, C. Schubert, W. P. Schleich, and A. Roura, "Taking atom interferometric quantum sensors from the laboratory to real-world applications," *Nature Reviews Physics*, vol. 1, pp. 731–739, Dec 2019.

[4] H. Katori, "Longitudinal ramsey spectroscopy of atoms for continuous operation of optical clocks," *Applied Physics Express*, vol. 14, p. 072006, jul 2021.

[5] D. Mishin, D. Provorchenko, D. Tregubov, N. Kolachevsky, and A. Golovizin, "Continuous operation of a bicolor thulium optical lattice clock," *Applied Physics Express*, vol. 14, p. 112006, nov 2021.

[6] C.-C. Chen, R. González Escudero, J. Minář, B. Pasquiou, S. Bennetts, and F. Schreck, "Continuous bose–einstein condensation," *Nature*, vol. 606, no. 7915, pp. 683–687, 2022.

[7] A. Golovizin, D. Tregubov, D. Mishin, D. Provorchenko, and N. Kolachevsky, "Compact magneto-optical trap of thulium atoms for a transportable optical clock," *Opt. Express*, vol. 29, pp. 36734–36744, Oct 2021.

[8] A. Golovizin, E. Fedorova, D. Tregubov, D. Sukachev, K. Khabarova, V. Sorokin, and N. Kolachevsky, "Inner-shell clock transition in atomic thulium with a small blackbody radiation shift," *Nature communications*, vol. 10, no. 1, p. 1724, 2019.

[9] D. A. Mishin, D. I. Provorchenko, D. O. Tregubov, A. A. Golovizin, K. Y. Khabarova, V. N. Sorokin, and N. N. Kolachevsky, "Effect of optical lattice field on characteristics of a clock transition in thulium atoms," *Quantum Electronics*, vol. 52, no. 6, p. 505, 2022.

[10] A. A. Golovizin, D. O. Tregubov, E. S. Fedorova, D. A. Mishin, D. I. Provorchenko, K. Y. Khabarova, V. N. Sorokin, and N. N. Kolachevsky, "Simultaneous bicolor interrogation in thulium optical clock providing very low systematic frequency shifts," *Nature communications*, vol. 12, no. 1, p. 5171, 2021.

[11] V. A. Khlebnikov, D. A. Pershin, V. V. Tsyganok, E. T. Davletov, I. S. Cojocaru, E. S. Fedorova, A. A. Buchachenko, and A. V. Akimov, "Random to chaotic statistic transformation in low-field fano-feshbach resonances of cold thulium atoms," *Phys. Rev. Lett.*, vol. 123, p. 213402, Nov 2019.

[12] M. O. Yaushev, D. A. Mishin, D. O. Tregubov, D. I. Provorchenko, N. N. Kolachevskii, and A. A. Golovizin, "Two-dimensional magneto-optical trap for producing a flux of cold thulium atoms," *Journal of Experimental and Theoretical Physics*, vol. 137, pp. 178–186, Aug 2023.